DEVELOPMENT, CHARACTERIZATION AND EVALUATION OF SELECTED TRANSITION METAL DOPED ZINC SULPHIDE NANOSTRUCTURE SURFACE LAYERS DECORATED WITH GRAPHENE FOR WATER SPLITTING

BY

JOAN JEPTUM KIPTARUS

A THESIS SUBMITTED TO THE SCHOOL OF ENGINEERING, DEPARTMENT OF MANUFACTURING AND TEXTILE ENGINEERING IN PARTIAL FULFILMENT OF THE REQUIREMENTS FOR THE AWARD OF THE DEGREE OF DOCTOR OF PHILOSOPHY IN INDUSTRIAL ENGINEERING

,

MOI UNIVERSITY

2025

Declarations

Declaration by the Student

This thesis is my original work and has not been presented for a degree in any other university. No part of this thesis may be reproduced without prior written permission of the author and/or Moi University.

Signature:..... Date: .....

Joan Jeptum Kiptarus,

ENG/DPHIL/IE/02/18

Declaration by the Supervisors

This research thesis has been submitted for examination with our approval as University supervisors.

Signature:..... Date: .....

Prof. Henry Kiriamiti,

Department of Chemical and Process Engineering,

School of Engineering, Moi University

Signature:..... Date: .....

Prof. David Njuguna Githinji,

Department of Manufacturing, Industrial and Textile Engineering, School of Engineering, Moi University.

Signature:..... Date: .....

Dr. Kiptiemoi Korir Kiprono,

Department of Mathematics, Physics and Computing,

School of Sciences and Aerospace Studies, Moi University.

Dedication

This research is dedicated to:

My late parents

and

Family

Whose love and support have seen me this far.

Acknowledgements

This work was supported by the African Development Bank (AFDB), the Center of Excellence in Phytochemicals, Textile and Renewable Energy (ACE II PTRE), Moi University, Kenya, the SAMat Research Facilities, the Jawaharlal Nehru Centre for Advanced Scientific Research (JNCASR), Bengaluru, India, and Strengthening mobility and Promoting Regional integration in Engineering Education in Africa (SPREE). The Centre for High Performance Computing (CHPC) in Cape Town is acknowledged for providing computing resources and support (under project: MATS0868). I sincerely thank Prof. C. N. Rao for allowing me to visit JNCASR, Bangalore, India for my research experiments. Much appreciation goes to Prof. Sebastian C. Peter for allowing me to work in his lab under his guidance. Much gratitude's to Prof. Umesh Waghmare for his overwhelming support and all the SCP family for their assistance. Sincere gratitude's to Moi University for giving me a chance to take part in staff research exchange program. I would also like to express my deep and sincere gratitude's to my research supervisors: Prof. Henry K. Kiriamiti, Dr. David N. Githinji, Dr. Kiptiemoi k. Korir for their positive criticism and providing invaluable guidance throughout this research. Many thanks to Prof. Ambrose Kiprop for his overwhelming support. I am grateful to all my colleagues from my department of Mehanical, Production and Energy Engineering (MPEE), Manufacturing, Textile and Industrial Engineering (MTI) and other departments who supported me to complete the PhD research work directly or indirectly. May God bless you all.

Abstract

Water splitting (WS) is the dissociation of Water (H_2O) into Hydrogen (H_2) and Oxygen (O_2). Zinc Sulphide (ZnS) provides an excellent option for the hydrogen reduction cathode in photo electrochemical (PEC) cells for WS. However, its low sensitivity to visible range in electromagnetic spectrum limits its practical applicability. Few comprehensive studies consider a wide range of transition metals as potential dopants to meet future energy requirements for greater PEC WS. The main objective of this research was to develop, characterize and evaluate the selected Transitional metal (TM) doped ZnS nanostructure (NS) surface layers decorated with graphene (rGO) for WS. The specific objectives were to: simulate the optimal dosage of TM dopants for ZnS nanostructure layers, synthesize TM doped ZnS NS layers decorated with graphene, characterize TM doped ZnS NS layers decorated with graphene and to evaluate the photocatalytic hydrogen production of TM doped ZnS NS layers decorated with graphene. Theoretical first principles Ab-Initio calculations based on Density functional theory (DFT) method was employed to examine the electronic structure of ZnS nanostructures (NSs) doped with selected TM dopants including; manganese (Mn), copper (Cu), cobalt (Co) and iron (Fe) in order to modify the structural properties of ZnS NSs. Highly distributed cobalt doped ZnS NSs were effectively fabricated on the surfaces of graphene sheets via simple hydrothermal technique. The structural, electronic and optical properties of the cobalt doped ZnS decorated with graphene (Co-ZnS-rGO-NS's) were examined using X-ray diffraction (XRD), X-ray photocurrent spectroscopy (XPS), Raman spectroscopic (RS), Fourier transmission infrared spectroscopy (FTIR), Scanning electron microscopy (SEM) and Ultra violet visible absorbance spectroscopy (UV-vis). The photocatalytic activity of $Co_xZn_{1-x}S$rGO NS's at (x = 0, 1, 2, 4 and 6) atomic percentage (atm.%) was determined in lab experiments using water and visible light. The stability of $3d$ orbital transitional metal dopant (TMD's)'s in ZnS NSs were shown to be dependent both on the dopant concentrations and the d orbital character of the TMD's. Evidently, the $3d$ orbital TMD's's (Cu, Co,Mn and Fe) showed low formation energies and appropriate band edge states due to their low lattice strain, hence absorbed into ZnS NSs. ZnS doped with 4 atm.% of Cu and Co was shown to be optimal for photocatalytic hydrogen generation based on theoretical studies. The findings of XRD, FTIR, RS, XPS and SEM investigation suggest that graphene oxide (GO) was successfully transformed into graphene sheets, $Co_xZn_{1-x}S$rGO NS's possessed a crystalline, cuboidal and spheroidal form of structure displaying a paper like appearance. UV-vis spectrophotometric analysis verified a notable rapid increase in transmittance and high transparency ($\approx 90\%$) within (180-800)

nm wavelength range. Calculations of transmittance spectra revealed a direct allowable band gap range of (1.26-5.46) eV, demonstrating a band gap decrease as cobalt content increased, consistent with theoretical predictions. Furthermore, the optimal cobalt loading of 0.04 atm.% generated a maximum hydrogen yield of $7649\mu molh^{-1}$ after 720 minutes of Ultra Violet (UV) light exposure, indicating that the ZnS NSs's electronic and optical characteristics were influenced by their stability with respect to dopant concentration. In conclusion, the results show that improved transfer of photo-generated electrons, increased surface area and better dispersion-absorption properties all contributed to higher photocatalytic hydrogen generation activity. The study recommended synthesis optimization for commercially viable technology.

Contents

List of Tables

List of Figures

Abreviations

CO_2 carbon dioxide.

H_2 Hydrogen.

H_2O Water.

NO_2 Nitrogen dioxide.

O_2 Oxygen.

TiO_2 Titanium oxide.

-C-O epoxy.

-COOH carboxyl.

-OH hydroxyl.

0D Zero dimensional.

1D One dimensional.

2D two dimensional.

3D Three dimensional.

AA ascorbic acid.

AIRSS Ab initio random structure searching.

C=O carbonyl.

CB Conduction band.

CBM Conduction Band Minimum.

CCG chemically modified graphene.

CHPC Centre for High performance Computing.

CIF Crystallographic Information File.

Co cobalt.

Cu copper.

DFT Density functional theory.

DOS Design of States.

DOS's Density of states.

ECUTWFC Cut off energy.

ELS electroluminescence sensors.

fcc face centred cubic.

Fe iron.

FESEM field emission scanning electron microscope.

FLGO few layer graphene oxide.

FTIR Fourier transmission infrared spectroscopy.

FWHM Full Width at Half Maximum.

GC Gas Chromatography.

GGA's generalized-gradient approximations.

GO graphene oxide.

Goal 7 Goal seven.

HER hydrogen evolution reaction.

HRTEM high resolution transmission electron microscopy.

HUMO Highest Occupied Molecular Orbital.

LDA local density approximation.

LUMO Lowest Occupied Molecular Orbital.

Mn manganese.

MPEE Mehanical, Production and Energy Engineering.

MS Metal Sulphide.

MTI Manufacturing, Textile and Industrial Engineering.

NHE Normal Hydrogen Electrode.

Ni nickel.

NM Nanomaterials.

NP Nanoparticles.

NPs nanoparticles.

NRM Nuclear magnetic resonance.

NS nanostructure.

NSs nanostructures.

NWs nanowires.

OER oxygen evolution reaction.

Pb lead.

PDOS projected density of states.

PEC photo electrochemical.

PL Photoluminiscense.

PW Physics Wallah.

QD's Quantumn dots.

QE Quantum ESPRESSO.

rGO Reduced graphene oxide.

RS Raman spectroscopic.

SA surface area.

SAED selected area electron diffraction.

scf self consistent field.

SEM Scanning electron microscopy.

STP Standard Temperature and Pressure.

TCD Thermal conductivity detector.

TEM Transmission electron microscopy.

TM Transitional metal.

TMD's transitional metal dopant.

TW Terra Watts.

UN United Nations.

UV Ultra Violet.

UV-vis Ultra violet visible absorbance spectroscopy.

V volume.

VB Valence band.

VBM valence Band Maximum.

WS Water splitting.

XPS X-ray photocurrent spectroscopy.

XRD X-ray diffraction.

ZnS Zinc Sulphide.

Chapter 1

Introduction

1.1 Background information

The global energy supply and related environmental issues are among the biggest technological challenges being confronted by chemists, technologists and engineers in the 21^{st} century Arutyunov & Lisichkin (2017); Kalogirou (2023). Two of the most pressing problems facing the globe currently are global warming and the energy crisis; Sustainable and carbon neutral sources may be promoted as alternatives to fossil fuels L. Chen et al. (2022); Peter (2018). Natural resources such as coal and petroleum products as a source of energy are nearly exhausted and it is predicted that oil supplies will run out in 50 to 150 years Lewis & Nocera (2006). Additionally, the use of fossil fuels has led to a number of environmental issues, including rising emissions of greenhouse gases, most notably carbon dioxide carbon dioxide (CO_2), Nitrogen dioxide (NO_2) and other air pollutants Netz et al. (2007) which has caused swerve climate change Ahmad et al. (2015); Fajrina & Tahir (2019); Faunce et al. (2013). The total amount of energy consumed worldwide in 2008 was 15Terra Watts (TW) Petroleum (2009) and by 2050, it is predicted that this figure or the burn rate of energy, will have roughly doubled due to the growing global production and population P. Du & Eisenberg (2012). On that account, exploring renewable, clean and carbon-neutral alternative energy

resources is desperately desired to limit our dependency on fossil fuels Quan et al. (2007); Yuan et al. (2022). The hunt for new renewable and sustainable energy sources sparked by rising energy consumption demand continuously presses for the creation of novel materials to address these issues as well as offering high alternative energy harvesting and storage capacities Shang et al. (2023); Sathre et al. (2016). With over 60% of all global greenhouse gas emissions coming from energy, the United Nations (UN) claims that it is the primary cause of climate change. As a result, one of the 17 Sustainable Development Goals adopted by the UN also calls for the exploration of new renewable energy sources Goal seven (Goal 7) Mai et al. (2022). Therefore, it is believed that creating alternative energy sources with no carbon trace is essential for the survival of the worldKorir et al. (2021).

Hydrogen presents itself as a prospective alternative to carboniferous fossil fuels but primarily with consideration of a suitable source. Given that all of the renewable sources (solar energy, wind, geothermal energy heat, tides, biomass, et al), solar energy is the most feasible and from a fundamental scientific view point of view, the most attractive alternative energy source Esswein & Nocera (2007); C. A. Simon (2024). Due to the major environmental consequences of the depletion of fossil fuels, there is growing interest in the conversion of water and solar energy into clean and sustainable H_2 fuels utilising elements that are abundant on earth X. Li et al. (2015). Hydrogen is one such fuel with no emission of pollutants when burned in oxygen X. Li et al. (2023); Q. Hassan et al. (2023), it is the most abundant and cleanest element in nature and has the highest energy content in common fuels which is almost three times that of gasoline in the same weight Bellani et al. (2019). As an ideal energy carrier, hydrogen can be used in various fields such as, communications and transportation, electric power, architecture, industry, in vehicles, spacecraft propulsion, aircraft and electric devices Joy et al. (2018). By using a hydrogen-oxygen fuel cell, hydrogen can be converted into electricity and the byproduct of this process is only water, thus used as a renewable

energy. So far, the main ways to obtain hydrogen are by reforming the natural gas, coal, oil, but these approaches usually come along with the emission of carbon dioxides which do not meet the vision of zero carbon emission M. Yu et al. (2021); Bauer et al. (2022); W. Liu et al. (2022). Scientists hypothesized that using solar, wind, hydro, geothermal and nuclear energy as power source to produce hydrogen will realize a real zero carbon source of hydrogen production Boretti (2023); Turner (2004). Future alternatives to fossil fuels that are considered are hydrogen and electric power. However, there remain significant obstacles impeding the growth of hydrogen energy, regardless of how hydrogen is produced, stored, transported, or used P. Chen et al. (2021). The quest for a clean, renewable and sustainable energy future has been highly sought for by the scientific community over the last four decades. Photocatalytic water splitting is expected to become the dominant method of hydrogen production as a promising approach for clean, economical and environmentally friendly production of hydrogen by using solar energy since Fujishima and Honda first reported the photoelectrochemical water splitting on a Titanium oxide (TiO_2) electrode in 1972 Gopinath & Nalajala (2021); Fujishima & Honda (1972). The relative high energy barrier and slow kinetic properties require utilization of catalyst to improve this situation. At present, noble metal-based materials including ruthenium, iridium, rhodium and platinum are the state-of-the-art water splitting electrocatalysts due to their high reactive in acidic and alkaline condition P. Wang et al. (2011); Y. Li et al. (2020); Cavaliere (2023). However, the cost of using these catalysts on a wide scale has significantly increased by their rarity and the mining whereby the refining procedures have a negative impact on the environment. Exploring a reliable and stable non-noble metal-based material is therefore the focus of many research efforts today P. Chen et al. (2021). Energy disciplines have increasingly put much interest in to transition metal base materials such carbides, nitrides, phosphides, sulfides, oxides and their composites Voiry et al. (2013); X.-T. Wang et al. (2020); Zhao et al. (2020). Transition metal base materials offer a wide range of applications in areas including

energy storage and conversion, sensors and photo or electrocatalysis due to their distinctive electrical structure and great physical properties Q. Wang et al. (2016); R. Patel et al. (2018). Nanostructures materials have become the main attraction for material researchers due to their contributions to different disciplines such as environment, electronics, photonics, medicine, etc. Various kinds of nanomaterials have been developed and are currently utilized in innumerable applications Razali & Ismail (2021). Due to their distinctive chemical and electrical structure, ZnS, a group II–VI semiconductor, has attracted a lot of interest because it has proven to be an effective photocatalyst Agorku et al. (2015). The large band gap (3.60 eV) prevents it from being utilized for photocatalysis in the visible light range. To fully utilize the potential of sunlight for hydrogen synthesis, a photocatalyst material with visible-light activity must be used Kurnia, Ng, Tang, et al. (2016); L. Wang et al. (2020); Villa et al. (2021); Hao et al. (2018); Fajrina & Tahir (2019).

1.1.1 Photocatalytic water splitting

The process of designing visible light driven photo catalysts begins with band engineering. It is well acknowledged that a material's performance in photo electrochemical PEC and other optoelectronic applications is influenced by its structure and morphology, which include defects in both the bulk and surface, as well as particle size, crystal structure and surface morphology. G.-J. Lee & Wu (2017); Kong et al. (2011); Bell et al. (2011). Photoelectrochemical (PEC) catalysis and electrocatalysis are some of the approaches of hydrogen fuel production via water splitting. PEC water splitting based devices utilize an active semiconductor anode material such as ZnS to absorb solar energy necessary to break the chemical bond of a water molecule. The oxygen evolution reaction oxygen evolution reaction (OER) and the hydrogen evolution reaction hydrogen evolution reaction (HER) are the two chemical processes of water splitting Nellist (2016). As seen in figure 1.1, these processes don't have favorable thermodynamics hence, an external potential bias is needed to cause the uphill response $\Delta E^0 = -1.23V$. The OER

takes place in electrolytic cells and involves four electron transfers (see Equation 1.1) and is viewed as the challenge in breaking down water molecules into H_2 and O_2 gases.

$$2H_2O(l) \longrightarrow O_2(g) + 4H^+(aq) + 4e^-. \tag{1.1}$$

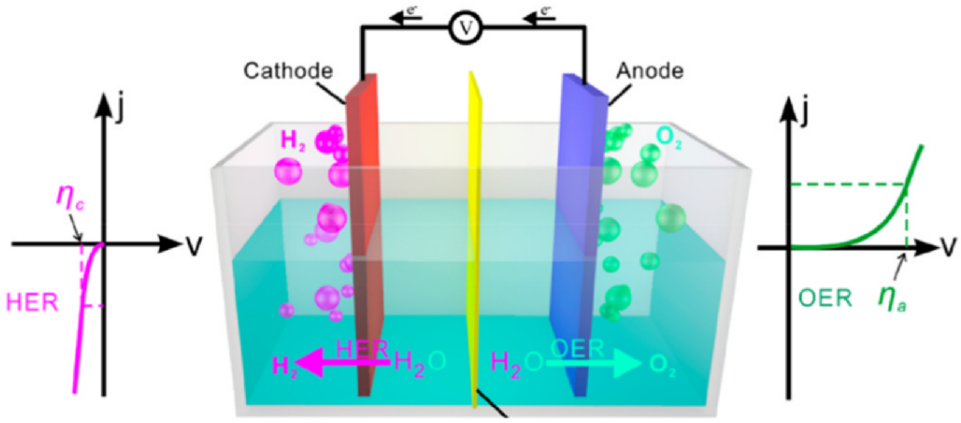

Figure 1.1: Schematic illustration of an electrochemical hydrogen and oxygen reaction. *(Source; J. Zhu et al. (2019))*

The electrochemical water splitting reactions that take place in electrolyzers with a cathode and anode are usually what allow water reduction and oxidation processes to happen Eßmann et al. (2016); McHugh et al. (2020). Commonly employed electrolytes are sulfuric acid and potassium hydroxide, which create an alkaline and acidic environment, respectively Ruetschi & Amlie (1966); Ranganatha (2023). The operations proceed in appropriate electrolytes where ions and charges diffuse between the electrodes. When an adequate voltage is provided to the electrodes during the electrochemical water splitting reaction, the water is separated into hydrogen and oxygen, which can be stated in Equation 1.1: This overall reaction includes two half reactions which is HER and OER respectively, as shown in Figure 1.1. The overpotential η is one of the essential criteria to evaluate the activity of the electrocatalysts. In theory, HER and OER have onset potentials to start the reaction, which is 0 V and 1.23 V, respectively. However, the practical HER and OER processes normally require an extra potential to overcome the kinetic barriers. This extra potential is called overpotential. The value

of overpotential at a specific current density can reflect the activity of catalyst, the lower overpotential, the better electrocatalytic performance of the catalyst.

To generate the required over potential for water splitting, conventional industrial electrolyzers depend on outside power sources. That being said, combining such electrolyzers with renewable energy sources, such as solar energy, is a more sustainable way to produce hydrogen. Both water and solar energy are widely available and abundant Roger et al. (2017); C. Hu et al. (2017). From this vantage point, the most anticipated approach of generating hydrogen by splitting water while employing solar light energy is PEC catalysis J. Zhang, Liu, et al. (2011) and it is an important reaction from the viewpoint of global energy and environmental concerns Kudo & Miseki (2009). Therefore, designing efficient photocatalytic materials for the production of clean energy fuels, such as hydrogen and for photocatalytic degradation of environmental pollutants represents a remarkable route to deal with energy crisis, environmental pollution issues and global warming problems. Fujishima and Honda's pioneering work from 1972 Fujishima & Honda (1972) documented water splitting for H_2 production over TiO_2 semiconductor. Since then, numerous semiconductor kinds have been studied for photocatalytic H_2 production. Multiple active photocatalysts including different oxide, sulfide, and oxynitride semiconductors have been developed for the aforementioned photocatalytic reaction J. Zhang et al. (2012). Because of their adequate band gap and catalytic function, metal sulfides and their composites are among them and are considered ideal candidates for photocatalytic H_2production. Recent years have seen a lot of interest in the exceptional physical and chemical properties of semiconductor metal sulfides. Very lately a number of binary metal sulfide Metal Sulphide (MS) compounds, including PbS, CdS, ZnS, MoS_2, SnS_2, Bi_2S_3, In_2S_3, Cu_2S, NiS/NiS_2 and CoS_2 as well as their derivatives and heterostructures, have been extensively utilized for a variety of uses Maeda et al. (2006); Bonde et al. (2009); Balayeva & Mamiyev (2016); Baran et al. (2015). The most popular metals used in photocatalytic hydrogen production as sulfide compounds have been

summarized in Figure 1.2. The majority of these compounds have been found to

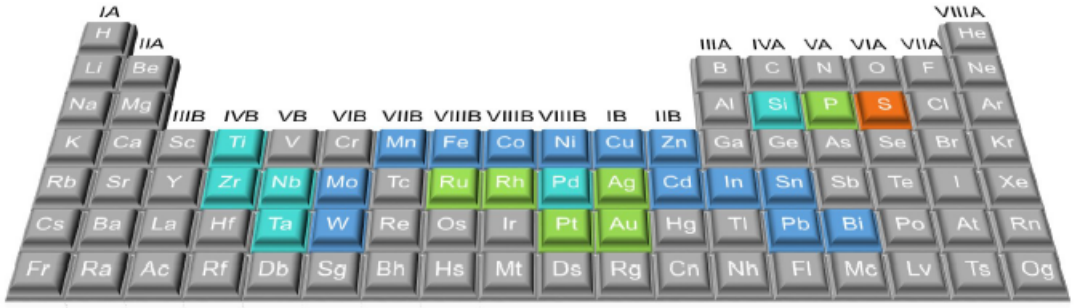

Figure 1.2: Chemical composition of metal sulfide photocatalysts for hydrogen generation. *(Source; Maeda et al. (2006))*

exhibit a remarkable reactivity to visible light, enough active sites and the right reduction potential of H^+/H_2 to function as an efficient photocatalyst. Additionally, new quantum size effects allow for further tuning towards quick charge transfer, longer excited state lifetimes Keimer & Moore (2017); Frame & Osterloh (2010). Therefore, a lot of effort has been put towards enhancing solar hydrogen generation over MS semiconductor photocatalysts over the past ten years Sivula & Van De Krol (2016); Amirav & Alivisatos (2010). Among other MS materials ternary sulfides, such as $CuInS_2$ and $CuGaS_2$, exhibit good selectivity and a high rate of photocatalytic generation, especially when combined with titanium dioxide TiO_2 Shiga et al. (2016); H. Hou et al. (2020). Additionally, More research currently is also focused on 2D nanosheets, flakes, and anisotropic structures MS with reduced dimensions. Another well known method for boosting photocatalytic activity is the functionalization of low dimensional MS structures. The goal of this growing field of study is to use different metals or chemicals as dopants in order to create large amounts of hydrogen (see, for example, Figure 1.2). Blue boxes represent chemical elements whose sulfide compounds have been widely used in photocatalysis to produce hydrogen. The elements that are used as dopants (green) and whose oxides or other compounds (cyan) are utilized to construct heterostructures with metal sulfides for hydrogen evolution are also marked. Specific qualities are essential to improving the yield of photocatalytic reactions, in addition to typical

environmental and industrial requirements H. Chen et al. (2021). Clearly, finding an ideal photocatalyst that meets all needs as indicated in Figure 1.3 has led to a great deal of research that has resulted in new and flexible photocatalysts and mechanisms for photocatalytic reactions. Adsorption, contact, desorption, and other fundamental catalytic stages control the overall reaction mechanism, products, and yield Balayeva & Mamiyev (2022). However, defect free parametrization of these variables enables the creation of a successful photocatalyst.

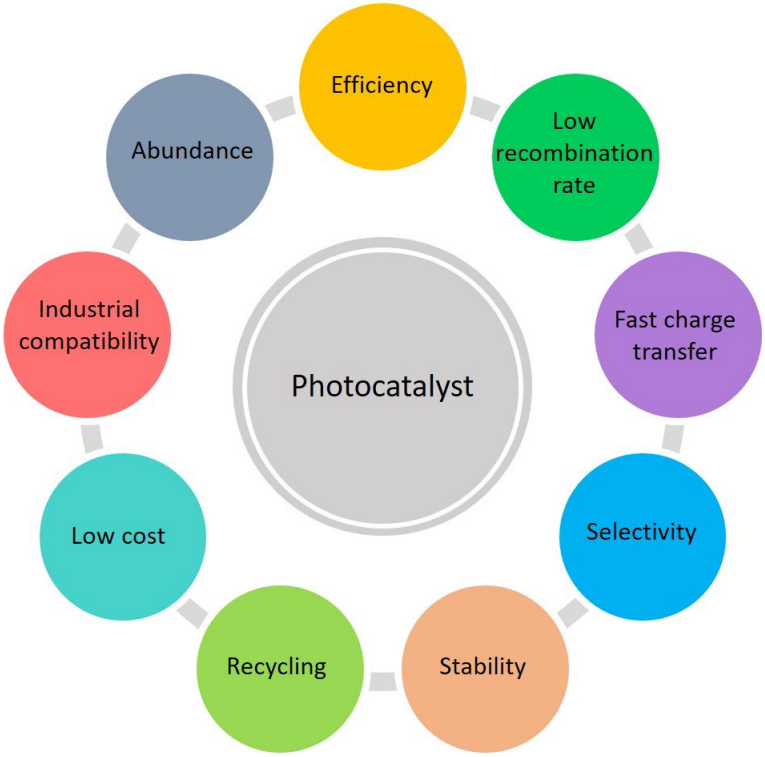

Figure 1.3: Criteria to develop photocatalysts exhibiting high efficiency in general. *(Source; H. Chen et al. (2021))*

It is therefore very difficult to find a highly effective visible light sensitive photo catalyst due to the fact that materials with outstanding photocatalytic activity and chemical stability, such as TiO_2 and ZnS frequently have band gaps that are too large for visible light absorption Maeda (2011). Chalcogenides have also been considered an appealing choice at the nanoscale because of their unique and tunable electrical, optical, and electronic capabilities in relation to their particle size. ZnS is a more stable and highly technologically sophisticated wide band gap II-VI semiconductor than other chalcogenide materials N. Kumar et al. (2015).

To be more precise, ZnS is one of the most widely utilized photocatalysts owing to its quick generation of electron-hole pairs upon photo-excitation and its incredibly negative reduction potentials of excited electrons J. Zhang et al. (2012); D. Huang et al. (2020); Juine et al. (2021); J. Zhou et al. (2020). Additionally, it suggests that there is a high activity for H_2 evolution under UV light irradiation even in the absence of noble metal co-catalysts J. Zhang, Yu, et al. (2011); Reber & Meier (1984). ZnS is selected as a target due to its rapid electron-hole pair formation by photo-excitation, the presence of highly active surface sites for H_2 production and its outstanding chemical stability against oxidation and hydrolysis when the particle size is reduced to only a few nanometers Y.-C. Zhu et al. (2004). As a result, ZnS generally displays the most promising nanoscale morphology among inorganic semiconductors, making it a novel material with a wide range of prospective application.

1.1.2 Transitional metal doping of ZnS

Doping is necessary in order to modify the intrinsic semiconductors properties. An average of one dopant atom for every 10^5 atom is found in the doping concentration Pereira (2017); Kripal et al. (2010). The intermediate gap states created by surface species are transferred outside the gap area to generate impurity centers when impurities, electrons and holes are doped into semiconductors Zunger & Malyi (2021). Doping has no effect on the absorption of a spectrum, but it greatly increases the intensity of its emission X. Yang et al. (2019). The process mixture is simply mixed with the dopant to achieve the desired doping. If, as in the case of rare earth elements and transition metals, the impurity induced transition is bounded, then the radiative efficiency of the impurity induced emission increases considerably. Consequently, doped nanomaterials bring about significant advancements in the domains of optics, photonics, electronics, medicine, biosensors, solar cells, Infra Red (IR) detectors, color television, phosphors, light emitting diodes, field emitting diodes, lasers, photocatalysts, photo detectors, and electrolumines-

cence sensors electroluminescence sensors (ELS) X. Chen et al. (2005); H. Zhang et al. (2020); Palani et al. (2022); Rahimi-Iman (2020). Because of their high surface to volume ratio, ZnS nanoparticles exhibit a considerable band gap, which makes them more promising carriers of photoluminescence Bhargava et al. (1994). ZnS nanoparticles with different chemical and physical properties can be produced by doping; this is required to use semiconductor nanocrystals for the production and sale of nanoscale devices. The impurity centers that interact with electrons and holes are created by dopants. In this regard, a number of researchers have attempted to build semiconductor nanostructures doped with transition metal Choi et al. (2005); Radovanovic et al. (2005); Yatsunenko et al. (2008). Since ZnS has a large band gap (3.6 eV), it can only absorb in the UV, but it is easy to change its absorbance by adding metal ions like Mn, Ni, Cu, or Pb Kudo & Sekizawa (2000); Tsuji & Kudo (2003). Significant progress has recently been achieved in the production of transition metal doped III-V and II-VI semiconductor nanostructures, since theoretical research shows that these materials could exhibit high Curie temperatures Dietl et al. (2000). By moving the center of recombination away from surface states and toward impurity states, impurities improve radiative efficiency. ZnS nanoparticles doped with transition metal ions are the most important material for studying semiconductor nanocrystals; they also hint at a new class of illuminating materials. The electronic configuration of the Mn^{+2} ion, for example, is $[Ar]3d^5$. Quantum efficiency is increased because the energy transition between the ZnS lattice's s-p states and these Mn^{+2} d states happens more quickly because of their hybridization. Numerous studies Bol & Meijerink (1998); X. Li et al. (2023, 2015); C. Li et al. (2008) indicate that the broad emission peak of the Mn^{+2} ions is influenced by the host lattice. Moreover, doping various optically active luminous materials has been shown to enhance a number of properties, most notably an increase in emission intensity throughout a wide wavelength range. Among the reported dopants, Cu doping has attracted the most attention because of its strong concentration dependency C. Lee et al. (2008); this

attracts the different energy levels, producing luminous spectra. In earlier research, ZnS doped with Cu, Ni, and Pb has been examined for the production of photocatalytic H_2 Arai et al. (2008); H. Yu et al. (2007); J. Liu (2010). Cu doped ZnS was found to have a low chemical stability but a high quantum efficiency of up to 3.7% at 420 nm Kudo & Sekizawa (2000). Although nickel (Ni) doped ZnS has less activity for generating H_2, its quantum efficiency was found to be 1.3% at 420 nm and 2.1% at 430 nm by Bang et al. (2008). Compared to Cu and Ni doped ZnS, lead (Pb) doped ZnS exhibited substantially poorer photocatalytic activity. ZnS only absorbs in the UV on its own, thus altering its absorbance by doping it with specific TM ions is simple Devi & Kavitha (2013); Mahmoud et al. (2018); Jothibas et al. (2018). The ZnS absorption edge may move in this way, moving into the visible region, and new energy levels may be created between the ZnS valence Band Maximum (VBM) and Conduction Band Minimum (CBM) Belver et al. (2019); Bai et al. (2018); Khaki et al. (2017); Kurnia, Ng, Tang, et al. (2016); Fadojutimi et al. (2022). As a result, doping can induce structural defects which can successfully modify band structure and control photo-activity. Also, TM dopants may enhance charge separation, reduce band gap and photo-corrosion impact and show noticeable light absorption photo-activity Korir et al. (2021) and can also increase PEC application performance.

1.1.3 Graphene effects

Regarding the effect of reduced graphene cobalt doping on the optical, structural, and photocatalytic properties of ZnS for hydrogen production, a significant amount of data has been presented in the current research. Improving charge separation and transfer, promoting optical absorption, maximizing band gap position, reducing cost and toxicity, and boosting stability and water splitting kinetics are the main effects of graphene which explains the advantage of how well heterogeneous semiconductors can split water using solar Razaq et al. (2022). A greater possibility of developing extremely effective photo catalysts appears to exist when various

engineering procedures are combined, particularly when co-catalyst loading and other strategies are used Ray (2015); Rowley-Neale et al. (2018). To determine the key efficiency limiting phase and develop highly efficient solar-to-fuel conversion systems, a comprehensive grasp of the fundamentals of electron and hole transfer thermodynamics and kinetics is essential Prasad et al. (2020). The combination of graphene and other inorganic functional materials holds great promise for many potential applications, including energy storage materials, nanoelectronic devices, and photovoltaics, given the notable physical, chemical, and mechanical properties resulting from the two dimensional two dimensional (2D) form of graphene sheets M. Xu et al. (2013); K. Khan et al. (2020). The network of conjugated sp^2 bonds in graphitic carbon results in a greater number of delocalized electrons, which in turn increases the transit of electrons optically created in semiconductor particles and so increases the photo conversion efficiency of the system. Typically, reduced graphene oxide rGO is synthesized from graphene oxide GO to create graphene-based metal or semiconductor nanocomposites Vivekchand et al. (2008). Xiang & Yu (2013) investigated the synthesis, evaluation, and possible uses of semiconductor and graphene-based photocatalysts in photocatalytic hydrogen production. This significantly improved the material's photocatalytic performance by raising adsorption capacity, gathering visible light and lowering band gap energy. In accordance with their band gap, semiconductor nanoparticles emit light that causes electrons and holes to form in the valence and conduction bands, respectively Kamat (2011); Y. Zhang, Zhang, et al. (2012). Studies have demonstrated that this strategy can prevent the recombination of electron hole pairs generated during photocatalysis An & Jimmy (2011); L. Han et al. (2012). A semiconductor photocatalyst with long-lived charge carriers, fewer charge trapping centers, the right energy level offsets, and stability against light are all highly wanted for increasing photocatalytic reactivity Xiang & Yu (2013). Notwithstanding extensive research on the photocatalytic development studies based on graphene for high photocatalyst efficiency, there are still more research gaps and challenges that require careful

attention in the future Ahmed & Mohamed (2023).

1.1.4 New advancements in hydrogen production

Despite being thought of as an economical, clean, sustainable, and environmentally helpful technology, the utility of MS semiconductor-based photocatalysis is limited, even though photo-excited electron hole pairs recombine quickly and require little solar energy there are several strategies that have been developed to overcome these innate limitations I. U. Hassan et al. (2023); H. Xue et al. (2022) the optimization of the light spectrum absorbed by semiconducting photocatalysts has recently progressed with the synthesis and decorating of novel particle morphologies. Phenolic structures, porous morphologies, One dimensional (1D) nanowires (NWs), Zero dimensional (0D) Quantumn dots (QD's), 2D sheets and layered structures are among the materials currently being studied and developed for photocatalytic hydrogen generation; these materials are depicted in Figure 1.4

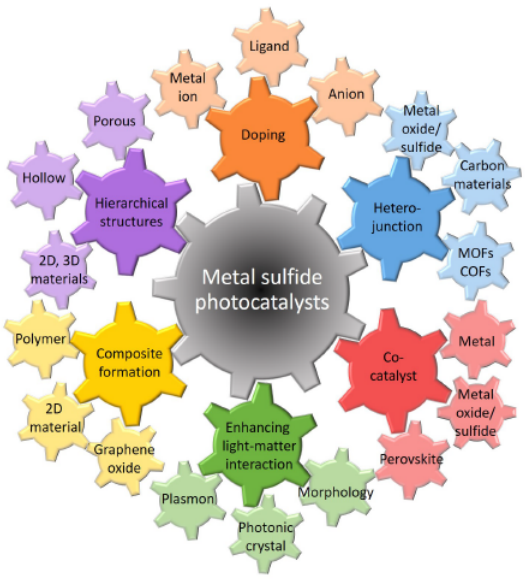

Figure 1.4: Metal sulfide strategies for hydrogen production. *(Source; Q. Hassan et al. (2023))*

In particular, band gap size reduction for MS enhances the contacting surface areas and inter-particle interactions, facilitating rapid photo-excited charge

transfer. Newly discovered quantum scale effects additionally provide rapid charge transfer and strong electronic interaction Adams et al. (2003); Kelley & Barton (1999). Additionally, the electron-hole separation is further promoted by the creation of discrete states and trap states at quantum particles, which lowers the charge recombination rate Clarke & Durrant (2010); Nozik (2008). Longevity and recycling cycles can be improved by resilient substances and protective surface treatments through the provision of a catalysts. The connection of plasmonic metallic structures with MS photocatalysts has also received a lot of interest lately Sayed et al. (2022); X. Zhang et al. (2013). When noble metal nanoparticles (NPs) are coupled to semiconductor NSs (e.g., Au, Ag, Pt), photogenerated electrons in the semiconductor's Conduction band (CB) might move to the surrounding metals due to the NPs lower Fermi energy level. The Schottky barrier that forms at the metal-semiconductor contact helps to separate electrons from holes because the metal acts as an electron sink. Redox processes involving photoinduced electrons in noble metals and holes in the Valence band (VB) of semiconductors M. R. Khan et al. (2015); X. Ma et al. (2016). Charge carriers' lifetime is extended during the process, which also increases photocatalytic activity. A facet or high active crystallographic orientation is an additional example. Co, Cu, Ni and Fe are inexpensive, widely available elements that are being used more and more as catalysts for water oxidation and reduction. With its intriguing basic characteristics and plethora of uses, including catalysts, UV light sensors, chemical sensors (including gas sensors), biosensors, field emitters, field effect transistors, p-type conductors, and nanogenerators.

1.1.5 Development methods of photocatalysts for hydrogen production

Photo-catalytic water splitting is a very promising technology to proffer a solution to present day environmental pollution and energy crises by generating hydrogen fuel through a "green route" without environmental pollution Fadojutimi et al.

(2022). In this sense, the focus of expanding basic and applied research has been on H_2 production as a sustainable energy source. In general, multiple chemical methods can be used to obtain hydrogen from various sources, such as coal or liquid fossil fuels, as shown in Figure1.5.

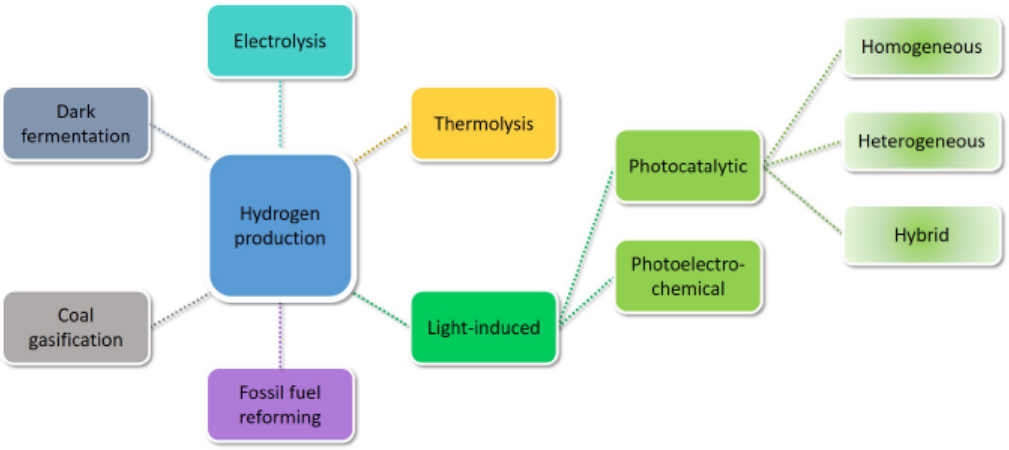

Figure 1.5: Chemical methods to obtain hydrogen. *(Source; Fadojutimi et al. (2022))*

In comparison to all other techniques, photocatalytic water splitting is the simplest since it only requires semiconducting particles to create hydrogen and oxygen when they are in solution with incident sunlight as shown in Equation1.2.

$$H_2O(l) \longrightarrow \frac{1}{2}O_2(g) + H_2(g); \delta G^{\circ} = 238kJ/mol \tag{1.2}$$

Water oxidation

$$H_2O + 2H^+ \Longrightarrow \frac{1}{2}O_2 + 2H^+(+0.82VvsNHE, pH = 7) \tag{1.3}$$

Water reduction

$$2H^+ + 2e^+ \Longrightarrow H_2(-0.41VvsNHE, pH = 7) \tag{1.4}$$

The photocatalyst must possess a valence band (VB) larger than the water oxidation potential (+0.82 V vs Normal Hydrogen Electrode; refer to Equation

1.3) in order to start the oxidation reaction. A bigger negative CB (0.41 V versusNormal Hydrogen Electrode (NHE) is required to drive the reduction processes, according to Equation 1.4. The result of this process is a clean, renewable source of hydrogen that emits no greenhouse gases or hazardous by products. While producing hydrogen and oxygen simultaneously from water splitting using a single photocatalyst is theoretically possible, it is actually a difficult process because the photocatalyst needs to meet specific requirements related to band structure, energy gap and Co-catalyst fusion is a commonly used approach because of this Jafari et al. (2016); Abdul Nasir et al. (2021). Catalysts of all kinds; homogeneous, heterogeneous and hybrid—have been developed. When compared to the others, heterogeneous photocatalysts are distinguished by their remarkable resilience or recycling, quick recovery or separation from the reaction medium, lack of toxicity, low cost of operation and materials, ability to aid in the synthesis of specific products, etc. K. H. Ng et al. (2021). Producing hydrogen energy from light is one fascinating aspect of photo-catalytic hydrogen synthesis from water splitting. Photocatalytic water splitting can be used to use solar energy to make H_2 that is affordable, clean and environmentally friendly Ran et al. (2014). In order to address the most important energy and environmental problems facing the world today, a sustainable energy infrastructure must be established. Because hydrogen is a clean, pure energy source that fuel cells can use, it will be important to the system Dincer & Acar (2015); Ghorashi & Maranlou (2021). The photocatalytic water splitting reaction consists of three main stages: charge separation and transportation, solar light collecting and catalytic H_2 and O_2 evolution processes Ran et al. (2014). The first two stages of the photocatalytic process have experienced significant advancements, but much less work has been done to improve the efficacy of the third step, which requires the use of co-catalysts—in this case, Transitional Metal dopants TMD's to increase efficiency in water splitting C. Wang et al. (2014); Y. Wang et al. (2017). Due to their continued dependence on expensive, rare noble metal co-catalysts, the majority of semiconductor-based

photocatalytic systems remain extremely challenging to extensively deploy. Utilizing co-catalysts that are inexpensive, widely available, and work well is crucial for low-cost and extremely effective photocatalytic water splitting. The present goal is to develop efficient catalysts or systems that will enable the use of solar energy whenever it is required. Solar-driven water splitting for hydrogen production is an interesting way to store and convert clean energy from visible light radiation into chemical bonds Navarro Yerga et al. (2009); Tee et al. (2017). Because they efficiently lower the energetic barriers to reaction, catalysts are essential to this process because they promote an upward or energy-storing reaction while reducing energy loss and increasing energy conversion efficiency. Costly noble metals including ruthenium, iridium, rhodium and platinum make up the majority of water splitting catalysts that are currently on the market. Nevertheless, for broad use, catalysts derived from inexpensive and abundant materials are of vital importance Tian et al. (2021).

From this angle, the potential for photoelectrochemical water splitting with cobalt dopant-containing catalysts is investigated in this work. Its development, characterization and methods for evaluating hydrogen are thoroughly looked at. The large scale applications of photocatalytic platforms for efficient solar hydrogen H_2 production have not yet been thoroughly explored, despite the fact that tremendous progress has been made in recent decades in the design of highly active photocatalysts, such as semiconductor bio-hybrids, organic semiconductors and plasmonic NPs Qi et al. (2011). However, there aren't many thorough studies that take into account a wide variety of transition metals as potential dopants to fulfill future energy requirements for increased PEC water splitting. The DFT framework, implemented in the Quantum ESPRESSO (QE) package, was used in this study to investigate the electronic and optical properties, as well as the chemical stability, of a chosen pristine $3d$ transitional metal doped ZnS Chaurasiya & Dixit (2019); A. Akhtar et al. (2017). Finding suitable dopants, figuring out the optimal concentration and stability, figuring out the electronic and optical charac-

teristics of the $3d$ TM doped ZnS and assessing the factors that could affect their photocatalytic performance were the main objectives. In order to achieve optimal hydrogen production, extensive experimental studies were carried out to evaluate the photocatalytic activity of different $Co_xZn_{1-x}S$ rGONSs produced hydrothermally. The surface morphologies and material properties of the nanostructures were described using a variety of techniques. A broad range of material metrics, including particle size, crystal structure, surface morphology, chemical composition, and band gap, were used in the analysis. These methods included RS microscopy, FTIR, XPS, SEM, UV-vis and XRD. Therefore, research on $Co_xZn_{1-x}S$ rGO nanostructure photocatalysts is desperately needed to confirm the photocatalytic effectiveness of graphene based semiconductors in the production of hydrogen H_2 molecules for industrial applications.

1.2 Statement of the problem

The supply of energy has become a major global concern in recent years. Approximately 66% of the world's electrical power and 95% of its total energy demands are currently provided by fossil fuels. However, it has been demonstrated that burning fossil fuels produces greenhouse gases that accelerate global warming and pollute the air. Furthermore, because fossil fuels take millions of years to develop, they are not renewable energy sources. The reserves are being depleted far more quickly than new ones are being generated due to our increasing demand for energy consumption. Therefore, in order to meet growing energy demands and address environmental issues, workable alternative energy solutions are desperately needed.

In an effort to address the current energy crisis, new technologies, such as nuclear, wind, and solar energy have emerged. Using hydrogen to create energy is one approach that has surfaced. Hydrogen is a clean energy source because it just releases heat and water vapor as byproducts and does not produce any

pollutants. There have been claims that this possible energy source will help the world's current energy dilemma. Numerous studies have been conducted on this technology and around 95% of hydrogen produced globally is derived from steam reforming of natural gas. With this technique, the hydrogen and carbon atoms in methane are separated. But this process produces greenhouse gases and does not reduce dependence on fossil fuel.

Another way would be photoelectrochemical water splitting. In this process, hydrogen is produced from water using sunlight and specialized semiconductors called photoelectrochemical materials. The semiconductor directly dissociates water molecules into hydrogen and oxygen through light energy. "Historically, the discovery of photo-electrolysis of water directly into oxygen at a TiO_2 electrode and hydrogen at a platinum (Pt) electrode by the illumination of light is attributed to Fujishima and Honda" Fujishima et al. (2007). However, this research does not hold much potential to be a future source of hydrogen energy.

ZnS NSs have been proposed as potential photo-anode materials for PEC water splitting due to their low toxicity, simple synthesis, easy modification routes and gives a very high quantum efficiency for the proton reduction reaction, without the need for an expensive co-catalyst such as platinum. However, ZnS suffers from low PEC activity due to its low sensitivity to visible range in electromagnetic spectrum hence limits its practical applicability and photo-corrosion effects. The main drawback of ZnS for photocatalyst is that it has a wide band gap of 3.6 eV which is active only under UV light ($\lambda < 340nm$) Kurnia, Ng, Amal, et al. (2016).

Therefore, application of ZnS NSs in PEC water splitting still awaits development of effective design and synthesis strategies to improve its PEC efficiencies to commercially viable levels. Given that most water splitting catalysts now on the market are made of expensive noble metals (such as ruthenium, iridium, rhodium and platinum), there is a dire need for catalysts made of elementally abundant and less expensive elements.

The large scale applications of photocatalytic platforms for efficient solar hy-

drogen H_2 production have not yet been thoroughly explored, despite the fact that tremendous progress has been made in recent decades in the design of highly active photocatalysts, such as semi-conductor bio-hybrids, organic semiconductors and plasmonic nanoparticles (NPs) Qi et al. (2011). Few comprehensive studies consider inclusion of graphene as a decorator and a wide range of transition metals as potential dopants to meet future energy requirements for greater PEC water splitting. The present study endeavors to address these limitations by;

1. Using the Quantum ESPRESSO package's implementation of the DFT framework to determine the optimal concentration and stability, find the right dopants, examine the structural, optical and electronic properties of the selected TM doped ZnS NSs and evaluate the variables that may have an impact on their photocatalytic performance Chaurasiya & Dixit (2019); A. Akhtar et al. (2017).

2. Conducting extensive experiments through the development of different TM doped ZnS NS surface layers decorated with graphene, with the goal of identifying the best NS that can provide optimum hydrogen energy.

3. Investigating the surface morphologies and material properties of the TM doped ZnS NS using approaches such as RS microscopy, FTIR, XPS, SEM, UV-vis, and XRD in order to analyze several different material metrics, including particle size, crystal structure, surface morphology, chemical composition and band gap.

4. Determining the photocatalytic activity of different hydrothermally produced cobalt doped ZnS decorated with graphene $Co_xZn_{1-x}S$ rGO NSs for improved hydrogen production.

Despite extensive research on the photocatalytic development studies based on graphene for excellent efficiency of photocatalysts, there are still more research gaps and challenges that need to be extensively examined Ahmed & Mohamed (2023). Therefore, research on TM doped ZnS NS photocatalysts decorated with

graphene is desperately needed to confirm the photocatalytic effectiveness of graphene based semiconductors in the production of hydrogen (H_2) molecules for industrial applications.

1.3 Justification

The current research is necessary because it provides a critical step toward the development of ZnS NSs decorated with graphene for high PEC activity, especially in visible light. A semiconductor photocatalyst with long lived charge carriers, fewer charge trapping centers, the right energy level offsets and stability against light are all highly required for increasing photocatalytic reactivity Xiang & Yu (2013); Kiptarus et al. (2023).

ZnS is a promising material for the hydrogen reduction cathode in photoelectrochemical cell for water splitting because the VB and CB edges of ZnS are favorably situated for overall water splitting and it exhibits large band gap of approximately 3.54 eV and 3.91 eV for Zinc blend and Wurtzite respectively Moon et al. (2022); Q. Li et al. (2019). Due to its large band gap, it is considered more suitable for visible and UV light based devices Kaur et al. (2016). It is able to efficiently catalyse the hydrogen reduction reaction without the need for an expensive co-catalyst. By identifying dopants that can modify the electronic structure of ZnS, an efficient visible light sensitive photocatalyst for hydrogen production can be achieved. Through band engineering TM doping, visible light absorption can be increased and photocatalytic efficiency under sunlight can be enhanced.

ZnS is a more stable, non toxic, abundant in bulk form, inexpensive, simple synthesis, high apparent quantum yields, easy modification routes and highly technologically sophisticated wide band gap II-VI semiconductor than other chalcogenide materials N. Kumar et al. (2015). More so, ZnS is one of the most widely utilized photo catalysts owing to its quick generation of electron-hole pairs upon photo-excitation and its incredibly negative reduction potentials of excited elec-

trons in its conduction band J. Zhang, Yu, et al. (2011); D. Huang et al. (2020); Juine et al. (2021); J. Zhou et al. (2020).

Additionally, it exhibits good selectivity and high rate of photocatalytic H_2 generation under UV light irradiation even in the absence of noble metal co-catalysts J. Zhang, Liu, et al. (2011); Reber & Meier (1984). The presence of highly active surface sites for H_2 production and its outstanding chemical stability against oxidation and hydrolysis when the particle size is reduced to only a few nanometers Y.-C. Zhu et al. (2004). As a result, ZnS generally displays the most promising nanoscale morphology among inorganic semiconductors, making it a novel material with a wide range of prospective application. The electronic and optical properties of ZnS strongly depend on particle size and morphology Goudarzi et al. (2009); Mendil et al. (2016); Chabou et al. (2019).

Efficient hydrogen production from water by photocatalysis under sunlight requires a significant improvement in light harvesting capability Kurnia, Ng, Tang, et al. (2016) with well established synthesis and modification routes. However the most limiting factor for ZnS to achieve high photocatalytic efficiency using solar energy are restriction of light absorption due to high energy (e.g.UV) wavelengths and the fast recombination of charge carriers Kurnia, Ng, Tang, et al. (2016); L. Wang et al. (2020); Villa et al. (2021); Hao et al. (2018); Fajrina & Tahir (2019). Expensive co-catalysts, such as platinum, are often needed to enhance charge separation and surface reaction kinetics Maeda (2011); Kudo & Miseki (2009); C. Jiang et al. (2017); X. Xu et al. (2019); Thorne et al. (2017); Kurnia, Ng, Amal, et al. (2016); T. Simon et al. (2014).

Additionally, due to the size dependence of the electron-hole interaction in semiconductor nanocrystals like nanowires, quantum confinement can be used to improve optical propertiesDel Águila et al. (2016); Brovelli et al. (2011). As a result, creating new photo-catalysts capable of effective photo-induced charge separation is crucial. Therefore, better design and synthesis techniques are still needed to increase the effectiveness of ZnS NSs for PEC water splitting to levels

where they may be used in practical applications. It is necessary to produce ZnS NSs with various physical and chemical properties, which can be accomplished via doping, in order to use semiconductor nanocrystals for the fabrication and commercialization of devices at the nanoscale because ZnS itself absorbs only in the UV, but its absorbance can be easily enhanced by doping with selected TM dopants and decorating it with graphene Devi & Kavitha (2013); Mahmoud et al. (2018); Jothibas et al. (2018). This may cause the shifting of the absorption edge of ZnS NSs towards the visible area and create new energy levels between the ZnS NSs VBM and CBM Belver et al. (2019); Bai et al. (2018); Khaki et al. (2017); Kurnia, Ng, Tang, et al. (2016); Fadojutimi et al. (2022).

Consequently, structural defects caused by doping can effectively adjust band structure and regulate photo activity. Improving charge separation and transfer, promoting optical absorption, maximizing band gap position, reducing cost and toxicity and boosting stability and water splitting kinetics are the main effects of graphene which explains the advantage of how well heterogeneous semiconductors can split water using solar because the network of conjugated sp^2 bonds in graphitic carbon results in a greater number of delocalized electrons, which in turn increases the transit of electrons optically created in semiconductor particles and so increases the photo conversion efficiency of the system Razaq et al. (2022). Therefore, TMD's and graphene inclusion can demonstrate visible light absorption photo activity, improve charge separation, minimize band gap and photo-corrosion impact and elevate PEC application performance Korir et al. (2021). Thus PEC water splitting is considered as a promising and environmentally benign approach for efficient and economic hydrogen generation by utilization of solar energy.

1.4 Research Objectives

The **main objective** is to develop, characterize and evaluate the selected transition metal doped ZnS nanostructures surface layers decorated with graphene for

water splitting.

The specific objectives are :

1. To simulate the optimal dosage of TM dopants for ZnS nanostructure layers by performing first principles calculations using density functional theory (DFT) within the framework of quantum espresso (QE).

2. To synthesize cobalt doped ZnS nanostructures layers decorated with graphene via hydrothermal technique

3. To characterize the cobalt doped ZnS nanostructures decorated with graphene in order to analyze the structural, electronic and optical properties on the surface layers of the ZnS NSs

4. To evaluate the photocatalytic hydrogen production of cobalt doped ZnS decorated with graphene by determining the optimal hydrogen production rate from the prepared photocatalysts with respect to dopant concentration through photocatalytic activity

1.5 Hypothesis

- Hybrid density functional theory (DFT) calculations carried out will accurately predict the best TM for doping ZnS 2D layers and determine the structural, electronic and optical properties of selected 3d TM doped ZnS layers and factors affecting their photocatalytic performance hence support the experimental findings.

- Doping ZnS with selected transition metal dopants, such as manganese, copper, cobalt and iron, will effectively decrease its band gap, enhancing its absorption of visible light and thereby increase its efficiency as a photocatalyst for hydrogen production.

- Graphene will significantly improve charge separation and transfer, promote optical absorption, maximize band gap position, reduce cost and toxicity,

boost stability and water splitting kinetics and prevent the recombination of electron hole pairs generated during photocatalysis

- Cobalt as an effective TM dopant will create defect states near the bottom of the CBM of ZnS 2D layer that will merge with the CB hence responsible for the lowering of band gap and therefore produce a staggered band structure arrangement which is perfect for PEC.

- Hydrothermal method will produce large amount of nanomaterials at relatively low cost and yielding high crystalline nanocrystals with well controlled dimensions, high reproducibility and quality.

- Techniques such as XRD, XPS, RS, FTIR, UV-vis and SEM employed in characterizing the cobalt doped ZnS NSs decorated with graphene will analyze the broad range of material metrics, including particle size, crystal structure, binding energies on the surface layers, surface morphology, chemical composition and band gap.

- Photocatalytic activity carried out on the fabricated TM doped ZnS NSs decorated with graphene will quantitatively determine H_2 evolution rate.

1.6 Significance

The use of fossil fuels has led to a number of environmental issues, including rising emissions of greenhouse gases, most notably CO_2, NO_2 and other air pollutants causing swerve climate change. Exploring renewable, clean and carbon-neutral alternative energy resources is desperately desired to limit our dependency on fossil fuels Quan et al. (2007); Netz et al. (2007). Therefore, the current goal is to create highly efficient catalysts (materials) or systems with no carbon trace which is essential for the survival of the world so that humankind can use solar energy whenever they want.

Hydrogen is one such fuel with no emission of pollutants when burned in oxygen, it is the most abundant and cleanest element in nature, has the highest energy content in common fuels which is almost three times that of gasoline in the same weight and since its sole oxidation product is H_2O X. Li et al. (2023); I. U. Hassan et al. (2023). Hydrogen is an eco-friendly energy source. So far, the main ways to obtain hydrogen are by steam reforming of the natural gas, coal, oil, but these approaches usually come along with the emission of carbon dioxides which do not meet the vision of zero carbon emission M. Yu et al. (2021); Bauer et al. (2022); W. Liu et al. (2022). It is possible to reduce reliance on fossil fuels and CO_2 emissions by using H_2 as a fuel on a large scale and this can be achieved either directly through photosynthetic artificial systems or through electrolysis using solar electricity. Therefore, the best and economic alternative for clean energy conversion and storage from visible light irradiation into chemical bonds is solar driven water splitting for the generation of hydrogen.

ZnS NSs have been proposed as potential photo-anode materials for PEC water splitting due to their low toxicity, simple synthesis and easy modification routes. However, ZnS suffers from low PEC activity and photo-corrosion effects and therefore, application of ZnS NSs in PEC water splitting still awaits development of effective design and synthesis strategies to improve its PEC efficiencies to commercially viable levels Kiptarus et al. (2024, 2023).

Given that most water splitting catalysts now on the market are made of expensive noble metals (such as ruthenium, iridium, rhodium, and platinum), there is a dire need for catalysts made of elementally abundant and less expensive elements. The effects on the surface chemistry, crystalline property, optical property, surface morphology and photocatalytic hydrogen generation of ZnS-graphene based photocatalysts were investigated in relation to rGO decoration and Co doping.

The present research reports the following as the major achievements:

1. *A*n ab initio Density Functional Theory (DFT) calculations that consider $3d$ TM doping as a potential route towards attainment of ZnS 2D nano layers

with superior PEC activity. The simulations provided the following results that are fully consistent with the experimental work; in addition, ideal $3d$ metal dopants and concentration were predicted

- The results showed that defects formation in ZnS NSs is strongly dependent on defect site and the d character of TM dopant. The Zn substitutional site is the most energetically favorable to most $3d$ TM dopants, with Mn, Cu, Co and Fe to be incorporated in such sites under equilibrium conditions.
- The formation energy for small atomic radii $3d$ of selected TM dopants (Mn, Cu, Co and Fe) were negative hence it can easily be incorporated in to Zn substitutional surface sites.
- The stability of $3d$ TM atoms in ZnS 2D nano layers is also critically dependent on dopant concentration, Cu and Co being the most energetically favourable within the dopant concentration range of 1-6 % considered in this study.
- Mn, Cu, Co, and Fe dopants were found to induce band-edge states at 4% and 2% dopant concentration, respectively, yielded a staggered band-structure configuration, which can be ideal for PEC water splitting and related applications when in shallow level donor states.
- The band alignment relative to the redox potential of water revealed that the VBM of Mn, Cu, Co and Fe doped ZnS 2D nano layers remains strongly positive above the oxidation potential of O_2/H_2O, favouring oxygen evolution with the reduction potential remaining negative below the reduction potential of H^+/H_2, thus maybe applicable in PEC.
- Additionally, Mn, Cu, Co and Fe should not be kept at concentrations above 4 and 6 atm.%, to ensure reduction potential remaining negative below the reduction potential of H^+/H_2 and to avoid semiconductor-metal transition likely to improve the ZnS catalytic conversion efficiency

compared to pristine ZnS.

2. Experimental findings suggest that controlling rGO inclusion and Co doping as a possible path to producing ZnS NSs with enhanced PEC activity. The experimental work yielded results that are entirely consistent with the theoretical work and the following conclusions may be taken from it as follows;

   - Extensive analysis of its development (hydrothermal technique) where noticeable improved solar energy utilization came from the narrowing of band gaps brought on by the mutually beneficial interaction of rGO and Co in the nanostructures.
   - Characterization techniques such as XRD, XPS, RS, FTIR, UV-vis,and SEM were conducted to investigate the structural, electronic and optical properties of the cobalt doped ZnS NSs layers decorated with graphene.
   - Hydrogen assessment demonstrated that cobalt doped ZnS decorated with graphene is an excellent photocatalyst for hydrogen generation.

In this study, H_2 was successfully produced by water splitting using cobalt doped ZnS decorated graphene photocatalysts.

1.7 Outline of the thesis

To effectively summarize and synthesize the findings from the research, the thesis is structured into five chapters:

1. *Chapter 1*; This section introduces the research topic under investigation by providing the background information of the research problem, statement of the problem, justification, objective, hypothesis, significance and outline of the study.

2. *Chapter 2* ; The previous research on theoretical models, development, characterization, and photocatalytic activity of transition metal-doped zinc sul-

fide nanostructures for hydrogen production is provided in the literature review.

3. *Chapter 3* ; Methodology entails the materials, equipment, theoretical and experimental procedures for data collection for developing, characterizing and optimising the cobalt doped zinc sulphide decorated with graphene for hydrogen production.

4. *Chapter 4* ; This chapter describes and explains the result's obtained from the set objectives in chapter one

5. *Chapter 5*; This chapter involves; summary, conclusion and recommendations.

Chapter 2

Literature Review

2.1 Introduction

This chapter describes the previous work done on theoretical and experimental results that explores the use of TM to enhance the PEC of ZnS synthesis, characterization and evaluation of TM doped ZnS NSs for photocatalytic H_2 production. The research gaps discerned from the literature review are also summarized.

Numerous active photo-catalysts for splitting water have been synthesized and investigated in the past few decades, whereas most of these photo-catalysts can solely absorb the UV light, which accounts for only 4% of the total sunlight and thus greatly restricts its practical applications. Hence, it is highly desirable to develop photo catalysts that can be utilized for the generation of optimum H_2 energy. ZnS exhibits exceptional features that can be used for a variety of applications, such as field emitters, electroluminescence, electrocatalysts and biosensors B. H. Kim et al. (2014); Kiptarus et al. (2024). Nano ZnS has peculiar physical and chemical characteristics when compared to bulk ZnS, including quantum size effect, surface and volume effect, macroscopic quantum tunneling effect, as well as higher optical absorption, chemical activity, thermal resistance, catalysis and low melting point as seen in Table 2.1. In order to use ZnS more effectively, it can be built with a variety of dimension features including; Three dimensional (3D)

Table 2.1: ZnS Properties. Source; Kaur et al. (2016)

Chemical		Electical		Thermal		Mechanical		Optical		Physical	
Chemical formula	ZnS	Dielectric Constant	8.9	Heat of Fusion	390 J/g	Density	4.079 g/cm3	Refractive Index	2.356	Solubility in water	Insoluble
Molecular weight	97.46 g/mol		Zinc [Ar] 3d10 4s2	Heat of Formation	477 KJ/mol	Boiling Point	1185 °C			Appearance	to yellow powder or pieces
	Zinc-12	Electronic configuration	Sulphur [Ne] 3s2 3p4	Thermal coefficient of Expansion	6.36 µm/m°C	Melting Point	1850 °C			Odour	Sulphurous odour
Group	Sulphur-16	Band Gap	3.54 eV	Thermal Conductivity	25.1 W/mK	Flexural Strength	103 MPa				
Crystal Str	Cubic	Electron Mobility	180 cm2/Vs	Specific heat capacity	0.472 J/g°C	Modulus of Elasticity	75 GPa				
Lattice Cor	5.4093Å	Hole Mobility	5 cm2/Vs			Poisson's Ratio	0.27				

particle structures, 2D thin film structures, 1D wire, rod, tube, ribbon, belt and sheet structures and 0D quantum dot structures, which are of particular interest Shu et al. (2014). Therefore, the size of ZnS varies owing to the bulk particle, nano scale structural level, or to become increasingly smaller in the future. Due to its wide range of possible uses, ZnS, a very significant II-VI semiconductor, has been the subject of extensive research. Because ZnS is more technologically advanced and chemically stable than its alternative chalcogenides such as ($ZnSe$), it is regarded as a good host material.

In its two crystalline forms, wurtzite and zinc blend (sphalerite), ZnS is a polymorphous substance Wright & Gale (2004). The co-ordination geometry at Zn and S is tetrahedral in both forms. Wurtzite has a hexagonal form (hcp), whereas zinc blend has a more stable cubic form (fcc). With a band gap of roughly 3.54 eV and 3.91 eV for zinc blend and wurtzite, respectively, ZnS exhibits a wide band gap. It is thought to be more appropriate for devices dependent on visible and UV light due to its larger band gap than zinc oxide (ZnO) (3.4 eV). Although the closest connections between the two structures are comparable, the distances and angles to neighbors are different. In comparison to wurtzite, zinc blend has four asymmetric units in its unit cell and therefore the edges of ZnS are oriented perfectly for universal water splitting.

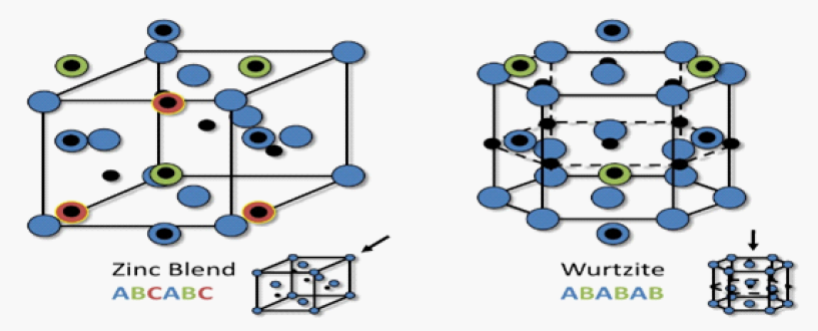

Figure 2.1: ZnS Crystal structures. Source;Kaur et al. (2016)

Without the requirement for a costlier co-catalyst like platinum, ZnS is a potential material that offers very high quantum efficiency for the proton reduction reaction. Because of its wide 3.6 eV band gap, which also lowers energy loss, ZnS possesses the fundamental drawback of functioning as a photocatalyst that only functions under UV light $\lambda < 340nm$ Hong et al. (2012). The development of photocatalysts depends critically upon decreasing the band gap and enhancing light absorption. An effective visible light sensitive photocatalyst for the generation of hydrogen can be created by finding dopants that can alter the electronic structure of ZnS. ZnS is a cheap, non-toxic, abundant and photo-stable photocatalyst that has become more and more popular for its application on an industrial scale, a few issues still need to be worked out, like a larger band gap, an agglomerating propensity during the synthesis process and challenges removing it from the reaction medium.

Technological progress requires the creation of an efficient water splitting system, a material that functions as a photocatalyst in the splitting of water needs to be developed in order to achieve this. Dopants including manganese, copper, cobalt and iron can change the electronic structure of zinc sulfide , resulting in the creation of an effective visible light sensitive photocatalyst that can produce hydrogen. Transition metal dopants have been shown to be effective in increasing visible light absorption Eyasu et al. (2013); Murugadoss (2012); Rajabi & Farsi (2015). However, other properties like conductivity may be affected by TM dopants. As an alternative, one can consider creating ZnS nanostructures and

doping only the surface layer Burda et al. (2003); F. Wang et al. (2014); Dholam et al. (2009); Hsu & Chang (2014). It is critically necessary to focus on the development of inexpensive, dependable and efficient catalysts for water splitting in artificial photosynthetic systems. This research considered cobalt as one of the best selected TM dopant as predicted in theoretical studies since there are few comprehensive done on this dopant.

Comparable in characteristics to iron and nickel, cobalt is a relatively uncommon magnetic element. Cobaltous (II) and cobaltic (III) are the two valence states; the former is most frequently employed in the chemical industry Hammond (2000). The main forms of cobalt found in nature are arsenides, oxides and sulfides. Cobalt is mostly produced in its metallic form, which is utilized to create cobalt super alloys. The phrase "hard metal" describes compounds that have tungsten carbide (80–95%) mixed with cobalt (5–20%) and nickel (0.5–5%) matrix. The periodic table places the element cobalt in group VIII. Co is an element that is silver-white in color, brittle, hard, ferromagnetic and stable in air. It may also be magnetic, just as other metals Shedd (2017). Table 2.2 illustrates how it slowly reacts with diluted acids, melting the metal at $1495°C$ and boiling it at $2927°C$.

Table 2.2: *Physical and chemical properties of Cobalt and its compounds; Adapted from Leghissa et al. (1994); Gialanella et al. (2020)*

Substance	Molecular formula	Molecular weight	Melting point	Boiling point	Solubility in water
Cobalt (II-III)*	Co	58.84	$1493°C$	$43100°C$	Limited
Cobaltious oxide (II)*	CoO	74.94	$1935°C$		0.313mg/100g
Cobaltious oxide (II-III)*	Co_3O_4	240.80$°C$	$900°C$		Limited
Cobaltious oxide (III)*	$Co_2O_3H_2O$	183.88			$84\mu g/100g$, $37°C$
Cobaltious sulfate	$CoSO_4$	155			39.3g/100g, $20°C$
	$CoSO_47H_2O$		$96.8°C$		
Cobaltious chloride	$CoCl_2$	129.84	$724°C$	$1049°C$	52.9 g/100g, $20°C$
Cobaltious carbonate	$CoCO_3$	118.94			0,11 g/100g,$15°C$
Cobaltious acetate	$Co(C_2H_3O_2)$	249.08			Under CO_2 pressure soluble

Cobalt alloys fall into several categories: high strength steels, electro deposited alloys, alloys with unique properties, magnetic alloys (aluminum, copper nickel, titanium), high-temperature, corrosion resistant super alloys (aluminum, chromium, nickel, tantalum, titanium, tungsten, zirconium) Raabe (2023); Shifler (2022). Since Co serves as a binder for the metal carbides, hard metals are not technically

Co alloys. Super alloys combine resistance to oxidation and creep at these high temperatures with high temperature mechanical characteristics Schlegel (2023). These super alloys can include iron, nickel, or cobalt as their foundation and their uses include the creation of magnetic materials and jet engines Gialanella et al. (2020); Hughart & Bashor (1999). Mostly cobalt is manufactured in its metallic form. For instance, 25–65% Co is found in heat resistant steels Barceloux & Barceloux (1999); Cobalt (1990) and roughly 65% cobalt is combined with chromium, nickel and molybdenum in vitallium alloys used in prosthetics. Cobalt is used in the powder metallurgy industry to bond tungsten carbide. These hard metals typically include 6–9% Co, with grinders and cutting tools containing the highest concentration at 30%. The magnetic characteristics of iron, nickel, platinum and phosphorus electrodeposited Co alloys are highly advantageous to the recording industry and computer applications Hughart & Bashor (1999); Aliofkhazraei et al. (2021). The most significant Co containing compounds in industry, excluding mixed oxides (II, III), are cobaltous (II) salts Sarangi et al. (1999); Schroeder et al. (1967).

Among the various classes of sp^2 nano-carbon materials, graphene is a single or few layered two dimensional sp^2 bonded carbon sheet with numerous remarkable features in chemistry and physics Tang et al. (2010); M. Zhou et al. (2009); X. Cao et al. (2011). According to Dresselhaus & Dresselhaus (2002), it has a mechanical stiffness of 1060 GPa and a thermal conductivity of up to $3000 W m^{-1} K^{-1}$. Recent research has demonstrated the remarkable electrical transport capabilities of individual graphene sheets Cui et al. (2011); Novoselov et al. (2005). Graphene sheets can be incorporated into a nanocomposite material as a potential means of utilizing these features for nanoscale purposes. GO, rGO, few layer graphene oxide (FLGO) and chemically modified graphene (CCG) are some of the derivatives of pure graphene that have been produced due to its poor aqueous solubility and amazing electrical conductivity C. Li & Shi (2011); J. Zhu et al. (2014). According to Hummers Jr & Offeman (1958), the Hummers process can be used

to generate GO sheets, which are the oxygenated equivalents of one atom thick graphene sheets, as a high surface single layer. Inhibiting electron transfer is the combined effect of the functional groups on the surface and at the margins of GO Gonçalves et al. (2014).GO low electrical conductivity can be attributed to this reason, while rGO its reduced version, displays stronger electrical conductivity. Approximately $2600 m^2 g^{-1}$ is their specific surface area, more than twice that of the majority of nanomaterials Montes-Navajas et al. (2013). In contrast to pristine graphene, GO demonstrates a high water dispersibility and possesses a pH dependent negative surface charge that contributes to its high colloidal stability. Therefore, GO is a potential material for nanomaterials applications because of its tiny size, intrinsic optical characteristics, large specific surface area, low cost and beneficial non-covalent interactions M. Zheng et al. (2014); Sun et al. (2006), which enhances its utility as a delivery vehicle. Graphene is an excellent medium for electron transport that participates in the photocatalytic hydrogen production process and helps transfer photogenerated electrons from semiconductor to graphene B. Jiang et al. (2011). A number of scholars have been hard at work attempting to figure out how to combine photocatalysts with different materials, like semiconductors Tatsuma et al. (2002), noble metals Hirakawa & Kamat (2005) and graphite like carbon L.-W. Zhang et al. (2008), in order to mitigate the recombination of photogenerated electron hole pairs. This research provides the possibility of doping ZnS using cobalt with a combination of graphene to produce an optimum material system that can be used to generate H_2 as source of green energy.

2.2 Review on the theoretical simulations of the selected transitional metal doped 2D ZnS surface layers

2.2.1 Theoretical background

The computation of the system's many nuclei, many electrons wave function is required for a complete quantum mechanical treatment of a material; however, due to the nucleus's relatively large mass, their behaviour is typically decoupled from that of the electrons in simulations, allowing them to be regarded as classical point like particles (the Born-Oppenheimer approximation) Michel Sellier & Kapanova (2017). The low mass of electrons, in contrast to nuclei, means that a full quantum-mechanical treatment is needed to understand their behaviour; however, for almost all material problems, a solution is beyond current or foreseeable technologies due to the computational complexity of the many body Schrodinger equation Weinbub & Kosik (2022).

By concentrating on the electron density rather than the many body wave function, DFT however, solves the computational challenge. Because the system's total energy is a unique functional of the electron density, according to the fundamental tenet of DFT, it is not essential to compute the system's entire many body wave function. But it is unknown exactly how the energy depends on density in terms of function S. Ghosh et al. (2018) in order to solve a set of independent particle equations. Hadjisavvas & Theophilou (1984) converted the DFT issue of calculating the ground state energy and particle density of an N-electron system.

The original (3N-dimensional) many body problem is significantly harder to solve than these Kohn-Sham equations, which are composed of N single particle 3D Schrodinger like equations De Martino et al. (2003) with a modified effective potential. Particle correlation and quantum mechanical exchange both contribute to the modified potential, which is itself a functional of the total particle density

Kohn & Sham (1965); Harbola & Sahni (1989). Since this exchange correlation $(\chi - C)$ potential is so weak in contrast to the single particle kinetic and Coulomb terms, no equation for it is known. However, It is well known that the electronic structure of many materials determines many of their properties, but it has only recently become feasible to accurately model this behaviour.

The first generic approximation for exchange and correlation was the local density approximation (LDA). The χC energy density at position r in the LDA is solely determined by the particle density at that place, n(r). This density dependence is a good approximation of the density functional because it has been determined exactly $n^{HEG} = n(r)$, the density of a homogeneous electron gas, must be the same. The exchange correlation hole, or the region around a particle where the likelihood of finding another of the same type is lowered, is an essential feature of any density functional. This hole arises from the Pauli exclusion principle and the total drop in the density of all the remaining particles is expected to be equal to (-1) Cline (1972). In other words, exactly one particle has to be removed. The LDA properly meets this exclusion principle, thus even if the shape of the exchange correlation hole is erroneous, it has the right spherical average Gunnarsson & Lundqvist (1976).

Most extensions to the LDA contain a dependency on the local density gradient, just like in the generalized-gradient approximations (GGA's), like the PW91 Perdew & Wang (1992) and Perdew, Becke, and Ernzerhof (PBE) functionals Perdew et al. (1996). These extensions, often based on the behavior of the homogeneous electron gas under modest perturbations, preserve the spherical average of the exchange correlation hole. GGA's provide systematic improvements in the atomization or cohesive energies of a wide range of molecules and solids Perdew et al. (1992); Winkler et al. (1995). They also rectify the severe over binding of hydrogen bonded solids by the LDA. However, they are not always a better solution than the LDA since their accuracy relies on some system dependent error cancellation in both cases. Beyond the GGA's, there are several approximations.

Often employed approximations include

- meta-GGAs Tao et al. (2003), in which the density's Laplacian can be included (practically, this is expressed in terms of the wave function's Laplacian, or the kinetic energy);
- hybrid functionals, in which the band gap problem is avoided by incorporating an empirical fraction, usually between 20 and 25%) of Hartree–Fock exchange; and
- DFT + U, in which the addition of an on-site Hubbard-U potential enhances electron localization, usually applied to the d or$f$ shells, optimizing the magnetic characteristics of materials.

The importance of theory and computing in the development of new materials is becoming more widely acknowledged Montoya et al. (2017). Modern science and technology are based on an understanding of the arrangement of atoms in materials and how that arrangement affects those attributes. To sustain the continual advancement in technology, new materials must be discovered and developed that are stronger, less expensive, lighter and more functional A. Jain et al. (2016). While there are numerous well proven techniques for optimizing a specific structure to determine the local energy (or enthalpy, at pressure) minimum, a global optimization technique is needed to forecast the best stable structure out of all potential configurations. Furthermore, due to the vast range of inter-atomic bonding that may be encountered throughout the searches, only purely quantum mechanical calculations are sufficiently dependable to achieve the requisite degree of accuracy.

First-principles DFT methods provide an economical high-level description of the electronic structure for the many thousands of structures that need to be taken into account during a trustworthy search Freysoldt et al. (2014). First-principles crystal structure prediction has been supported by a variety of global optimisation techniques, such as simulated annealing Schön & Jansen (2001), ge-

netic/evolutionary algorithms Hart et al. (2005) N. L. Abraham & Probert (2006); N. Abraham & Probert (2008); Glass et al. (2006), minima hopping and particle swarms Y. Wang et al. (2010). Ab initio random structure searching (AIRSS) is a very simple and effective method Pickard & Needs (2006). The AIRSS method creates random structures; the atoms' kind and quantity can be chosen at random or can be specified. Then, if a crystal is desired, these atoms are randomly arranged in a unit cell of arbitrary form, with a volume selected to mimic the initial density.

Using first principles DFT, a vast ensemble of random starting structures is produced and each one is structurally optimised to minimise the cell stresses and atomic forces Pickard & Needs (2011). Consequently, every initially random structure is shifted to a local energy (or enthalpy) minimum in the vicinity. While the calculations can be done sequentially, this problem is very suitable for high throughput computation, where each random structure is optimised separately on a portion of the total number of compute cores. Since there is no parallel communication overhead, using a single core for every structure will result in the highest throughput. Parallelizing the optimisation of each structure over a multicore compute node is feasible and yields preliminary results quickly because the communication cost between compute cores inside a single compute node or workstation is low.

Several different structural, chemical, optical, spectroscopic, elastic, vibrational, and thermodynamic phenomena can be computed using modern DFT modeling algorithms. Experimental domains like vibrational and solid state Nuclear magnetic resonance (NRM) spectroscopy, where it is the main technique for analyzing and interpreting experimental spectra, have been transformed by the capacity to anticipate structure property connections. The electronic structure of bulk and defect states in semiconductor physics has advanced significantly despite the significant difficulties in characterizing excited states. Research is no longer limited to crystal structures that are known because of the application of DFT

an exploratory tool for materials discovery and computational experimentation is growing, leading to the development of ex-nihilocrystal structure prediction, which solves the challenging limitation of predicting crystal structure poly-morphs from a given crystal structure.

2.2.2 Simulation of transitional metal doped 2D ZnS surface layer nanostructures

Kurnia & Hart (2015) investigated the electronic properties of TM doped ZnS by means of first principles calculations. Furthermore, they clarified that by permitting electronic transitions at energies that coincide with visible light wavelengths, TMD's may result in increased photocatalytic efficiency in the presence of sunlight. They concluded that Ni and Co doped ZnS will be promising materials for photocatalytic hydrogen production because of their low formation energy and appropriate band energies. Their calculations also showed that ZnS could readily accept TM atoms including Co, Ni, Mn and Fe that result in low lattice strain as shown in Figure 2.2(**i**).

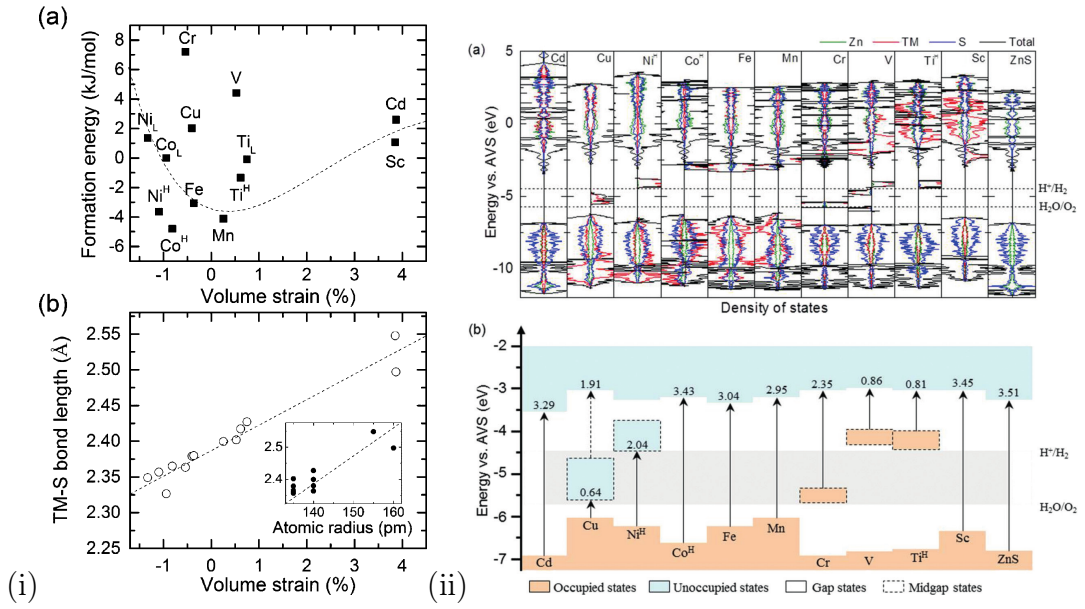

Figure 2.2: Formation energies; *Source; Kurnia & Hart (2015)*

From the Figure 2.2, it can be seen that the amount of lattice strain is generally

consistent with the ionic radius of the TM, with the bond length increasing with increasing radius (inset Figure). For TMD's with large ionic radius (e.g. Cd and Sc), the TM doped ZnS formation energy is relatively high, indicating that the lattice expansion caused by large ions makes incorporation of these dopants in ZnS unfavorable. The formation energy generally decreases as the volume strain decreases and the lowest formation energies are found when the lattice strain is close to zero.

Formation energies appear to increase as volume strain decreases significantly below 0 % (i.e. < 1 %), although not many data points are available at these large negative strains. The formation energies for Cr, V and Cu doped ZnS lie significantly above the general trend between formation energy and lattice strain. This is consistent with a relatively large difference between the TMD's bond length in doped ZnS compared with the TMD's bond length in the transition metal sulfide. This bond length strain is 9.0, 7.5, and 4.8 % for Cr, V and Cu doped ZnS respectively, compared with 0.7, 1.2 and 2.7 % for Co (high spin), Fe, and Mn doped ZnS, respectively, which have much lower formation energies.

Hence, to understand the formation energies of doped semiconductors, it is necessary to consider both strain in the host lattice as well as strain in the dopant atom bonds. The projected density of states (PDOS) show that TM doping causes electronic structure modification and the introduction of states within the ZnS band gap as seen in Figure 2.2(**ii,a**). For Ti, Co and Ni doping, the high spin state is lowest in energy and the Density of states (DOS's) for this spin state are shown in Figure 2.2(**iib**). However, Kurnia & Hart (2015) studies was scattered since it made it difficult to the know the ideal dopant for the PEC application.

According to Korir et al. (2021), water splitting using photo-electrochemistry may be able to use ZnO NWs as photo-anode materials. Utilizing $3d$ TMD's as a potential strategy to produce ZnO NWs with increased PEC activity, Ab-*initio* DFT simulations were also carried out. Their results showed that the doping site, concentration and d character of dopant, all affected how stable $3d$ TMD's were

in ZnO NWs as seen in Figure 2.3(**i**); in both O-rich and Zn-rich conditions, the majority of TM atoms were energetically most advantageous at the Zn substitutional site as seen in Figure 2.3(**ii**). Their research was based on ZnO as the semiconductor unlike the vcurrent research where the base material is ZnS.

Additionally, they discovered that at dopant concentrations of 1–6% at thermodynamic, all $3d$ TMD's in ZnO NWs under O-rich conditions and Sc, Ti and V under Zn-rich conditions had negative formation energies. This suggested that, the dopants could be easily incorporated into ZnO NWs as described in Figure 2.3(**i and ii**). Figure 2.3(**V**) illustrates how the dopant concentration had a major effect on the band gap of TM doped ZnO NWs. When the dopant concentration in Mn and Fe doped ZnO NWs increases, a noticeable band gap reduction is seen, which at larger dopant concentrations shifts towards the visible light spectrum. When Mn was present, the system turned metallic at 6 atm. %, when the band gap became zero. Fe doped ZnO NWs on the other hand, maintained its semiconducting nature at the same dopant concentration, with a band gap of 1.78 eV. Their results provided an insight on what could happen in doping ZnS for PEC applications.

The authors proceeded to claim that whereas dopants such as Sc, Cr, Mn, Co, Ni, and Cu in ZnO NWs yielded band-edge states, the electronic properties of Ti and V at 2% and 4% dopant concentration, respectively, produced a staggered band structure configuration as seen in Figure 2.3(**iv**) . Moreover, by reducing the band gap, $3d$ TM dopants caused ZnO NWs's absorption edge to be considerably red-shifted as seen in Figure 2.3(**iii**) ; these effects were predicted to improve the material's ability to collect visual light. The study's findings indicated that the VBM of ZnO NWs doped with Sc, V, Ni, and Cu remained strongly positive above the oxidation potential of O_2 and H_2O, while their reduction potential remained negative below the reduction potential of H^+/H_2.

They further divided the $3d$ TM doped ZnO NWs into two groups: those that introduce band-edge states and those that induce mid-gap defect states. Whereas

Sc, Cr, Mn, Fe, Co, Ni, and Cu introduce valence edge and conduction edge states with an overall reduction of energy band-gap as shown in Figure 2.3(**vi**), Ti and V induce mid-gap states, which are attributed to hybridization between $3p$ and $2d$ orbitals. This indicated that the band alignment relative to the redox potential of water could have favoured PEC application. Indeed, this study have been instructive and formed part of the literature evaluation that served as the foundation for the current study.

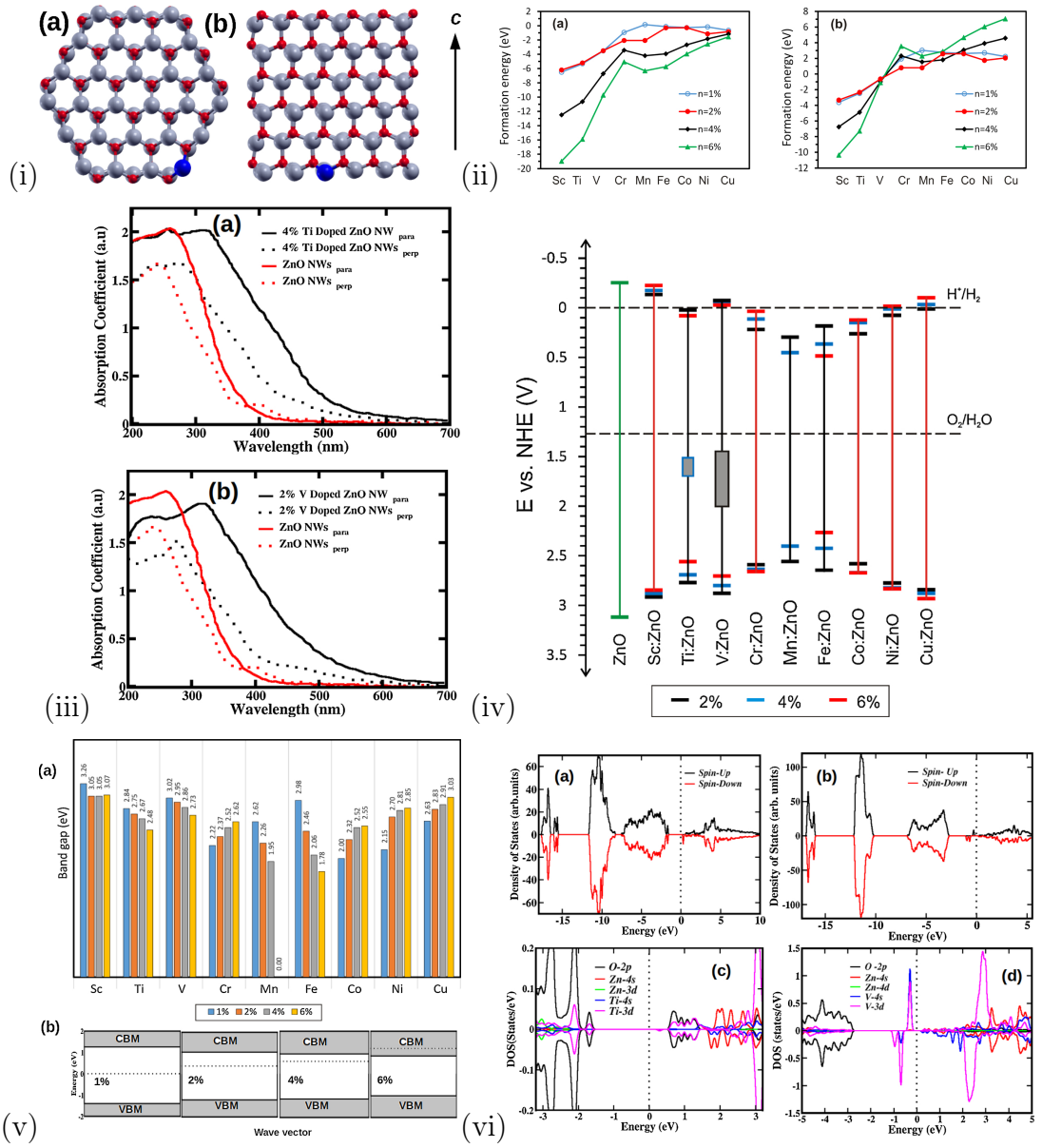

Figure 2.3: Crystal structure, stability, band gap, pdos and optical characterization

Azouaoui et al. (2020) investigated the structural, electrical and magnetic char-

acteristics of Mn_4N having a cubic perovskite structure by density functional theory calculations using first principles. The findings demonstrated that the Mn_4N exhibited a metallic behaviour with a low magnetic moment and a ferrimagnetic spin arrangement. The Design of States (DOS) analysis indicated that the primary source of the DOS at the Fermi level was Mn's $3d$ band contributions as shown in Figure 2.4(**i**).

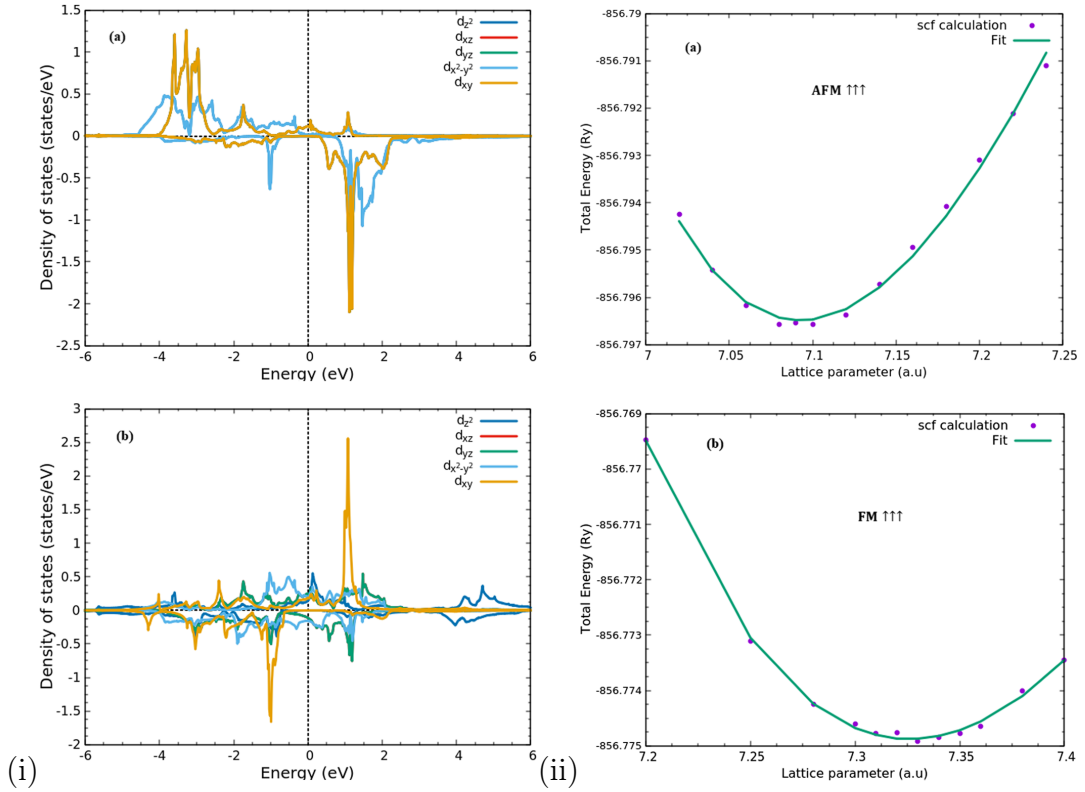

Figure 2.4: (i)projected dos of Mn-d orbital: a at the corner and b at the face, (ii)Total energy versus lattice parameter a with AFM configuration and b with FM configuration. Source; Azouaoui et al. (2020)

The magnetic moments increased with an increase in lattice parameters and in the vicinity of the optimal lattice parameter, both magnetic moments had large deviations as shown in Figure 2.4(**ii**). This research was very informative on the effects of Mn dopant in perovskite structure. However, it would have served well if other TMD's were considered for comparison and further investigation to give a highlight on what happens when doping occurs.

First-principles calculations of the lattice constants, the band gap and the DOS of ZnO:Mg ($Zn1_xMg_xO$) was performed by T. Han et al. (2011) within the

framework of DFT and showed to be in good agreement with experimental results in the literature. The Zn-4s DOS was responsible for the band gap widening of ZnO: Mg. This work provided a powerful tool for tailoring the band gap and electronic properties of ZnO with doping elements. However, the base material was ZnO and other dopants were not considered to predict the best dopant instead magnesium was used.

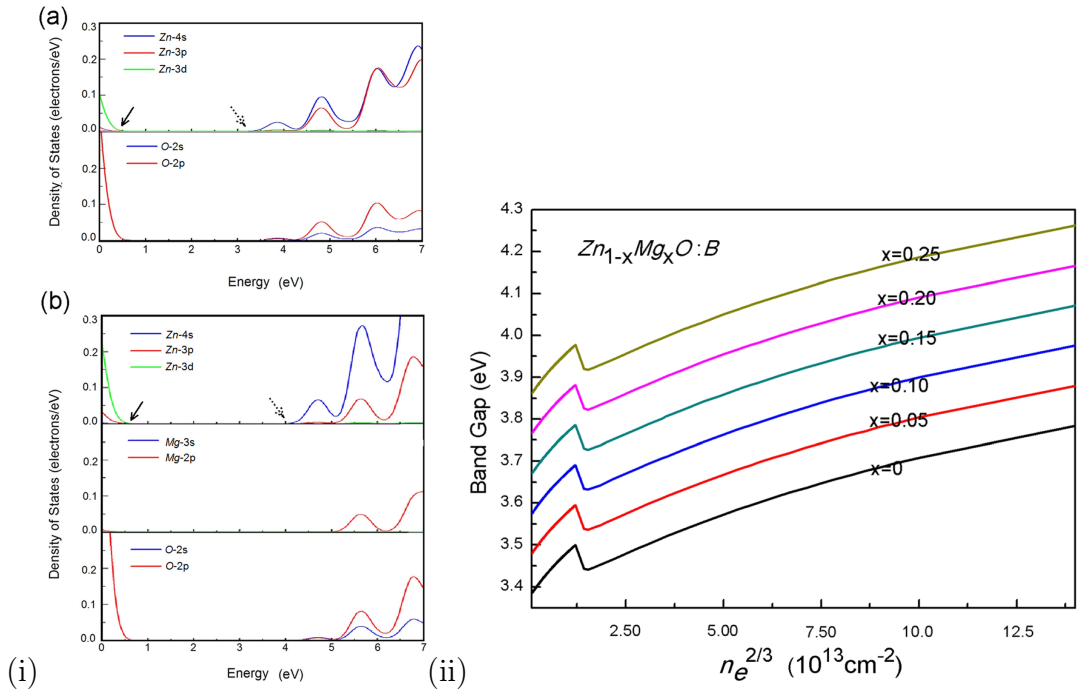

Figure 2.5: (i)Density of states vs energy for (a) ZnO and (b) $Zn_0.5Mg_0.5$, (ii)Calculated band gap of $Zn1_xMg_x$ O:B as a function of the electron concentration for (x =0, 0.05, 0.10, 0.15, and 0.20). Source; T. Han et al. (2011)

2.3 Review on development, characterization and hydrogen production evaluation of the selected transitional metal doped ZnS decorated with graphene

2.3.1 Overview on the properties of nanostructures

A Nanomaterials (NM) is 10^{-9} meters. Rizwan et al. (2021); Saleh (2020) categorized NM into four types according to their shapes and size. The initial kind, known as zero dimension: Materials, such as nano dots, have three nanoscale dimensions and are incredibly small nearly zero. Viswanath et al. (2014). One dimension makes up the second sort where its two other dimensions are outside the nanoscale, such as extremely thin surface coatings, while its one length (x, y or z) is contained within the nanoscale Almuhammady et al. (2021). The third type of material is 2D; like nano carbon tubes, its two dimensions fall within the range of nanometers, while its third dimension is outside of the nano range. The final type of NM has 3D, all of which are at the nanoscale. Its dimensions are marginally larger and are not ignored (often more than 10 nm), which sets it apart from the zero dimensions. classical mechanics in the case of NM is unable to adequately describe the phenomena that take place in them because of the tiny dimensions Kibble & Berkshire (2004); Lostaglio et al. (2015); Woit (2011); Gutzwiller (1970). In this work 2D is the utilized classification.

Quantum mechanics allows for the description of a wide range of objects in tiny dimensions Giamarchi (2003); Vollath (2008) and the characteristics of NM are different from those of materials with their original dimensions Ealia & Saravanakumar (2017). There are numerous reasons why characteristics change, but the primary one is: The NM stand out due to their exceptionally enormous surface area (SA) in relation to their size. In this instance, the ratio of SA to volume (V) will be as shown in Equation 2.3 $= 3 * 10^9$ if we assume that the value of r in

the equation is 1 nm Horikoshi & Serpone (2013). A sphere with radius r has the following characteristics:

$$SA = 4\pi r^2 \tag{2.1}$$

$$V = \frac{4}{3\pi r^3} \tag{2.2}$$

and

$$SA : V = \frac{3}{r} \tag{2.3}$$

The SA would be $6m^2$ for a cubic length of 1 m. The area would be $12m^2$ if the cube were divided into two equal pieces $18m^2$ will be the area if it is divided into three equal sections. Hence, when a bulk material is separated into an ensemble of individual NM, the total volume stays the same but the collective surface area increases significantly Kulkarni et al. (2015). Furthermore, the NM has the ability to collapse into extremely small dimensions, thereby dominating the quantum effect on matter behavior at the nanoscale Cassone (2020) rather than using the classical mechanics model to explain motion and energy, quantum mechanics will do. The gravitational forces become very minor and ignored within specific limitations when the three dimensions of NM are very small (less than 10 nm), as they depend on very small and insignificant parameters such as mass and distance Viswanath et al. (2014). In the case of Nanoparticles (NP), the electromagnetic forces are quite high. The band gap and lattice parameters vary on the size of the particles, which is another reason to alter the properties of NM Vollath (2008).

1. **Physical Properties**. The bulk material's structure is the same as the NM crystal structure, its lattice parameter however, varies Kulkarni et al. (2015) and this can be an amazing unique qualities that can differ greatly from the bulk material's physical characteristics. Although many of these peculiar qualities are still unknown, some are known, the physical characteristics of NM are the same for materials of different origins in terms of the large distribution of atoms on the surface, the large surface energy resulting from interactions with the external environment, the increased surface area and

the spatial confinement of the electrons due to the small dimensions, which prevents the electrons from moving freely Viswanath et al. (2014); Mageswari et al. (2016)

2. **Optical properties**. Nair et al. (2018) highlights that optical qualities are among the most entrancing and helpful properties of nanomaterials and have been widely examined utilizing an assortment of optical spectroscopic strategies and are among the most significant features since they are essential for numerous applications J. Li & Zhang (2009). According to J. Z. Zhang (2009); Mandal & Ganguly (2011); Parola et al. (2016), these applications include solar cells, photocatalysis, photo-chemistry, optical detectors, lasers, sensors, imaging, and bio-medicine. Molecular size, shape, surface characteristics and other factors, such as enhanced contact with the surrounding environment or other nanostructures, are factors that determine the optical properties of NM H. Kumar et al. (2018); Tshabalala et al. (2020). When the particle size varies, the optical absorption coefficient shifts, causing a change in the color of NM J. Z. Zhang (2009). Small dimensions allow the electron to be spatially confined, preventing it from moving freely R. Ma et al. (2020); Viswanath et al. (2014).

3. **Chemical properties**. According to Fernandez-Garcia et al. (2004); Bunaciu et al. (2015), the size of a material mostly influences its chemical stability and reaction, which in turn influences its electronic structure. Mu et al. (2014); L. Xu et al. (2018) explains that NM have a low chemical stability and a large surface area, which enhances the likelihood of interaction with the outside world and the poor stability of nanoparticles, offers an opportunity to design and fabricate unique nanomaterials, such as by chemically transforming the "captured" intermediate nanostructures during a changing process, assembling destabilized nanoparticles into larger ordered assemblies, or shrinking/processing pristine materials into the desired size or shape via selective etching , NM typically interact more than bulk materials. Fur-

thermore, Viswanath et al. (2014) argues that alterations in the electronic structure and a comparatively high ionization factor are two factors that may contribute to reduced chemical stability X. Du et al. (2019).

4. **Electronic properties** Due to the differing electronic structures of the two, the strength of the energy levels in the conduction range of the NM fluctuates differently from the bulk Kulkarni et al. (2015). An energy gap is produced when the gap between two levels is greater than the product of the Boltzmann constant $k_BT(k)$ or (k_B) and temperature (T). Depending on the electronic structure and energy level separator, relevant nanoscale components will result in varying sizes Almuhammady et al. (2021). Compared to bulk materials, NP have more potential for ionization and the main factors influencing the wide variations in NM's electronic characteristics are charge quantization, the energy bands separating the valance and conduction bands, which determine the electronic transition from lower to upper and the quantum confinement of electrons with their freedom of movement Barhoum & García-Betancourt (2018).

5. **Magnetic Properties** The two main features that dominate the magnetic properties of NP are finite-size effects (single-domain, multi-domain structures and quantum confinement) and surface effects (symmetry breaking of the crystal structure at the particle surface, oxidation dangling bonds, and surface stain) Obaidat et al. (2015); Giorgalli (2021). Due to an increase in the ratio of surface to core atom counts, surface impacts become more pronounced as particle size reduces Kulkarni et al. (2015). Many magnetic characteristics, including coercivity field, magnetic anisotropy, curie temperature and magnetic moment per atom, can differ between nanoparticles and bulk material Kodama (1999); Hernando et al. (2005). Compared to the interior of a particle, the surface magnetization of a particle drops more quickly as temperature rises. NP magnetic anisotropy can be greatly influenced by the poor symmetry surrounding their surface atoms Lisjak & Mertelj (2018).

Additionally, there may be fewer magnetic neighbour atoms influencing the magnetic structure around defects in the interior and on the surface, which can result in non-collinear spin configurations in ferri-magnetic particles Mørup (2003); Sharmin (2023). Differential magnetic characteristics result from a significant number of atoms in magnetic materials with large surface area to volume ratios having varying magnetic couplings with surrounding atoms Coey (2010); Tronc et al. (2000). When a magnetic field is introduced, the magnetization's of the particles are arbitrarily orientated and aligned; this alignment vanishes when the external field is removed, a phenomenon known as super paramagnetism is seen in magnetic nanoparticles Mikhaylova et al. (2004). This is because, in contrast to the numerous domains of bulk magnetic materials, magnetic nanoparticles only have one domain Caizer (2016); Peddis et al. (2014). The behavior of the particle is ferromagnetic due to the charge localized at the particle surface. This finding suggested that metallic clusters may exhibit ferromagnetic-like behavior as a result of chemical bonding-induced band structure alterations Batlle et al. (2022); Y. Hu et al. (2021).

6. **Mechanical properties** The mechanical characteristics of NM vary significantly when compared to bulk materials. Inter-atomic distance reduces as the number of atoms on the surface rises, increasing inter-atomic force in the process. According to Q. Wu et al. (2020), this increase in inter-atomic force raises the shearing strength of NM. According to Bunaciu et al. (2015), the young modulus of nano-solids increases in tandem with the shearing strength. This mechanical property represents the stiffness of a solid material and is defined as the relationship between stress (force per unit area) and strain (proportional deformation) in a material in the linear elasticity regime of a uni-axial deformation Wiederhorn et al. (2011); Baumgart (2000). In addition, compared to bulk materials, NP have the largest tensile property, less plastic deformation, are more delicate and have

less surface flaws. Better mechanical qualities result from these causes and modifications Kulkarni et al. (2015); Viswanath et al. (2014); Vollath (2008).

2.3.2 Overview on the role of transitional metal dopants and graphene

ZnS NPs have high surface to volume ratio thus exhibit large band gap and hence are more promising carriers of photoluminescent Bhargava et al. (1994). In order to utilize the semiconductor nanocrystals for the fabrication and commercialization of devices at nanoscale, it is required to synthesize ZnS NPs with different physical and chemical properties and this can be achieved by doping. The dopants form the impurity centres that interact with the electrons and holes. The addition of impurities shifts the central recombination from surface states to that of impurity states thus enhancing the radiative efficiency. In this regard, many researchers have tried to synthesize TM doped semiconductor nanostructures Choi et al. (2005); Yatsunenko et al. (2008). Owing to its large band gap (3.6 eV), ZnS itself absorbs only in the UV, but its absorbance can be easily tuned by doping with metal ions, including Mn, Ni, Cu, Pb Kudo & Sekizawa (2000); Tsuji & Kudo (2003). Recently, many advances have been made in the synthesis of transition metal doped III-V and II-VI semiconductor nanostructures as the theoretical work predicted these materials could exhibit high curie temperatures Dietl et al. (2000).

ZnS NPs doped with transition metal ions are the most important material for research in semiconductor nanocrystals and suggest a new class of photoluminescent materials. For example, the Mn^{+2} ion have the electronic configuration $[Ar]3d^5$, these d states of Mn^{+2} hybridize with the s-p states of ZnS lattice thus resulting in faster energy transition between the two, hence increasing the quantum efficiency. The Mn^{+2} ions have the broad emission peak that depends upon the host lattice Bol & Meijerink (1998); Van Sark et al. (2001). Doping of various optically active luminescent materials has also been reported by K. Dutta et al. (2009) to improve various properties specially increase in intensity of emission in

wide range of wavelength. Various dopants have been reported in which Cu doping have received much attention due to strong dependence properties on concentration. It attracts the different energy levels resulting in luminescent spectra C. Lee et al. (2008)

In the previous reports, ZnS doped with several metal ions such as Cu, Ni and Pb was already examined for photocatalytic H_2 production Arai et al. (2008); H. Yu et al. (2007); J. Yu et al. (2010). The quantum efficiency of Cu doped ZnS was found to be as high as 3.7% at 420 nm Kudo & Sekizawa (2000), but its chemical stability was low. Ni doped ZnS was chemically stable but its activity for H_2 production was lower and the quantum efficiency was found to be 1.3% at 420 nm by Kudo & Sekizawa (2000) and 2.1% at 430 nm by Bang et al. (2008). The photocatalytic activity of Pb doped ZnS was much lower than that of Cu, Ni doped ZnS.

Khosravi et al. (1995) reported the photo physical and photocatalytic properties of ZnS NPs and explained the role of defect levels in influencing the luminescence characteristics of quantum particles. Photoluminiscense (PL) studies revealed a peak at 325 nm (3.82 eV) which was due to transition of trapped electrons to valence levels. It was concluded that capping agents were important in removing Zn dangling orbitals (electron traps) from the gap. Observation of broad red shift in luminescence and absence of band edge luminescence may have been due to unsaturated sp^3 hybridized orbitals of surface S atoms. PL emission for various excitation wavelengths was measured. They observed a broad peak at about 363 nm (3.41 eV) for all samples in the PL spectra for all organic passivating agents at 220 nm excitation wavelength.

New insights into the reaction mechanism of graphene semiconductor photocatalysts have provided designers of rGO based composite photocatalysts with new avenues for solar energy conversion design. This has additionally stimulated comprehensive investigation into the microscopic charge carrier transfer pathway associated with the interface between the semiconductor and the rGO Y. Zhang,

Zhang, et al. (2012); Kiptarus et al. (2024). In recent decades, graphene and its derivatives have come to be recognized as promising starting points for the creation of new materials. Excellent electronic, thermal, optical and mechanical properties are possessed by graphene and its compounds Iqbal et al. (2020).

Researchers have always searched for innovative technologies to generate graphene and its derivatives in an efficient and safe way. NM are used in a wide range of industries, such as superconductors, biology, sensors, nano-electronics and research. It has been found that a number of NPs can be used to make everyday objects. However, creating carbon based composite materials that may be used in a variety of applications is simple and reasonably priced Egbedina et al. (2022). When compared to conventional materials, composite elements are found to exhibit some extraordinary qualities and to be easy to fabricate.

Numerous allotropes of carbon exist, including fullerene, which is 0D; carbon nanotubes, which are 1D graphene and its derivatives, which are 2D; and graphite, which is 3D Adetayo et al. (2019). Graphene is the thinnest, stiffest and most effective heat and electrical conductor known to science. Graphene is a 2D substance having a hexagonal lattice structure, sp^2 hybridization and carbon atoms organized in a honeycomb pattern as demonstrated in Figure 2.6.

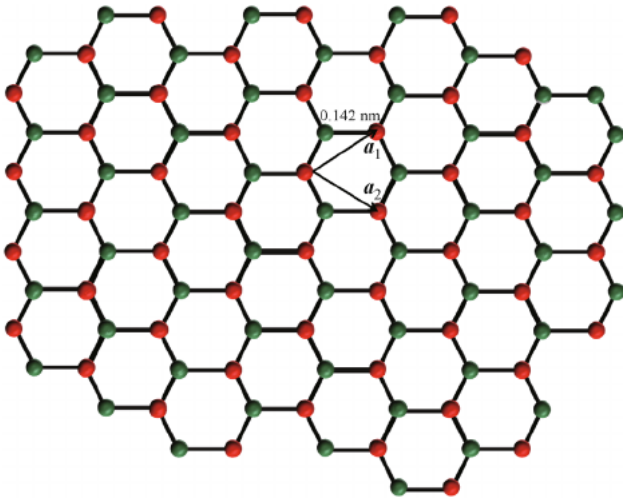

Figure 2.6: Honeycomb structure, a_1 and a_2 are the lattice units. Source; Adetayo et al. (2019)

It's mechanical, thermal and electrical qualities are exceptional with a mi-

nuscule band gap. High electrical characteristics (6000S/cm), high mechanical strength (130 GPa), high optical transmittance (97.7%), high thermal conductivity ($5000Wm^1K^1$), huge theoretical surface area ($2630m^{-2}g^1$) and Young's modulus of 1 TPa are all present in graphene Kazempour et al. (2019). To create a structure similar to graphene, rGO can be reduced utilizing a number of methods, such as thermal reduction, photochemical reduction, electrochemical reduction, microwave reduction, solvothermal reduction, and chemical reduction. Y. Chen et al. (2015); J. Chen et al. (2015). By eliminating the oxygen functional groups from GO, compounds such as hydrazine, dimethylhydrazine, hydroquinone, sodium borohydride, hydrohalic acids and strong alkali can be used to produce rGO Lavin-Lopez et al. (2017). These compounds all carry the potential to be hazardous to both human health and the environment. It is crucial to find a lowering agent that can lower GO without sacrificing the consistency and responsiveness of rGO.

Recently, natural or non-toxic ingredients have been used in the "green reduction" process: sugar, green tea, ethylene glycol, leaf extracts from natural products, aromatic amino acids, and sodium carbonate W. Chen et al. (2010). It has been discovered that ascorbic acid (AA) is an effective reducing agent. Since the reaction produces no hazardous gaseous byproducts and is not environmentally hazardous, AA has no toxic properties. By adding potassium permanganate to a solution of graphite, sulfuric acid and sodium nitrate, Hummers' technique yields graphite oxide. It is widely used by lab staff and engineers as a trustworthy method of producing large amounts of graphite oxide. It can also be modified to provide a graphene oxide compound with a single molecule thickness Marcano et al. (2010). Graphite flakes can be oxidized using three alternative methods, as seen in Figure 2.7; the improved technique, Hummers' method and Hummers' method with extra $KMnO_4$ Singh et al. (2016).

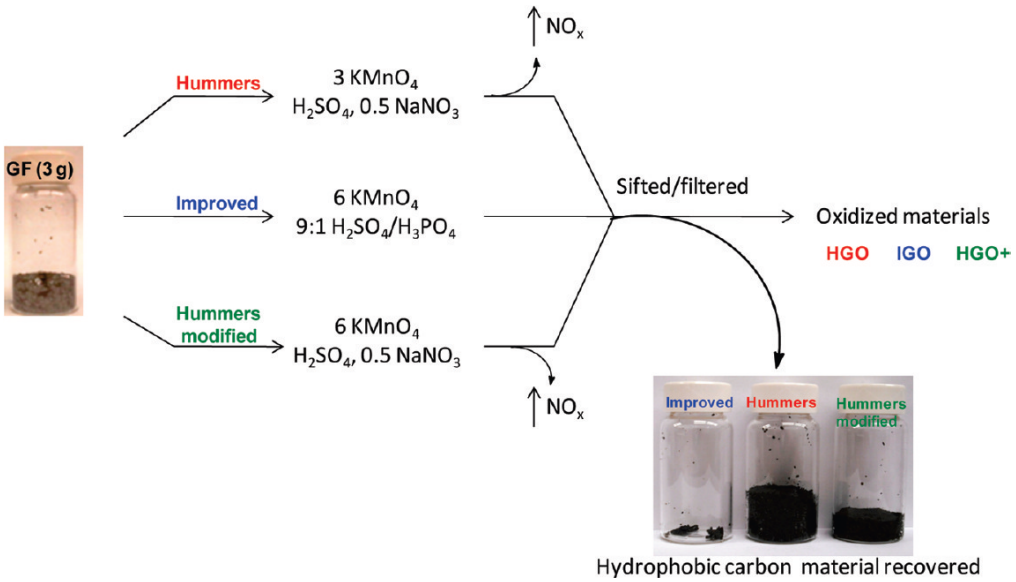

Figure 2.7: Hummers procedures for the synthesis of graphite oxide. Source; W. Chen et al. (2010)

Sujiono et al. (2020) synthesised graphene oxide based on coconut shell waste by successfully using a modified Hummers method and the obtained GO was confirmed using XRD, FTIR, RS, UV-vis and SEM-EDX. In coconut shell charcoal, where the GO sample tends to form a rGO phase, the XRD spectroscopy yielded the fractional content of the 2D graphite phase at 71.53%, 14.47% phosphorus, 10.02% calcium and 3.97% potassium. The FTIR spectra revealed compound functional groups that are similar to the way GO is made from pure graphite: hydroxyl (-OH) at peak 1 (3449.92cm^{-1}), carboxyl (-COOH) at peak 2 (1719.42cm^{-1}), peak 3 (1702.62cm^{-1}), alcohol (C–OH) at peak 4 (1628.12cm^{-1}) and epoxy (-C-O) at peak 5 (1158.51cm^{-1}).

$$Band\ \ Intensity = \frac{D\ \ band\ \ intensity \quad (Id)}{G\ \ band\ \ intensity\ \ (Ig)} \tag{2.4}$$

The RS investigation revealed that the GO sample had an intensity ratio [see Equation 2.4] of 0.89 with a 2D single layer. The surface morphology with a large number of granular particles and a broad size distribution was shown by the SEM data. The spectrum, which formed as a result of light absorption of the energy impinge on the material, showed sufficient optical characteristics in the UV-visible

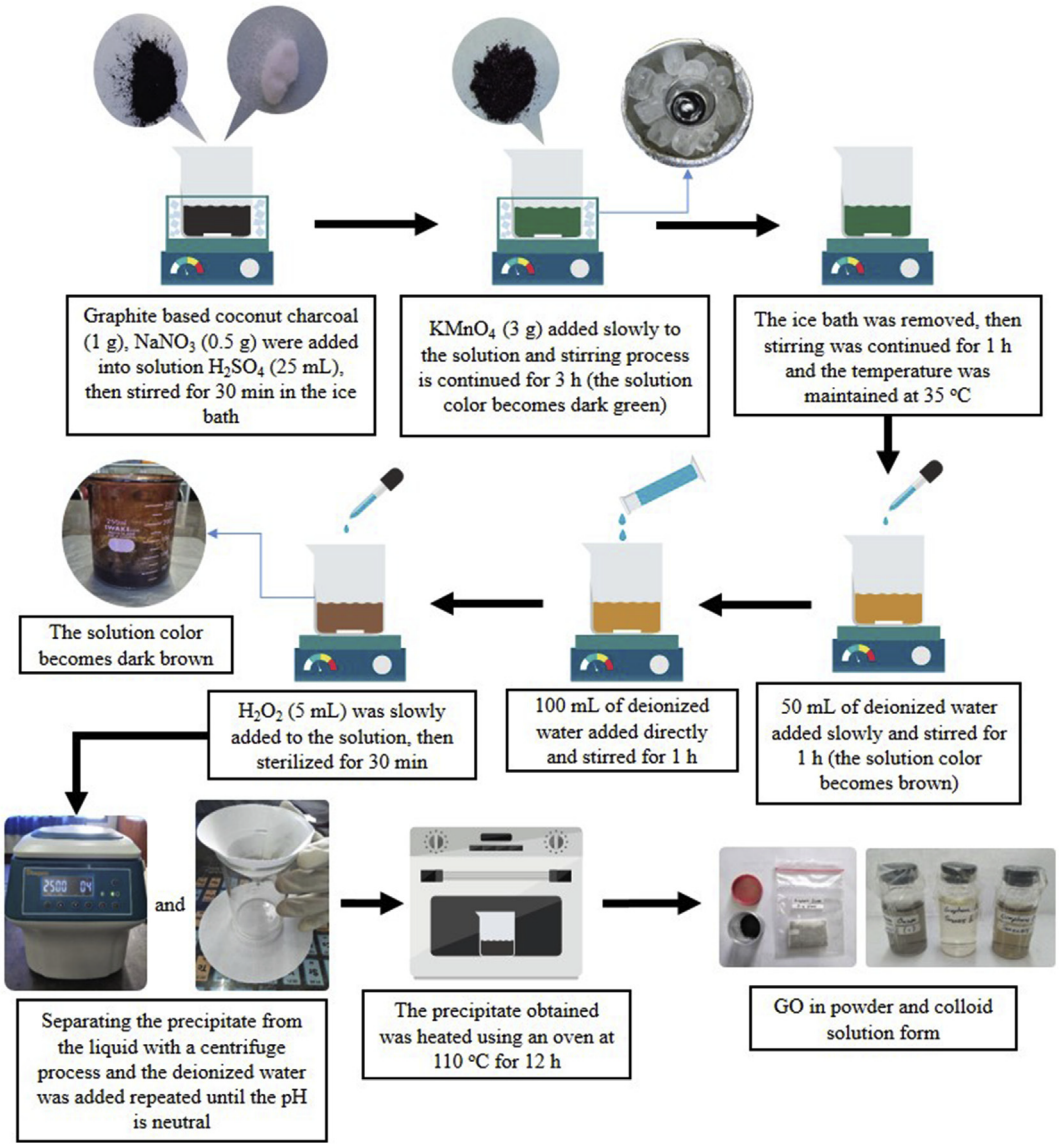

Figure 2.8: Hummers modified method for the synthesis of reduced graphene. Source; Sujiono et al. (2020)

range of findings. Using the Tauc plot approach, the sample's band gap energy value at 4.38 eV revealed characteristics of a semiconductor.

Due to the distinctive physical, chemical and mechanical properties of 2D graphene sheets, the combination of graphene and other inorganic functional materials holds great promise for a variety of potential applications, including energy storage materials, composites, sensors, nanoelectronic devices and photovoltaics Vivekchand et al. (2008). The production of graphene sheets can be facilitated by GO. Owing to the profusion of functional groups, including hydroxyl, carboxyl and epoxyl groups on the surface of their carbon sheets, GO platelets are highly

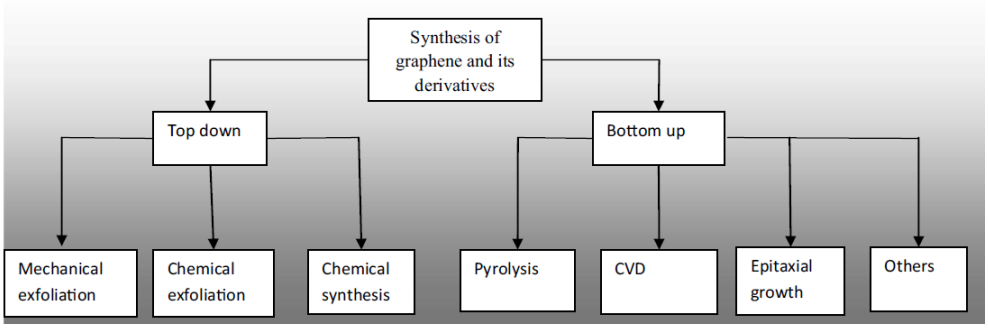

Figure 2.9: Graphene synthesis and its derivatives. Source; Tewatia et al. (2021)

hydrophilic and dispersible in water Kotov et al. (1996); Szabó et al. (2006). As graphene is no longer the starting material for materials based on graphene, GO's interlamellar space feature has taken its place Yao et al. (2009).

Tewatia et al. (2021) successfully synthesized GO using a modified version of Hummer's process using an environmentally friendly reducing agent AA. It was observed that all of the data from XRD Figure 2.11(**i**), UV-vis, RS andFTIR agreed with previously published literature. They did, however, add that the chemical reduction approach used fewer hazardous chemicals and was a more affordable technique for large scale production. FTIR, Figure 2.11(**iii**), UV-vis, Figure 2.11(**iv**) XRD and RS Figure 2.11(**ii**) were used to examine the surface and structural characteristics. FTIR verified that during the reduction process, the majority of groups, including hydroxyl (-OH), epoxy (-C-O), carboxyl (-COOH) and carbonyl (C=O), may have been eliminated. Various techniques for synthesizing graphene and its derivatives are shown in Figure 2.9. This research work considered using graphene as a decorator because of the discussed benefits.

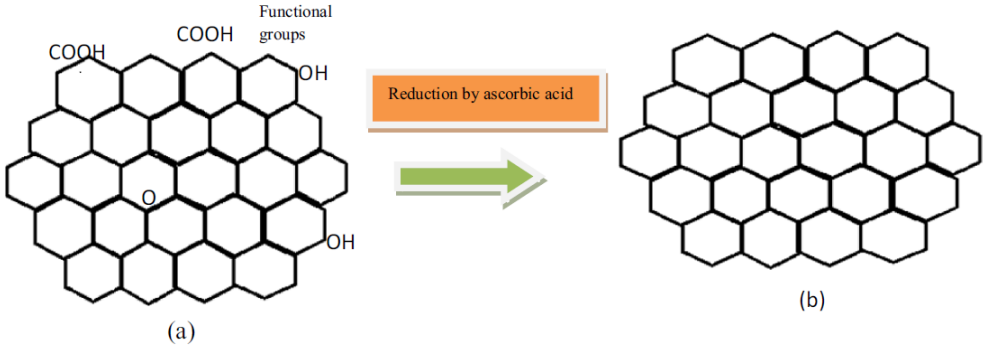

Figure 2.10: Graphene structure. Source; Tewatia et al. (2021)

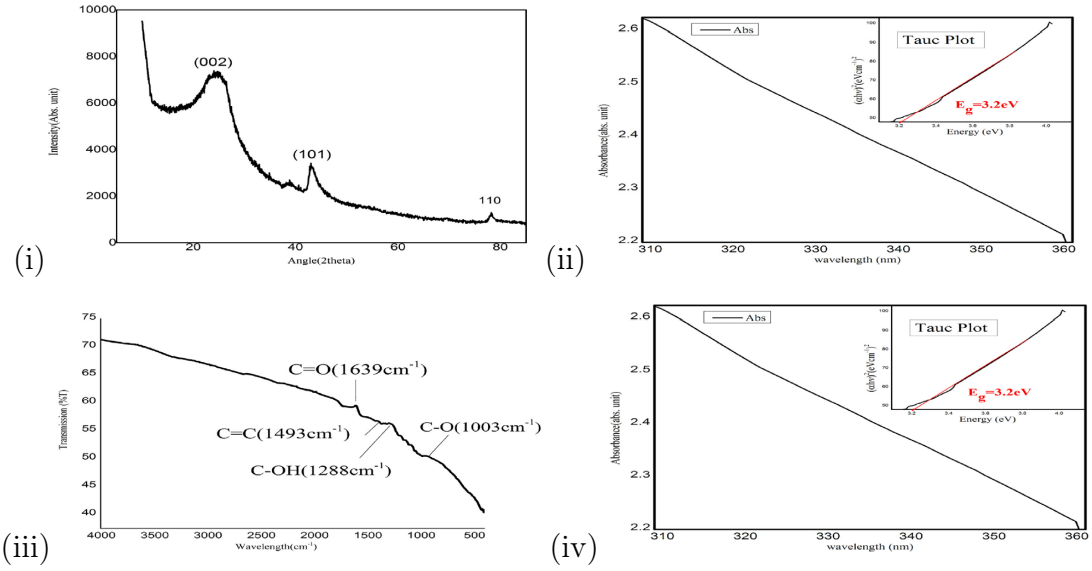

Figure 2.11: The XRD, SEM, FTIR and PL Spectra images of graphene. Source; Tewatia et al. (2021)

2.3.3 Overview on the synthesis of ZnS nanostructures

The earliest techniques for preparing NM are physical ones, particularly those that involve hand grinding Rao & Biswas (2009). According to Almuhammady et al. (2021); Mageswari et al. (2016), physical methods involve mechanical pressure, high energy radiation, thermal energy or electrical energy to cause material corrosion, smelting, evaporation or condensation, which results in the generation of nanoparticles. These physical techniques are advantageous because they generate standardized mono-NP and operate on a top-down system without solvent contamination. Physical approaches are less expensive both operationally and economically. There are a number of techniques, such as laser pyrolysis Shin

et al. (2021), inert gas condensation synthesis Suryanarayana & Prabhu (2007); K. Zheng & Branicio (2020), high energy ball milling Fecht et al. (1990) and electron beam lithography Tseng et al. (2003).

The primary source of mechanical or thermal forces needed to create molecules or gather atoms to produce materials with nanoscale sizes is chemical reactions, which are the basis of chemical procedures Naresh & Lee (2021). The main constituents of the powder are a blend of minerals, oxides and chlorides that combine by heat treatment or grinding to create a powder with ultra-pure particles distributed across a stable salt matrix. The most significant chemical techniques for recovering these particles from the matrix's removal selectivity via one pot synthesis , sol-gel method Bokov et al. (2021); Ward & Ko (1995), hydrothermal synthesis Gan et al. (2020); da Rocha et al. (2015), solvothermal method Lai et al. (2015), polyol synthesis Kulkarni et al. (2015), micro emulsion technique Viswanath et al. (2014) and microwave assisted synthesis Nüchter et al. (2004), solid-state reaction as shown in Figure 2.12.

These techniques are applied with the proper solvents for each washed compound. Numerous synthetic techniques and modifications to ZnS based composites are required in order to increase the high efficiency of ZnS and further enhance the good solar cell material features. Additional properties that can be added to ZnS NSs include spherical shape thick and thin film creation, rod and tube like features Fang et al. (2011). The current research considered using hydrothermal technique for the synthesis of cobalt doped ZnS decorated with graphene as discussed below.

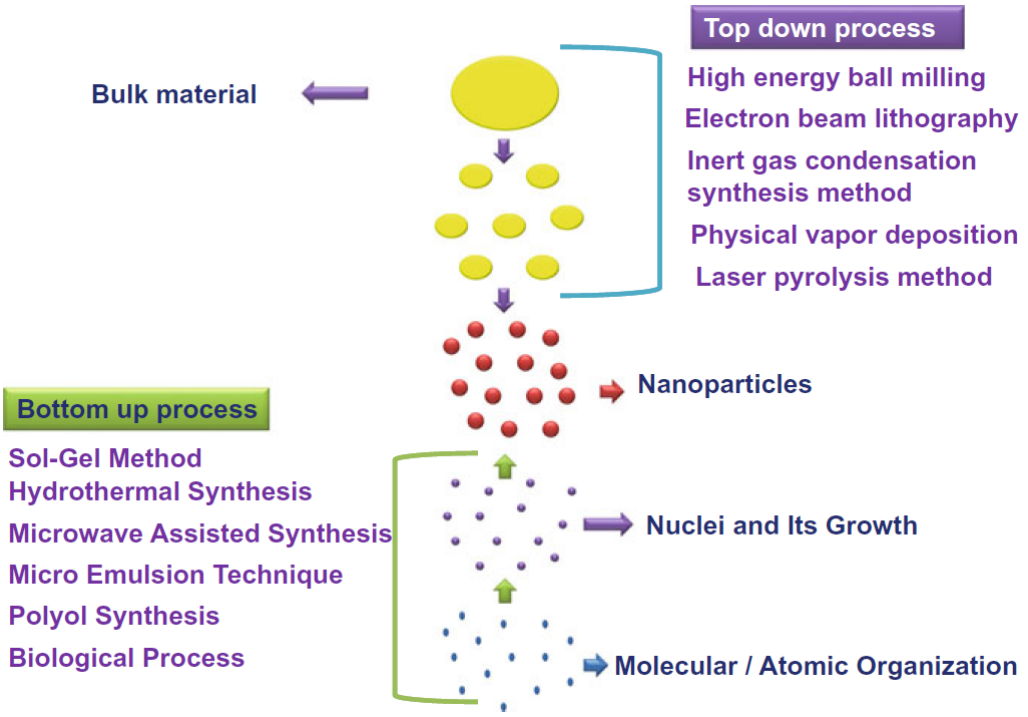

Figure 2.12: Techniques for producing nanomaterials both chemical and physical processes. Source; Almuhammady et al. (2021)

Hydrothermal method is one of the most popular techniques for producing nanomaterials. Essentially, it follows a solution-reaction-based methodology Gan et al. (2020); B Djurisic et al. (2012). NM can be formed via hydrothermal synthesis at temperatures ranging from ambient temperature to extremely high temperatures X. Wu et al. (2011). By use of a heterogeneous reaction in an aqueous medium at high pressure and temperature near the critical point in a sealed vessel, the hydrothermal approach produces nanostructured materials S. Cao et al. (2016). The hydrothermal and solvothermal methods are similar. The use of a non-aqueous medium is the only distinction. In general, closed systems are used for hydrothermal and solvothermal procedures Chen & Holt-Hindle (2010). Depending on the vapor pressure of the primary component in the reaction, either low-pressure or high-pressure conditions can be utilized to control the morphology of the materials to be synthesized. Hydrothermal method has garnered significant attention recently for engineering nanomaterials and many types of nanomaterials have been successfully synthesized using this approach Meng et al. (2016).

The hydrothermal synthesis method has several advantages over other methods. For the purpose of creating diverse nano-geometries of materials, including nanowires, nanorods, nanosheets, and nano-spheres, hydrothermal and solvothermal techniques are fascinating and practical Dong et al. (2020); Y. Jiang et al. (2018); B. Chai et al. (2018). There are many benefits to using hydrothermal and solvothermal processes, such as low temperature synthesis energy efficiency, closed system conditions that protect the environment, high crystallinity, phase purity and high yield products Devaraju & Honma (2012); Komarneni et al. (2010). A few drawbacks of hydrothermal and solvothermal processes include the requirement for costly autoclaves made of stainless steel and Teflon liners, potential safety concerns during reaction processes and the impossibility of studying in-situ reactions because of their closed systems Dong et al. (2020).

For the synthesis of simple oxides like TiO_2, ZnO P.-K. Chen et al. (2012); P. Chen et al. (2013), Bi_2O_3 Muruganandham et al. (2012); Hsieh et al. (2013), InOOH Muruganandham et al. (2013) and Fe_2O_3, hydrothermal preparation was thoroughly studied and many of the important parameters were investigated. This was achieved by heating the contents in an autoclave or an inert atmosphere and adding a surfactant, stabilizer, or capping agent to prevent the growth of nanoparticles. These stabilizers aid in the dissolving of the particles in various solvents and stabilize against agglomeration, producing extremely crystalline phase pure homogeneous particles with a restricted size distribution Amutha et al. (2013).

Tiwari & Dhoble (2017) used a straightforward hydrothermal technique and several sources of zinc as a precursor, solvents and surfactant to produce range of ZnS NSs with adjustable crystal phase and morphology. With this technique, the ZnS nanocrystals' surface energy can be altered and the shape of ZnS synthesized under comparable experimental conditions can be regulated at various reaction times and temperatures L. Jiang et al. (2008). Smaller ZnS NPs in a vacuum are more thermodynamically stable in the wurtzite phase than in the sphalerite phase, according to the low surface energy that is produced Subramani et al.

(2023). The shape of ZnS produced in water or solvents at varying reaction times under comparable experimental conditions is also worth noting. Additionally, when the reaction time increases, the ZnS products' surface area reduces, which could be caused by larger particles on the microsphere surface L. Chai et al. (2007). Meanwhile, the morphology of the products may vary depending on the initial concentration of the precursors, different zinc precursors, solvents and surfactants G.-J. Lee & Wu (2017).

2.3.4 Critical review on the synthesis, characterization and hydrogen production evaluation of transition metal doped ZnS nanostructures

Addition of Co to a ZnS matrix is one potential dopant with an ionic radius less than Zn Hoy-Benítez et al. (2020). This results in an easy-to-use doping method that produces high quantities of dopants. High concentrations of Co result in band gap states that allow absorption in the visible spectrum. The study examined ZnS and $Zn_{1-x}Co_xS$ thin films for atomic structural distortions at two distinct heavy dopant concentrations: 3% (x = 0.03) and 1% (x = 0.01414). Their work generated a structural model of this heavily doped material that is realistic. According to Kang et al. (2018), a high doping concentration raises the likelihood of a direct transition by relaxing the selection rule of transition metal ions and raising defect levels. This work provided an insight on how well cobalt can be used as a dopant at specific concentration but it did not proceed to analyse for the possibility of harvesting hydrogen gas.

Cobalt doped ZnS was utilized by P. C. Patel et al. (2015) to investigate anti-ferromagnetism. They found that at normal temperature, ferromagnetism or half-metallicity was reduced by high Co concentrations. In this work, ferromagnetism was the subject of study hence lacked the investigation on cobalt as a photocatalyst for hydrogen production.

Mohapatra et al. (2021) explained field emission scanning electron microscope (FESEM) micrographs where rGO was discovered to have a paper like structure consistent with the current research. A regular hexagonal pattern was produced on the sheet, indicating the presence of ZnS particles Figure 2.13, however their study was based on ZnS without the TM dopants. The same study was done by L. Yu et al. (2013) where the graphene sheets were integrated in order to allow ZnS NPs to develop and disseminate on their surface and prevent the sheet from aggregating. Compared to pure ZnS and rGO, ZnS reduced graphene oxide nanocomposites exhibited fluorescence. Again the use of TM was missing while the use of rGO gave informative results to be compared with the current research.

By enhancing interfacial charge transfer, reducing charge recombination and effectively harvesting light, enhances photocatalytic activity L. Tong et al. (2017), this was also in tandem with current work on the use of graphene. Figure 2.14 displays FTIR analyses of both pure reduced graphene and a combination of rGO and ZnS at different ratios. An infrared spectrum of a reduced graphene oxide revealed large peaks indicating O-H bonding at $3386cm^{-1}$, $3467cm^{-1}$, $3419cm^{-1}$, and $3484cm^{-1}$. The study compared well with the results obtained in the current work although the use of TM dopant was missing.

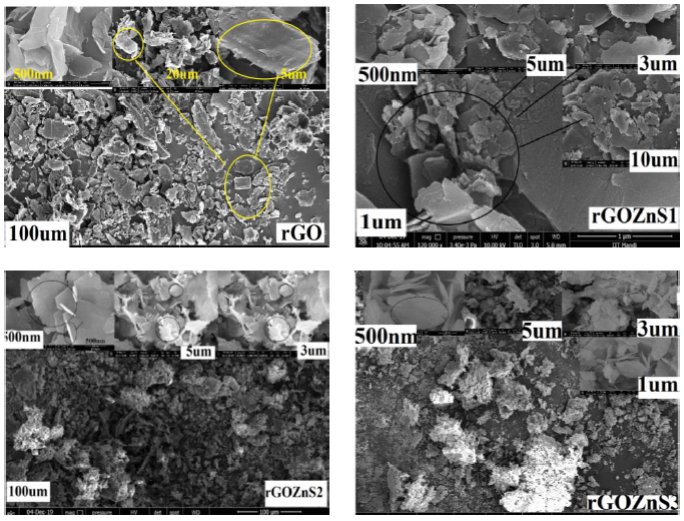

Figure 2.13: The FESEM micrographs of reduced graphene with ZnS nanocomposites. Source; Mohapatra et al. (2021)

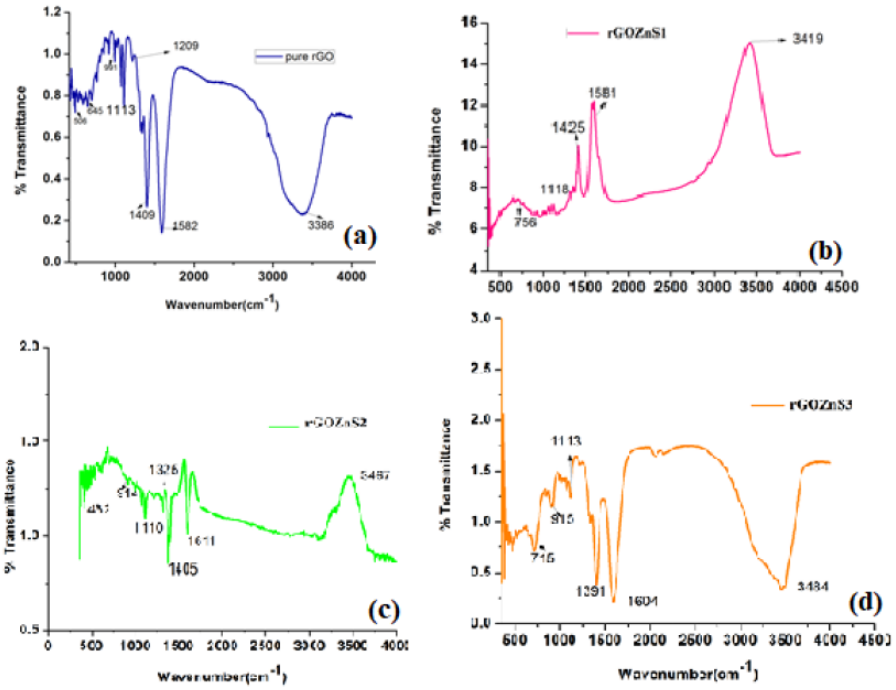

Figure 2.14: Reduced graphene and ZnS synthesis with FTIR spectra analysis. Source; Mohapatra et al. (2021)

Reducing the metal precursors on a rGO surface was the only stage in the straight forward chemical procedure that produced reduced graphene oxide nanosheets decorated with ZnS and ZnS-Ag NPs Naeem et al. (2023) as shown in Figure 2.15. Using ethyl violet (EV) and malachite green (MG) as model dyes, the synthesized rGO-ZnS nanocomposite was employed as an adsorbent material against them. An Ag doped rGO-ZnS nanocomposite stimulated the breakdown of the selected organic contaminant, resorcinol. XRD 2.15(**i**), SEM-EDX 2.15(**iv**), FTIR Figure 2.15(**ii**) and Transmission electron microscopy (TEM) Figure 2.15(**iii**) analysis were used to analysis the properties of the prepared Ag-coated rGO-ZnS nanosheets which exhibited good photocatalytic properties for the degradation of phenolic compounds, rendering them valuable as antimicrobial agents and efficient adsorbents for the treatment of wastewater. This research worked on the waste water treatment and used Ag as the dopant. However, there is lack of hydrogen analysis which could have provided some informative results for comparison purposes.

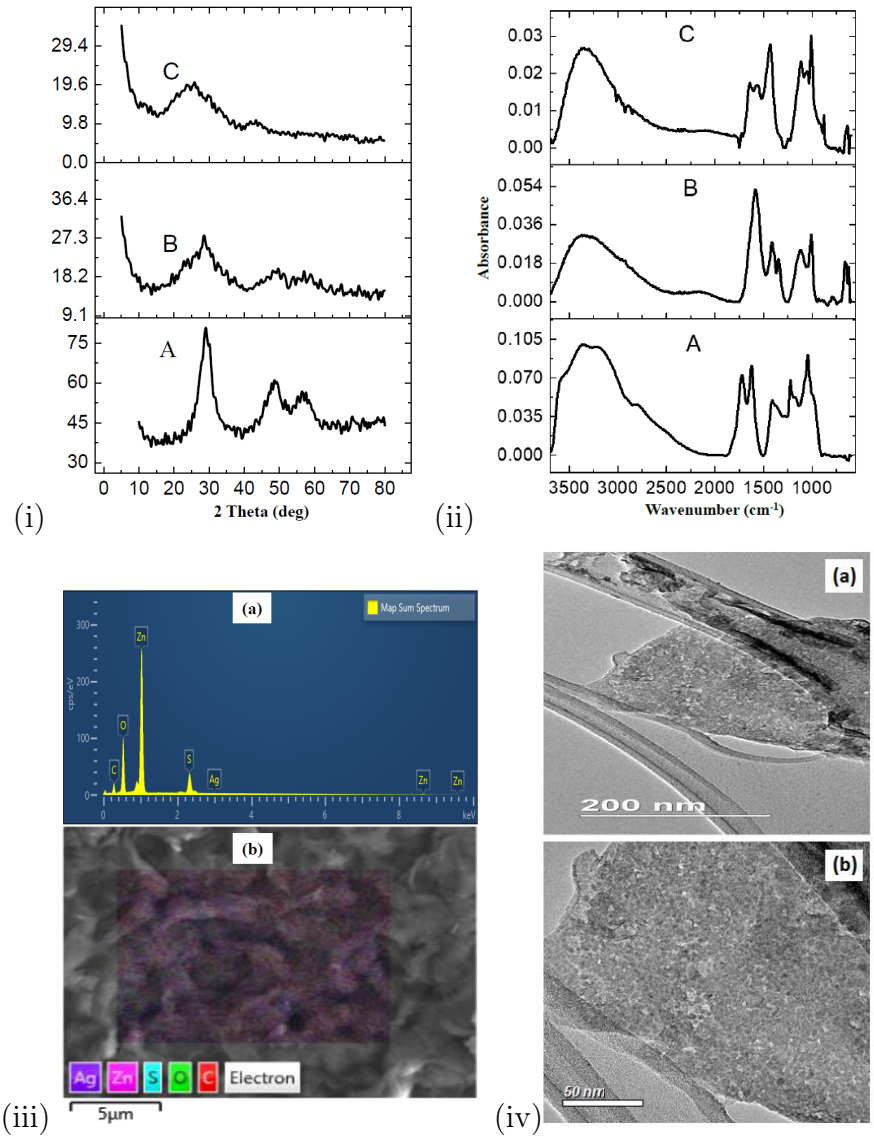

Figure 2.15: The XRD, SEM-EDX, FTIR and TEM characterization of Ag-ZnS-rGO. Source; Naeem et al. (2023)

L. Xue et al. (2011) developed graphene ZnS quantum dot nanocomposites by using Na_2S as a sulfide source and reducing agent and by widely spreading ZnS nanodots over the surfaces of graphene sheets using a simple hydrothermal and HummersHummers Jr & Offeman (1958) technique. The effective reduction of GO to graphene sheets was demonstrated by the results of FTIR as shown in Figure 2.16(**iii**) and XRD 2.16(**i**). A wrinkly paper-like structure of the graphene sheets decorated with ZnS nanoparticles was revealed by the sample's morphological characterisation as seen in Figure2.16(**ii**) .

Additionally, the PL measurement, as illustrated in Figure 2.16(**iv**), revealed

a smooth spectrum, suggesting fewer flaws in the composite. Moreover, PL measurement showed a smooth spectrum, indicating fewer defects in the composite as shown in Figure 2.16. In summary, the SEM and TEM characterizations revealed homogeneous distribution of ZnS nanoparticles on graphene sheets for optical applications. This work provided some insights on the effects of graphene on ZnS NSs but the use of dopants was missing and the study was done for PL measurements. Cobalt NPs were deposited on the surfaces of graphene sheets via

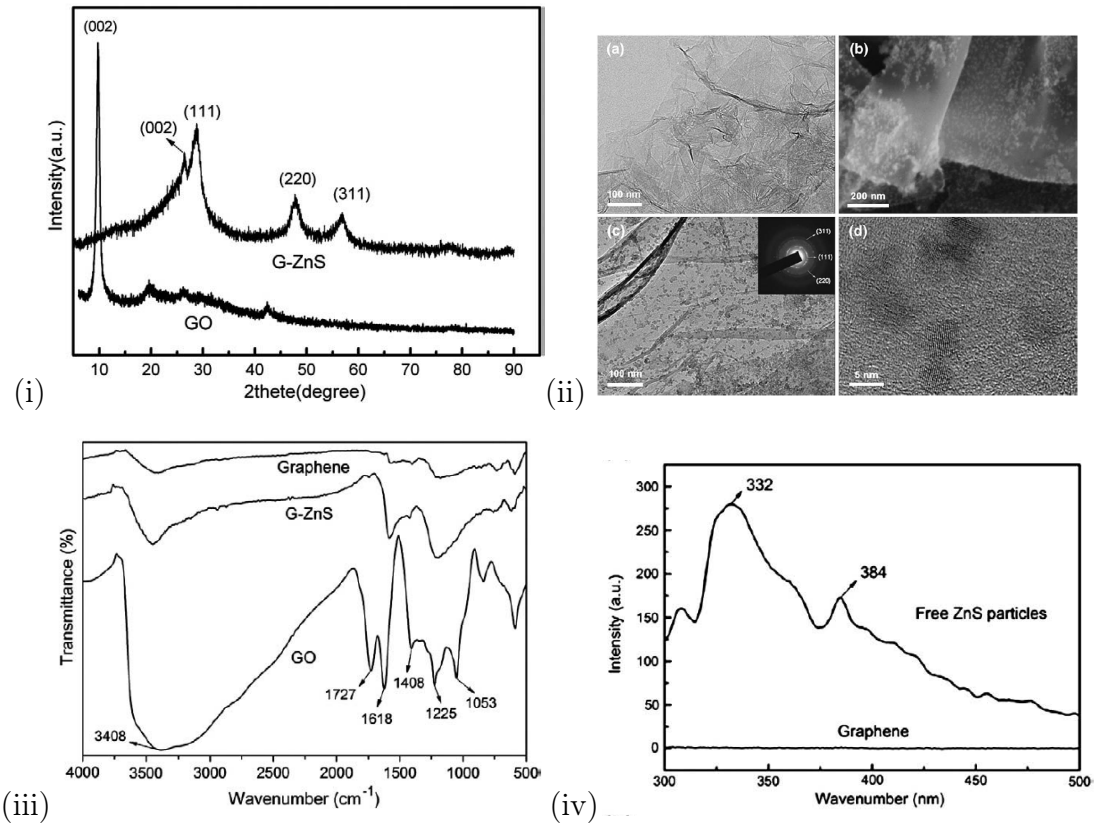

Figure 2.16: The XRD, SEM, TEM, HRTEM, FTIR and PL analysis of G–ZnS composite. Source; L. Xue et al. (2011)

hydrazine hydrate reduction. The as-synthesised composites were assessed using TEM, XRD, FTIR, RS, thermo-gravimetry and differential scanning calorimetry Ji et al. (2011). Figure 2.17 revealed that the as-formed Co NPs were uniformly and densely deposited on the graphene sheet surfaces, thereby preventing the as-reduced graphene sheets from stacking again. The graphene/Co nanocomposite showed ferromagnetic activity with saturation magnetization, according to experiments done; XRD in Figure 2.17(**iv**), RS Figure 2.17(**iv**), FTIR Figure 2.17(**iv**)

and SEM Figure 2.17(**iv**) analysis. The study was done to find potential application of cobalt doped ZnS in ferromagnetism. Despite the fact that the data were helpful for characterization and comparison, no analysis of photocatalytic activity was carried out.

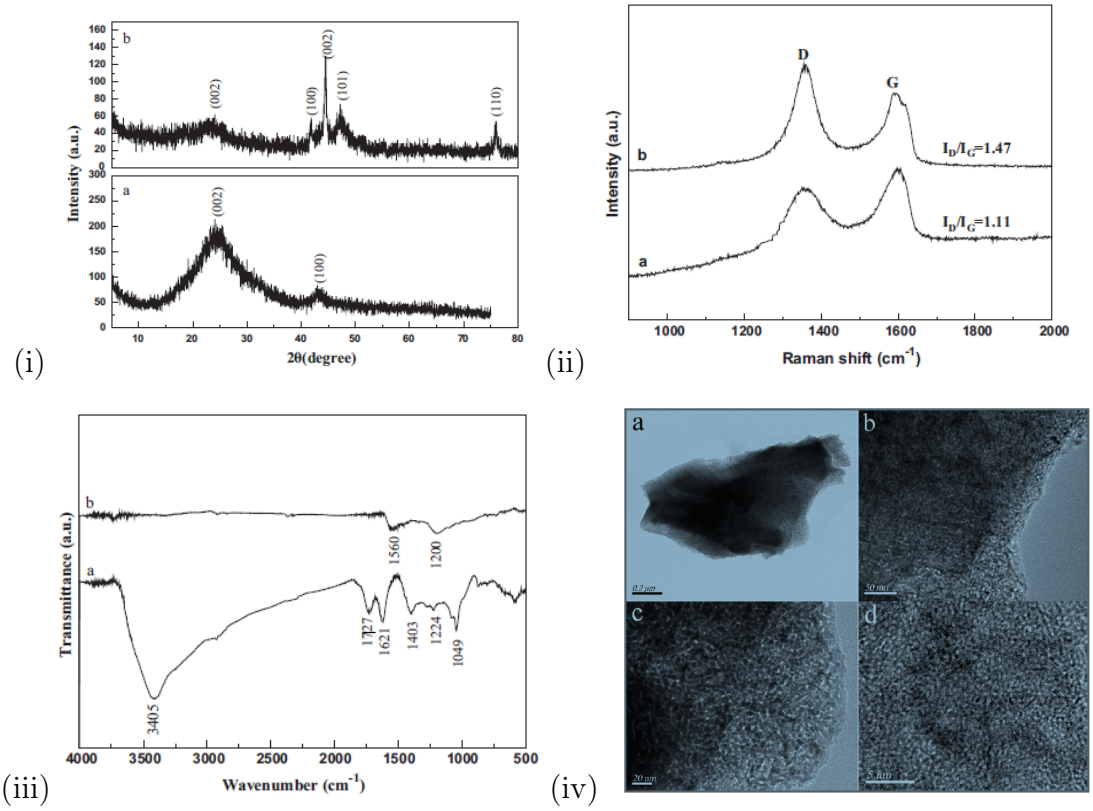

Figure 2.17: The XRD, SEM, FTIR and PL characterization of Graphene/Co. Source; Ji et al. (2011)

Y. Zhang, Zhang, et al. (2012) assembled nanosized ZnS particles on the 2D platform of a GO sheet by a facile two-step wet chemistry process, during which the rGO and the close interfacial contact between ZnS NP and the rGO sheet was achieved simultaneously. The XRD in Figure2.18(**i**) patterns of GO, rGO and the resulting nanocomposites of ZnS-GR showed a sharp diffraction peak at 2θ value of *ca.*10.1° for the rGO obtained from the hydrothermal reduction, the diffraction peak at *ca.*10.1° disappeared and a very broad diffraction peak at 2θ of ca. 25.0° appeared, suggesting practically that all GO sheets were converted to rGO with a random packing and much less functions following hydrothermal reduction and GO sheets were successfully exfoliated from the raw graphite.

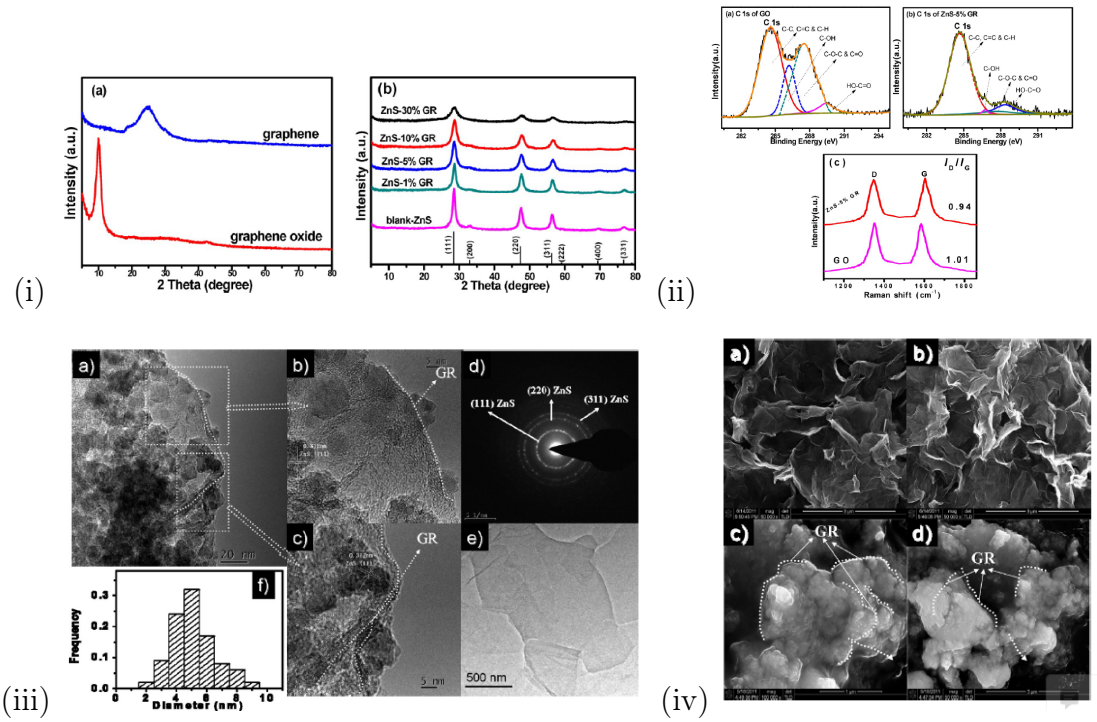

Figure 2.18: The XRD, FESEM, SAED, XPS and RS characterization of graphene-ZnS as a photo-sensitizer. Source; Y. Zhang, Zhang, et al. (2012)

XPS illustrated in Figure 2.18(**ii**) of GO and ZnS-rGO, FESEM Figure 2.18(**iv**), TEM Figure 2.18(**iii**)analysis of ZnS-5% rGO was performed and showed a nice dispersion of nanosized ZnS particles on the surface of the rGO sheet support, selected area electron diffraction (SAED) Figure 2.18(**iii**) pattern as shown in Figure 2.18 (**i**) indexed as (111), (220), and (311) crystal planes of ZnS. In addition, the SAED pattern revealed that the ZnS-5% rGO nanocomposite had a polycrystalline structure, which was consistent with the findings of the XRD analysis for the current study.

The combined SEM and TEM characterization also revealed that the ZnS NPs and the 2D rGO sheet had an interfacial contact created. This strategy was recommended because the transfer of charge carriers in rGO-semiconductor nanocomposites was intimately related to the contact between the rGO and the semiconductor. It was evident that adding different concentrations of rGO significantly affected the optical property of light absorption for rGO-ZnS nanocomposites. With an increase in rGO content, there was a higher absorption of visible

light in the 400–800 nm region, which correlated with the color change of the samples. In this work, ZnS decorated graphene was utilized as a photo-synthesizer; TMD's was not taken into consideration. The acquired results showed a good analysis of NSs which is consistent with current research; nonetheless, hydrogen evaluation and TM were not performed.

C.-J. Chang et al. (2015) investigated the abilities of photocatalytic H_2 production by Ni-doped ZnS graphene composite photocatalysts. Undoped and Ni-doped ZnS was loaded on the surface of graphene to prepare a series of composite photocatalysts. Properties of the photocatalysts were characterized by XRD Figure 2.19(**i**), ultraviolet visible diffuse reflectance spectroscopy Figure 2.19(**ii**) FESEM Figure 2.19(**iii**), high resolution transmission electron microscopy (HRTEM) Figure 2.19(**iv**).

C.-J. Chang et al. (2015) furthermore investigated the abilities of photocatalytic H_2 production by using Ni doped ZnS graphene composite photocatalysts. Properties of the photocatalysts were characterized via BET 1 Figure 2.20(**i (a)**), BET 2 Figure 2.20(**i (b)**), photoinduced current and photocatalytic hydrogen evolution test Figure 2.21(**ii**). HRTEM Figure 2.20(**i**), XPS2.21(**ii**). The results of this examination were highly helpful and could be compared to the current research.

Nevertheless, graphene and Ni dopant were utilized for photocatalytic hydrogen production and the results demonstrated extremely high rates of hydrogen production, demonstrating the necessity of TM doped ZnS decorated with graphene for high rate photoactivity.

The incorporation of graphene oxide was demonstrated by Y. H. Ng et al. (2010) to improve the photocurrent generation and photoelectrochemical water oxidation of Bismuth Vanadate $BiVO_4$ thin films. A simple, one-step photocatalytic reaction was used to improve the photoresponse in visible light and a noteworthy ten fold enhancement in the photo-electrochemical water splitting reaction was observed on $BiVO_4 - rGO$ composite compared with pure $BiVO_4$. Since the

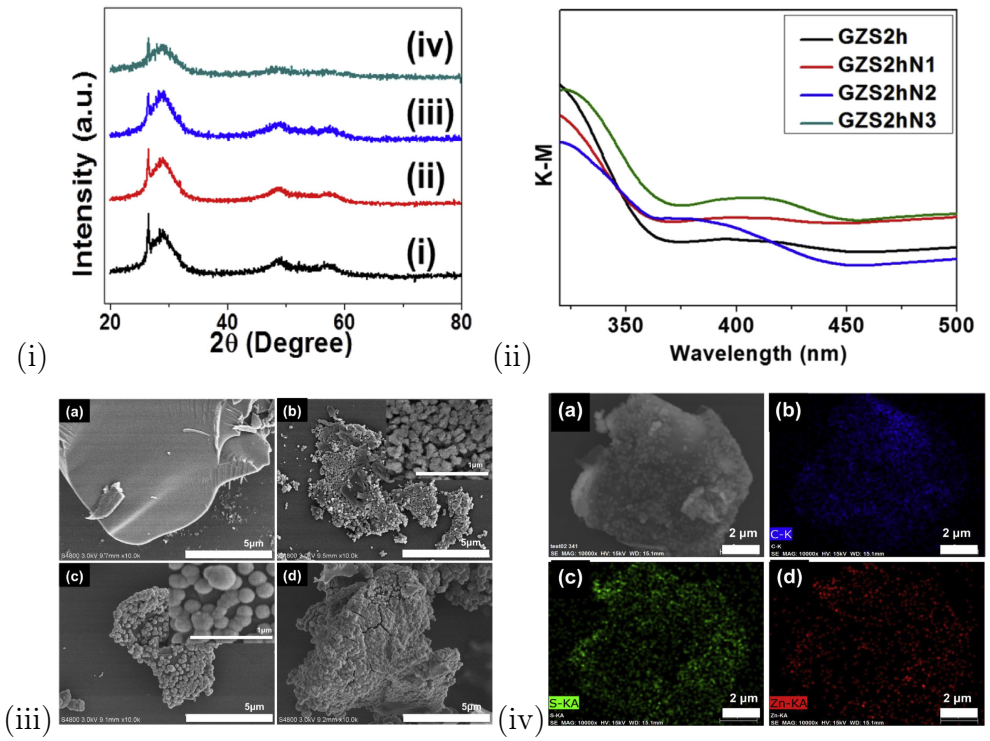

Figure 2.19: The XRD, UV-Vis-FESEM characterization of Graphene-Ni-ZnS. Source; C.-J. Chang et al. (2015)

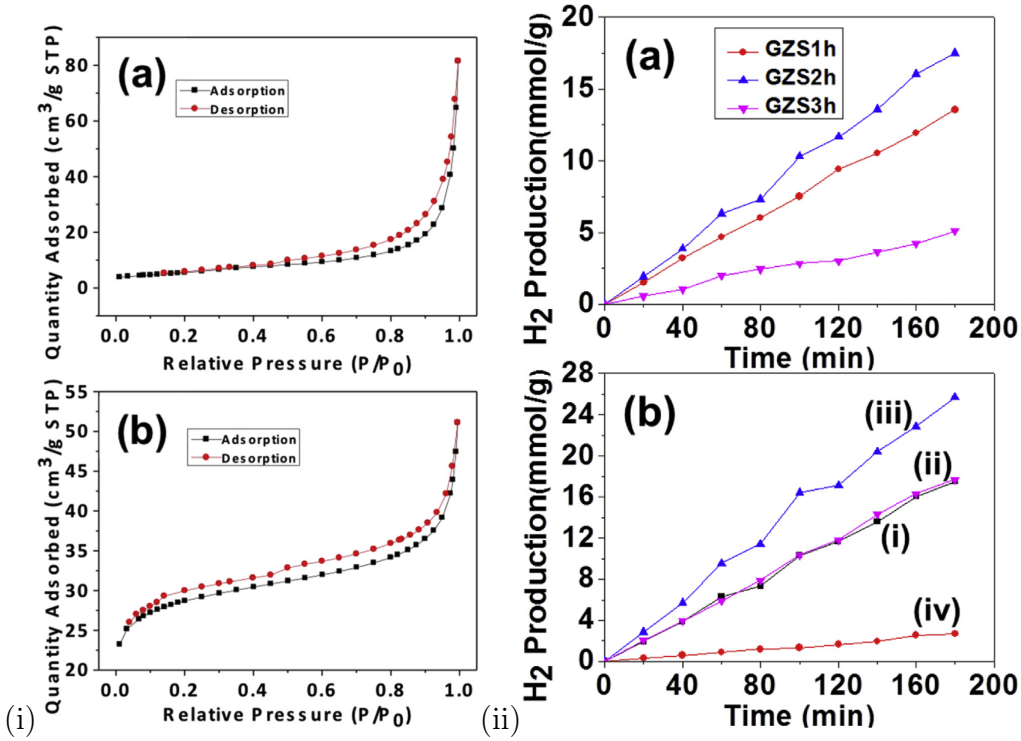

Figure 2.20: The XPS and BET analysis of Graphene-Ni-ZnS. Source; C.-J. Chang et al. (2015)

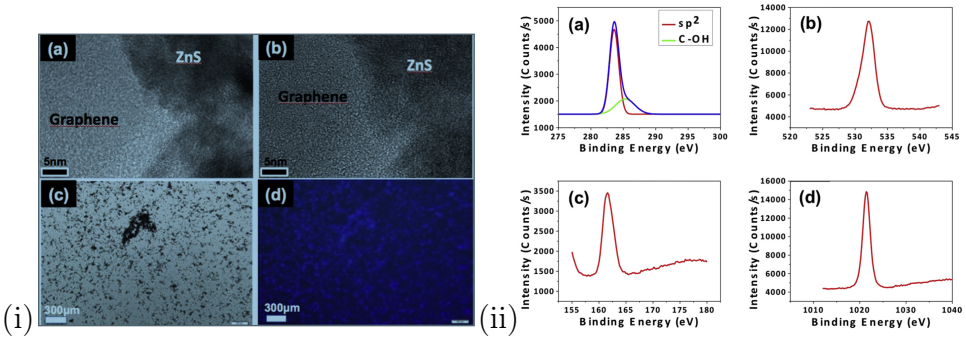

Figure 2.21: The HRTEM and hydrogen energy analysis of Graphene-Ni-ZnS. Source;C.-J. Chang et al. (2015)

electrons were injected into rGO instantaneously at the site of production, there was less charge recombination, which was explained by the longer electron lifetime of excited $BiVO_4$.

This photo-response increase was also assisted by improved contact between $BiVO_4$ particles and transparent conducting electrode utilizing rGO scaffold. Properties of the photocatalysts were characterized by SEM Figure 2.22(**ii**), XRD and XPS Figure 2.22(**i**), electron transfer Figure 2.23(**ii**), UV-vis Figure 2.23(**i**). This study examined graphene and bismuth vanadate for PECWS. Nevertheless, it clarified the significance of adding various atoms to graphene in order to enhance hydrogen generation, and the study excluded the usage of TMD's.

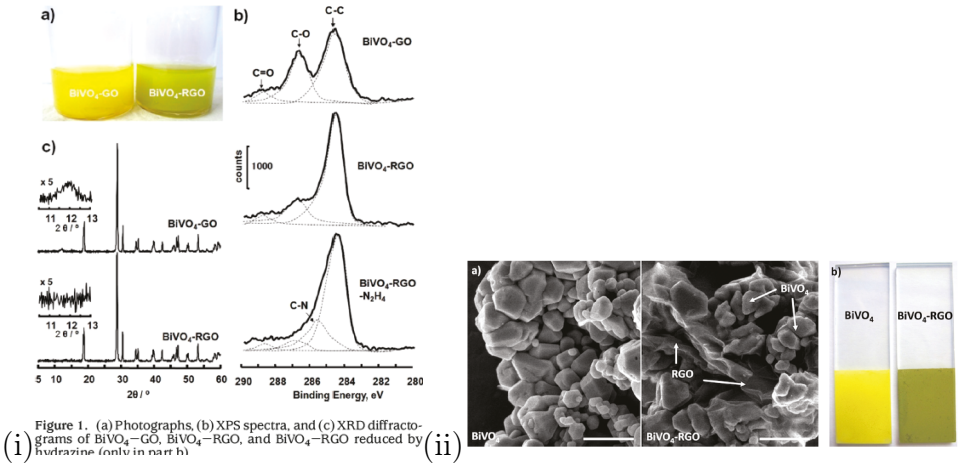

Figure 2.22: The XRD/XPS and SEM characterization of $BiVO_4 - rGO$. Source; Y. H. Ng et al. (2010)

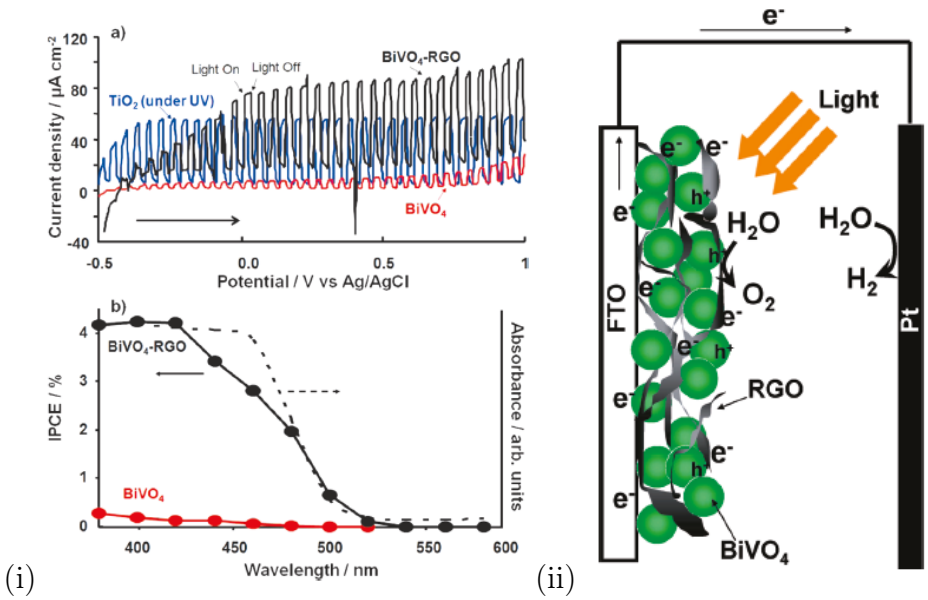

Figure 2.23: The UV-vis and Hydrogen activity analysis of $BiVO_4 - rGO$. Source; Y. H. Ng et al. (2010)

Poly(vinyl pyrrolidone) capped and uncapped Co:ZnS nanoparticles was synthesized by co-precipitation method. These synthesized nanoparticles were characterized using spectral techniques, the optical and photoluminescence properties of nanoparticles were also studied. Poly(vinyl pyrrolidone) capped nanoparticles was studied for the electrochemical sensing of various bio-molecules Sumadevi et al. (2021). The photocatlytic activity on Eriochrome black T dye in the visible region using nanoparticles was been determined using XRD Figure 2.24(**i**), (SEM and RS) Figure 2.24(**iii**) and FTIR Figure 2.24(**i**) analysis. It was found that the capped nanoparticles were more effective in photocatalytic degradation due to low energy consumption and safe recovery of it after catalytic performance from polluted water. This work did not use graphene and instead examined cobalt as the TM dopant for photocatalytic disintegration of pollutants, rather than generating hydrogen.

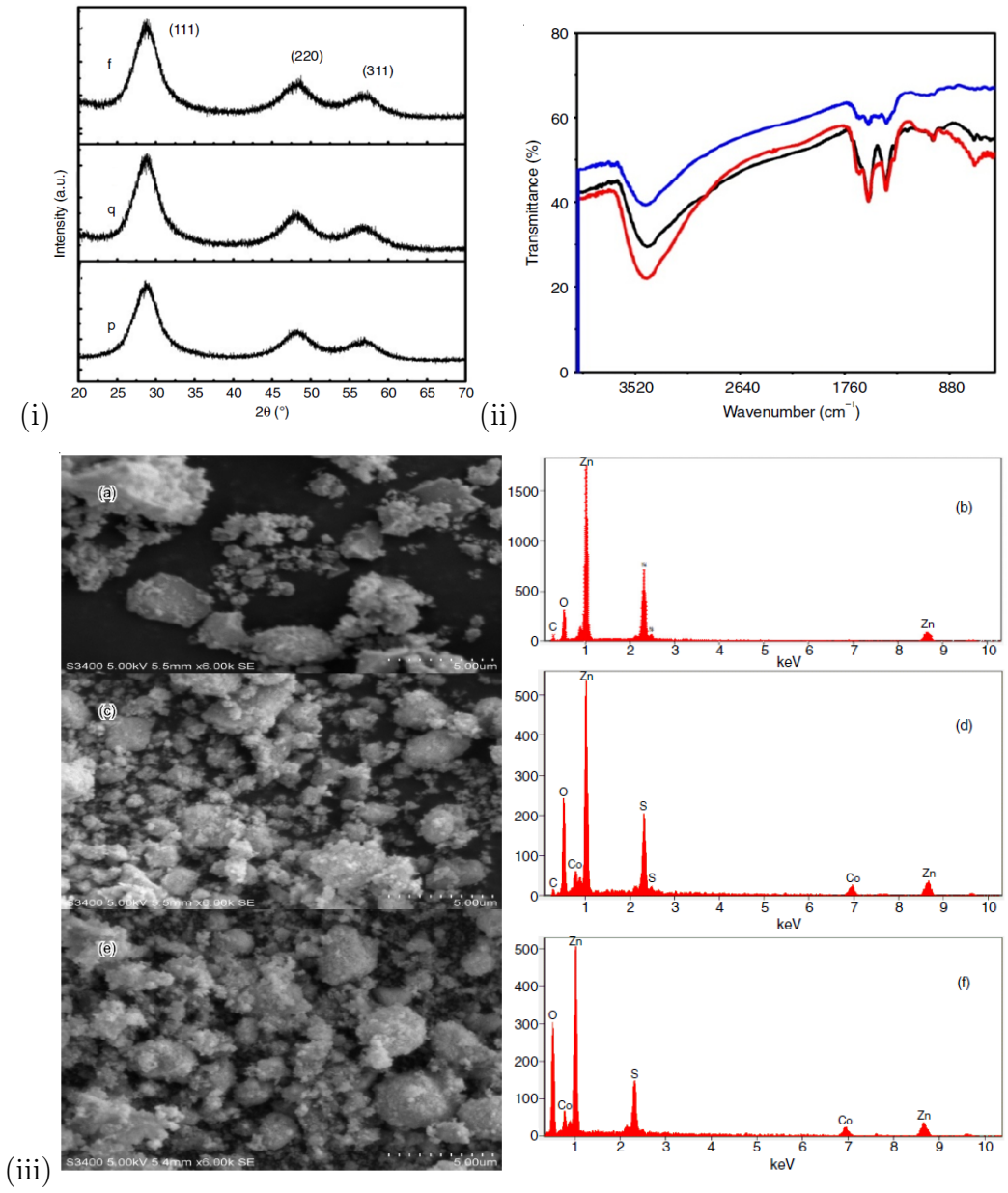

Figure 2.24: The XRD, SEM, RS and FTIR analysis of Poly(vinyl pyrrolidone) capped and uncapped Co:ZnS nanoparticles. Source; Sumadevi et al. (2021)

The literature review conducted by Shakil et al. (2018) revealed that there was no discussion regarding the use of graphene to decorate cobalt doped ZnS for hydrogen production. Different TMDs were discussed in general. Nonetheless, the cobalt-doped ZnS was examined in relation to its possible uses in advanced optoelectronics and spintronics. Its absorbance and transmittance were described using the PL Figure 2.25(**ii**) and Bandgap Figure 2.25(**i**) spectra. Since the work was intended primarily for optoelectronics and sprintonics, only the band gap

and PL spectra were briefly discussed. Graphene was absent and there was no hydrogen analysis.

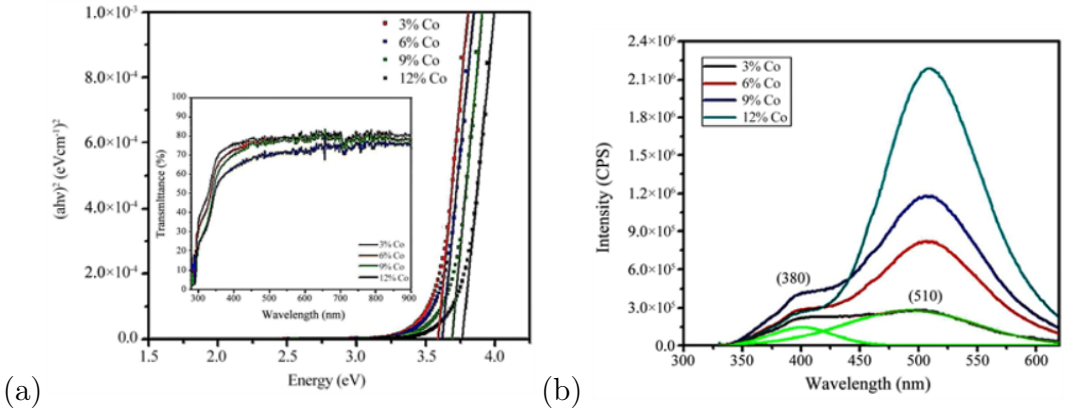

(a) (b)

Figure 2.25: The Bandgap, PL images of Co-ZnS nanoparticles;(*Review 2018*). Source; Shakil et al. (2018)

Mamiyev & Balayeva (2022) further highlighted particularly recent findings in metal sulfide based photocatalysts for hydrogen evolution reactions, considering the swift development and excellent research in this field and found out that the photocatalytic hydrogen evolution rate was still limited mainly by fast recombination rate, poor solar energy utilization and lack of surface active sites for H_2 reduction.

Wasly (2018) successfully created ZnO nanoparticles using a modified hydrothermal approach and these particles were examined using XRD Figure 2.26(**i**), HRTEM and other methods as shown in Figure 2.26 (a) and (b). HRTEM was carried out to investigate the shape and size of the obtained ZnO nanoparticles with different reaction times.The size and form of the produced ZnO nanoparticles were discovered to be affected by the reaction time. ZnO nanoparticles were produced in spherical and rod shapes with longer reaction times due to an increase in growth rate, see Figure 2.26(**ii**).

Additionally, due to smaller nanoparticles gathering and creating larger particles, nearly all of the ZnO nanoparticles emerged as clusters of nanorods S. N. Shah et al. (2016). The equivalent strain and grain size was calculated from the diffraction patterns using the Scherrer and Williamson-Hall method. The average values

of the ZnO nanoparticles' D crystallite size with a range of 30-34 nm to represent the typical values of the crystallite size, D of the ZnO nanoparticles produced at various reaction durations.

The Figure 2.26(**iii**) and Figure 2.26(**v**) showed the optical absorption and transmittance spectra of the manufactured samples for times 7, 15, and 23 hours at near normal incidence over a spectral range between 200 and 800. The direct optical band gap Figure 2.26(**vi**) and crystallite size Figure 2.26(**iv**) obtained from Scherrer calculated using the relation:

$$\alpha hv = B(hv - E_g)^{\frac{1}{2}} \tag{2.5}$$

where B is a constant whose value depends on the likelihood of a transition, hv is the photon energy, is the absorption coefficient and E_g is the optical band gap. From Figure 2.26(**vi**), the plot of hv against hv^2 was used to estimate the energy gap E_g. According to the reaction time, the values of E_g were 3.58, 3.14, and 2.90 eV for S1-S3 respectively using Equation 2.5. The calculated values differ from the bulk ZnO value 3.37eV. The produced zinc oxide samples' quantum confinement effects may be to blame for this blue shift Jay Chithra et al. (2015); S. N. Shah et al. (2016). According to the reaction time, the values of E_g were 3.58, 3.14, and 2.90 eV for S1-S3 respectively using Equation 2.5. It was apparent that as reaction time was increased, the band gap value dropped as a result of an increase in crystallite size. This demonstrated that the aforementioned behavior may result from rising nucleation and growth rate of NPs Wasly (2018); Jay Chithra et al. (2015). Figure 2.26 (**iii and v**) shows absorbance and transmittance spectra of ZnO nanoparticles synthesized at different times. The blue shift of the absorption of ZnO in the UV–Vis spectra was gradually increased with the increase in reaction time due to the decrease of particle size. The morphology showed that with increasing the reaction time, smaller nanoparticles combined themselves and formed larger particles and the average size of the ZnO nanoparticles is in in agreement with XRD calculations. Regarding the UV-vis analysis, this study offered insightful

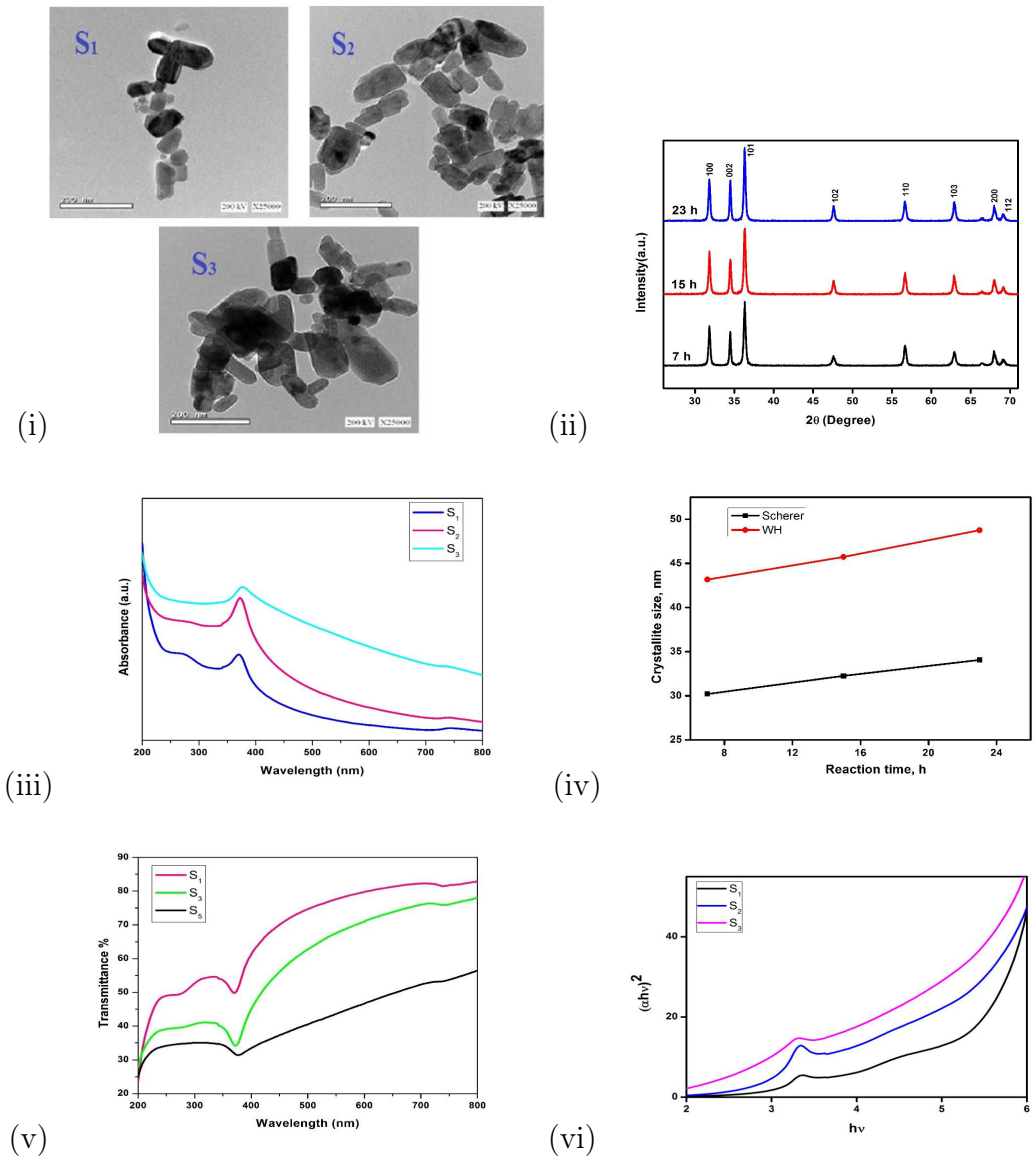

Figure 2.26: The XRD, SEM, Absorbance, Transmittance, crystallite size obtained from Scherrer and Direct band gap of ZnO nanoparticles synthesized at different times. Source; Wasly (2018)

information that was highly pertinent to the ongoing investigation. Nevertheless, the samples' basis material was ZnO rather than ZnS, the study was done for optical purposes rather than hydrogen, and graphene and TM dopants were also absent.

The annealing effects on the XRD patterns of the Co^{2+} ions doped ZnS samples are displayed in Figure 2.28(**b**) Ashokkumar et al. (2015). Up to five hours of annealing at $100°C$ did not cause any change in the three diffraction peaks that corresponded to the (111), (220), and (311) planes after annealing 3 mole% Co^{2+}

ions doped ZnS in different time interval samples. Furthermore, reflections at $2 = 28.9°, 48.4°, and 57.5°$, respectively, indicated that the cubic crystalline ZnS was annealed in an open atmosphere. For this annealing, no other impurity phase peak (Co, CoS, ZnO, and CoO) was detected for any of the time intervals. The absence of any diffraction peaks in the sample's XRD pattern suggested the absence of the crystalline CoS, CoS, and ZnO phases. Making Use of the Debye-Scherrer Equation Cullity (1956).

$$D = \frac{0.9\lambda}{\beta cos\theta} \tag{2.6}$$

The full width at half maximum (FWHM) of the primary XRD peak was used to compute the size of the crystallite, where D is the crystallite size, λ is the X-ray wavelength, θ is the Bragg angle and the full peak width. Based on the Debye Scherrer Equation 2.6 from the peak with the maximum intensity, the average grain size of the Co^{2+} doped and undoped ZnS samples were determined.

Ashokkumar et al. (2015) employed a simple, optimized wet chemical co-precipitation method to produce clean, distinct Co^{2+} ion doped ZnS nanocrystals. The 3 mole% of Co^{2+} ions doped particles were produced by annealing ZnS NPs at $1000°C$ for (1, 2, 3, 4 and 5) hours, respectively as seen in Figure 2.27(**b**). According to the results of the experiments, NPs were stable for a few minutes before aggregation and growing in size as a result of their high SA to V ratio and an increase in the attractive force between them, as seen in Figure 2.28(**c and d**). Following annealing, Co^{2+} ions doped with ZnS nanostructures were analyzed via UV-Vis spectrometer, XRD, SEM and energy dispersive analysis of X-rays (EDAX).

XRD measurements shown in Figure 2.28(**a and b**) revealed a phase singularity in the cubic structure of Co^{2+} ions doped ZnS particles. This indicated the incorporation of Co^{2+} ions into the Zn^{2+} lattice positions. According to these findings, the chemical was in a homogeneous phase and stable at $1000°C$. Based on the broadening of the X-ray diffractogram pattern lines, the pure and doped

sample contained nano size crystals with diameters of around 4-6 nm. The Zinc blend phase and crystalline size were unaffected by Co^{2+}. Co^{2+} doped ZnS was discovered to have a lower band gap value than pure ZnS.

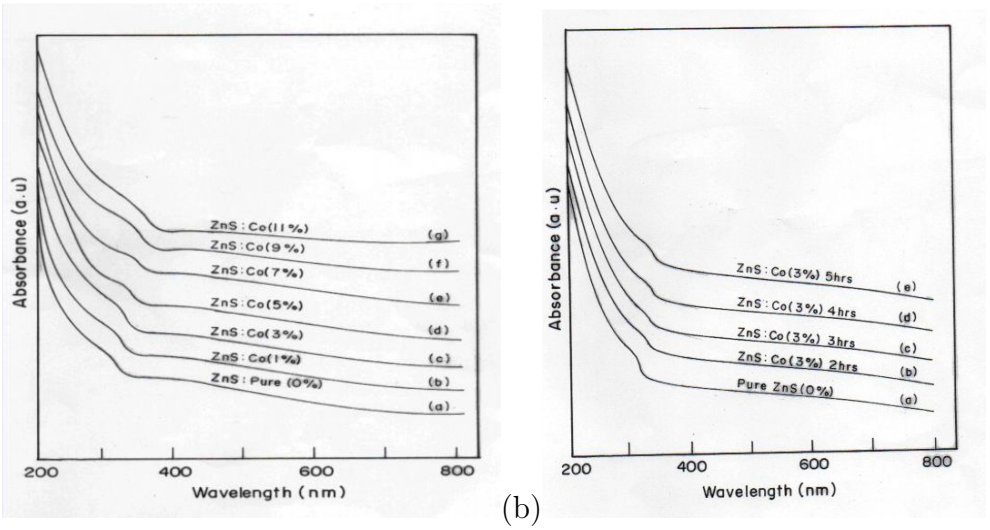

Figure 2.27: The UV-Visible spectrum of (a) (1, 3, 5, 7 and 11 %) and (b) 3% at (0, 2, 3, 4 and 5 hours) of Co^{2+} ions doped ZnS compound, Source; Ashokkumar et al. (2015)

It was demonstrated that cobalt doped ZnS NPs had a cubic structure and a uniform size distribution with a range of 4-6 nm based on XRD studies and Debye Scherrer's Equation 2.6. As a result of the XRD Figure 2.28(**a**) analysis, the ideal doping concentration was found to be 3% of Co^{2+} ions. Both the crystalline size of the ZnO that was produced and the cubic phase of ZnS NPs remained unchanged in response to doping the concentration of Co^{2+} ions or varying annealing times. The crystalline size of ZnS was not affected by annealing at $1000°C$ for varying durations, or by increasing the doping concentration, as observed in XRD in Figure 2.28(**b**) images, due to aggregation and a high surface to volume ratio of Co cluster formation. As the concentration of Co^{2+} ions grew, the optical band-gap energy of the cobalt doped ZnS nanoparticles decreased. Ashokkumar et al. (2015) reported photoluminescence measurements of the produced nanoparticles at room temperature Figure 2.28(**c**).

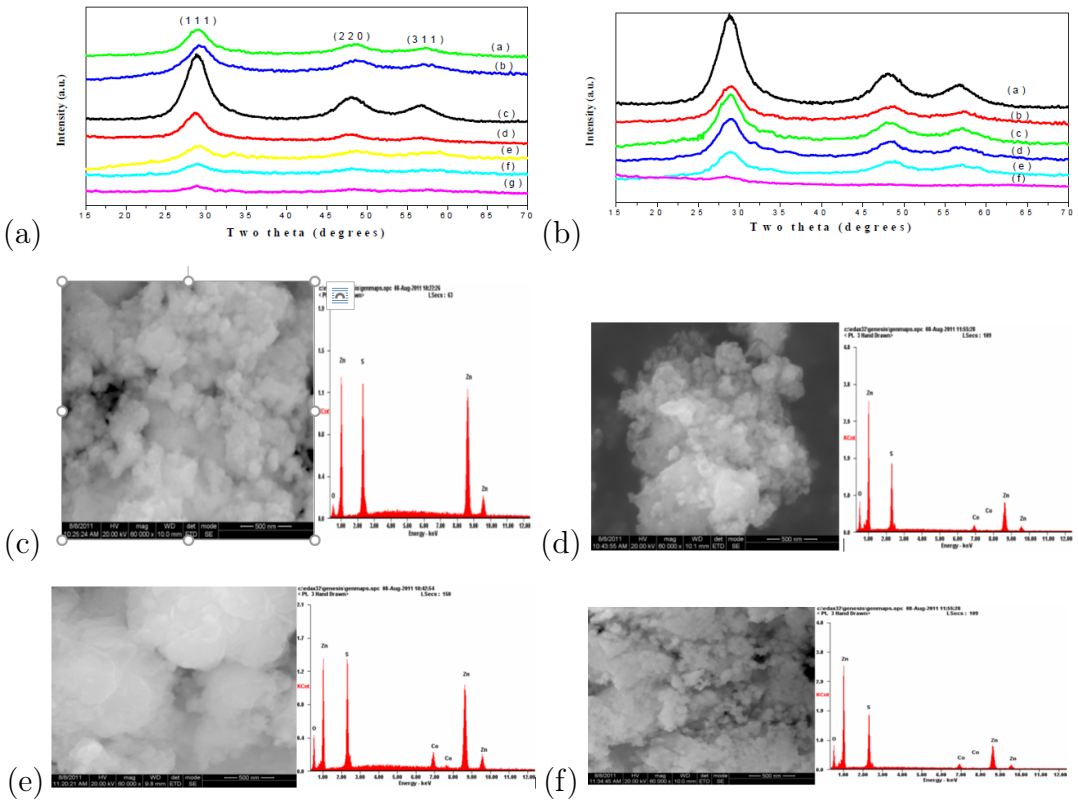

Figure 2.28: The XRD patterns and SEM images of 3% Co^{2+} ions doped ZnS at $100°C$ annealed at different time interval (a) 1hr (b) 2 hrs (c) 3 hrs (d) 4 hrs (e) 5 hrs (f) 6 hrs. Source; Ashokkumar et al. (2015)

While the undoped sample showed PL emission peaks at 450 nm, the Co^{2+} doped ZnS sample generated PL emission throughout the visible range with several peaks at 405, 468, and 495 nm. For optical purposes, cobalt doped ZnS was the subject of the investigation. Nonetheless, this work offered insight into the optimal cobalt dosage, corresponding to at 3% nearly consistent with the current study. Insightful data on XRD, SEM, UV-vis and lattice analysis being the subjects of the current study are also provided. There was a lack of graphene and additional research on hydrogen analysis.

Mahvelati-Shamsabadi & Goharshadi (2018) embedded ZnS NPs on different numbers of rGO nanosheets using ultrasonic waves. It was determined how well the rGO-ZnS nanocomposites worked as a photo-anode for the oxygen evolution reaction. The photo-electrocatalytic activity of the rGO-ZnS nanocomposite with 10% rGO (rGO10-ZnS) was remarkably high when compared to ZnS, rGO and

other manufactured nanocomposites. With a negative starting potential of around 200 mV, it showed a five-fold higher maximum photocurrent density ($1.1 mA cm^2$) at 1.23 V (against RHE) than ZnS NPs in Na_2SO_4 (0.5 M) solution.

The power produced by the solar simulated light, which was stored from the external power source, was $0.9 mW cm^2$, or 1 V. The photovoltaic voltage of rGO 10-ZnS rose by approximately 400 mV in comparison to ZnS. The goal of this endeavor was to generate power using voltage and photocurrent. Finding out the impacts of graphene incorporated in ZnS NPs for photocurrent/voltage generation was made possible thanks in significant portion to the analysis. TM dopant, which may have allowed for comparison with the current research, was absent from this paper.

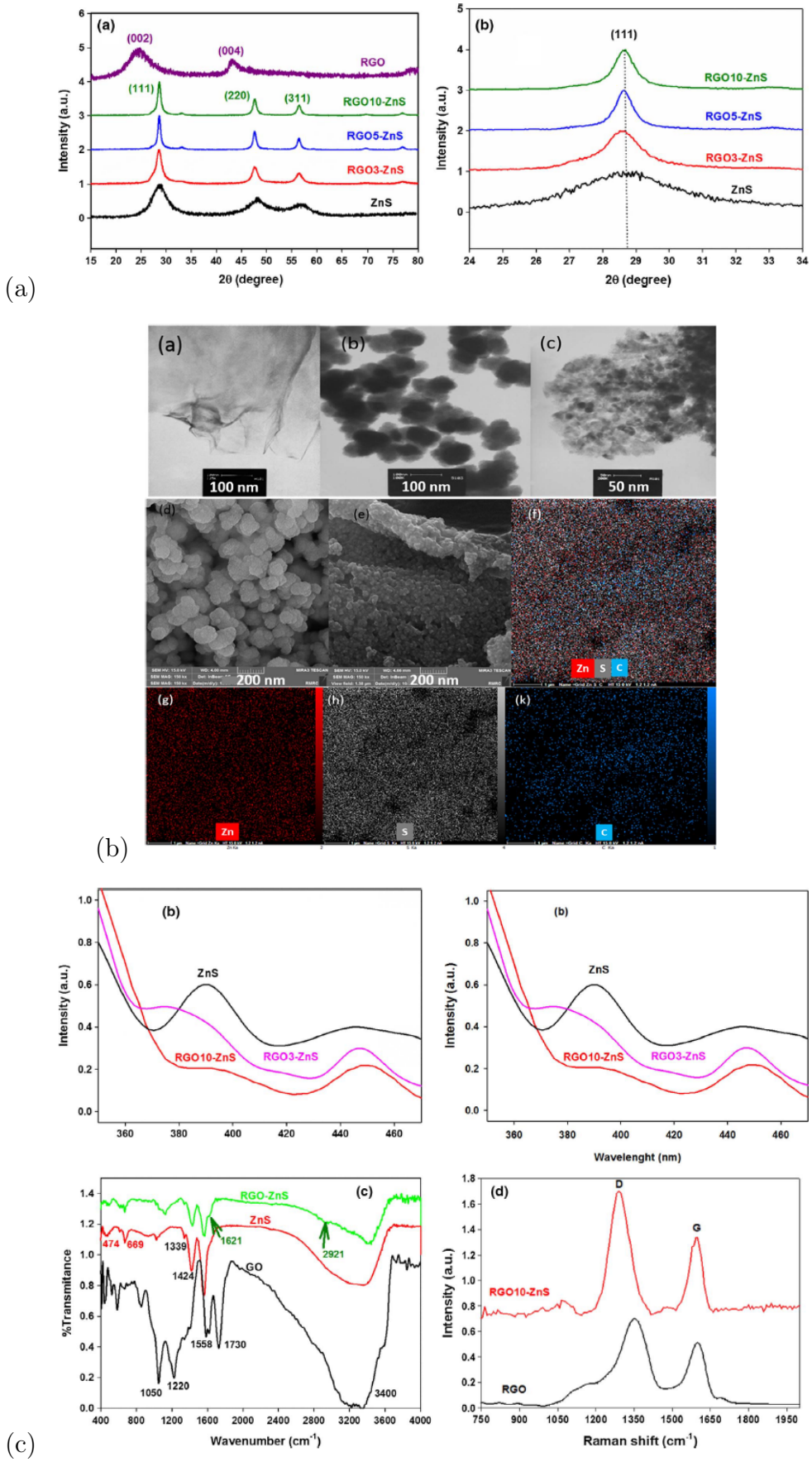

Figure 2.29: The XRD, SEM, UV, IR, PL and RS investigation of the rGO-ZnS nanocomposites. Source; Mahvelati-Shamsabadi & Goharshadi (2018)

R. K. Sharma et al. (2016) produced ZnS nanoparticles utilizing a chemical technique without the use of a capping agent. Cobalt was added to the particles in concentrations ranging from 1% to 8%. XRD, TEM, UV-vis and X-ray fluorescence (XRF) were used to analyze the produced materials for their structural and optical features. The zinc blend structure was corroborated by the measured XRD patterns, which showed that ZnS:Co particles ranged in size from 3.2 to 3.7 nm. Data from a UV study were used to calculate the optical band gap.

Doping caused the band gap to vary, ranging from 4.95 to 5.8 eV. Studies on the ultraviolet spectrum revealed a blue shift as particle size decreased starting with bulk ZnS, indicating quantum confinement. When utilized in many layers, this material may have the potential to be used as a filter or as a window layer in solar cells. It was found that the band gap results from simulation in the cases of nickel and cobalt doping were similar to those from experimental UV-vis spectroscopy data, which revealed changes of 5.1 eV to 5.66 eV in the case of nickel doping Sud & Sharma (2016) and changes of 5.0 eV to 5.6 eV for different doping concentrations in the case of cobalt as shown in Figure 2.30**a**.

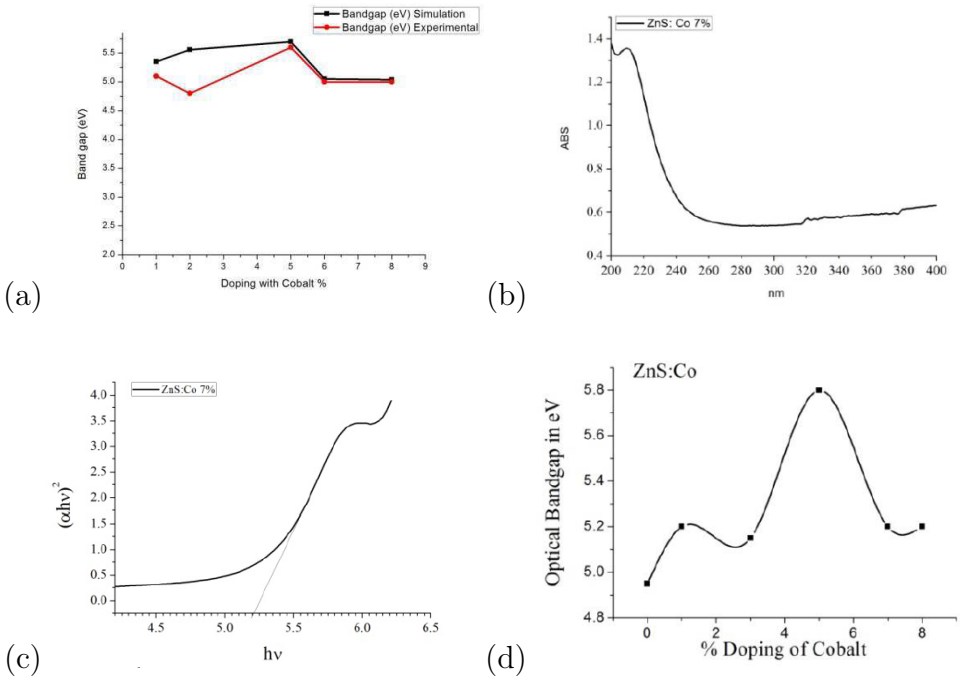

Figure 2.30: The (a) Band gap verse concentration (b) UV-vis Spectrum (c) Tauc plot (d) Optical band gap verses concentration variation of cobalt doped ZnS. Source; R. K. Sharma et al. (2016); Sud & Sharma (2016)

One way to vary the electronic properties of a ZnS thin layer was to change the band gap as seen in Figure 2.30(**b**). The blue shift, or large band gap created in cases of doping, can be explained by the confinement effect in nanostructure. The material may have been useful in the UV spectrum as a result of this wavelength modification. As the particle size decreases, the ZnS characteristic peak, which corresponds to the 3.66 eV band gap, shifts to shorter wavelengths. Figure 2.30(**b**) illustrates the blue shift that results from doping, which may have caused the cutoff wavelength to drop into the ultraviolet spectrum.

The study revealed that cobalt doping in ZnS alters the optical band gap significantly, increasing from 5.2 nm for 1% Co to 5.8 nm for 5% Co by extrapolating the straight section of the curve to the x-axis Figure 2.30(**c**), while the pure ZnS band gap was 4.95 eV at 3.8 nm crystallite size. For both 1% and 5% cobalt doping, the crystallite size was the same.

A maximum band gap of 5.8 eV was attained at a cobalt doping level of 5%, as shown in Figure 2.30(**d**), as opposed to the measured band gap of 4.95 eV for pure ZnS. At 1%, 3%, 7%, and 8% doping levels, band gaps are less. Additional investigation reveals that the crystallite size was almost consistent within reasonable error limits. Hydrogen analysis was not done and graphene was absent from this paper. The application is in the solar cell's window layer. In terms of comparison, especially when applying UV-vis analysis to ascertain the band gap of the cobalt doped ZnS NSs at different concentrations, the findings were extremely relevant to this study.

Yan et al. (2013); Z. Liu et al. (2008); Czerw et al. (2002) clarified that graphene has a work function of 4.4 eV compared to ZnO as depicted in Figure 2.31 which has an estimated work function of 4.5 eV Sundaram & Khan (1996). During the development of ZnO/GR composites, certain electrons from the graphene sheet may have diffused towards the ZnO and subsequently gather at the interface to form potential barriers. The barriers may have prevented the electron from diffusing into ZnO. These electrons may be found in the bases of the conduction bands

of ZnO. There was a substantial population of low energy levels in the conduction band following thermal relaxation.

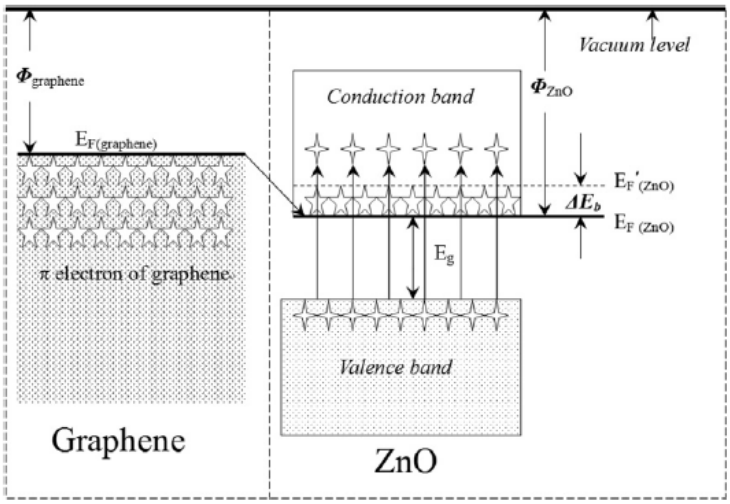

Figure 2.31: Schematic of the Burstein–Moss shift in ZnO/GR. Source; Sundaram & Khan (1996)

From curves a to g, the UV emission peak site progressively changed from 384 to 379 nm as shown in Figure 2.32(**i**). The UV emission peak's blue-shift may have been brought on by the interaction between the graphene sheets and the ZnO particles.

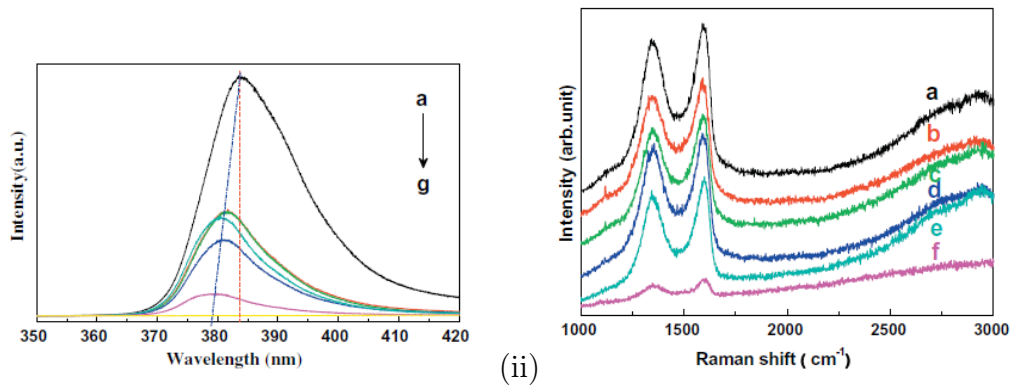

Figure 2.32: The (i) blue shift of the UV peak (ii) Raman spectra (Samples a to f represent 1 mM ZnO suspension at different GR concentrations: (a) 0.025, (b) 0.033, (c) 0.05, (d) 0.1, (e) 1, and (f) 5 mg/mL) of graphene and ZnO/GR composites. Source; Yan et al. (2013)

The RS of ZnO/GR composites revealed the presence of two fundamental vibrations, as Figure 2.32(**ii**) illustrates. Typically, the E_{2g} phonon of carbon sp^2

bonds was identified as the source of the G band at $1580cm^{-1}$. As a breathing mode of p-point phonons of A_{1g} symmetry, the D band was found at $1357cm^{-1}$. It was linked to many local defects and disorders, especially those seen at the edges of graphene and graphite platelets Tuinstra & Koenig (1970); Ferrari & Robertson (2000). The D/G intensity ratios were shown to exhibit unpredictable changes as GRs concentrations rose from 0.025 mg/mL to 5 mg/mL. Greater than the 0.75 D/G intensity ratio observed in GO, a D/G intensity ratio of roughly 0.90 was observed in all ZnO and GRs. According to this, ZnO/GR's disorder may have increased and more sp^2 domains may have formed as GO disappeared. The increase at $2937cm^{-1}$ associated with the D+G band was more indication that graphene was becoming more disordered Ferrari et al. (2006); Ni et al. (2007).

This work was significant since it expanded on the knowledge of how to compute band gap at various graphene concentrations using UV-vis analysis. It also shed light on the role that graphene plays in semiconductor band gap reduction for PEC applications. Unlike the current research, the study did not take into account TM dopants for future improvement in band gap reduction. Furthermore, ZnO rather than ZnS was used as a base material in the work.

G.-J. Lee et al. (2019) synthesized (In, Cu) co-doped ZnS NPs in DI water and ethanol solvent by a sonochemical approach using citric acid as surfactants in aqueous for photoelectrochemical hydrogen production and the as-synthesized photocatalysts were tested for the photocatalytic hydrogen evolution from water splitting via the irradiation of simulated sunlight. Among In and Cu co-doped ZnS products,$4In4CuZnS$ photocatalyst achieved the maximum hydrogen production rate $752.7\mu molh^{-1}g^{-1}$ in 360 minutes under simulated sunlight illumination. Hydrogen and oxygen cells were separated by using an ion exchange membrane.

Both electrodes (working electrode and Pt electrode) were dipped into each cell containing an aqueous solution containing 0.1 M Na_2S at pH-3 to convert water into hydrogen and oxygen under solar irradiation. $4In4CuZnS$ NPs showed the photoelectrochemical performance with photocurrent density of $12.2\mu molAcm^{-2}$

at 1.1V and hydrogen evolution rate of $1189.4 \mu molh^{-1}g^{-1}$. It also showed an excellent photocatalytic activity due to the maximum surface area, the minimum particle size and the minimum charge transfer resistance because this may have provided more active centers for catalysis reaction. This work involved the use of platinum, which is highly expensive.

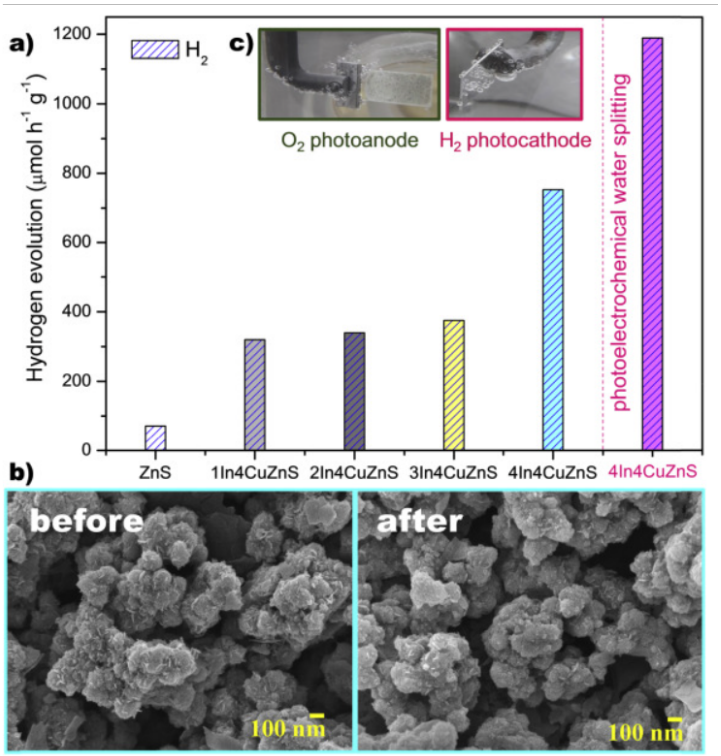

Figure 2.33: Hydrogen evolution and characterization of $4In4CuZnS$ nanoparticles. Source; G.-J. Lee et al. (2019)

G.-J. Lee et al. (2016); G.-J. Lee & Wu (2017) synthesized Cu/ZnS microspheres using microwave irradiation method as seen in Figure 2.34 without using any template. The photocatalytic activity was studied towards the photocatalytic hydrogen evolution under visible-light-driven Cu/ZnS photocatalysts in the presence of Na_2S solution as a sacrificing agent. ZnS with $2 \mu mol$ % Cu^{2+} ion doped shows the maximum hydrogen evolution rate of $973.1 \mu molh^{-1}g^{-1}$ at pH-3 solution. In and copper were taken into consideration as the metal dopants for photocatalytic reactions in this investigation. Nevertheless, the results were very informative about the effects of doping and provided a basis for comparing different doping agents to boost photoactivity.

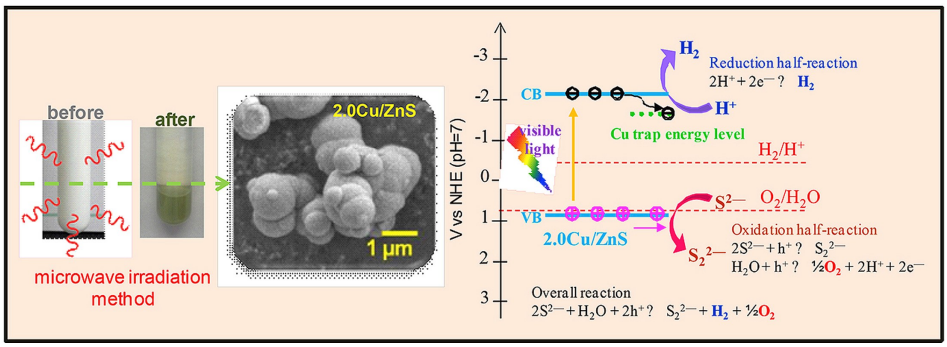

Figure 2.34: The photocatalytic hydrogen evolution illustration. Source; G.-J. Lee et al. (2016); G.-J. Lee & Wu (2017)

A novel Cu/ZnS/COF composite photocatalyst with a core shell structure was synthesized for photocatalytic hydrogen production via water splitting by W. Wang et al. (2021) as shown in Figure 2.35. The photocatalytic hydrogen production results showed that the hydrogen production rate reached 278.4 $\mu g^{-1}h^{-1}$, attributed with its special structure, which has a large number of active sites, a more negative conduction band than the reduction of H^+ to H_2 and the ability to inhibit the recombination of electron–hole pairs. The research offered a novel idea for building a very effective catalyst for the creation of hydrogen and expanded uses for ZnS-based materials.

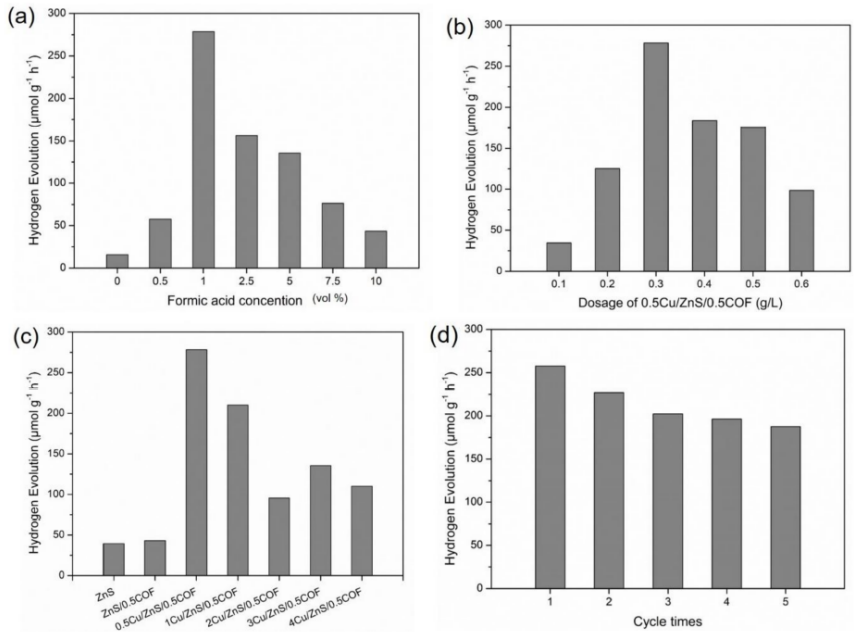

Figure 2.35: Photocatalytic hydrogen production of Cu/ZnS/COF composite. Source; W. Wang et al. (2021)

C.-J. Chang et al. (2015) established a photocatalytic activity of synthesized graphene@ZnS nanocomposites and evaluated by measuring H_2 production from water splitting in an Na_2S/Na_2SO_3 aqueous solution. As shown in Figure 2.36, photocatalytic H_2 production performances of undoped graphene ZnS photocatalysts. The as-prepared graphene Ni-doped ZnS nanocomposites showed a highly active photocatalysts for hydrogen ZnS evolution and the highest photocatalytic activity reached 8683 $\mu h^{-1}g^{-1}$.

This also showed that Ni-doping and decorated ZnS on graphene improved the photocatalytic H_2 production activity because of improved dispersing property, increased surface area, increased absorption and enhanced transfer of photo generated electrons as shown in Figure 2.37. The results of this work were useful and were utilized to track and contrast the outcomes of the current study. However, the TM dopant in this experiment was nickel. In the present instance, cobalt, additional TM dopants were required in order to determine the photoactivity rates for various TM.

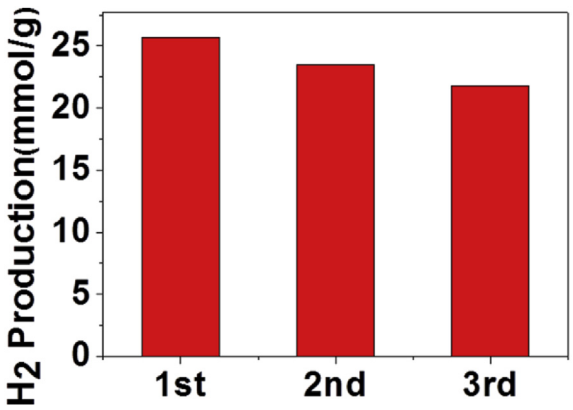

Figure 2.36: Hydrogen quantification of graphene@ZnS nanocomposites. Source; C.-J. Chang et al. (2015)

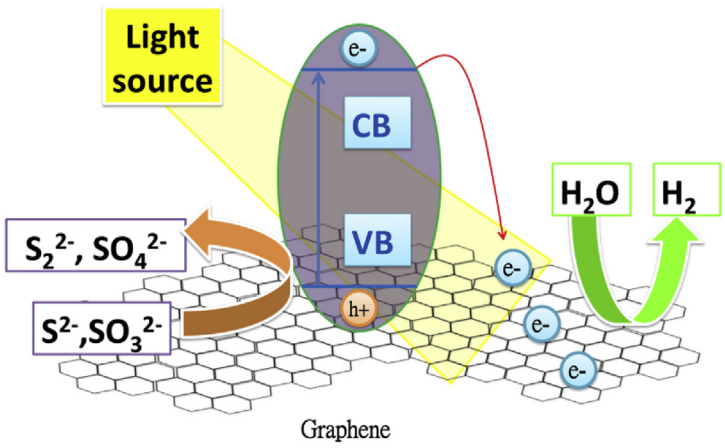

Figure 2.37: Proposed visible light induced photocatalytic mechanism of nickel doped ZnS–rGO photocatalyst. Source; C.-J. Chang et al. (2015)

Agorku et al. (2015) examined the degradation of indigo carmine dye in water by employing graphene based photocatalysts to significantly increase visible light induced photocatalytic activity in a series of Co-doped ZnS–rGO nanocomposites made by co-precipitation technique. Their research focused on optimizing graphene based ZnS for water remediation through photo-degradation of indigo carmine an organic contaminates as shown in Figure 2.38.

The degradation of indigo carmine is primarily addressed by the photo-degradation model, optimum cobalt concentration and other insights. Although there is some overlap between the current study and the cited work, applying such results in ZnS water splitting would be challenging. This highlights the necessity for research projects like the current study to optimize graphene-based ZnS for single-use water splitting.

In contrast to the current study employing cobalt and graphene for hydrogen generation, Y. H. Ng et al. (2010) proposed a photocatalytic process to increase electron migration with the help of graphene, as illustrated in Figure 2.39. However, the doping was done using Bismuth vanadate $BiVO_4$.

A one step solvothermal technique was used by H. Zhou et al. (2019) to evaluate the photocatalytic performance of TM doped amorphous molybdenum sulfide/graphene ternary co-catalysts depicted in scheme 2.40. Characterizations included their morphology, structure and characteristics. The graphene sheets

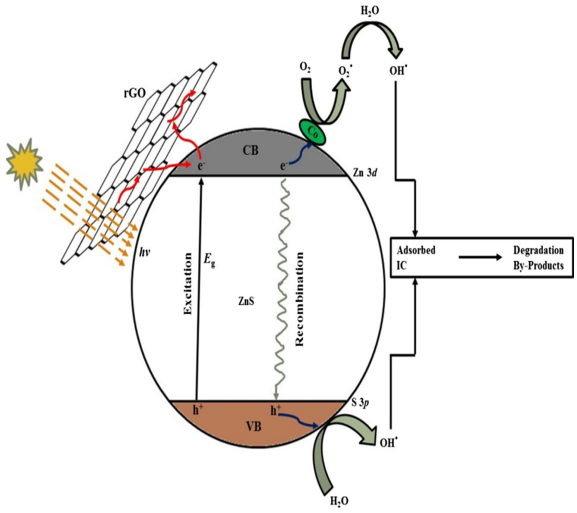

Figure 2.38: Proposed visible light induced photocatalytic mechanism of Co-doped ZnS–rGO photocatalyst towards degradation of Indigo Carmine (IC). Source; Agorku et al. (2015)

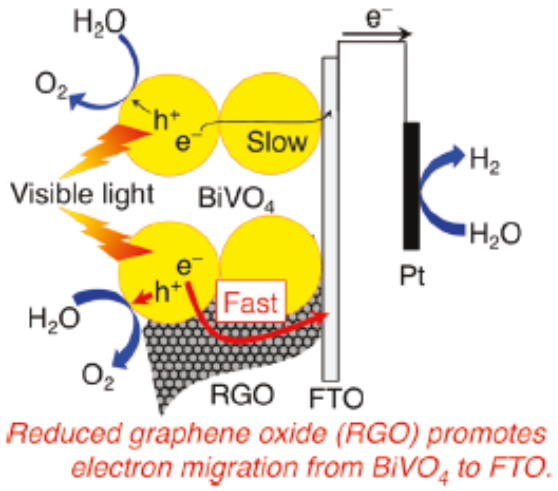

Figure 2.39: Reduced graphene oxide to promote electron migration in $BiVO_4$. Source; Y. H. Ng et al. (2010)

of the ternary composites and the metal-doped MoS_x nanoparticles were evenly dispersed. Moreover, the intrinsic activity of amorphous MoS_x was significantly increased by metal doping and the incorporation of graphene significantly aided in the separation of photo induced carriers. Under the combined influence of graphene and transition metal, the photocatalytic H_2 development using amorphous MoS_x as a co-catalyst was significantly enhanced. Molybdenum sulfide was utilized as a basis material in this endeavor, which may have hazardous effects on human health and the environment. Nonetheless, this work was rather

enlightening.

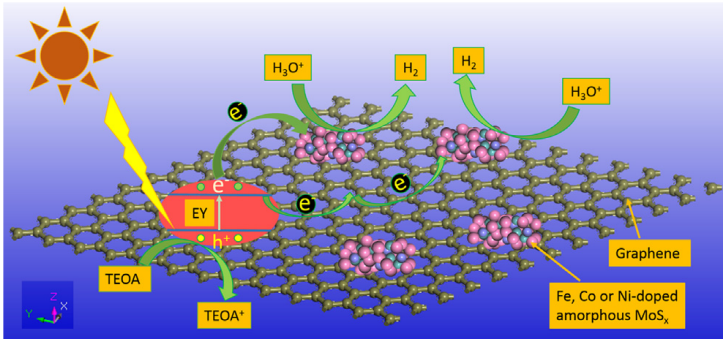

Figure 2.40: Transition metal doped amorphous molybdenum sulfide and graphene ternary co-catalysts for excellent photocatalytic hydrogen evolution H. Zhou et al. (2019)

2.4 Literature gaps summary

Modern industrial electrolyzers rely on external power sources to produce the necessary over-potential for WS. Thus, coupling such electrolyzers with renewable energy source such as photovoltaic is a more sustainable approach for production of hydrogen Roger et al. (2017); C. Hu et al. (2017). Fujishima and Honda's pioneering work on catalysis Fujishima & Honda (1972) showed that TiO_2 can be used as a photocatalyst in hydrogen production via WS. Since then, several photocatalysts have been identified, that include oxides, sulfides and oxynitride semiconductors J. Zhang et al. (2012). In particular, ZnS has been identified as a promising photocatalyst due to its fast generation of electron-hole pairs upon photo-excitation and high hydrogen evolution D. Huang et al. (2020); Juine et al. (2021); J. Zhou et al. (2020). However, mainstream adoption of ZnS in aforementioned application has been constrained by its response to UV spectrum and rapid recombination of charge carriers Kurnia, Ng, Tang, et al. (2016); L. Wang et al. (2020); Villa et al. (2021); Hao et al. (2018); Fajrina & Tahir (2019).

At present, noble metal based materials including ruthenium, iridium, rhodium and platinum are the state of the art water splitting electrocatalysts due to their high reactive in acidic and alkaline condition P. Wang et al. (2011); Kiptarus et

al. (2024); C. Jiang et al. (2017); X. Xu et al. (2019); Kurnia, Ng, Amal, et al. (2016). However, the cost of using these catalysts on a wide scale is significantly increased by their rarity, mining and refining procedures have a negative impact on the environment. Exploring a reliable and stable non noble metal based material is therefore the focus of many research efforts P. Chen et al. (2021). Energy disciplines have been increasingly interested in transition metal-base materials such carbides, nitrides, phosphides, sulfides, oxides and their composites X.-T. Wang et al. (2020); Zhao et al. (2020).

According to studies, ZnS can have its band gap edge modified and its optical characteristics altered by doping it with transition metals. The electronic and optical properties of ZnS are strongly dependent on the particle size and surface morphology Mendil et al. (2016); Chabou et al. (2019). Additionally, low dimensional ZnS exhibits improved optical response in visible light spectrum and has TM dopants have been shown to modify electronic properties, particularly the band gap edge of ZnS thus its optical response Belver et al. (2019); Kurnia, Ng, Tang, et al. (2016); Fadojutimi et al. (2022); Kiptarus et al. (2024). For example, Korir et al. (2021) showed that TM dopants enhances visible light absorption of ZnO nanowires and charge separation.

The selected TM dopants (Mn, Cu, Co and Fe) are attributed to their larger ionic radii, valence electrons, variable oxidation states, thermodynamic stability and half-metallic nature (Mn and Co) with 100% spin polarization induced by strong hybridization between the TM-3d and S-3p states with ZnS system M'hid et al. (2024). Therefore, there are limited systematic studies that considers ZnS and various optimization routes. Hence, the current work is envisaged to guide the current and future work that may yield the development of robust PEC devices based on ZnS. In this work, effects of the selected TM on the opto-electronic properties of 2D ZnS are explored and the PEC activity of the modified system investigated using density functional theory (DFT) approach.

The incorporation of graphene into semiconductors significantly improves the

photocatalytic performance by improving the adsorption ability, light harvesting in the visible domain and reducing the band gap energy. It has also been studied that such a strategy can prevent the recombination of the photogenerated electron hole pairs An & Jimmy (2011); L. Han et al. (2012). Long lived charge carriers, fewer charge trapping centers, the right energy level offsets and stability against light are all extremely desirable for enhancing the photocatalytic reactivity of a semiconductor photocatalyst Xiang et al. (2012). Despite extensive research on the photocatalytic development studies based on graphene for excellent efficiency of photocatalysts, there are still more research gaps and challenges that need to be extensively examined in the future Ahmed & Mohamed (2023).

A thorough investigation into the effects of cobalt doping on the structural, electrical, and optical properties is lacking, as the literature survey demonstrates. The water splitting capacity and hydrogen production efficiency of graphene decorated cobalt doped ZnS NSs are also missing. In order to demonstrate for the first time the impacts of cobalt doping and graphene inclusion on the structure, electronic and optical properties of ZnS NSs for PEC hydrogen production, the current study seeks to specifically lay out these effects.

The current investigation also seeks to ascertain the photocatalytic activity of several hydrothermally generated cobalt doped ZnS decorated with graphene $Co_xZn_{1-x}S$ rGO NSs in order to enhance hydrogen production. A number of techniques, such as SEM, XRD, XPS, RS, FTIR, and UV-vis, shall be used to characterize the surface morphologies and material properties of the developed NSs in order to clarify the different material parameters, such as particle size, crystal structure, surface morphology, chemical composition and band gap.

To be able to validate the photocatalytic efficiency of TM dopants and graphene inclusion on ZnS semiconductor for the generation of hydrogen (H_2) molecules for commercial applications, investigations on $Co_xZn_{1-x}S$rGO NSs photocatalysts are therefore urgently needed.

Chapter 3

Methodology

3.1 Introduction

This chapter describes the materials, equipment, methods/techniques, experimental design as well as methods of data analysis used to achieve the objectives of the research in chapter one are also described. This study used hydrothermal technique to create cobalt doped ZnS 2D layers decorated with graphene.

3.1.1 Materials and Methods

Materials

All reagents were of analytical grade and used without any further purification, this include; zinc acetate ($C_4H_6Zn.2H_2O$) $MolarMass = 219.5g/mol$, sodium sulfide Na_2S or $MolarMass = 78.0452g/mol$, cobalt sulphate $CoSO_4.7H_2O$ $MolarMass = 281.10g/mol$, acetone, distilled water, ethanol, methanol, thiourea $SC(NH_2)2$, graphite powder, sulfuric acid H_2SO_4, sodium nitrate $NaNO_3$, hydrogen peroxide H_2O_2 sodium sulphate Na_2SO_3, sodium chloride, potassium permanganate $KMnO_4$ which were all purchased from Fisher scientific, Alfa Aesar and Sigma Aldrich having a purity of 99.99%.

Apparatus and Equipment's

The apparatus and equipment's include; Magnetic stirrer and string bar, ice water bath, weighing scale (Sartonious), autoclaves, fume hood, hot air oven, pasteur Pipettes, beakers, measuring cylinders, sample holders, centrifuge (REM PR-24), vacuum oven, sonicator (Elma), SEM/FESEM, XRD, RS, FTIR, gas chromatography, photocatalytic reactor.

3.2 Theoretical simulations of the selected transitional metal doped ZnS 2D surface layers

3.2.1 Computational analysis

Centre for High performance Computing (CHPC) cape town SA, QE suite was used to perform the theoretical simulations on the selected TM doped ZnS 2D layers. First principles calculations were performed to determine the structural, electronic and optical properties of cobalt doped ZnS 2D layers and factors affecting its photocatalytic performance were analysed. All the calculations were performed in the framework of the DFT, as implemented in the QUANTUM ESPRESSO suite Giannozzi et al. (2009). The generalized gradient approximation to the exchange and correlation functional was employed in the form proposed by Perdew, Burke and Ernzerhof (PBE) Perdew et al. (1996). The core-electrons were replaced by ultra-soft pseudo potentials following Vanderbilt's formulation and the electronic wave functions (charge densities) were expanded in a plane wave basis set with a well converged energy cutoff of 35 Ry and (350 Ry) Vanderbilt (1990).

ZnS was modelled as 1100 surface that was found to be the most stable, consistent with other studies Hao et al. (2018). A supercell of 12 ZnS layers slabs with 2×2 and 3×2 the unit cell was used to model the undoped and doped surfaces, respectively. A thick vacuum layer ≈ 15Å was included in the direction perpendicular to the surface to avoid fictitious interaction between the periodic

replicas. Integration over the Brillouin zone (BZ) was performed on a $4 \times 4 \times 1$ k-point Monkhorst and Pack Monkhorst & Pack (1976) grid and structures were relaxed until forces on the atoms were smaller than $0.02eV/$Å.

3.2.2 Structural properties simulation of the selected $3d$ transitional metal doped 2D ZnS surface layers

Convergence test performed the self consistent field (scf) computation for various values of Cut off energy (ECUTWFC) and the K input points. By using XM-GRACE software, the total energy against various K points and ECUTWFC were recorded. The calculation were carried out with lower values, in order to determine the lowest value convergence, saving computational resources and time.

Lattice parameters simulations

Lattice parameters were optimized by varying the lattice parameters; cell dm (1), cell dm (3), ECUTWFC tag in the QE input file in Table A.1 and computing the scf energy. The lattice data were recorded and tabulated in Table A.1, Table A.2 and Table A.3

Crystal structure and doping sites

In order for the dopant to be introduced to the surface of the bulk ZnS, the surface had to be relaxed. Relaxed functionality of the Physics Wallah (PW) module keeps the initial optimized lattice parameter constant and simulates the forces between the surface and the molecule. Hence allows to investigate the behavior of the molecule being absorbed on the surface. Relax also does the atomic coordination, optimization and force calculations applied to each atom by changing the atom location and cell size.

Calculation methods and models for ZnS doped with selected transitional metal dopants

1. **Total energies for the selected transitional metal doped ZnS**

   The total energies were computed and obtained from the Vc-relaxed output file after completion of calculations in the CHPC as shown in Table A.4.

2. **Chemical potentials for the selected transitional metal dopants**

   The chemical potentials of the transition metal dopants, were determined from their respective pure crystalline phases and the results were obtained and recorded in Table A.5.

3. **Formation energies for both Zn-rich and S-rich condition**

   Evaluation of the formation energy (ΔEF)) of each doped system was conducted to determine the stability of various TM dopants in ZnS 2D layers.

   Formation Energy (ΔEF) is a function of the elemental chemical potentials as well as the electron Fermi level and this can be calculated using the supercell model as defined. In order to prevent interactions between the adjacent mono layers, a $4 \times 4 \times 4$ 2D hexagonal mono layer with periodic boundary conditions in the x and y directions was taken into consideration for pristine and TM doped ZnS material.

   The (Δ_{EF}) of the selected TM dopants were determined using Equation 3.1 from their specific pure crystalline phases.

$$\Delta_{EF} = E_{ZnS:M} - E_{ZnS} + (\mu_{Zn/S} - \mu_M) \tag{3.1}$$

   Where $E_{ZnS:M}$ is the total energy of the TM doped ZnS , E_{ZnS} is the total energy of undoped ZnS, $\mu_{Zn/S}$ is the chemical potential of the substituted zinc and sulphide atoms and μ_M is the chemical potential of the $3d$ metal dopant atoms.

In this work, formation energy of the $3d$ transition metal atoms at Zn and S substitutional sites both under S-rich and Zn-rich growth conditions as described by Kudo & Miseki (2009) was also determined.

Under the,

S-rich growth condition

The formation energies for Mn, Cu, Co and Fe were calculated and recorded in Table A.6 using Equation 3.2 and 3.3 respectively;

$$\mu_S^{max} = \frac{1}{2}ES \tag{3.2}$$

$$\mu_Z n^{min} = EZnS - \mu_S^{max} \tag{3.3}$$

while under the,

Zn-rich limit conditions

Equation 3.4 and 3.5 were used to calculate the formation energies of Mn, Cu, Co and Fe. The results were recorded in Table A.7.

$$\mu_Z n^{max} = EZn \tag{3.4}$$

$$\mu_S^{min} = EZnS - \mu_Z n^{max} \tag{3.5}$$

Where $E(S)$, $E(Zn)$ and ZnS were the calculated total energies of the sulphur molecule, pure crystalline Zn and ZnS unit cells respectively.

The E-Fermi energy calculations were also carried out in order to understand the location and behaviour of defect state within the band gap of the different dopants when doped with ZnS and the results were tabulated in Table A.8.

Stability patterns of 3d transition metals dopants in 2D ZnS surface layers

1. **Stability as a function of dopant concentrations**

   The investigation on the stability of ZnS 2D surface layers as a function of dopant concentration by increasing the number of TM dopants randomly distributed in the surface layers at substitutional Zn sites was first carried out to examine the impact of TM dopants on the structural, electronic and optical properties of ZnS 2D layers for PEC applications. All doping concentrations utilised in this investigation preserved the same doping location for each individual transition metal atom. The calculations on the concentration of dopants under the Zn-rich and S-rich were determined;

   (a) As an individual dopant (Mn, Cu, Co and Fe) under the Zn-rich and S-rich

   Table A.9, Table A.10, Table A.11, Table A.12

   (b) With different dopant concentration (1, 2, 4 and 6 atm.%)

   Table A.13, Table A.14, Table A.15, Table A.16

2. **Direct calculations for formation energies under the Zn-rich and S-rich for all the 3*d* TMD's as a function of dopant concentration**

   (a) Formation energies under the Zn-rich for all the 3d TMD's as a function of dopant concentration Table A.17

   (b) Formation energies under the S-rich for all the 3d TMD's as a function of dopant concentration. Table A.18

   (c) Formation energy profile of 3d transition metal defects in ZnS 2D surface layers under the Z-rich and S-rich condition. Table A.19

3.2.3 Electronic properties simulation of the selected $3d$ transitional metal doped 2D ZnS surface layers

The band gap was determined from the difference between the Highest Occupied Molecular Orbital (HUMO) and Lowest Occupied Molecular Orbital (LUMO). The band gap calculations were calculated from the relaxed output file submitted in the high computing performance and tabulated in Table A.20. To understand the role that different orbitals played in the band structure, PDOS's were simulated and results analysed in chapter four.

3.2.4 Optical properties simulation of the selected $3d$ transition metal doped 2D ZnS surface layers

Using Liouville-Lanczos technique and time dependent density functional perturbation theory (TDDFPT) Malcıoğlu et al. (2011); Motornyi et al. (2020); Gorni et al. (2022), the impact of Cu and Co dopants (at 4% concentration) on the optical properties were examined. The optical response were assessed using the dielectric response of the modified ZnS as expressed in Equation 3.6 below and the results were analysed in chapter four.

$$\epsilon\omega = \epsilon_1\omega + i\epsilon_2\omega \tag{3.6}$$

Where $\epsilon 1$ and $\epsilon 2$ stand for the real and imaginary parts of the dielectric function respectively. Imaginary part of the dielectric constant is a summation of all possible transitions from unoccupied to occupied wave functions via dipole transition matrix, while the real part of dielectric function is obtained using Kramers- Kronig relation Lucarini et al. (2005); Ortega-Guerrero et al. (2020); Ramaniah & Boero (2006). The optical absorption response (α_abs) was determined using dielectric response function Gajdoš et al. (2006) as shown in Equation 3.7 below and the

results were analysed in chapter four.

$$\alpha_{abs} = \sqrt{2\omega}(\sqrt{\epsilon_1^2\omega + \epsilon_2^2\omega - \epsilon_1\omega})^{\frac{1}{2}} \tag{3.7}$$

3.2.5 Photocatalytic activity simulations of the selected 3*d* transition metal doped 2D ZnS surface layers

Band edge alignment computations were done to provide useful insights on photocatalytic activity of the modified ZnS 2D surface layers. These computation were used to determine NHE at the CBM potential Equation 3.8 and VBM potential Equation 3.9 Z. Wang et al. (2023); Xi et al. (2021); Kurnia & Hart (2015); Z. Zhou et al. (2016) as depicted below.

$$E_{CB}^{NHE} = \chi - E_e - 0.5E_g \tag{3.8}$$

$$E_{VB}^{NHE} = E_{CB}^{NHE} + E_g \tag{3.9}$$

Where χ is the absolute electro-negativity of the semiconductor, E_e is the energy of a free electron on the NHE scale (4.5 eV) and E_g is the band gap of the semiconductor. The results were obtained from the calculations and are represented in Table A.21.

3.3 Development of cobalt doped ZnS nanostructure surface layers

3.3.1 Synthesis of ZnS and cobalt doped ZnS via hydrothermal method

The hydrothermal process was carried out in an autoclave, a thick-walled steel cylinder sealed hermetically to withstand high temperatures and pressures for extended periods of time. As shown in Figure 3.1, a Teflon vessel designed to withstand corrosion was positioned inside the autoclave's interior chamber. The vessel's specifications were ; 120 mL capacity and an inner diameter of 30 mm. There was no further purification applied to several of the compounds, which were of the analytical form and reagents were measured using the weighing scale (Shimadzu AUX220) as shown in Figure 3.1. The experiments were carried out using various composition concentrations at $200°C$.

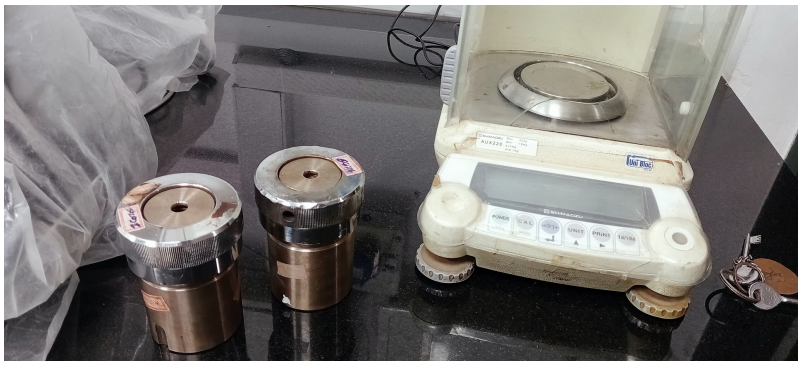

Figure 3.1: Autoclaves and Weighing scale

- **Synthesis of ZnS**

  Synthesis of ZnS was done in accordance with the L. Xue et al. (2011) standard and involved:

  Procedure

1. Adding 440 mg of zinc acetate in 15 ml of water for 10 to 15 minutes was prepared
2. 312 mg of Na_2S in 15 ml of water was added slowly drop wise to the above solution
3. The mixture was transferred in to an autoclave and was magnetically stirred for 30 minutes continuously using a magnetic stirrer with stirrer
4. The autoclave was sealed and heated to $200°C$ within 30 minutes and maintained at this temperature for 16 hours in the furnace Figure 3.2 and cooled to room temperature naturally
5. The precipitate were separated by a centrifuge (REMI PR-24) Figure 3.5 for 6 minutes at 7000 rpm
6. The precipitate was washed with distilled water severally and finally rinsed with ethanol to remove all unreacted reagent
7. The washed precipitate was dried in an oven ($60°C$)
8. The dried precipitate was grounded to fine powder using mortar and pestle and stored ready for characterization.

Figure 3.2: Furnaces and Ovens

- **Synthesis of cobalt doped ZnS**

  Samples for cobalt doped ZnS were fabricated with respect to their dopant concentration atm.% via hydrothermal method as shown in Figure 3.4 using cobalt sulphate, zinc acetate and sodium sulfide ingredients as shown in Figure 3.3

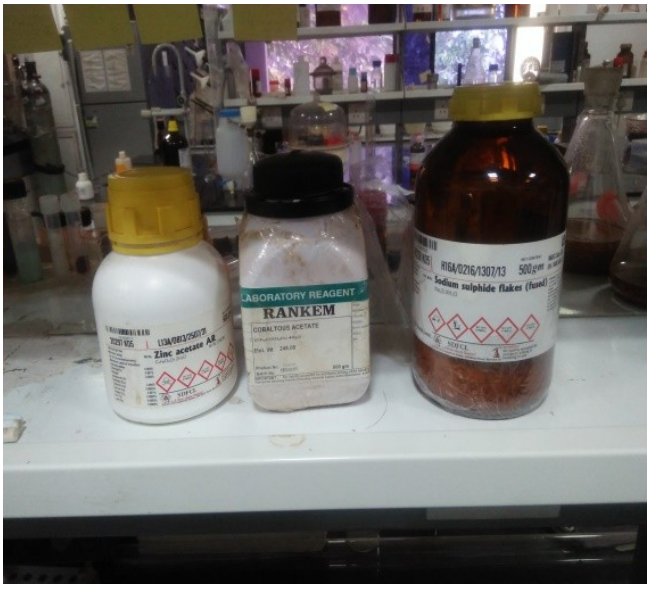

Figure 3.3: Cobalt sulphate, zinc acetate and sodium sulfide ingredients

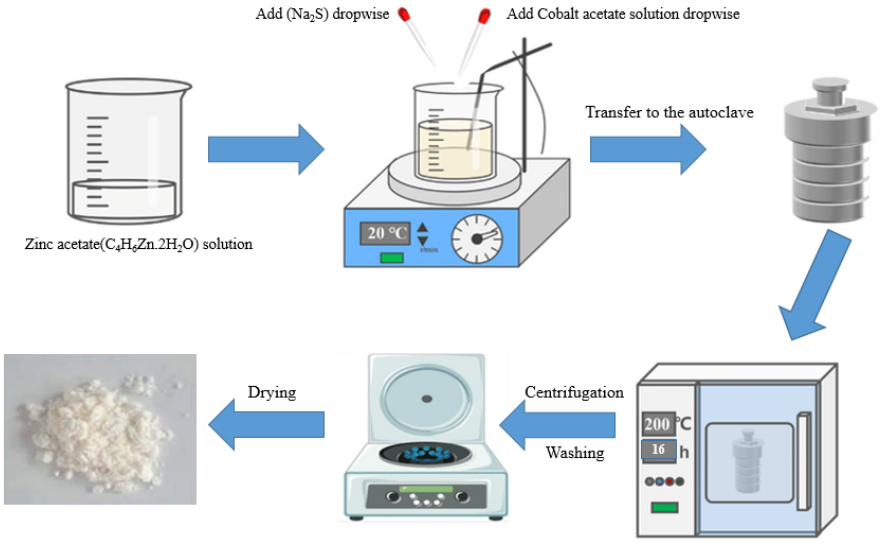

Figure 3.4: Preparation of cobalt doped ZnS by hydrothermal method

- **Synthesis of 1% cobalt doped ZnS**

  Procedure

  1. 440 mg of zinc acetate was added in 15 ml of distilled water (DI)
  2. 312 mg of Na_2S in 15 ml of DI was added drop wise to the above solution
  3. 5.622 mg of cobalt sulphate dissolved in 15 ml of DI was slowly added to the mixture
  4. The mixture was then transferred in to an autoclave and was magnetically stirred for 1 hour continuously using a magnetic stirrer with stirrer.
  5. The autoclave was sealed and heated to 200°C within 30 minutes and maintained at this temperature for 16 hours in the furnace and cooled to room temperature naturally
  6. The precipitate was separated by using a centrifuge (REMI PR-24) for 6 minutes at 7000 rpm
  7. The precipitate was washed with distilled water severally and finally rinsed to remove all unreacted reagents
  8. The washed precipitate was dried in an oven Figure 3.5 60°C and stored ready for characterization. The observed color during synthesis was greenish and bright light green after drying in the oven. The residue was colorless.

Figure 3.5: Centrifuge (REMI PR-24) and Vacuum oven

The same procedure was followed for the synthesis of 2%, 4% and 6% cobalt doped ZnS NSs, except that varying concentrations of the cobalt sulphate precursor were combined with the zinc acetate precursor during the hydrothermal process.

3.3.2 Preparation of graphite oxide, reduced graphene by Hummers method

All chemicals were obtained from Sigma Aldrich and used without further purification. GO was prepared from graphite powder by the Hummers method Hummers Jr & Offeman (1958).

- **Synthesis of Graphite Oxide**

  The synthesis of GO was prepared in the fume hood shown in Figure 3.6 considering the hazardous effects of sulphuric acid and potassium permanganate being exothermic.

Figure 3.6: Fume hood

Procedure

1. 25 ml of concentrated sulphuric acid was taken in a beaker and put in an ice bath to maintain temperature to less than $20°C$, 1 g graphite powder was added to the solution with proper stirring at 500 rpm. Sulphuric acid acts as the oxidizing agent for graphite
2. 3 g of potassium permanganate was gradually added within an ice water bath since the reaction is exothermic
3. After few minutes the ice bath was removed and the reaction was stirred properly by maintaining the temperature at $(40 - 50°C)$ for 3 hours
4. After the 3 hrs, the ice bath was placed again and 100ml of DI was added to the reaction drop wise carefully.
5. After 15 minutes, 75 ml of DI was added again.
6. Then 5 ml of hydrogen peroxide was added slowly to stop the reaction. The color of solution changed to yellow from dark brown after the addition of H_2O_2
7. The solution was centrifuged at 4000 rpm for 5 minutes to separate unwanted extracts from the solution
8. After this the solution was washed by using 1:9 aqueous hydrochlo-

ride acid (HCl) to remove sulphate ions followed by washing with DI severally

9. The solution was dried at $60°C$ in hot air vacuum oven for 12 hours.
10. The obtained powder was graphene oxide

- **Synthesis of reduced graphene**

Reduced graphene was synthesized according to the procedure of Tewatia et al. (2021) as described below;

Procedure

1. 1 g prepared graphite powder was added in 150 ml of DI.
2. The PH of the mixture was adjusted to between 9 and 10 with 25% ammonium solution to promote the colloidal stability of the GO sheets through electrostatic repulsion.
3. 1 g of AA (vitamin C) was added to the solution and the reaction was stirred at 600 rpm by maintaining the temperature at $60°C$.
4. After 12 hours, the sample was centrifuged and washed with DI.
5. The obtained sample was dried in a hot air vacuum oven at $60°C$ and kept to room temperature ready for characterization as shown in Figure 3.7

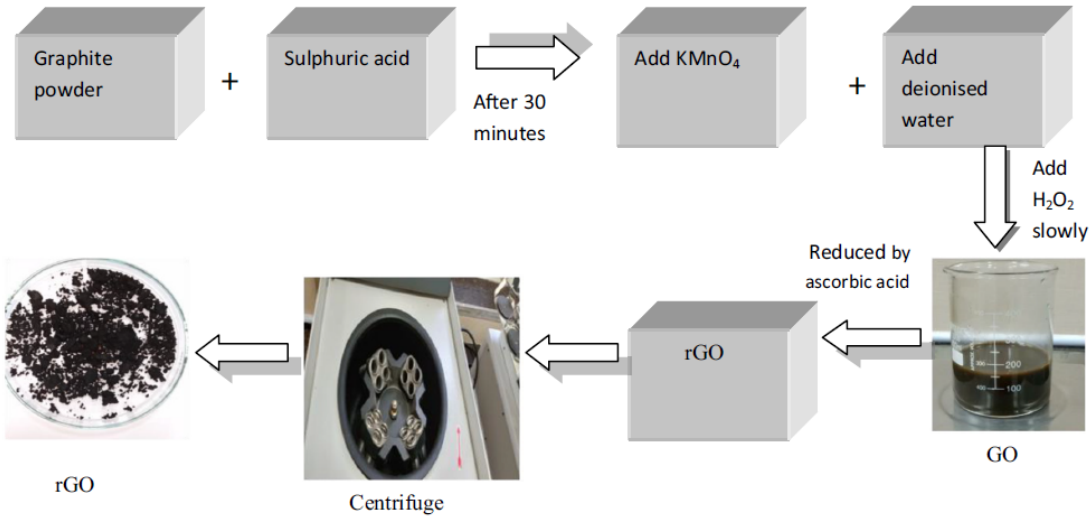

Figure 3.7: Preparation of graphite oxide and reduced Graphene by Hummers method

- **Synthesis of ZnS-Graphene**

  Procedure

  1. 60 mg of rGO was dispersed in to 50 ml of DI completely by ultrasonication.
  2. 440 mg of zinc acetate dissolved in 15 ml DI was added and suspension heated to $60°C$ with magnetic stirring for 2hours.
  3. 312 mg of sodium sulfide dissolved in 15 ml DI was added slowly drop by drop and kept stirring for 4 hours for the formation of ZnS NSs on the GO platform.
  4. The mixture was then transferred in to a 100ml Teflon sealed autoclave and heated to $200°C$ within 30 minutes and maintained at this temperature for 16 hours in the furnace and allowed to cool to room temperature naturally.
  5. The reaction products were centrifuged for 6 minutes at 7000 rpm.
  6. The reaction precipitate was washed with DI severally to remove unreacted reagents.

7. The washed precipitate was dried in vacuum oven at 60°C and stored ready for characterization.

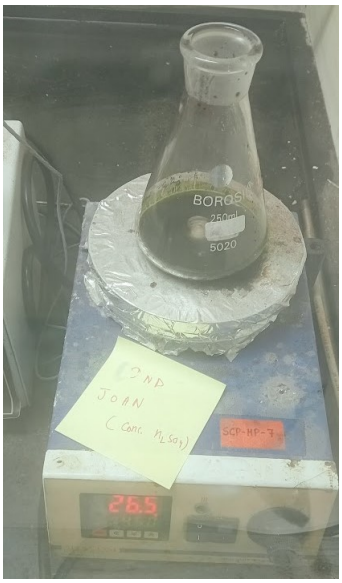

Figure 3.8: Reduced graphene synthesis using magnetic stirrer

- **Synthesis of 1% Co-ZnS-Graphene**

  Procedure

  1. 60 mg of rGO was dispersed in to 50 ml of DI completely by ultrasonication as shown in Figure 3.9.
  2. 440 mg of zinc acetate dissolved in 15 ml DI was added and suspension heated to 60°C with magnetic stirring for 2 hours.
  3. 312 mg of sodium sulfide dissolved in 15 ml DI was added slowly drop by drop and kept stirring for 4 hours for the formation of ZnS NSs on the GO platform.
  4. 5.622 mg of cobalt sulphate dissolved in 15 ml of DI was slowly added to the mixture above while stirring
  5. The mixture was then transferred in to a 100 ml Teflon sealed autoclave and heated to 200°C within 30 minutes and maintained at this

temperature for 16 hours in the furnace Figure 3.2 and allowed to cool to room temperature naturally.

6. The reaction products were centrifuged for 6 minutes at 7000 rpm.
7. The reaction precipitate was washed with DI severally to remove unreacted reagents.
8. The washed precipitate was dried in vacuum oven at $60°C$ and stored ready for characterization.

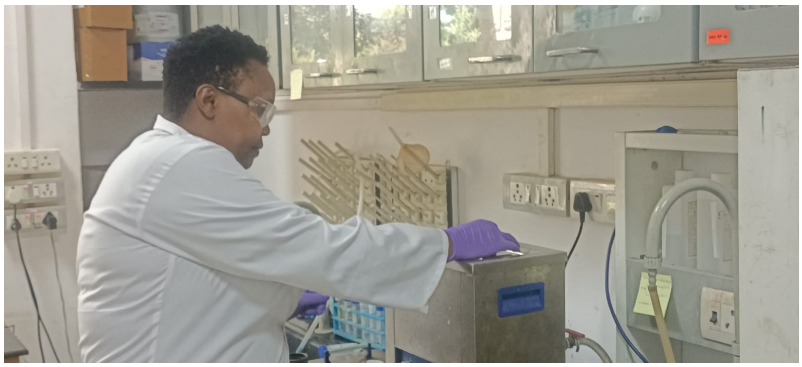

Figure 3.9: Joan preparing samples using the sonicator

The same procedure was followed for the synthesis of 2%, 4% and 6% cobalt doped ZnS decorated with graphene NSs, except that varying concentrations of the cobalt sulphate precursor were combined with the zinc acetate precursor during the hydrothermal process.

ZnS and ZnS-rGO were synthesized in a similar manner without the addition of either cobalt sulphate or both rGO and cobalt sulphate. The synthesized cobalt doped ZnS with and without graphene were packed in plastic centrifuges ready for characterization and photocatalytic activity as shown in the Figure 3.10.

3.4 Characterization of cobalt doped ZnS nanostructure surface layers decorated with graphene

The following techniques were employed in characterizing the cobalt doped ZnS decorated with graphene samples:

Figure 3.10: Synthesized samples of ZnS, ZnS-rGO, cobalt doped ZnS with and without graphene

1. Scanning Electron Microscopy **(SEM)**

2. Raman Spectroscopy (RS)/ Fourier Transform Infrared Spectroscopy **(FTIR)**

3. X-ray diffraction **XRD**, X-ray photocurrent spectroscopy **XPS**,

4. UV–visible **UV-vis**

3.4.1 Determination of the structural properties of cobalt doped ZnS decorated with graphene

Determination of crystallinity (crystal size and disorder) of cobalt doped ZnS decorated with and without graphene

X-ray diffraction was used to characterize crystallinity of the developed NSs. R. Jain et al. (2016); Letts et al. (2018) state that XRD provides information on the phase, preferred orientation and other structural characteristics of crystals in texture, as well as average grain size, crystal, stress and crystal defects Kiptarus et al. (2015); Horikoshi & Serpone (2013).

Sample preparation

The samples were mounted on the sample holder and evenly distributed on a low background slide on the area illuminated by the X-ray beam when the samples were analyzed.

Method

X-ray diffraction patterns were performed by a Bruker D8-Advance diffractometer equipped with graphite monochromatized Cu $K\alpha$, radiation $\lambda = 0.15405nm$ in the 2θ range from 10° to 80° with a scan rate of 0.08° per second to determine the crystalline structure of the samples. X-rays were produced in a sealed tube under vacuum when current was applied to the heating filament that emitted electron when it got heated up. The electrons were accelerated towards an anode (copper plate) by a potential difference of 30 kV. These high energy electrons when bombarded, the metal copper plate ionized copper $1s$ K shell, thereby electron from $2p$ ($K\alpha$) or $3p$ ($K\beta$) dropped down to occupy the $1s$ and release energy as X-rays of particular wavelength ($CuK\alpha = 1.5406$). Cu $K\alpha$ was removed by using nickel filter. The X-rays were allowed to fall on the sample under analysis and the diffraction pattern were recorded.

3.4.2 Determination of the binding energies of cobalt doped ZnS nanostructures decorated with graphene

XPS was used to analyse the binding energies on the surface of cobalt doped ZnS NSs decorated with graphene. The basic principle of XPS was that the sample under investigation was irradiated by an X-ray beam and the photoelectrons generated were collected by an energy analyzer Zemlyanov (2023). The binding energy of the photoelectrons correlated with the energy of an electron level providing information about the element composition and chemical state of elements. The intensity of the photoelectrons was proportional to the number of atoms,

"emitters" and thus, the quantitative data were extracted.

Sample preparation

Typical samples for XPS are 5 mm to 10 mm square and up to 4 mm thick. The powder was pressed into clean, high purity indium foil. The powder was then dissolved in a suitable solvent and then drop cast onto the surface of a clean silicon wafer. The powder was further sprinkled onto the surface of sticky carbon conductive tape or pressed into a tablet for analysis.

Method

XPS measurements were carried out using a Thermo K-alpha+ spectrometer using micro focused and monochromated Al K α radiation with an energy of 1486.6 eV. The pass energy for the spectral acquisition was kept at 50 eV for individual core levels. The electron flood gun was utilized for providing charge compensation during data acquisition. Further,the individual core level spectra were checked for charging using C 1s at 284.6 eV as the standard and corrected. The peak fitting of the individual core levels was done using CASAXPS software (CasaXPS Version 2.3.19PR1.0; `https://drive.google.com/drive/folders/1TBhxcPSrD66w07gIFuFfywDNiXhr`
`-k?usp=drive_link`) with a Shirley-type background. The spectra obtained for each sample was recorded for further analysis.

3.4.3 Determination of the phase and chemical of cobalt doped ZnS nanostructures decorated with graphene

Raman scattering phenomenon was used to study the shape, size, doping, amorphous or crystalline regions, defects distributions and doping of nanomaterials Popović et al. (2011); Drescher & Kneipp (2012). In particular, for carbon based nanostructured materials, the Raman bands were utilized to distinguish between various allotropes and to investigate their composition, structure and conductivity Bokobza et al. (2014); Y. Wang et al. (1990). The investigation of the lattice

dynamics and vibrational properties of sp^2, sp^3 hybridized carbons were greatly aided by Raman spectroscopy Reich & Thomsen (2004). The Raman scattering was depicted using intensity in arbitrary units as a function of wave number (cm^2). The stronger Stokes line were typically observed in Raman spectroscopy Jones et al. (2019); Rangan et al. (2020)

Sample preparation

The cover glass was gently put on a powder sample taken on a slide glass and measured as it was. The mounted cover glass was gently removed.

Method

The Phase and chemical identification, molecular structure and their bonding effect of the Co-ZnS-rGO NSs were determined using RENISHAW InVia Raman Microscope Figure 3.11 with raman shift range 0f (100–4000)cm. The samples to be measured were placed in a glass bottle and a raman spectrum of the glass plus sample was taken. A raman spectrum of just the glass bottle was taken as a "dark" spectrum. The effective raman spectrum was obtained from the spectrum of sample in bottle minus the dark spectrum (The subtraction was done automatically by the software). The data from several runs were exported and combined using Excel. The spectra of the different samples were saved on a floppy disk for analysis via Excel and Origin software.

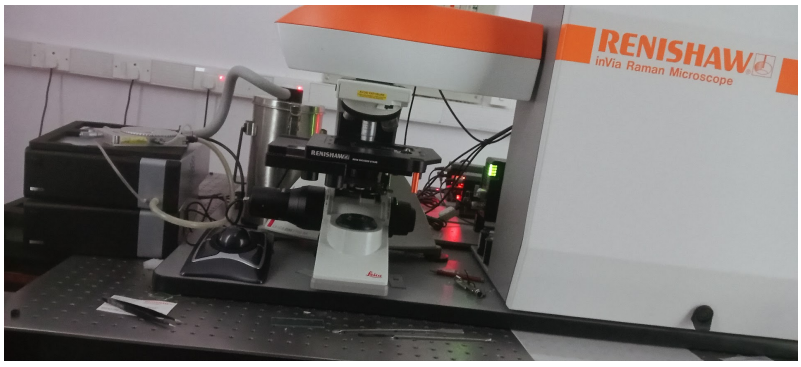

Figure 3.11: Raman spectroscopy

3.4.4 Determination of chemical bonding and molecular structure of the cobalt doped ZnS nanostructures decorated with graphene

FTIR is an efficient analytical method for identifying the chemical composition of a substance in a timely and accurate manner A. Dutta (2017). The Fourier spectrum simultaneously collected high-resolution spectral data across a broad spectral range S. A. Khan et al. (2018). This offered a significant benefit over the spectrum dispersion scale, which concurrently evaluated the intensity over a small range of wavelengths Y. Chen et al. (2015); Sankadiya et al. (2016). A sample's absorption of infrared light was measured by a Fourier infrared spectrometer, which produced a spectrum based on the functional groups of the material Izzo et al. (2020).

Sample preparation

About 5 to 10 mg of cobalt doped ZnS decorated with graphene samples of different concentrations were placed onto the face of a KBr plate, a small drop of mineral oil was added and the second window was placed on top. With a gentle circular and back and forth rubbing motion of the two windows, the mixture was evenly distributed between the plates. The mixture appeared slightly translucent, with no bubbles, because it was properly prepared. The sandwiched plates were placed in the spectrometer and a spectrum was obtained.

Method

The phase and chemical identification, molecular structure and their bonding effect was determined using Perkin-Elmer Spectrum 100 FTIR spectroscope to study the Co-ZnS-rGO NSs. During FTIR analysis, the samples were subjected to an infrared light spectrum where different molecules absorbed IR light and molecular vibration occurred. Different molecules and bonds vibrate in a way characteristic

to them, leading to different amounts of light being absorbed at specific wavelengths depending on the sample's composition. The amount of IR light that passed through the samples were measured with a detector and the data was converted to a spectrum friendly form via a mathematical process called Fourier transform. The final spectrum represented light intensity as a function of wave number.

3.4.5 Determination of morphological and size thickness of the cobalt doped ZnS nanostructures decorated with graphene

SEM was used to analyze and specify the characteristics of the material's thick or thin sample surfaces, as well as to identify the material's shape and external dimensions Chu & Li (2006).

Sample preparation

Cleaning of the samples was done by using acetone then it was mounted on a stub and dried using IR light ready for SEM analysis. Since the samples were metallic there was no need of coating.

Method

The morphology of cobalt doped ZnS decorated with graphene samples were examined using a (Zeiss Gemini SEM500) scanning electron microscopy. An electron beam was produced by the thermionic emission of tungsten filament cathode. The acceleration voltage of energy ranging from 0.2 keV to 40 keV was focused by 2 condenser lenses to a spot on the sample. This scanned the different samples in raster scan mode over a rectangular area. When the electron beam felled on the sample surface, it emitted secondary electrons due to inelastic interaction. These secondary electrons were attracted towards an electrically biased grid and accelerated towards a phosphor or scintillator. When the secondary electron felled on the

scintillator it produced flashes of light that were conducted to a photo-multiplier outside the SEM column. The amplified electrical signal from the photo-multiplier were viewed as a two dimensional intensity distribution and photographed using analog to digital converters.

3.4.6 Determination of optical and electronic properties of the cobalt doped ZnS nanostructures decorated with graphene

The most fundamental prerequisite for visible light active photocatalysis is essentially visible light harvesting Moradi et al. (2021); Kokilavani et al. (2021). For visible light active photocatalysts to be designed, the light harvesting region must be expanded from UV to visible, and the light utilization efficiency must be improved. According to Gaur et al. (2019), typical measurements only require a little amount of the sample. The light absorption ability mainly originates from inter band electron transitions and is controlled by the band gap of semiconductors. Electron excitation to any point in the conduction band occurs when the energy of a photon is equal to the sum of the band gap energy and the width of the conduction band.

Sample preparation

The different samples were prepared by compacting each into a wafer and fitting this wafer to the reflectance integrating sphere ready for UV-vis absorbance analysis.

Method

UV–visible optical absorption and transmittance studies of $Co_xZn_{1-x}S$ rGO nanostructures were carried out to investigate their optical properties using UV–visible spectrometer (Model: Perkin Elmer UV Win Lab 6.0.4.0738 / 1.61.00 Lambda 900) with an excitation wavelength from 320 to 560 nm at ambient temperature.

3.5 Evaluation of cobalt doped ZnS nanostructure surface layers decorated with graphene for photocatalytic hydrogen production

The photocatalytic H_2 production was measured under the light intensity similar to the air mass (AM) 1.5G condition for the ZnS, Co-ZnS, ZnS-rGO, $Co_xZn_{1-x}S$ rGO NSs. The generation of H_2 was recorded using Gas Chromatography (GC) peaks. Design-Expert 13 software-Central composite design (CCD) was used to demonstrate how different cobalt dopant concentrations (atm.%) and deposition times (hrs) may result in high quality cobalt doped ZnS NSs decorated with graphene. A two-factor CCD, each having five replications at the center of the design was used. The design in Table A.22 basically represents the coordinate arrangement of the design, with the response representing the hydrogen evolution ($\mu molh^{-1}$). With the use of a 430W Xenon lamp UV light source, the concentration of H_2 in the gas product was determined and the amount of hydrogen generated via photo-catalysis was quantified using a GC. All of these experiments were conducted in the photocatalysis lab depicted in Figure 3.12.

Figure 3.12: Photo catalysis Lab

3.5.1 Photo-catalytic hydrogen production

Procedure

1. Photocatalytic water splitting to generate hydrogen Y. Zhang, Zhang, et al.

(2012); Iwase et al. (2011); Ahmad et al. (2015) was carried out in a quartz photo reactor with a volume of 50 mL.

2. A 430W Xenon lamp was employed as the side irradiation light source equipped with cut-off filter $\lambda \geq 420nm$ due to remove UV part.

3. 10 mg of the photocatalyst was dispersed by magnetic stirring in a 50 mL reactor containing 20 mL H_2O solution with addition of 0.1 M $Na_2SO_3$and 0.1 M Na_2S mixed sacrificial agent faced to the lamp.

4. Prior to irradiation, the system was deaerated by bubbling high-purity nitrogen for 30 min, then illuminated for 12 hours under magnetic stirring.

5. Cobalt doped ZnS with and without graphene were used as a photocatalysts.

6. The top of the Pyrex cell was sealed with a silicone rubber septum.

7. A needle-type probe was inserted into the reactor to withdraw generated gas in 120 minutes' intervals through the septum during experiments.

8. Analyses were conducted on a gas chromatography (Agilent 8890 GC), Figure 3.14 equipped with a thermal conductivity detector and a 5Å molecular sieve packed column.

9. Nitrogen was used as the carrier gas at a flow rate of $30cm^3/min$.

10. The photocatalytic activity of the samples was determined by the quantitatively detected H_2 evolution rate using an external standard in the same concentration range.

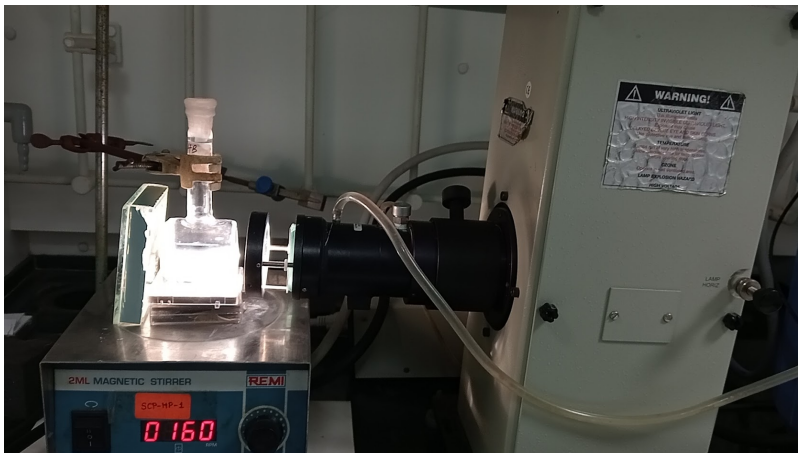

Figure 3.13: Photo-catalysis taking place using photo-reactor and simulator

3.5.2 Gas chromatography analysis

GC technique is used to separate the mixture of compounds according to their boiling point. The various gas components travels through the long columns inside the instrument before they reach the detector which is what triggers the response (peaks) found on the gas chromatogram. Once a compound is in the gas phase they will be carried along the internal column by a carrier gas which is an inert (non reactive) gas that pushes the other gasses through the column at a steady flow rate.

Method

The gas chromatogram separated and analysed the volatile compounds. When the sample was injected in to the GC, it was vaporized in the heated inlet and was transferred on to the column and the sample was carried through the column by the carrier gas and interacted with the stationary phase which lines the column. The column which was typically heated between $150-300°C$ in the GC oven separates the sample mixture in to its individual constituent or analyte through a repeated process of absorption and desorption by the station phase. The speed of travel through the column by individual components in the mixture depended on the combination of their volatility, polarity and molecular mass which influenced the separation and the elusion time of each compound as each analyte was eluted from

the column passed through a detector to enable the identification of the compound. The Thermal conductivity detector (TCD) was the universal detector and it could detect air, hydrogen, carbon monoxide, nitrogen, sulfur oxide, inorganic gases and many other compounds.

A measurement channel was reached by the sample components in the carrier gas. The carrier gas was contained in the second channel, which acted as a reference channel. Both channels contained electrically heated resistance wires. A voltage signal equal to the difference in thermal conductivity between the reference flow of carrier gas alone and the column effluent flow (sample components in carrier gas) was produced. The signal was proportional to the concentration of the sample components. A few crucial parameters needed to be adjusted in order to get the best possible response from the TCD i.e. the filament resistance, carrier gas and reference gas flow rates and detector block temperature.

The carrier gas in the GC-TCD served as the reference gas in addition to being utilized to move the sample through the column and into the TCD-detector. The reference gas, detector gas and carrier gas for the GC-TCD must match.

Similar to other chromatographic analytical procedures, GC was a relative approach that necessitated calibration with a standard mixture for both sample calibration and linearity verification. Concentration amount in GC was done automatically when norm% option was selected

$$\%\ composition\ \ X = \frac{Area\ \ of\ \ Peak\ \ X}{Total\ \ area} * 100 \tag{3.10}$$

For each sample concentration, the GC in Figure 3.14 was able to calculate the areas and percentage composition of the different cobalt doped ZnS NSs. The component with the largest percent composition, which was the primary product, is defined by Equation 3.10 when measurements of the product mixture in the GC were taken. Certain levels of stability and low energy state confirmation tend to lead to the formation of major products. Retention time measured how long it took for the compound to enter the gas phase following injection before it actually

Figure 3.14: Gas chromatography (Agilent 8890 GC)

made contact with the detector and produced a signal.

3.5.3 Hydrogen evolution quantities for cobalt doped ZnS with graphene

H_2, CH_4, CO, N_2, and O_2 with concentrations in ppm were the standard gases used to calibrate the GC equipment. In order to determine the response factor for hydrogen, a standard graph was generated. For other chemicals, such as $(CO, CO2, CH4)$, the standard response factors for TCD were $CO = 42, CO_2 = 48, N_2 = 42, and CH_4 = 35.7$. With these criteria, the chromatographic region was splitted and calculations were performed.

The GC gave each peak area corresponding to ppm of the standard gas used. Calibration plots for individual gases were plotted by varying the volume injected to the GC (0.1 - 1ml). Since the current research was interested in determining the amount of hydrogen, the other gases $CH_4, CO, N_2 and O_2$ in the mixture were

ignored and calculations for hydrogen were performed.

$$mol = ppm * 10^{-6} * vol(ml)/22400(ml)/mol(avgconst) \tag{3.11}$$

The volume of a mole of any gas that behaves like an ideal gas is 22.4 liters at 0 °C (273.15 K) and 1 atm (101325 Pa), or Standard Temperature and Pressure (STP). This volume is dependent on temperature and pressure.

Steps for calculation

1. A calibration graph was plotted i.e. concentrations versus corresponding peak areas and the points were fitted with a linear curve to construct a standard graph Figure A.1.

2. Area of H_2 after analyses of 0.5 ml of gas of each concentration samples were recorded. Therefore, by using standard graph equation, each area correlated to specific amount of H_2 ml.

3. The head space of the media was at 50 ml and calculations were done for each analyte.

4. The volume of the media was at 20 ml and calculations were also done for each analyte using excel Table A.23 and Table A.24.

5. As per the STP, 0 °C and 1 atmosphere), 22400 ml of gas = 1000 micro moles (μm) as described in Equation 3.11.

Chapter 4

Results and Analysis

4.1 Introduction

This chapter discusses the $Co_xZn_{1-x}S$ rGO NSs sample materials findings in relation to the study methodology employed to meet the research project goals. Effective prediction of optimal TM for doping ZnS 2D surface layers was achieved by hybrid DFT computations. Hydrothermal technique was employed to synthesize the cobalt doped ZnS NSs decorated with graphene. Lattice parameters and crystal structure were calculated using the crystal patterns yielded via XRD. XPS revealed vital information about the elemental and binding energies of the developed cobalt doped ZnS decorated with graphene NS surface layers and interfaces. Molecular weight, optical transparency, smoothness, quantity of contaminants, and chemical composition of the samples were all ascertained by the findings of the FTIR and RS, while SEM supplied the morphological data. The attenuation of light as it traveled through the NSs and returned after reflection was measured by UV-vis.

4.2 Computational analysis of the selected transitional metal doped ZnS 2D surface layers

First-principles simulations were utilized to examine the structural, electronic and optical properties of ZnS doped with the selected TMD's.

4.2.1 Structural and stability properties of the selected $3d$ transition doped ZnS 2D surface layers

It has been demonstrated that transitional metal dopants, such as Mn, Cu, Co, and Fe, alter the opto-electronic characteristics of ZnS Chauhan et al. (2023); Zafar et al. (2020); Axelevitch & Apter (2017). At the right dosage, these dopants can also improve the stability of the devices and cause blue shifting in the optical response Navarro Yerga et al. (2009). $3d$ TM dopants may be added to ZnS 2D layers as substitutional dopants or point defects, depending on the synthesis technique Bourgoin (2012); Z. Chen et al. (2013). Similar to how dopants are projected to be randomly inserted in different crystal sites in experimental setups, in this work a situation where the dopants randomly appeared as substitutional dopants was anticipated.

Lattice Parameter Optimization

The lattice parameters and atomic locations of pure ZnS were all optimised and the estimated lattice parameters recorded in Table A.1, A.2, A.3 were analyzed. The total energy values with respect to the lattice parameter were plotted using XMGRACE software to determine the lattice parameter with the minimum energy.

1. **Lattice data analysis for Ecutwfc**

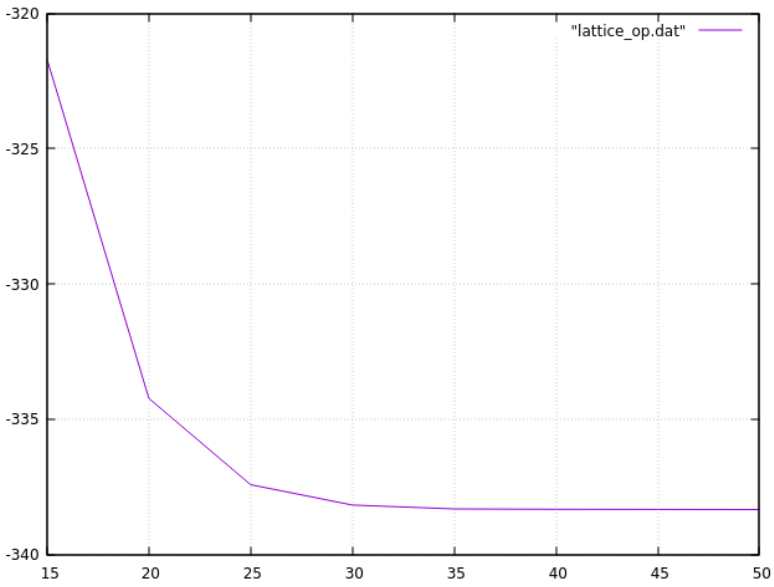

Figure 4.1: Lattice-Ecutwfc

2. **Lattice-Cell dm (1)**

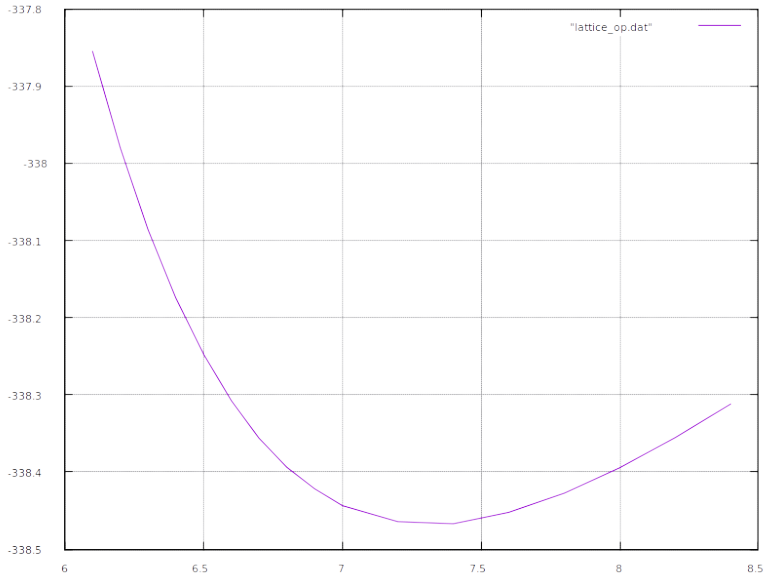

Figure 4.2: Lattice data for Cell dm (1)

3. **Lattice data analysis for Cell dm (3)**

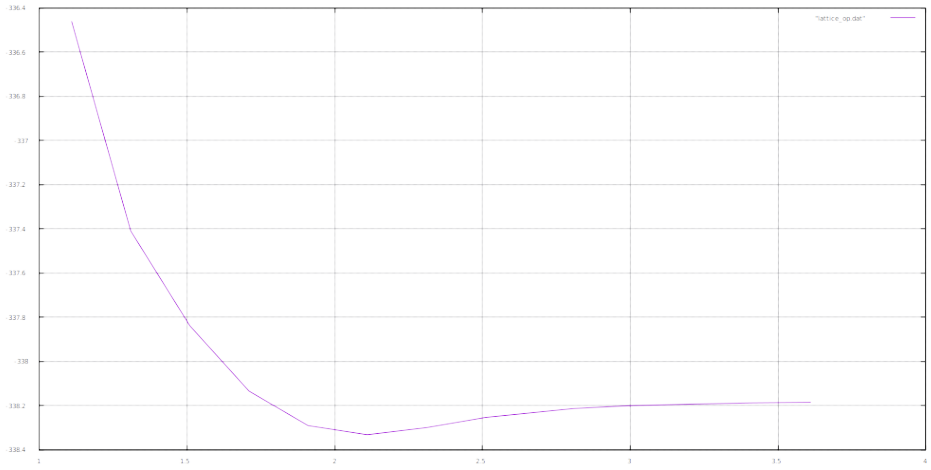

Figure 4.3: Lattice-Celldm(3)

Cut-off energy, bond lengths and Lattice parameter; 35Ry, 2.11Å , 7.4 were recorded for optimized pristine ZnS as shown in Figure 4.1, 4.2, 4.3.

Crystal structure and doping sites

Considering that transition metal defects are known to alter the structural, electrical, and optical characteristics of semiconductors, they can be strategically employed to boost the host semiconductor's characteristics for desired uses Korir et al. (2021). Depending on the development method employed, random point defects—akin to substitutional defects—may appear in a periodic crystal Bourgoin (2012); X. Chen et al. (2013). The ZnS 2D surface layers and nearby surface were examined for substitutional sites in this work since the catalytic reaction was expected to occur at the surface of the nanostructures.

1. **Manganese**

   The top and side views of optimized ZnS 2D surface layer doped with manganese at (1, 2 and 4 %) is shown in Figure 4.4.

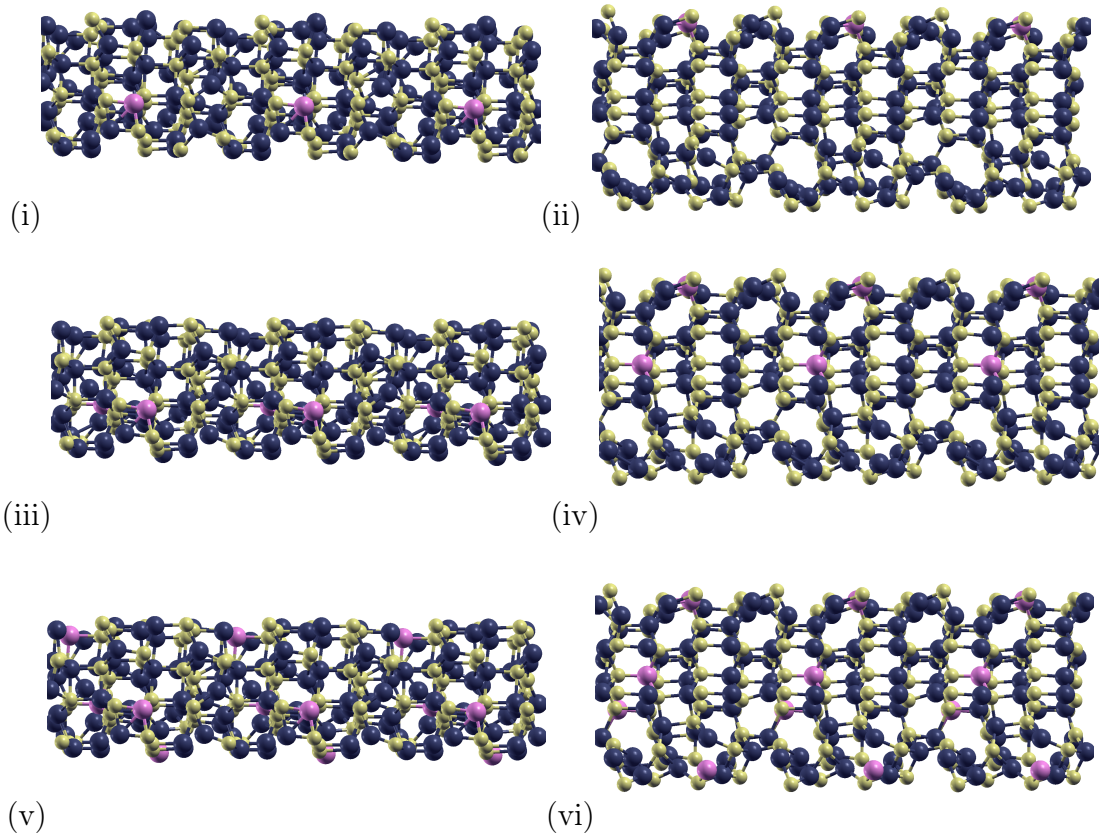

Figure 4.4: The top and side views of optimized ZnS 2D layers doped with 1% (**i and ii**), 2% (**ii and iii**) and 4% (**v and vi**) manganese. The atoms of zinc, sulfur, and manganese are represented by the gray, green and pink spheres (The reader is directed to the Web version of this research for an interpretation of the color references in this figure legend.)

2. **Copper**

   Figure 4.5 illustrates the top and side views of optimized ZnS 2D surface layers doped with Copper atoms at (1, 2, 4 and 6 atm.% Copper)

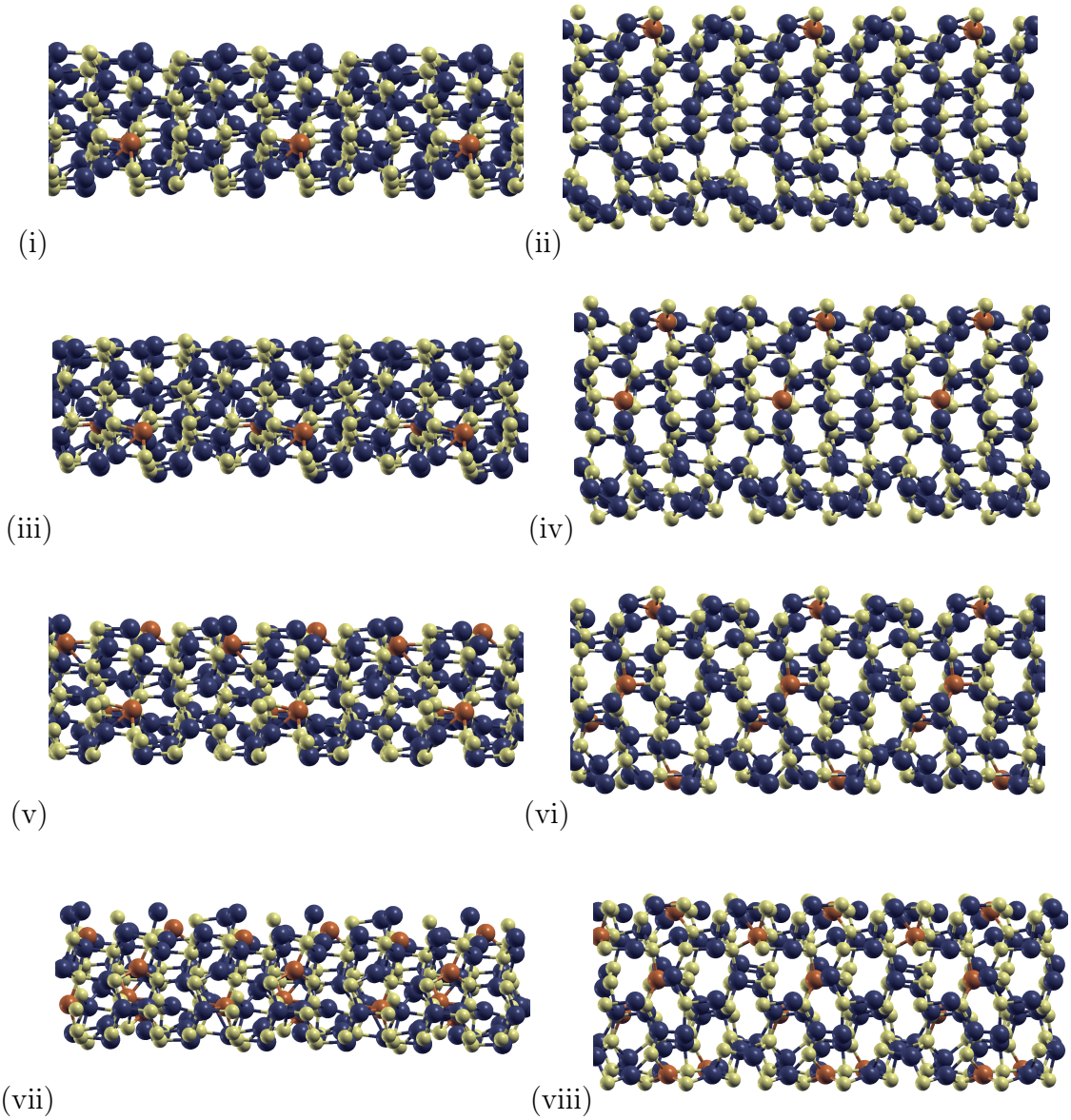

Figure 4.5: The top and side views of optimized ZnS 2D Layers doped with 1% (**i and ii**), 2% (**ii and iii**) and 4% (**v and vi**) and 6% (**vii and viii**) Copper. Zn, S, and Cu atoms are represented by gray, green and brown spheres, respectively. (The reader is directed to the Web version of this research for an interpretation of the color references in this figure legend.)

3. **Cobalt**

   The top and side view of optimized ZnS 2D surface layers doped with (1, 2, 4 and 6 atm.% Cobalt) are demonstrated in Figure 4.6

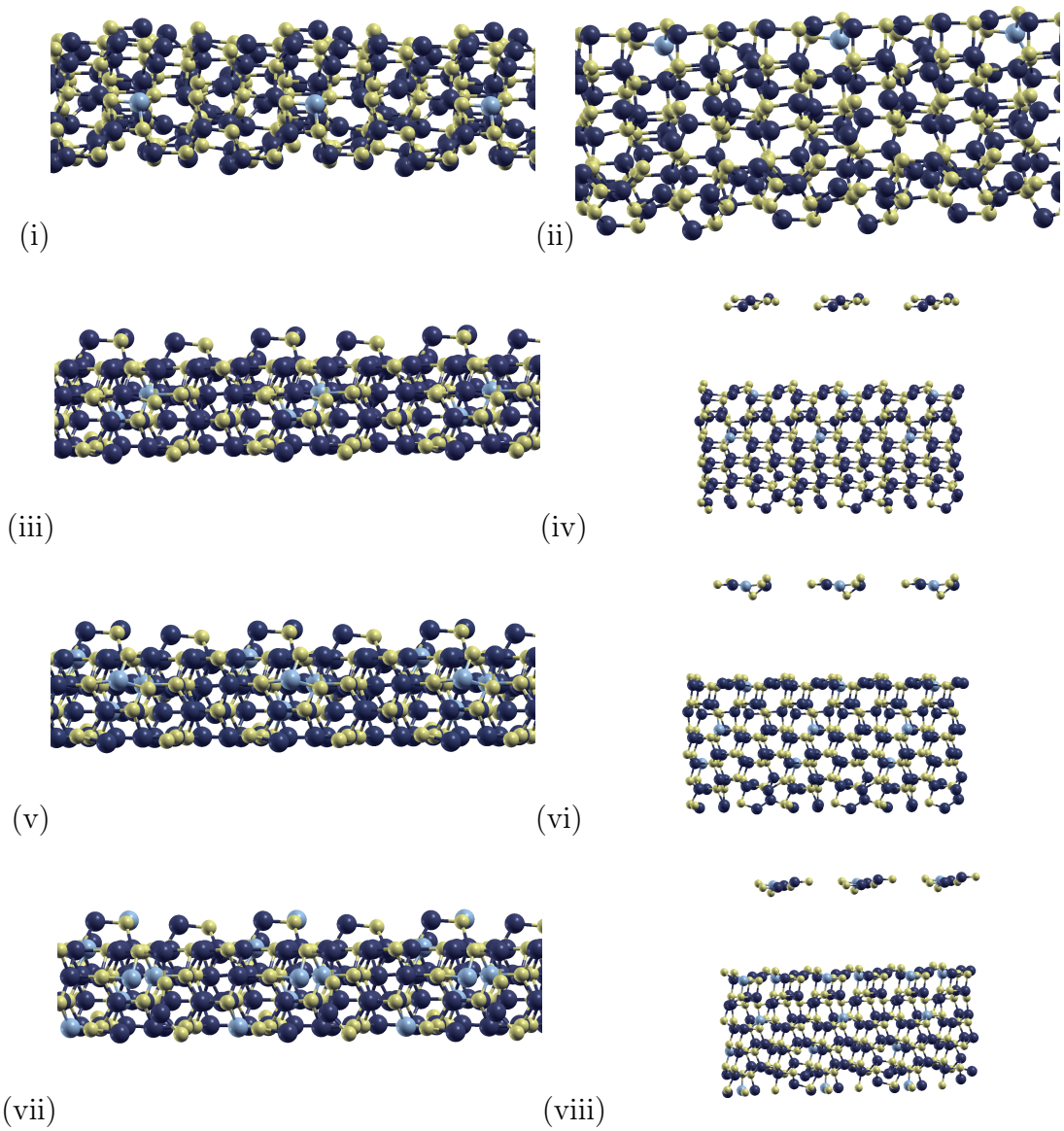

Figure 4.6: The top and side views of optimized ZnS 2D layers doped with 1% (**i and ii**), 2% (**ii and iii**) and 4% (**v and vi**) and 6% (**vii and viii**) cobalt. Gray, green and blue spheres represent Zn, S and Co atoms respectively. (The reader is directed to the Web version of this research for an interpretation of the color references in this figure legend.)

4. **Iron**

   The top and side view of optimized ZnS 2D surface layers doped with (1, 2, 4 and 6 atm.% Iron) are depicted in Figure 4.7

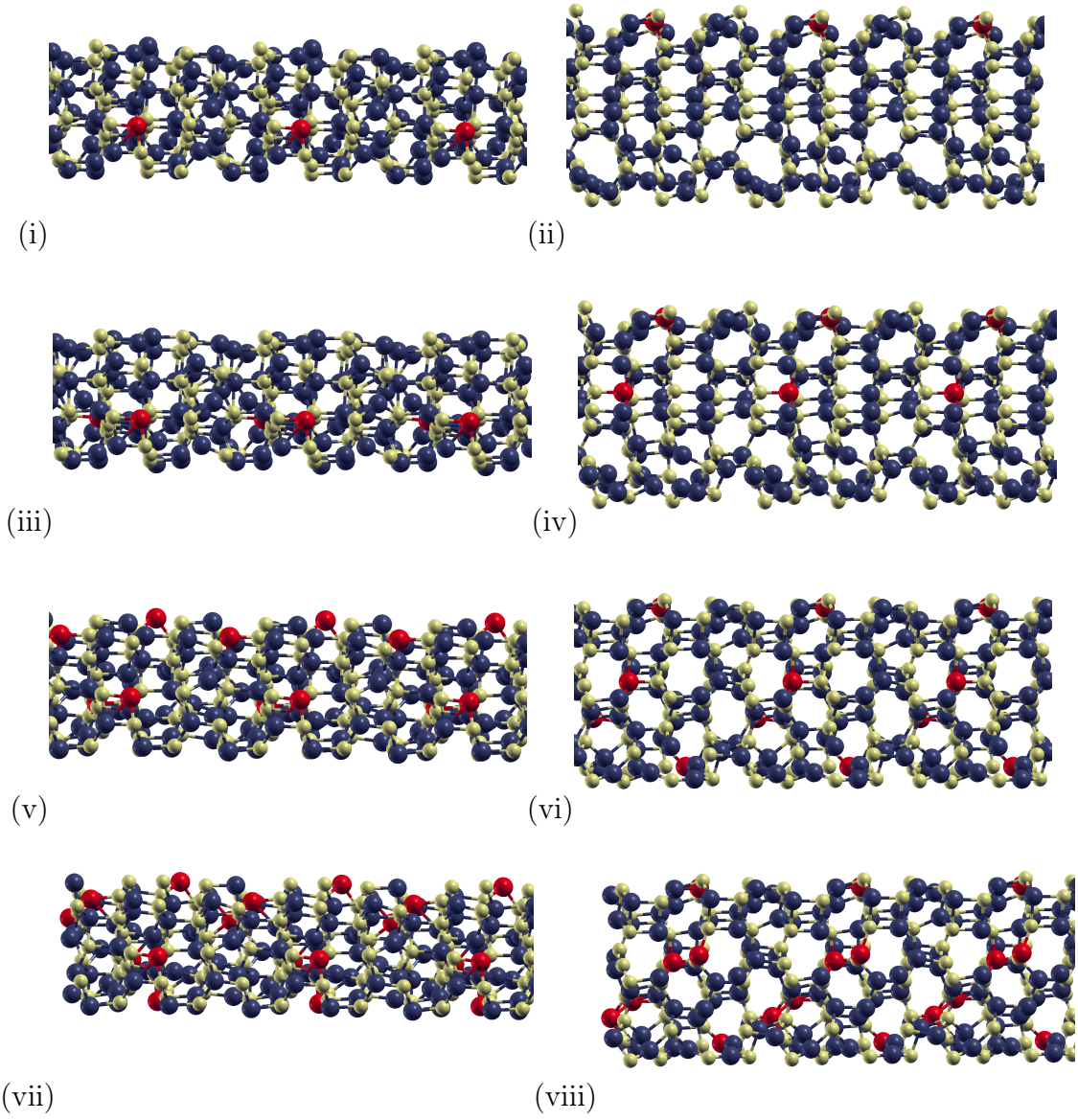

Figure 4.7: The top and side views of optimized ZnS 2D Layers doped with 1% (**i and ii**), 2% (**ii and iii**) and 4% (**v and vi**) and 6% (**vii and viii**) Iron. Gray, green and red sphere represent Zn, S and Fe atoms respectively. (The reader is directed to the Web version of this research for an interpretation of the color references in this figure legend.)

Since a catalytic reaction takes place at the surface of the ZnS 2D layer here, substitutional sites at the surface and near surface of the individual ZnS 2D layer were taken into consideration, as shown in Figure 4.4, 4.5, 4.6 and 4.7 respectively. Impurity centers produced by Mn, Cu, Co and Fe dopants may have interacted with electrons and holes. Because of this interaction, the middle gap states arising from surface species may have been shifted outside

the gap region which in turn may modify the structural, electronic and optical properties of the ZnS 2D layer semiconductor producing properties that may suite PEC applications.

Stability patterns of 3d transition metals dopants in ZnS 2D surface layers

Transitional metal dopants can strategically be employed to modify the properties of semiconductor hosts for specific objectives B. Zheng et al. (2022), as they are known to alter the structural, electronic and optical characteristics of semiconductors Dolabella et al. (2022); Raizada et al. (2021). Understanding the incorporation, stability and behavior of such defects in ZnS 2D Layer was therefore essential for its successful application in PEC water splitting.

1. **Stability as a function of dopant concentrations under the Zn-Rich and S-Rich**

   The investigation on the stability of ZnS 2D layers as a function of dopant concentration was determined under the Zn-rich and S-rich as follows;

   (a) **As an individual dopant (Mn, Cu, Co and Fe)**

   - **Manganese**

     Based on the Zn-rich and S-rich conditions shown in Figure 4.8, the formation energy of Mn dopant reduces as dopant concentration rises. The formation energy is more negative under Zn-rich conditions, ranging from 2.4 to 4.6 eV, as shown in Table A.9. This showed that, under equilibrium conditions, the Mn dopant may be readily integrated into the ZnS 2D surface layer at the Zn substitutional site, improving the PEC water splitting process. Energy-wise, the S-rich circumstances are less favorable for formation since the formation energies at the S-substitutional sites were

higher than those at the Zn substitutional site.

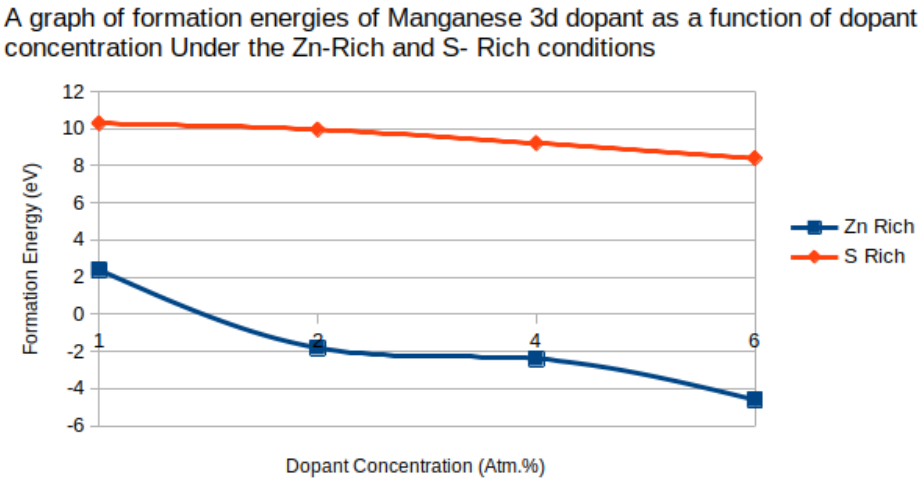

Figure 4.8: Mn Zn-S-Rich

- **Copper**

  From the Figure 4.9, the formation energy of Copper dopant slightly decreased with increase in dopant concentration under the Zn-rich and S-rich conditions this can be explained by the fact that Cu is less sensitive to changes in dopant concentration. Under the Zn-rich condition the formation energy was consistently more negative from (-5.2 to -6.2 eV) as shown in Table A.10. This showed that the Cu dopant can easily be incorporated in to the surface of ZnS 2D Layer at the Zn substitutional site under equilibrium conditions and so enhance PEC process. The formation energy under the S-rich condition at the S-substitutional sites was much higher compared to the Zn substitutional site, because they are energetically less favorable under S-rich conditions.

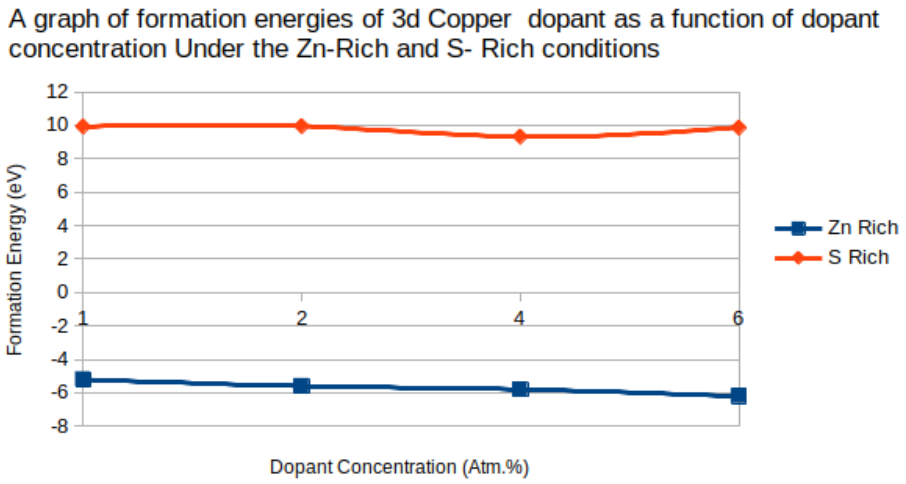

Figure 4.9: Cu Zn-S-Rich

- **Cobalt**

  As shown in Figure 4.10, the formation energy of cobalt dopant falls linearly with an increase in dopant concentration in both Zn-rich and S-rich environments. Table A.11 shows that the formation energy was constantly more negative from (4.2 to -6.4 eV) under the Zn-rich condition. This suggests that, under equilibrium conditions, the Co dopant can be integrated into the ZnS 2D Layer at the Zn substitutional site and improve the PEC water splitting process. Compared to the Zn substitutional site, the formation energy at the S-substitutional sites was significantly greater and less favorable energetically under S-rich circumstances. The stronger bonding and stable structure for Co doped ZnS 2D layers are supported by their comparatively larger formation energy.

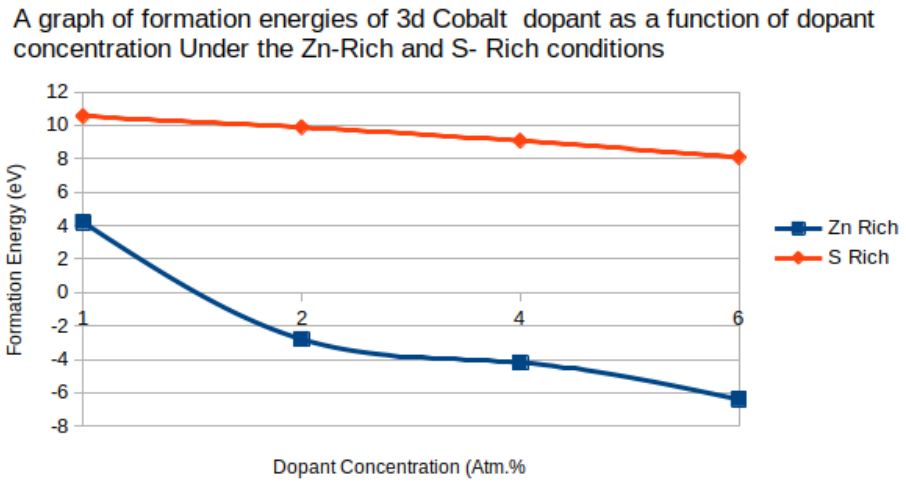

Figure 4.10: Co Zn-S-Rich

- **Iron**

  From the Figure 4.11, the formation energy of Iron dopant systematically decreases with increase in dopant concentration under the Zn-rich and S-rich conditions. Under the Zn-rich conditions, the formation energy was consistently more negative from (3.0 to -4.4 eV) as seen in Table A.12. This indicates that the Fe dopant can be incorporated in to the surface of ZnS 2D Layer at the Zn substitutional site under equilibrium conditions therefore enhancing PEC water splitting process. The formation energy under the S-rich condition at the S-substitutional sites was much higher compared to the Zn substitutional site, and this explained as to why they are energetically less favorable under S-rich conditions.

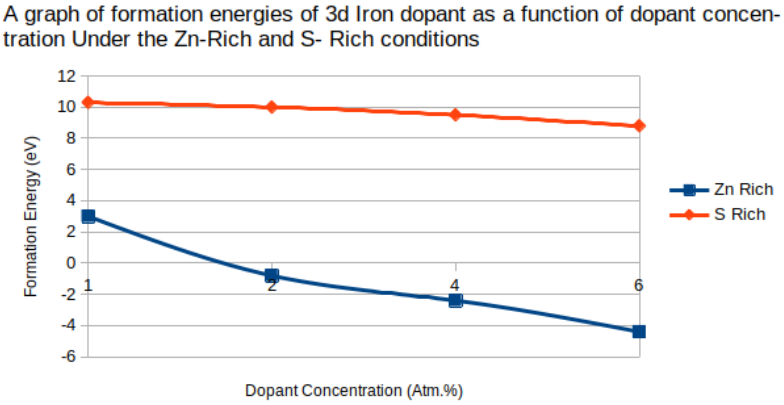

Figure 4.11: Fe Zn-S-Rich

(b) **Different Dopant Concentration (1, 2, 4 and 6 atm.%)**

- **1 amt.% Zn-S-Rich**

  The formation energy of copper at 1% is more negative than that of the other dopants under Zn-rich conditions, as shown in Figure 4.12, and this is further supported by Table A.13. Given that, Cu at $-5.2eV$ is less sensitive to variations in dopant concentration therefore can be readily integrated into the ZnS 2D surface layers. Less improvement in the PEC water splitting process can be attributed to Mn, Co, and Fe demonstrating a slightly positive formation energy at 1% atm dopant concentration. These configurations are energetically less favorable under S-rich conditions because the formation energy at the S substitutional site was significantly higher.

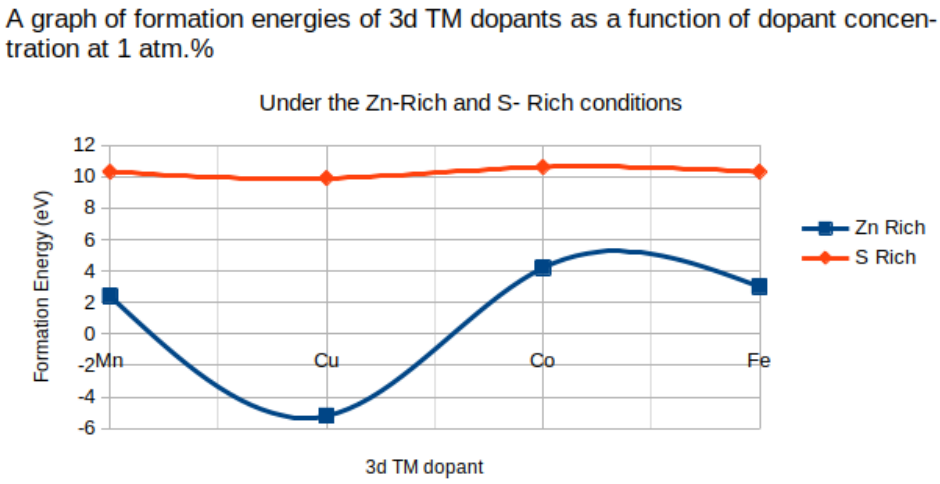

Figure 4.12: 1 amt.% Zn-S-Rich

- **2 amt.% Zn-S-Rich**

  From the Figure 4.13 the formation energy of copper at atm. 2% is more negative than the other dopants. However, the other dopants as seen in Table A.14 recorded negative values meaning that all the four dopants can easily be incorporated in to the ZnS 2D Layer surfaces at the Zn substitutional site under equilibrium conditions and so improve the PEC water splitting process. Under the S-rich conditions, the formation energy was isothermally higher at the S substitutional site hence were energetically less favorable under the S-rich condition.

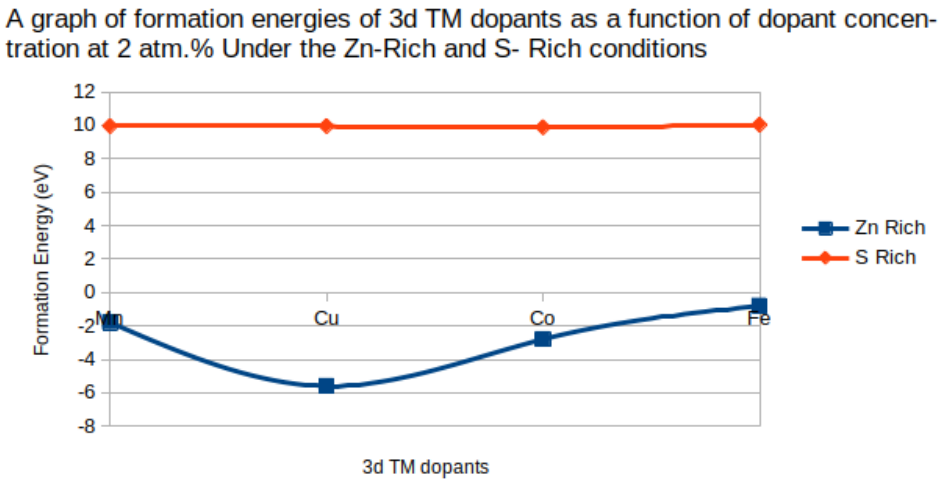

Figure 4.13: 2 amt.% Zn-S-Rich

- **4 amt.% Zn-S-Rich**

  From the Figure 4.14, the formation energy of copper at atm. 4% is more negative than the other three dopants, this shows that Cu is less sensitive to changes in dopant concentration as recorded in Table A.15. However, the other dopants recorded negative values under the Zn-rich condition, which depicts that all the four dopants could easily be incorporated in to the ZnS 2D layer at the Zn substitutional site under equilibrium conditions and so improve the PEC water splitting process. Under the S-rich conditions, the formation energy was consistently higher at the S substitutional site hence were energetically less favorable under the S-rich condition.

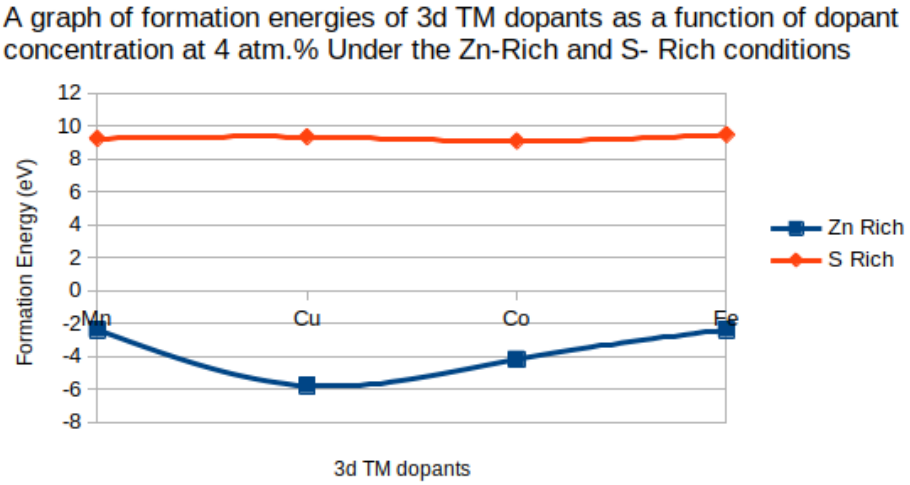

Figure 4.14: 4 amt.% Zn-S-Rich

- **6 amt.% Zn-S-Rich**

  From the Figure 4.15, the formation energy of copper and cobalt recorded higher negative formation energy values under the Zn-rich conditions than the other two dopants. This shows that Cu and Co are less sensitive to changes in dopant concentration as confirmed in Table A.16. However, the four dopants recorded high negative values under the Zn-rich condition. Therefore, the dopants can easily be incorporated in to the ZnS 2D layer surfaces at the Zn substitutional site under equilibrium conditions and so improve the PEC water splitting process. Furthermore, a higher amount of dopant concentration could cause light scattering of the samples, hence reduce effective irradiation absorbed by the reaction suspension and shielding of light thus reduce PEC water splitting process. Under the S-rich conditions, the formation energy were higher at the S substitutional site hence were energetically less favorable under the S-rich condition.

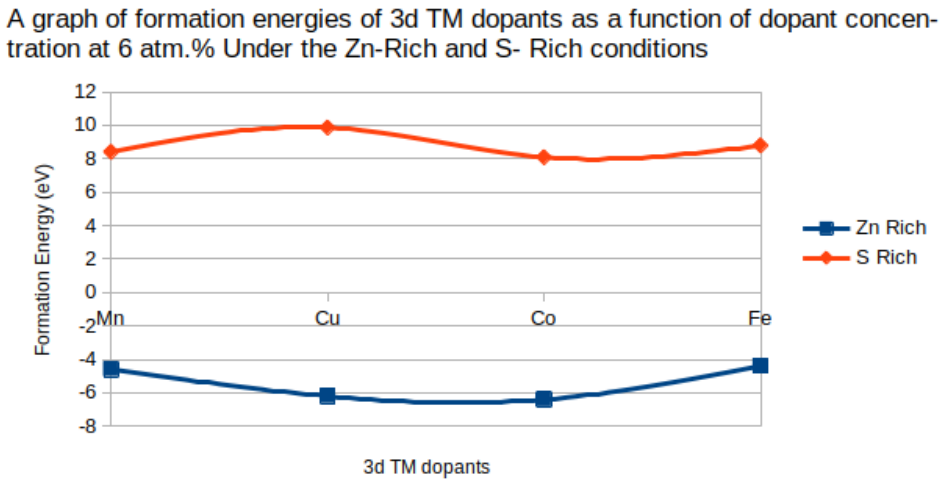

Figure 4.15: 6 amt.% Zn-S-Rich

2. **Direct calculations for formation energies under the Zn-rich and S-rich for all the 3*d* TM dopants as a function of dopant concentration**

   (a) **Formation energies under the Zn-rich for all the 3*d* TM dopants**

   The Figure 4.16 describes the trends in the formation energies of 3*d* TM dopants in ZnS 2D surface layers for various dopant concentrations (1, 2, 4 and 6 atm.%) under the Zn-rich conditions Figure 4.16. It was observed that the formation energy of 3*d* TM atoms in ZnS 2D surface layer was sensitive to dopant concentration. Under Zn-rich conditions, the defect stability decreased with increase in dopant concentration. The more the dopant concentration the more it induces dramatic changes in the structural morphology of the NSs. These observations may be attributed in part to lower atomic radii of these elements compared to that of Zn, thus subjecting the ZnS crystal to substantial local structural relaxation. These elements may have fewer unoccupied **d** orbitals hence affect the level of their chemical interaction with nearest neighbor sulphur atoms. The diagram also shows that copper was less sensitive to changes in dopant concentration under the Zn-rich conditions and that Cu was stable at the Zn substitutional site.

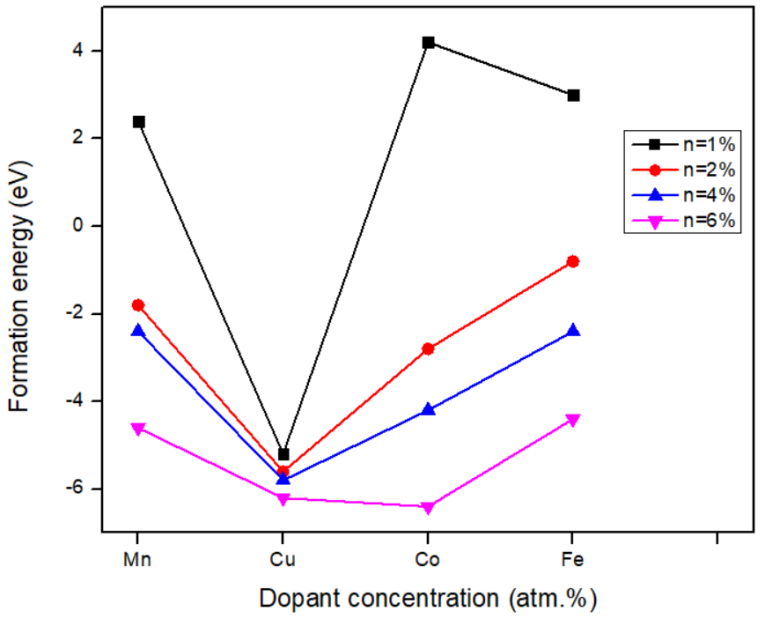

Figure 4.16: Formation energies under the Zn-rich for all the 3*d* TM dopants as a function of dopant concentration

(b) **Formation energies under the S-rich for all the 3*d* TM dopants**

From the Figure 4.17 under the S-rich conditions in Table A.18, the stability of TM doped ZnS 2D layers increased with an increase in dopant concentration. Copper and iron were less sensitive to changes in dopant concentration since it indicated a minimal change in defect stability.

Under both S-rich and Zn-rich conditions, the results suggested that the defect stability remains insensitive to changes in dopant concentration of 1–2 atm.%. Under S-rich conditions, the change in stability of TM doped ZnS 2D surface layers with dopant concentration was minimal with Cu-doped ZnS and Fe-doped ZnS being the least sensitive to changes in dopant concentration. On the other hand, in the Zn-rich limit, the change in stability was minimal with Cu-doped ZnS being the least sensitive to changes in dopant concentration.

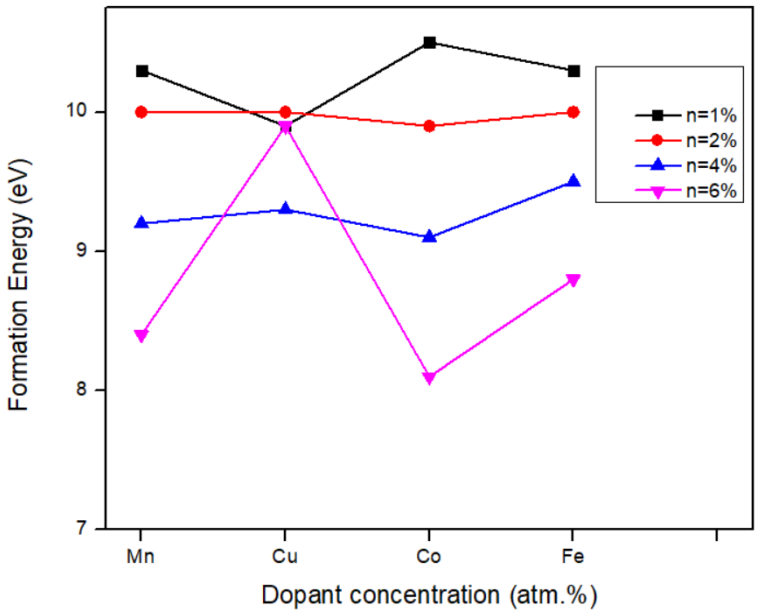

Figure 4.17: Formation energies under the S-rich for all the 3d TM dopants as a function of dopant concentration.

3. **Formation energy profile of 3d transition metal defects in ZnS 2D surface layers under the Z-rich and S-rich Condition.**

   From the Figure 4.18, S substitutional sites are energetically less favorable under S-rich conditions. S-rich conditions was much higher in energy compared to the Zn substitutional site, as recorded in the Table A.19. This observation can be associated with the large crystal strain due to relatively large atomic radii of TM atoms compared to S atoms. Importantly, the calculated formation energies of the 3d transition metals in ZnS at the Zn substitutional site in the S-rich condition were negative. The negative formation energies explains that these transition metals can readily be incorporated into ZnS at the Zn substitutional site under equilibrium conditions.

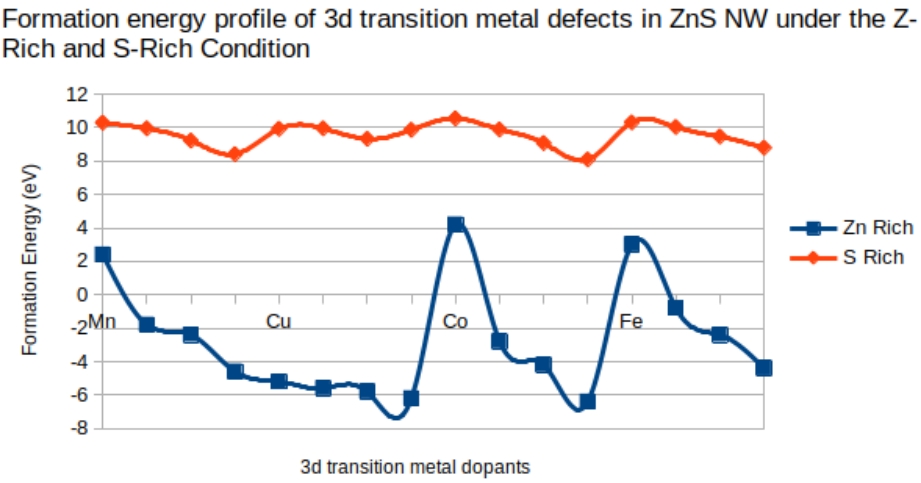

Figure 4.18: Formation energy profile of $3d$ transition metal dopants in ZnS 2D layer under the Z-rich and S-rich Condition

4.2.2 Analysis on the electronic properties of the selected $3d$ transition dopants in ZnS 2D surface layers

In this study, electronic properties were assessed in terms of the changes of the electronic band gap with the introduction of the selected $3d$ TM dopants. Employing dopants presents another effective pathway for achieving the desired band gap in ZnS. The band gap of $3d$ TM doped ZnS were performed for dopants concentration between 1-6% and presented in Figure 4.19. It was observed that, the considered dopants (Mn, Cu, Co, and Fe) reduced the band gap with varying degrees for the various dopant concentration.

Band gap

The Figure 4.19 demonstrated the difference between the HUMO and LUMO. The band gap calculations were determined from the relaxed output file submitted in the high computing performance and analyzed as seen in Figure 4.19. The results showed that the band gap of TM doped ZnS 2D surface layers were strongly dependent on the dopant concentration. Cu recorded the lowest band gap reduction from 1 to 6 amt%.

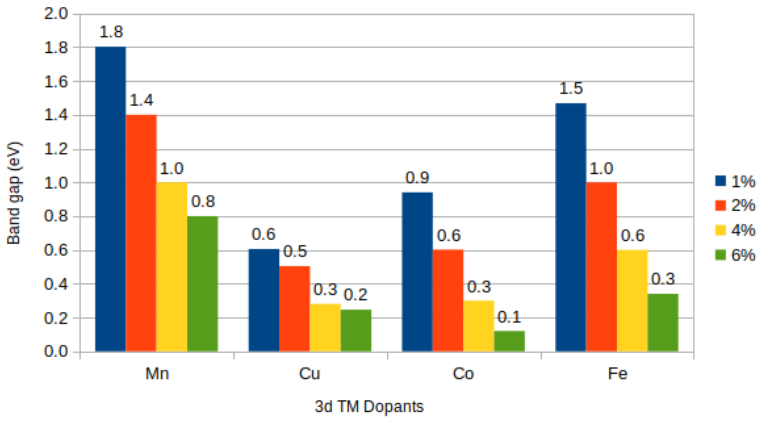

Figure 4.19: Band gap energy of $3d$ transition metal doped ZnS 2D layers at the Zn substitutional as a function of dopant concentrations.

Band gap reduction was observed with increase in dopant concentration from 1 to 6%, shifting optical response towards the visible light spectrum at higher dopant concentrations. The observed reduction in band gap in these case can be attributed to upward shift of the VBM and downward shift of CBM due to the introduction of defect states. The band gap energy of TM doped ZnS 2D layers at the Zn substitutional as a function of dopant concentration as shown in the Figure 4.20. The concentration of the dopant had a significant impact on the band gap of TM doped ZnS 2D layers.

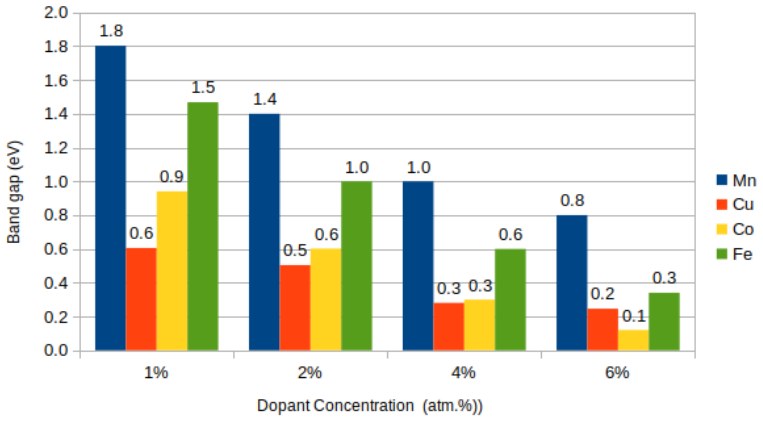

Figure 4.20: Bandgap energy of $3d$ transition metal doped ZnS 2D layers at the Zn substitutional as a function of dopant concentrations.

Due to the shifting of the band edge levels, doping generally resulted in a reduction in the ZnS 2D layer band gap. The concentration of the dopant had a

significant impact on the band gap of TM doped ZnS 2D layers. In some instances, dopants may induce mid gap defect states that can aid electron and hole transfer essential for oxidation of water J. Li & Wu (2015). In this work, Cu and Co were found to induce defect states thus producing a staggered band structure which could be ideal for optimal performance in PEC water splitting.

Projected Density of states

PDOS gives information on the kind of interaction that happens in a supercell and understanding on the contribution of different orbitals in the band structure. By increasing the number of TM dopants randomly dispersed in the 2D layer at substitutional Zn sites, the stability of ZnS 2D layers as a function of dopant concentration was firstly explored in order to discover how TM dopants affects the electronic and optical characteristics of ZnS 2D layers for PEC applications. All doping concentrations taken into account in this investigation preserved the same doping position for every distinct transition metal atom.

1. **PDOS of bulk and Relaxed ZnS**

   The Figure 4.21 and Figure 4.22, shows the bulk ZnS and relaxed surface ZnS respectively. In order for the dopant to be introduced to the surface of the bulk ZnS, the surface had to be relaxed. Relax functionality of the PW module keeps the initial optimized lattice parameters constant and simulates the forces between the surface and the molecule. Hence, these allowed investigation on the behavior of molecule being adsorbed on the surface. Relax functionality also performed the atomic coordination, optimization and force calculations applied to each atom by changing the atom location and cell size. The following were the PDOS calculations results obtained from each dopant under investigation.

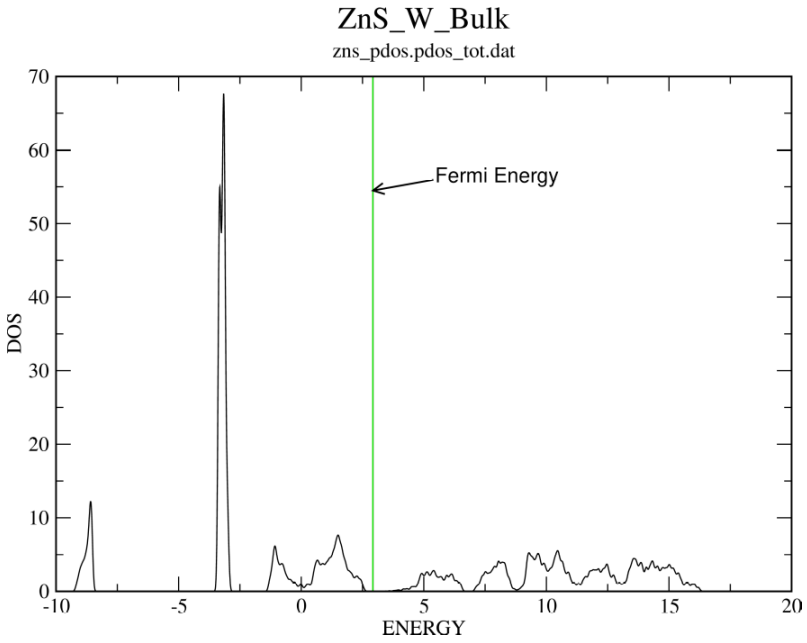

Figure 4.21: PDOS ZnS BULK

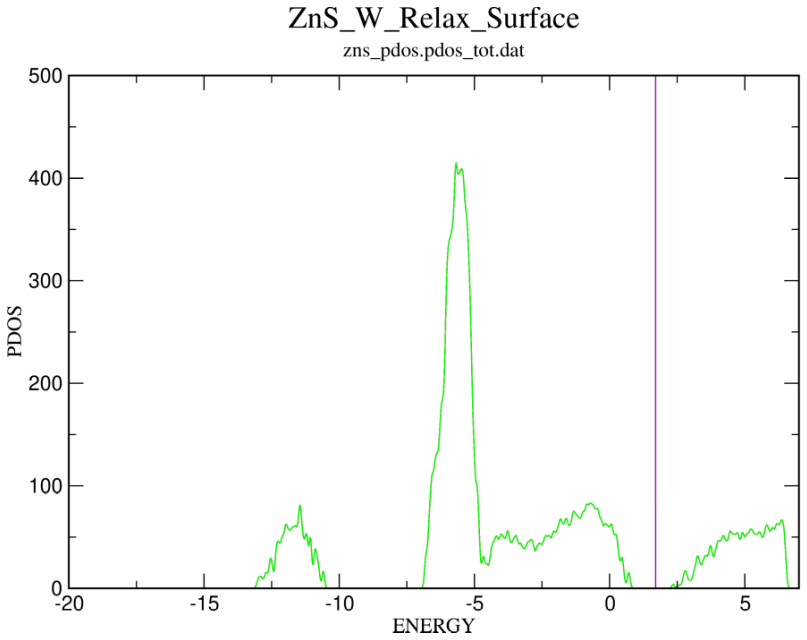

Figure 4.22: PDOS ZnS RELAXED

2. **Manganese PDOS Relaxed surface**

- *PDOS of ZnS-1% Mn relaxed surface*

  The Figure 4.23, showed the PDOS of ZnS doped with 1% Manganese dopant. The 1% Mn defect introduces the defect states located at the Fermi energy line which can be attributed to creation of new energy levels between the VBM and CBM within the ZnS band gap. This

may cause electronic structure modification by reducing the energy gap hence could allow visible light absorption which may be ideal for PEC water splitting. The PDOS around the Fermi level originated mainly from the $3d$ band contributions of Mn.

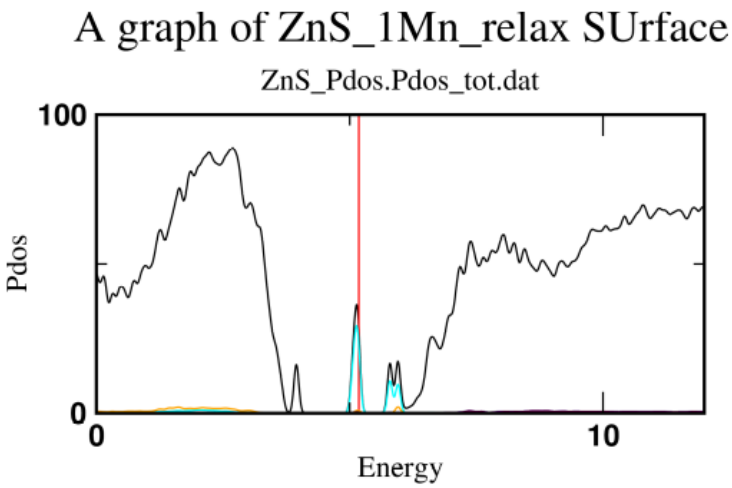

Figure 4.23: 1Mn PDOS

- *PDOS of ZnS-2% Mn relaxed surface*

  The Figure 4.24 shows the PDOS of ZnS doped with 2% Manganese dopant. With an E-Fermi =1.19. The 2% Mn defect introduces the defect states located at the Fermi energy line which can be attributed to creation of new energy levels between the VBM and CBM within the ZnS band gap which may cause electronic structure modification by reducing the energy gap hence allow visible light absorption which can be ideal for PEC water splitting. The $3d$ band of Mn dopant contributes to the PDOS around the Fermi level.

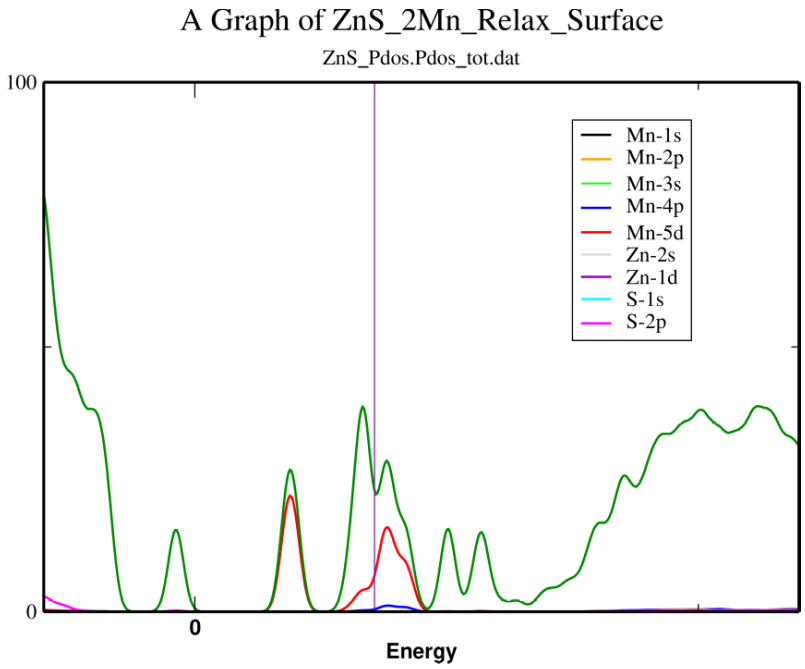

Figure 4.24: 2Mn PDOS

- *PDOS of ZnS-4% Mn relaxed surface*

  The projected density of states (PDOS) of ZnS doped with 4% manganese dopant is displayed in Figure 4.25 having E-Fermi = 1.1423 value. Defect states at the Fermi energy line were introduced by the 4% Mn defect, which was explained by the formation of new energy levels in the ZnS band gap between the VBM and CBM. By closing the energy gap, this may modify the electronic structure and make it possible for visible light to be absorbed, which may be perfect for PEC water splitting. The $3d$ band contributions of Mn may be the principal source of the PDOS near the Fermi level. Compared to 2% Mn, 4% Mn has more energy levels within the Fermi line hence more absorption for more hydrogen production.

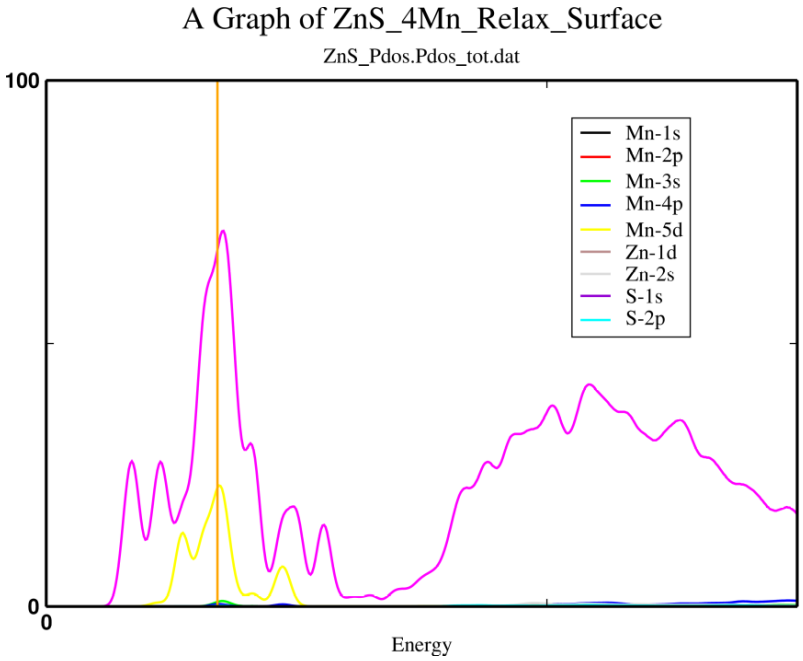

Figure 4.25: 4Mn PDOS

3. **Copper PDOS Relaxed surface**

Copper has high electronic conductivity and can effectively reduce the wide band gap of ZnS by creating defects and d band states of Cu in ZnS and also act as active trap centers of electrons to reduce carrier recombination. The defect states very near to the valence band also smear the valence band edge deep inside the gap. Therefore, on both sides of the VBM and CBM, an energy tail may be formed hence more UV light absorption which can enhance more hydrogen production.

- *PDOS of ZnS-1% Cu relaxed surface*

  The projected density of states of ZnS doped with 1% Copper dopant at E-Fermi=4.3278 is shown in Figure 4.26. The 1% Cu defect introduces the defect states located at the Fermi energy line which can be attributed to creation of new energy levels between the VBM and CBM within the ZnS band gap. This may cause electronic structure modification by reducing the energy gap hence allow visible light absorption which is ideal for PEC water splitting. The PDOS around the Fermi

level originates mainly from the $3d$ band contributions of Cu.

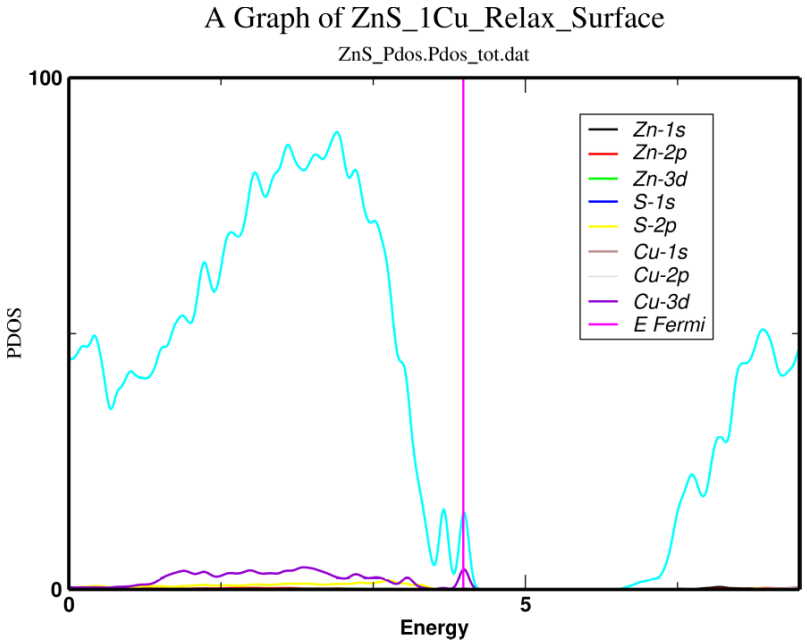

Figure 4.26: 1Cu PDOS

- *PDOS of ZnS-2% Cu relaxed surface*

  As seen in Figure 4.27, the PDOS of ZnS doped with 2% Copper dopant at E-Fermi=2.7024 eV was recorded. Defect states at the Fermi energy line have been introduced by the 2% Cu defects and this is well explained by the formation of new energy levels in the ZnS band gap between the VBM and CBM. By closing the energy gap, this may modify the electronic structure and could make it possible for visible light to be absorbed, which will be perfect for PEC water splitting. Cu's 3 d band contribution could be the principal source of the PDOS near the Fermi level.

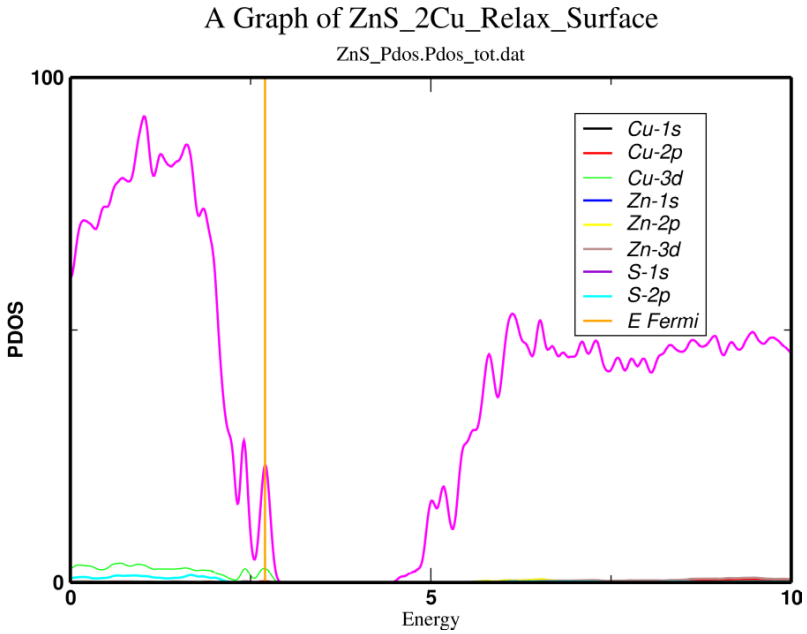

Figure 4.27: 2Cu PDOS

- *PDOS of ZnS 4% Cu relaxed surface*

  At E-Fermi=1.6373 eV, the PDOS of ZnS doped with 4% Copper dopant is shown in Figure 4.28. The development of new energy levels in the ZnS band gap between the VBM and CBM may explain why the 4% Cu defect may introduce defect states at the Fermi energy line. This may alter the electronic structure and permit visible light absorption by closing the energy gap, which may be ideal for PEC water splitting. Near the Fermi level, the main source of the PDOS could be Cu's three d band contribution.

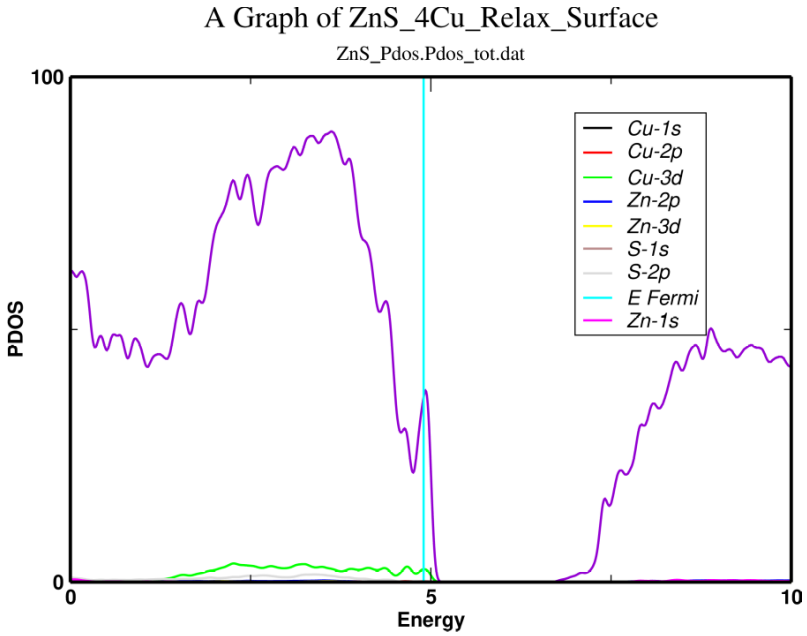

Figure 4.28: 4Cu PDOS

The d states of Cu^{2+} and Sulphur defects may be responsible for the narrowing of the band gap of ZnS. As the band gap decreases, the magnitude of defect energy increases. These defects may increase the magnitude of Urbach energy and the magnitude of this energy may increase as Cu loading increases. Absorption edge shifting and band gap reduction may be controlled by the surface of the ZnS 2D layers, lattice strain and vacancies. Doping can induce smearing of the valence and conduction band edges in Cu. This can effectively reduce the wide band gap of ZnS by creating defects and d band states of Cu in ZnS 2D layer and can also act as active trap centers of electrons to reduce carrier recombination.

4. **Cobalt PDOS Relaxed surface**

- *PDOS of ZnS-1% Co relaxed surface*

  Figure 4.31 illustrates the 1% Co relax surface defect states of the Co doped ZnS 2D layer, which has an E-Fermi energy of = 0.2271 eV with additional energy bands within the E-Fermi line. Cobalt doping may have created grain boundary defects along the E-Fermi line, which could lead to valence and conduction band bending. These defects limit

electron mobility to the interface and halt charge carrier recombination. Sub-band states that form between the valence and conduction bands may cause the band gap to narrow. Because there may be more defects below the conduction band, which pushes the band edge more into the forbidden gap, ZnS's effective band gap may reduce as doping increases.

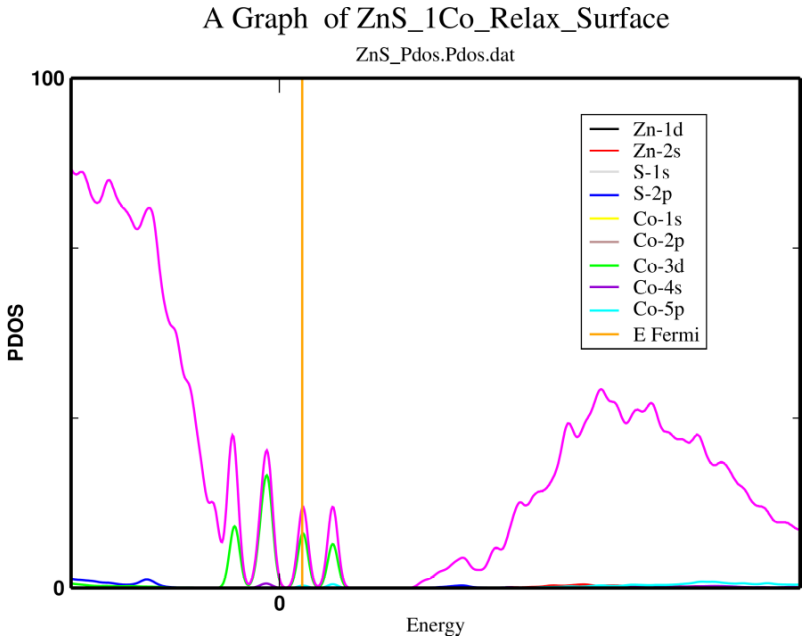

Figure 4.29: 1Co PDOS

- *PDOS of ZnS-2% Co relaxed surface*

  Figure 4.30 displays additional energy bands within the E-Fermi of the Co doped ZnS 2D layer with a 2% Co relax surface defect states and an E-Fermi energy of = 2.44 eV. The Co doping may have generated grain boundary defects around the E-Fermi line, which may lead to bending of the valence and conduction bands. Electron mobility may be limited to the interface of these imperfections, which may also prevent charge carrier recombination. Sub-band states that form between the conduction and valence bands are what may have caused the band gap to narrow. When the doping level increases, more defects are present below the conduction band, which may push the band edge farther into

the forbidden gap and may reduce the effective band gap of ZnS 2D layers.

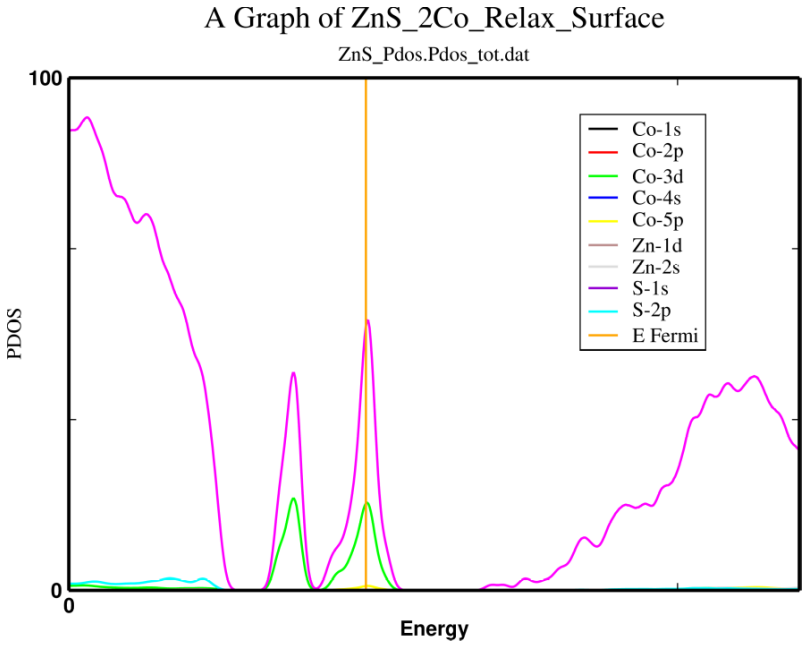

Figure 4.30: 2Co PDOS

- *PDOS of ZnS-4% Co relaxed surface*

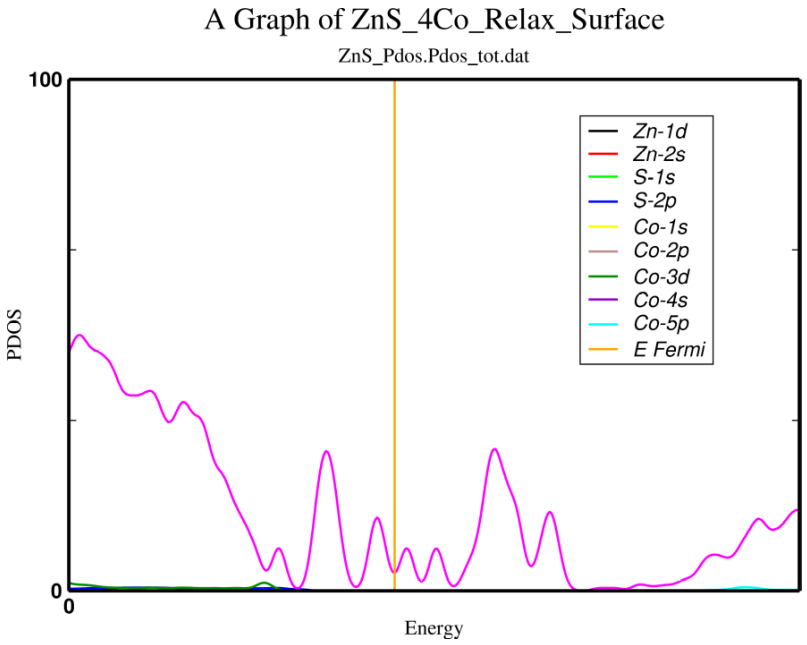

Figure 4.31: 4Co PDOS

Figure 4.31 displays the 4% Co relax surface defect states of the Co doped ZnS 2D layer with an E-Fermi energy of = 2.23 eV, revealing

additional energy bands within the E-Fermi. Co doping may produce grain boundary defects around the E-Fermi line, which can bend the valence and conduction bands. These imperfections limit electron mobility to the contact and prevent charge carrier recombination. Sub-band states between the valence and conduction bands may cause the band gap to narrow. Because more defects are present below the conduction band, which pushes the band edge deeper into the forbidden gap, ZnS's effective band gap may fall as the doping level grows.

- *PDOS of ZnS-6% Co relaxed surface*

  The defect states of the 6% Co relax surface of the Co doped ZnS 2D layer with an E-Fermi energy = 2.7063 eV is represented by the Figure 4.32. As the amount of Co content rises, the Co doping may cause more grain boundary defects to form and may cause the valence and conduction bands to bend. Compared to 4% Co amount, the energy levels may be higher and as a result charge carrier recombination may be inhibited and electron mobility could be restricted to the interface by these imperfections.

  On the other hand, complex defects and defect clusters within the structure may have been created by severe doping and these may be undesirable side effects. Consequently, 6% Co doping may limit the optical adsorption of the NSs at the surface by causing complicated defects and clustering around the E-Fermi line, which may not be desirable and may induce a recombination effect. In the case of cobalt, the band gap becomes 0.1 at 6 atm.%, making the system metallic due to upward shift of the Fermi level.

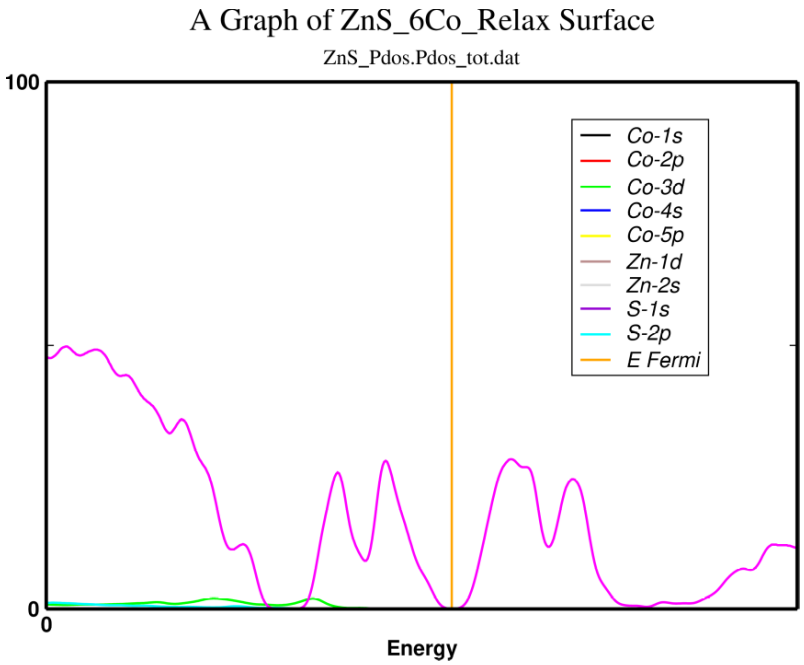

Figure 4.32: 6Co PDOS

5. **Iron PDOS Relaxed surface**

Fe doping may lead to the creation of grain boundary defects and could result in the bending of the valence and conduction bands. These defects may limit the electron mobility to the interface and prevent charge carrier recombination. Sub-band states formed in between the valence and conduction bands may result in the narrowing of the band gap with doping level, the number of defect levels below the conduction band may increase to such an extent that the band edge could be shifted deep into the forbidden gap, thereby reducing the effective band gap of ZnS.

- *PDOS of ZnS-1% Fe relaxed surface*

  The Figure 4.33 represents the defect states of 1% Fe relax surface of the Fe doped ZnS 2D layer with an E-Fermi energy = 4.544 eV. The Fe doping may lead to the creation of grain boundary defects around the E-Fermi line and this may result in the bending of the valence and conduction bands. These defects may limit the electron mobility to the interface and prevent charge carrier recombination. Sub-band states

formed in between the valence and conduction bands may result in the narrowing of the band gap. With doping level, the number of defect levels below the conduction band may increase to an extent that the band edge may be shifted deep into the forbidden gap, thereby reducing the effective band gap of ZnS.

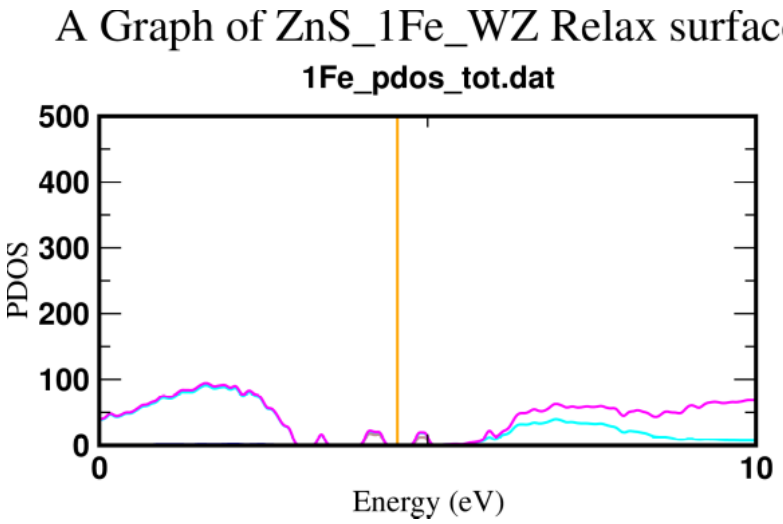

Figure 4.33: 1Fe PDOS

- *PDOS of ZnS-2% Fe relaxed surface*

  The defect states of the 1% Fe relax surface of the Fe doped ZnS 2D layer with an E-Fermi energy = 1.1709 eV is represented by the Figure 4.34. The valence and conduction bands may bend as a result of the Fe doping, which may produce grain boundary defects around the E-Fermi line. Charge carrier recombination may be inhibited and electron mobility could be restricted to the interface by these imperfections. The band gap may narrow as a result of sub-band states that arise between the valence and conduction bands. The effective band gap of ZnS may be lowered as a result of the doping level thus increase the number of defect levels below the conduction band to the point where the band edge may be moved far into the forbidden gap.

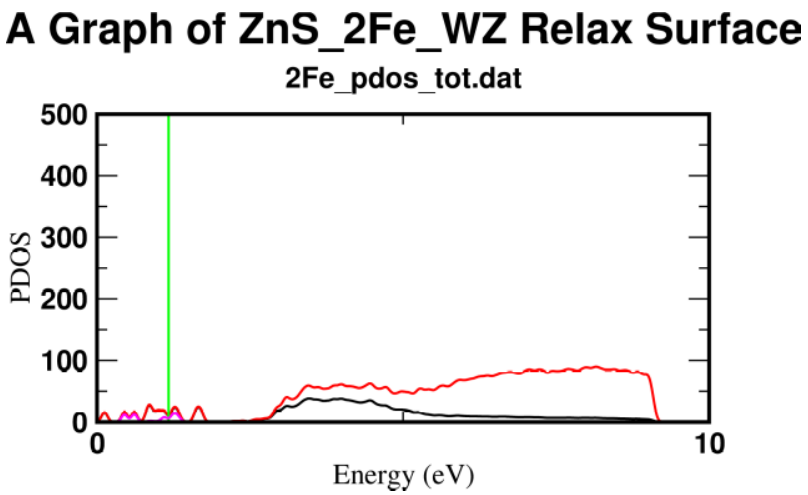

Figure 4.34: 2Fe PDOS

- *PDOS of ZnS-4% Fe relaxed surface*

  The 4% Fe relax surface defect states of the Fe doped ZnS 2D layer with an E-Fermi energy of = 1.7512 eV is shown in Figure 4.35 showing more energy bands within the E-Fermi. Grain boundary defects surrounding the E-Fermi line are created by the Fe doping and this may cause the valence and conduction bands to bend. These defects may stop charge carrier recombination and restrict electron mobility to the interface. The narrowing of the band gap may be caused by sub-band states that arise between the valence and conduction bands. The effective band gap of ZnS may decrease as the doping level rises because more defects could be present below the conduction band, shifting the band edge further into the forbidden gap.

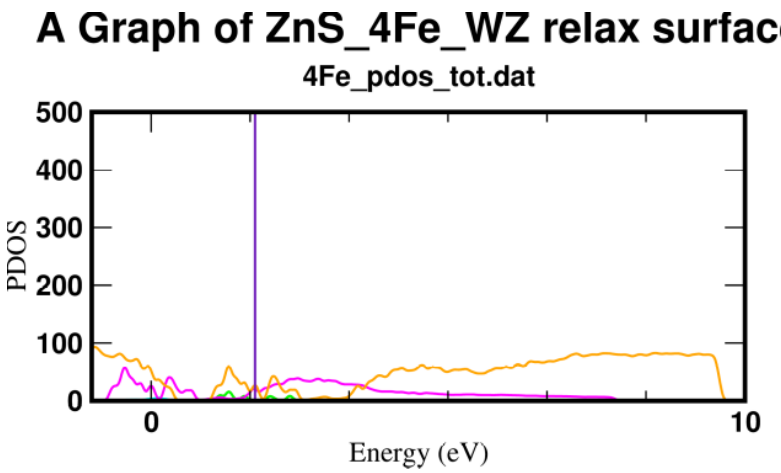

Figure 4.35: 4Fe PDOS

- *PDOS of ZnS-6% Fe relaxed surface*

  The Figure 4.36 represents the defect states of 6% Fe relax surface of the Fe doped ZnS 2D layer with an E-Fermi energy = 0.8012 eV. The Fe doping may lead to the creation of more grain boundary defects as the number of Fe content increases and it may result in the bending of the valence and conduction bands. Comparing to 4% Fe amt., there are more energy levels and therefore more defect states. These defects may limit the electron mobility to the interface and prevent charge carrier recombination.

  However, heavy doping induce the formation of complex defects and defect clustering within the structure, which are in general not desirable side effects. Therefore 6% Fe doping may cause complex defects and clustering around the E-Fermi line which may not be desirable and may cause recombination effect therefore limit the optical adsorption of the nanowires at the surface.

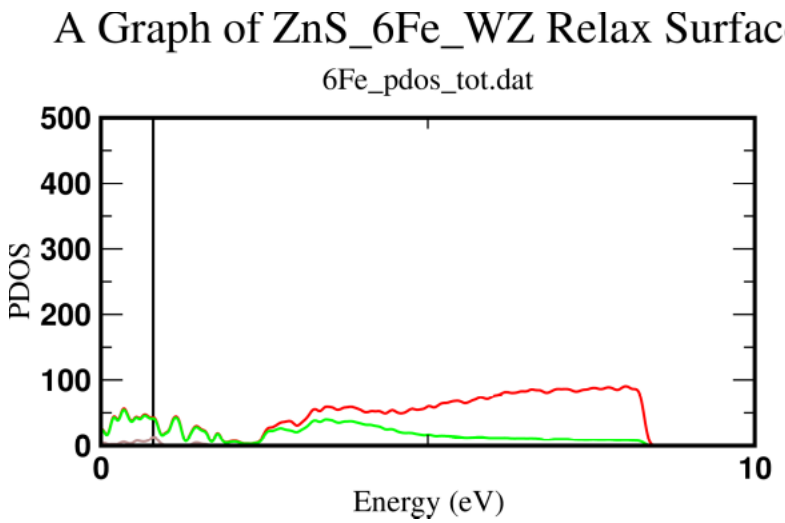

Figure 4.36: 6Fe PDOS

6. Projected Density of States (PDOS) Hybridization

   PDOS was simulated to understand the role that different orbitals play in the band structure. Additionally, the valance band's S-p and Zn-p orbitals hybridize with one another. Comparable findings from the electron difference density investigation showed that the Zn and S atoms share charges. Higher conduction band energy states were attributed to the Zn-p orbitals, while lower conduction band states were attributed to the Zn-s orbitals. The presence of mid-gap states between VBM and CBM may shift the absorption spectral spectrum of wide band-gap semiconductors from the UV to the visible light range. The findings demonstrate that mid-gap states were induced by ZnS 2D layers doped with Cu and Co at 4% and 2% dopant concentrations. This was well demonstrated by the hybridization of S-2p and Cu/Co-3d orbitals, as depicted in Figure 4.37 and Figure 4.38 respectively.

   - *2Co-2Cu-ZnS PDOS Hybridization*

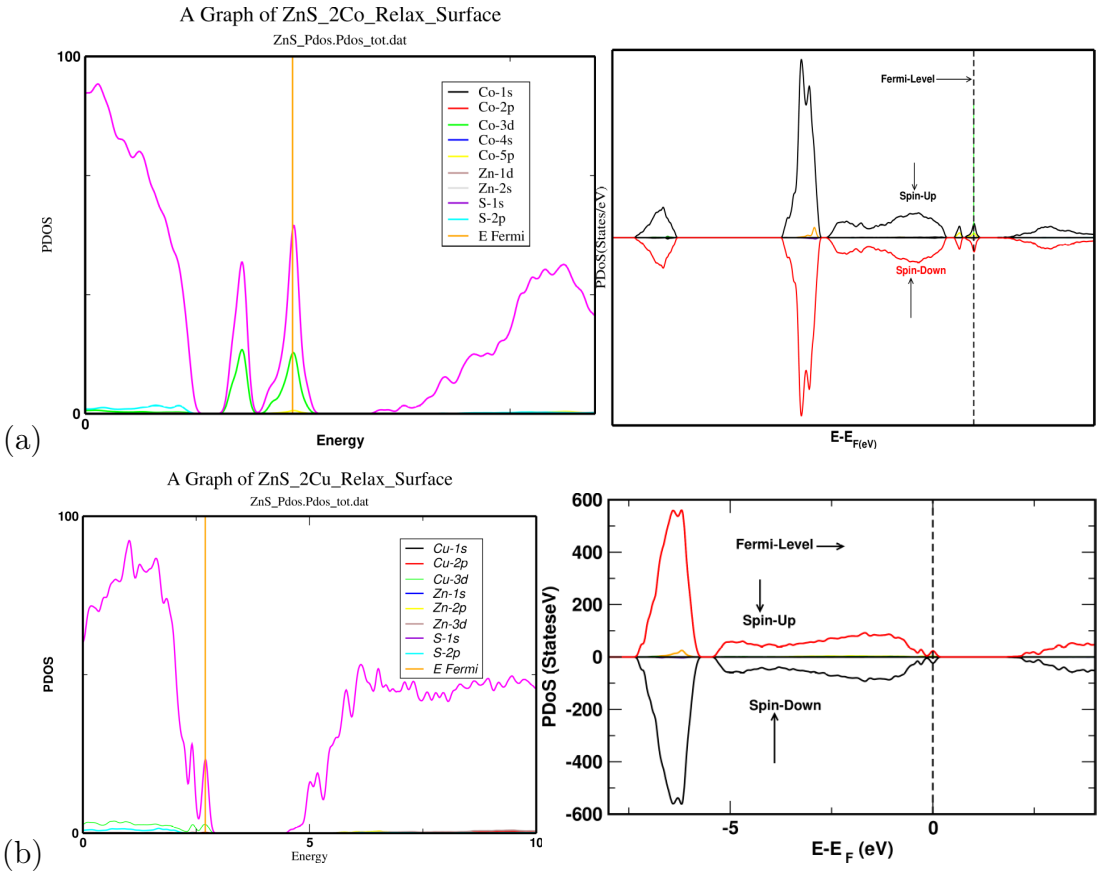

Figure 4.37: PDoS of ZnS NSs doped with (a)2%Co and (b)2%Cu.The Fermi level is indicated with the dotted line

Wide band gap semiconductors' absorption spectral range can be expanded from UV to visible light spectrum by the existence of mid-gap states between VBM and CBM. By bringing the catalyst level close to the H_2O/O_2 redox level, shallow mid-gap states may affect the transfer of holes in the oxidation of water J. Li & Wu (2015). Therefore, both Cu and Co can produce a staggered band-structure arrangement with the right amount of dopant, which may be perfect for PEC and related applications.

- *4Co-4Cu-ZnS PDOS Hybridization*

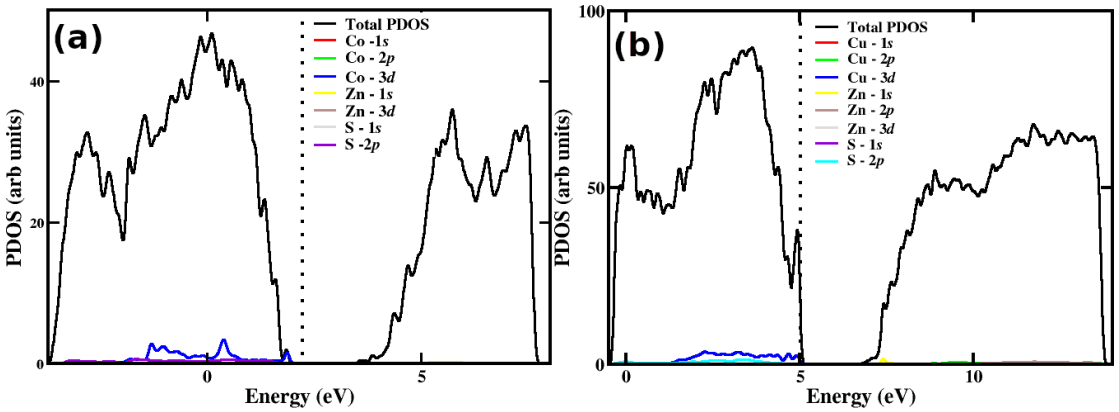

Figure 4.38: PDOS of ZnS NSs doped with 4% Co and 4%Cu. The Fermi level is indicated with dotted line

Thus controlled introduction of dopant can result in the creation of superior catalyst for PEC water splitting.

4.2.3 Analysis on the optical properties of Cu and Co doped ZnS 2D layer

Transitional metal dopants are anticipated to modify the optical response of ZnS 2D layered system. In particular, Cu and Co at 4% dopant concentration were explored because of their staggered configuration. The optical response were assessed using the dielectric response of the modified ZnS as expressed in Equation 3.6 The optical absorption response ($\alpha_a bs$) was determined using dielectric response function Equation 3.7 .

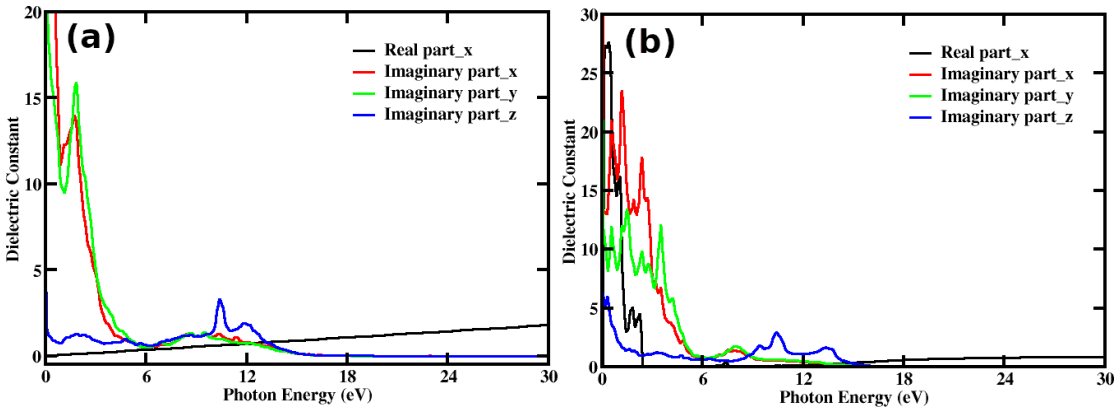

Figure 4.39: Dielectric constant verses photon energy plots for ZnS layer doped with (a) 2%Co and (b) 4%Cu.

Figure 4.39 shows the real and imaginary part contribution to dielectric function with peaks showing different energy transition with the sharps peaks being attributed to $\epsilon 2$. Indeed, ZnS doped with Co (2%) shows $\epsilon 2$ peaks at 0.4-2.7 eV energy range as shown in Figure 4.39(a). In the case of ZnS doped with Cu (4%), $\epsilon 2$ were observed to be from 0.2-3.4 eV energy range as plotted in Figure 4.39(b). The optical absorption response ($\alpha_a bs$) was determined using dielectric response function Gajdoš et al. (2006) as shown below,

$$\alpha_{abs} = \sqrt{2\omega}(\sqrt{\epsilon_1^2\omega + \epsilon_2^2\omega - \epsilon_1\omega})^{\frac{1}{2}}. \tag{4.1}$$

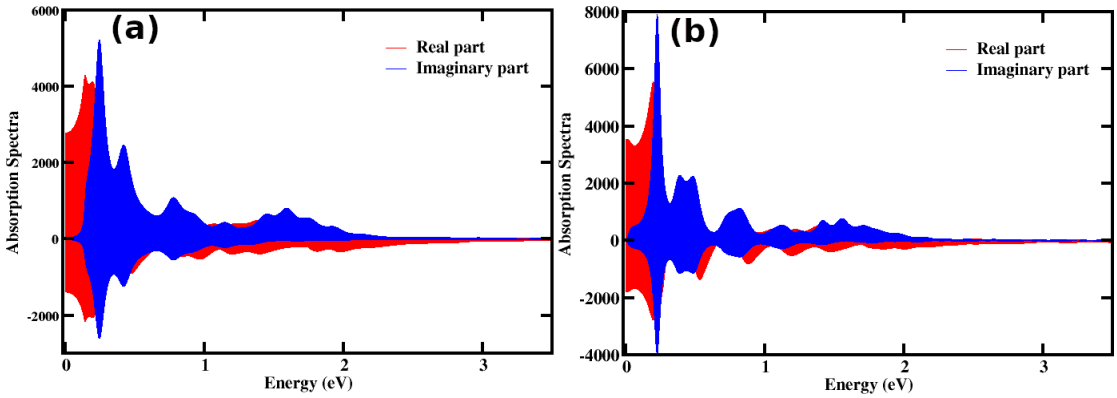

Figure 4.40: Absorption spectra for ZnS layer doped with (a) 2 %Co and (b) 4 %Cu. Red and blue shaded regions represent real and imaginary contribution, respectively.

Pristine 2D ZnS has the highest absorption peak located at a wavelength of 444.52 nm, which is within the visible part of electromagnetic spectrum consistent with previous work Lashgari et al. (2016). In the case of ZnS doped with Co (2%) absorption range was observed between 0.4 - 1.8 eV with highest peak at 405.01 nm (see Figure 4.40(a)), while in ZnS doped with Cu (4%) the absorption starts at 0.2-1.7 eV with the highest peak at 371.94 nm, as shown in Figure 4.40(b). Overally, a blue shift in the absorption response of the modified ZnS was noted, in particular, ZnS doped with Cu (2%) and Cu (4%) showed a reduction in wavelength by 8.89 % and 16.33%, respectively. Thus, the doped ZnS system is anticipated to offer superior performance in opto-electronic and related application owing improved

optical response to visible range known to posses high energy density compared to infrared or near infrared spectrum that the pristine system is known to operate.

4.2.4 Photocatalysis activity of TM doped ZnS 2D layer

Production and transfer of photo-induced electron-hole is critical for PEC water splitting and assessment of such process is essential in optimization S. Chen et al. (2020); Ghorai et al. (2019); Poornaprakash et al. (2020). The effect of TM dopants on ZnS catalytic activity were analysed by plotting band-edge alignment of pristine and doped ZnS for the various dopant concentrations compared with the water reduction and oxidation potential as shown in Figure 4.41. The CBM

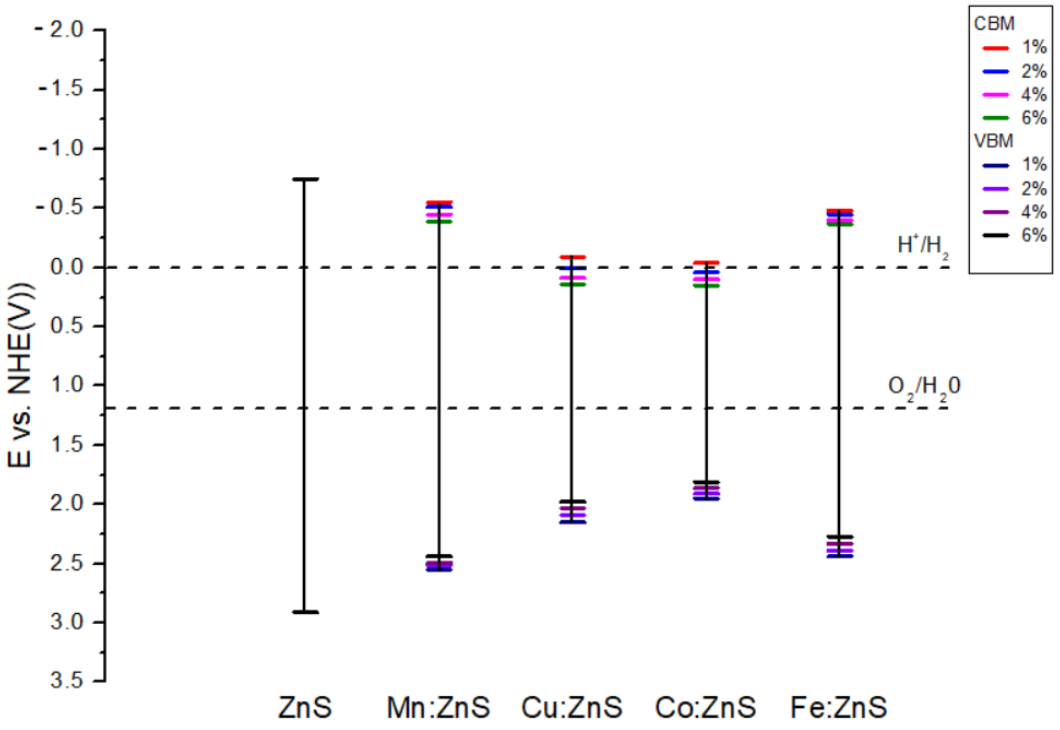

Figure 4.41: Band edge alignment for $3d$ transition metal doped ZnS 2D surface layers with varying dopant concentrations in relation to water's redox potential (1%, 2%, 4%, 6%).

of the intrinsic ZnS 2D surface layer was greater by $\approx 0.75eV$ than the reduction potential of H^+/H_2 and the VBM was more positive (by 1.64 eV) than the oxidation potential of O_2/H_2O, as illustrated in Figure 4.41. It can be inferred that the pure ZnS 2D Layer has strong oxidation and reduction capabilities; yet,

its 3.66 eV band gap necessitates UV light irradiation. Band gap engineering was necessary to enable water splitting at visible light frequencies. The ideal TM dopant is the one that narrows the ZnS 2D Layer's band gap while preserving its semi-conductor character by shifting the CBM and VBM relative to pure ZnS 2D surface layer, making it a candidate for visual light illumination as opposed to UV light. As these characteristics have a substantial impact on the overall PEC activity of the photocatalyst, they must be taken into consideration in addition to band gap engineering. These considerations include levels of CBM/VBM relative to redox potentials of water and any defect levels in the band gap. All $3d$ TMD's have oxygen evolution as preferred by the VBM of the doped ZnS 2D Layer with $3d$ TM remaining significantly positive above the O_2/H_2O oxidation potential. Yet, depending on the dopant concentration, the reduction potential of ZnS 2D layers doped with Mn, Cu, Co and Fe stays negative below the reduction potential of H^+/H_2. This finding suggests that ZnS 2D surface layers doped with transition metals dopants such as; Mn, Cu, Co and Fe could be used as a photocatalyst for the simultaneous evolution of oxygen and hydrogen as demonstrated in Figure 4.42. Thus, adjusting the dopant concentration offers a chance to enhance the driving power for photocatalysis.

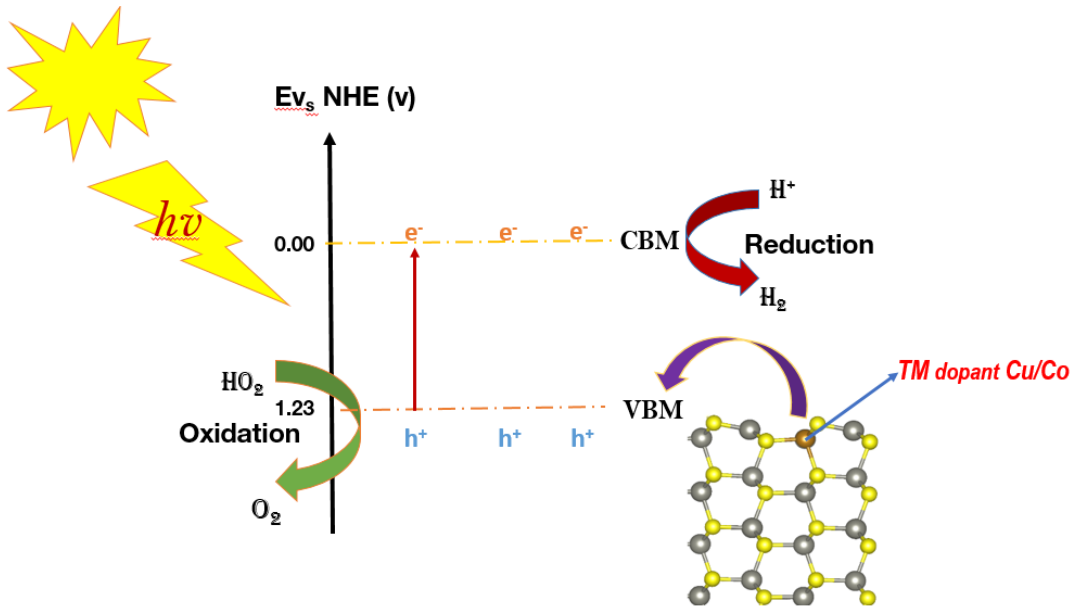

Figure 4.42: Theoretical mechanism

4.3 Experimental analysis of cobalt doped ZnS nanostructure surface layers on the structural, electronic and optical characteristics

4.3.1 Structural analysis of cobalt doped ZnS nanostructures surface layers

Ideal crystal is an infinitely large and perfectly ordered array. Inter planar spacing is related to Miller indices and the lattice constant by;

$$\frac{1}{d_{hkl}^2} = \frac{h^2}{a^2} + \frac{k^2}{b^2} + \frac{l^2}{c^2} \tag{4.2}$$

for specific kind of crystal. The Bragg's Law of diffraction;

$$2dsine\theta = n\lambda \tag{4.3}$$

where d is the d_{hkl}. n is the diffraction order for the 1^{st} order n=1; Cu $k\alpha = \lambda$ is the X-ray wavelength which is equal to 1.506 Å from the experimental set up. d is the inter-planar spacing in Å; θ is the Braggs angle which is measured in degrees. The inter planar spacing and 2 sine θ is the path difference between the two rays of X-rays. For simple cubic lattice then (*Source; JCPD software database*) three sides are equal i.e. $a = b = c$ hence replace h, k, l with a as shown in Figure 4.43. This will give an expression such as;

$$\frac{1}{d_{hkl}^2} = \frac{h^2}{a^2} + \frac{k^2}{b^2} + \frac{l^2}{c^2} \tag{4.4}$$

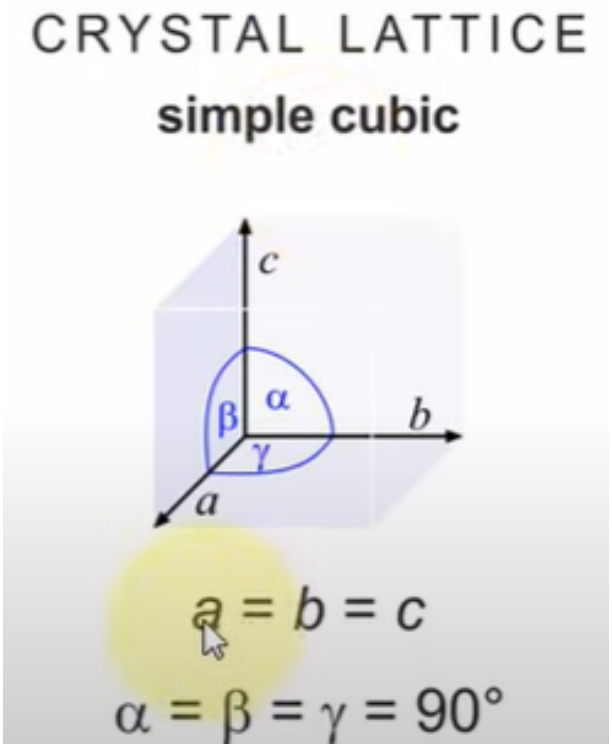

Figure 4.43: Simple cubic lattice *Source;JCPD software database*

Where $\alpha = \beta = \gamma = 90°$. Therefore

$$\frac{1}{d_{hkl}^2} = \frac{h^2 + k^2 + l^2}{a^2} \tag{4.5}$$

$$d_{hkl} = \frac{a}{\sqrt{h^2 + k^2 + l^2}} \tag{4.6}$$

d_{hkl} is found from the XRD graph while the (hkl) values are taken from the JCPD cards Omurzak et al. (2011).

1. **Crystallinity (crystal size and disorder) analysis**

   Origin software was used to determine the values of all the doped ZnS, undoped ZnS and cobalt doped ZnS decorated with and without graphene.

   - **Crystal size and disorder analysis without graphene**

     The experimental patterns obtained from XRD analysis were compared to the simulated pattern obtained from the Crystallographic Informa-

tion File (CIF) and the results obtained were further analyzed.

(a) *The crystalline structure of the synthesized ZnS*

The Figure 4.44 shows powder XRD patterns of the synthesized ZnS. This indicated that both structures share a similar degree of symmetry with the modelled structures of the ZnS database. The Bragg's peak at $2\theta = 28.25°, 47.84°, 56.93°, 69.68°, 77.08°$ were assigned to the crystallographic planes (111), (220), (311), (300) and (110) for hexagonal system respectively. The diffraction pattern and inter-planar spacing's matched well with the face centred cubic (fcc) cubic phase of ZnS.

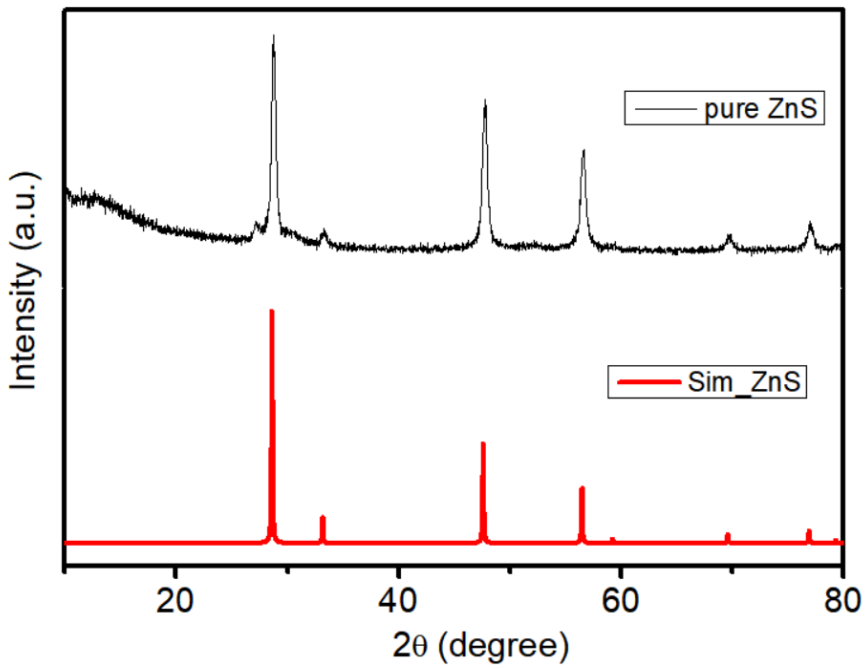

Figure 4.44: Pure ZnS

(b) *XRD 1Co-ZnS*

The Figure 4.45 shows powder XRD patterns of the synthesized ZnS and 1% cobalt doped ZnS. This indicated that both structures share a similar degree of symmetry with the modelled structures of the ZnO and CoO database. The Bragg's peak recorded at $2\theta = 28.25°$, $47.84°$, $56.93°$, $69.68°$ and $77.08°$ were assigned to

the crystallographic planes (111), (220), (311), (300), and (110) for hexagonal system respectively. There was an asymmetric broadening on the high angle side of the ZnS (111) diffraction peaks due to the addition of 1% cobalt. The diffraction pattern and inter-planar spacing's matched well with the fcc phase of ZnS.

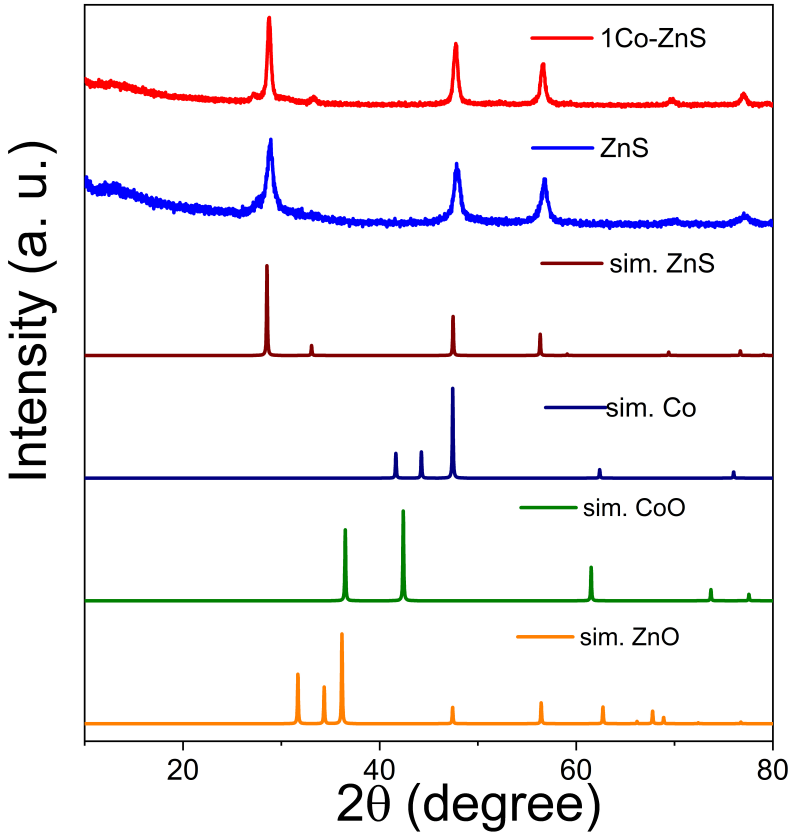

Figure 4.45: Pure-ZnS-1Co-ZnS

(c) *XRD 2Co-ZnS*

The Figure 4.46 illustrates powder XRD patterns of the synthesized ZnS and 2% cobalt doped ZnS. This showed that both structures share a similar degree of symmetry with the modelled structures of the ZnO and CoO database. The Bragg's peak at $2\theta = 28.25°$, 47.84°, 56.93°, 69.68° and 77.08° were assigned to the crystallographic planes (111), (220), (311), (300) and (110) for hexagonal system respectively. There was an asymmetric broadening on the high angle side of the ZnS (111) diffraction peaks due to the addi-

tion of 2% cobalt. The diffraction pattern and inter-planar spacing's matched well with the fcc phase of ZnS.

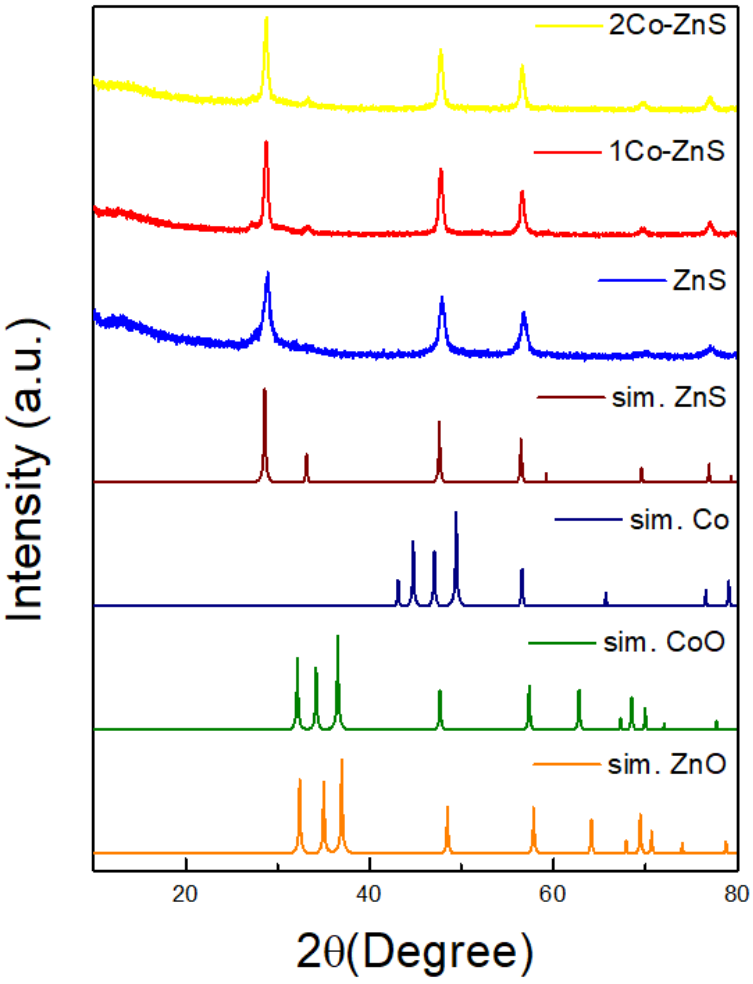

Figure 4.46: Pure ZnS-2Co-ZnS

(d) *XRD 4Co-ZnS*

The Figure 4.47 depicts powder XRD patterns of the synthesized ZnS and 4% cobalt doped ZnS. This indicated that both structures shared a similar degree of symmetry with the modelled structures of the ZnO and CoO database. The Bragg's peak at $2\theta = 28.25°$, 47.84°, 56.93°, 69.68° and 77.08° were assigned to the crystallographic planes (111), (220), (311), (300), and (110) for hexagonal system respectively. There was an asymmetric broadening on the high angle side of the ZnS (111) diffraction peaks due to the addition of 4% cobalt. The diffraction pattern and inter planar

spacing's matched well with the fcc phase of ZnS.

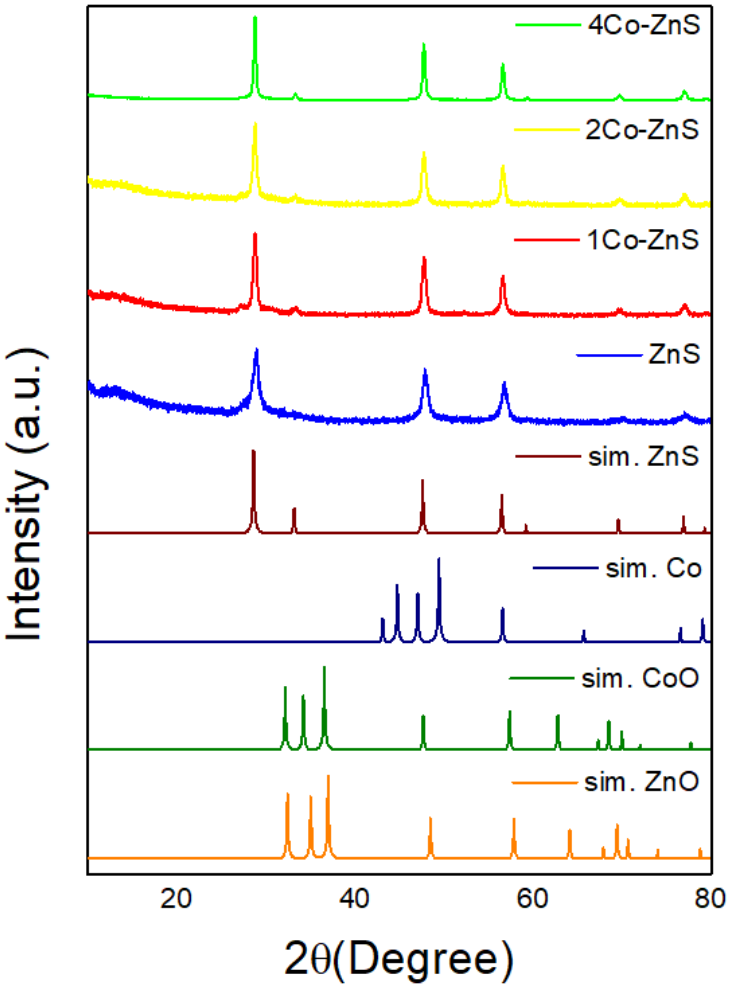

Figure 4.47: Pure-ZnS-4Co-ZnS

(e) *XRD 6Co-ZnS*

The Figure 4.48 describes powder XRD patterns of the synthesized ZnS and 6% cobalt doped ZnS. It indicated that both structures shared a similar degree of symmetry with the modelled structures of the ZnO and CoO database. The Bragg's peak at $2\theta = 28.25°$, 47.84°, 56.93°, 69.68° and 77.08° were assigned to the crystallographic planes (111), (220), (311), (300), and (110) for hexagonal system respectively. There was an asymmetric broadening on the high angle side of the ZnS (111) diffraction peaks due to the addition of 6% cobalt. The diffraction pattern and inter planar spacing's matched well with the fcc phase of ZnS.

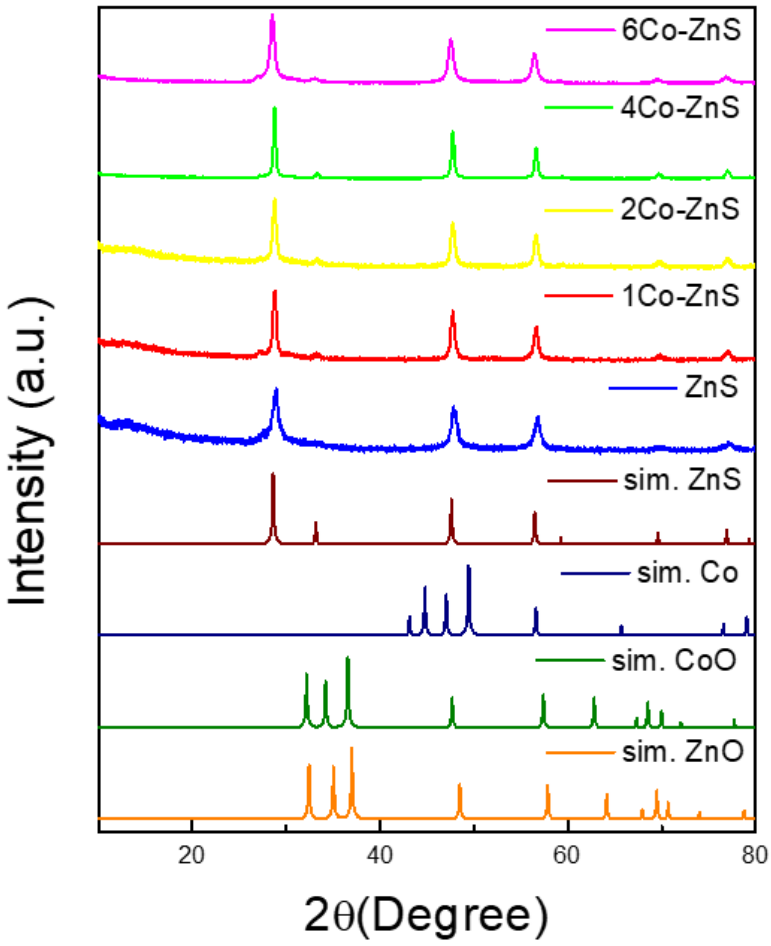

Figure 4.48: Pure-ZnS-6Co-ZnS

- **Crystal size and disorder analysis with graphene**

  (a) *Graphite oxide analysis*

  The XRD pattern of pure graphite as shown in Figure 4.49 exhibits the distinctively strong diffraction peak of graphite at $2\theta = 26.4°$, which corresponds to the graphite oxide inter-layer of (002) with the d spacing of 0.34 nm. During the chemical oxidation process, hydroxyl, carbonyl and epoxide groups may have intercalated in the graphite inter-layer, as evidenced by the loss of the distinctive graphite peak at 26.4° and the emergence of a wide peak at 10.6° (d= 0.83 nm) in the dried GO from the formulae; Bragg's law 4.3.

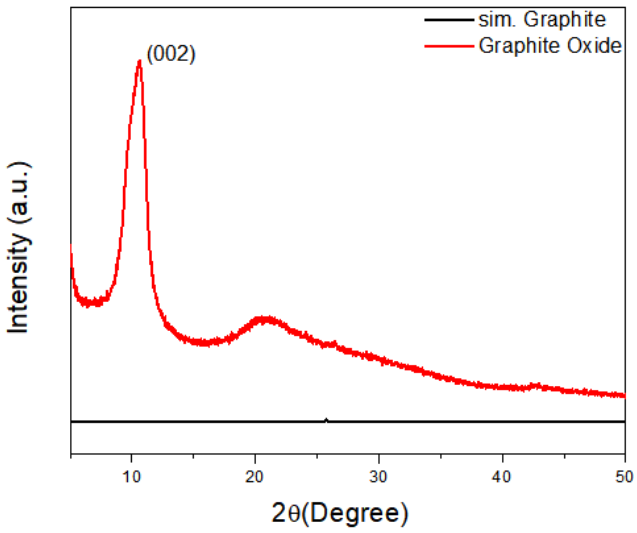

Figure 4.49: Pure GO

(b) *Graphite oxide analysis and reduced graphene data analysis*

The XRD pattern in Figure 4.50 shows the crystalline structure and phase of the GO and rGO nanostructures. Sharp diffraction peaks with no extra signal confirmed the formation of crystalline phase nanocomposite material. Functional groups were removed from the surface of GO during the thermal treatment to obtain reduced graphene. The absence of significant diffraction peak in the XRD pattern of rGO indicates the exfoliated feature of rGO after the thermal reduction of GO. Notably, no graphene diffraction peaks could be seen in the nanostructures of ZnS/graphene. This may be because graphene has a poor crystallinity and a low diffraction intensity in these materials.

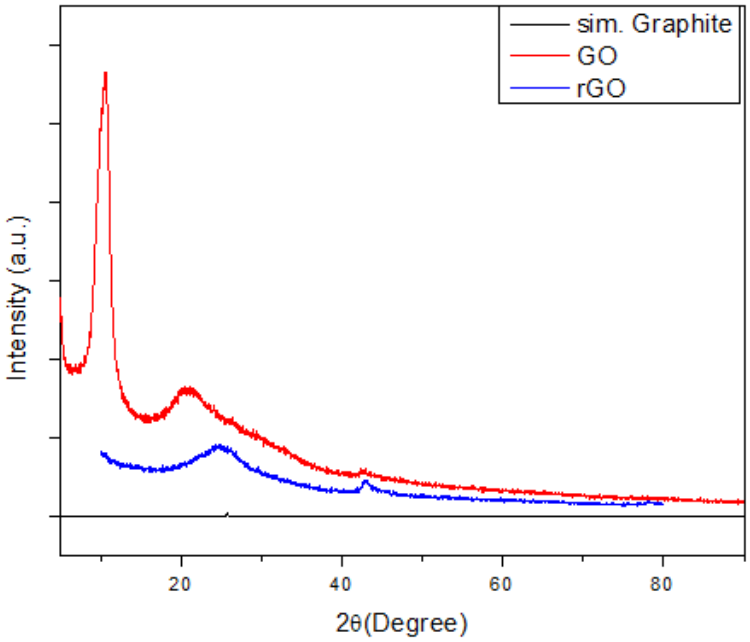

Figure 4.50: Pure GO-rGO

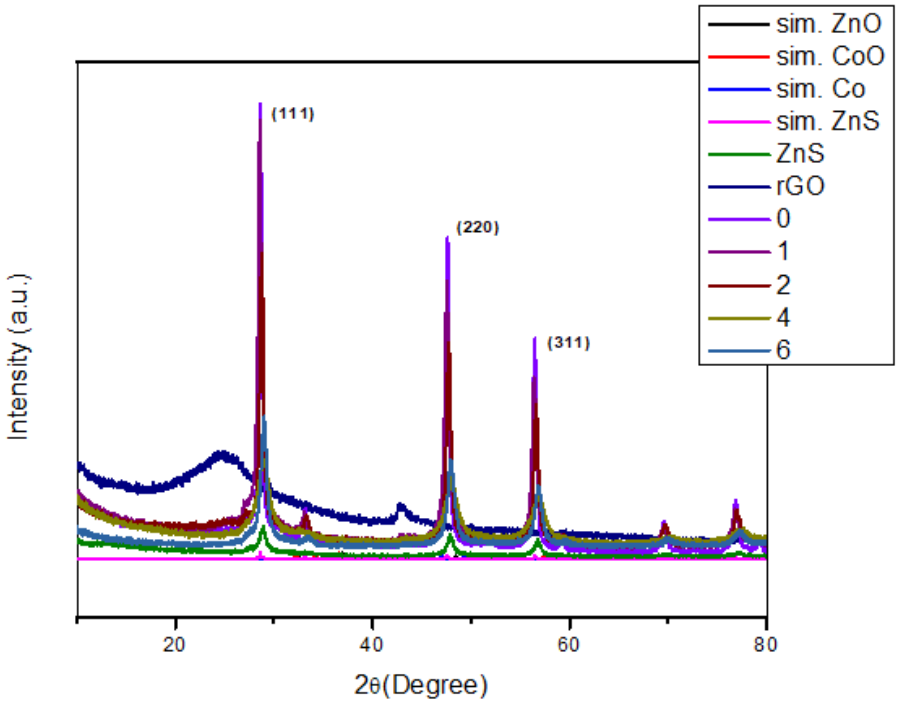

Figure 4.51: XRD patterns of pure Co-ZnS-rGO nanostructures with simulated ZnS, ZnO, Co and CoO database structures

(c) *ZnS-rGO data analysis*

The Figure 4.52 describes powder XRD patterns of the synthesized GO with rGO and ZnS NSs. The aforementioned patterns exhib-

ited a comparable level of symmetry to the modelled ZnS, ZnO, Co, and CoO database structures as seen in Figure 4.51. The crystallographic planes (111), (220) and (311) for the hexagonal system were given to the Bragg's peak at $2\theta = 28.71°, 47.59°, 56.46°$. The absence of the typical rGO signal in the XRD pattern for ZnS-rGO and Co-ZnS-rGO NSs could possibly be caused by the formation of ZnS NSs between rGO layers, which would damage the rGO's regular layered structure and so the graphene was incorporated into the ZnS lattice.

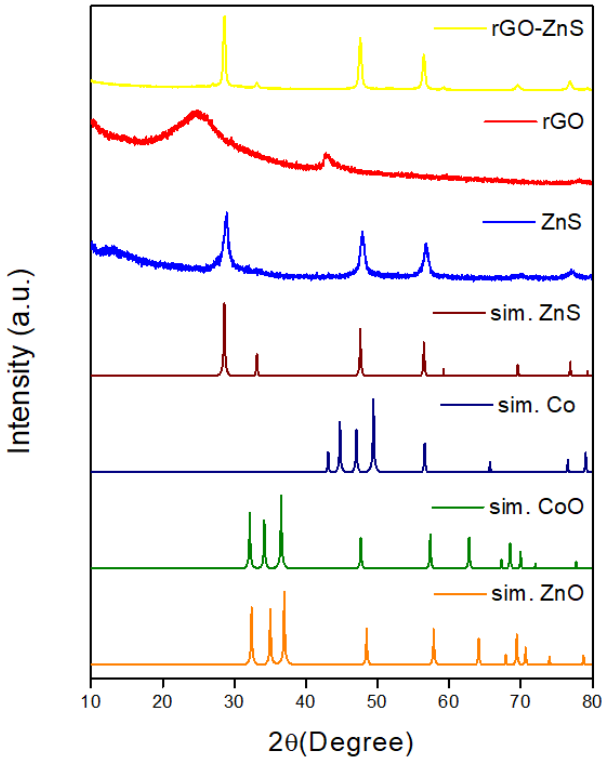

Figure 4.52: Pure ZnS-rGO

(d) *1Co-ZnS-rGO*

The Figure 4.53 shows powderXRD patterns of the synthesized GO, rGO and 1% reduced cobalt doped ZnS NSs. The aforementioned patterns exhibit a comparable level of symmetry to the modelled ZnS, ZnO, Co, and CoO database structures. The crystallographic planes (111), (220) and (311) for the hexagonal system were given

to the Bragg's peak at $2\theta = 28.65°, 47.73°, 56.66°$. The ZnS matrix was successfully filled with Co^{2+} ions, which occupied the Zn^{2+} sites. The absence of the typical rGO signal in the XRD pattern for ZnS-rGO and Co-ZnS-rGO NSs could possibly be caused by the formation of zinc sulfide NSs between rGO layers, which would damage the rGO's regular layered structure and so the graphene is incorporated into the cobalt doped ZnS lattice.

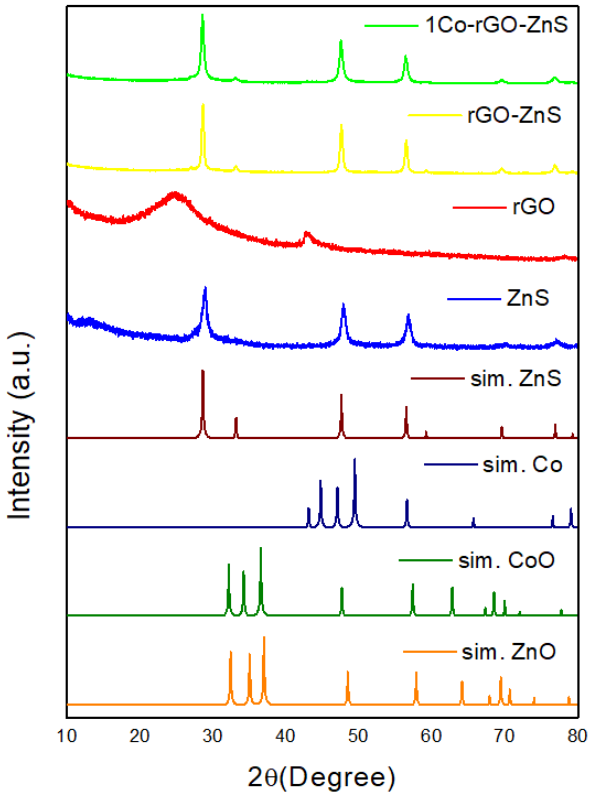

Figure 4.53: Pure ZnS-1Co-ZnS-rGO XRD analysis

(e) *2Co-ZnS-rGO*

The Figure 4.54 shows powder XRD patterns of the synthesized GO, rGO and 1, 2% of cobalt doped ZnS-rGO NSs. The aforementioned patterns exhibited a comparable level of symmetry to the modelled ZnS, ZnO, Co, and CoO database structures. The crystallographic planes (111), (220), and (311) for the hexagonal system were given to the Bragg's peak at $2\theta = 28.79°, 47.77°, 56.68°$

for 2% respectively. The ZnS matrix was successfully filled with Co^{2+} ions, which occupied the Zn^{2+} sites. The absence of the typical rGO signal in the XRD pattern for ZnS-rGO and Co-ZnS-rGO NSs could possibly be caused by the formation of ZnS NSs between rGO layers, which might have damaged the rGO's regular layered structure and so the graphene was incorporated into the cobalt doped ZnS lattice.

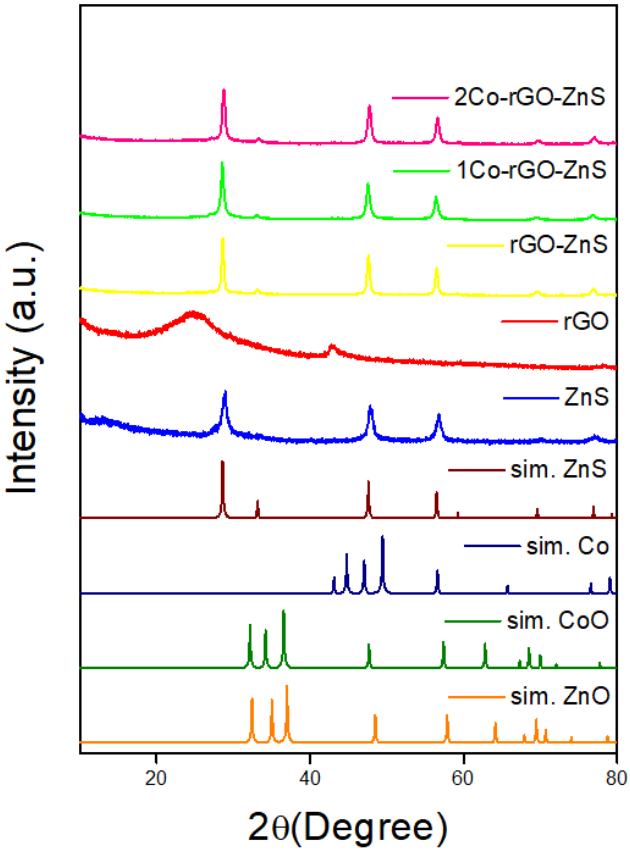

Figure 4.54: Pure ZnS-2Co-ZnS-rGO

(f) *4Co-ZnS-rGO*

The Figure 4.55 describes the powder XRD patterns of the synthesized GO, rGO and 1, 2 and 4% cobalt doped ZnS-rGO NSs. The aforementioned patterns exhibited a comparable level of symmetry to the modelled ZnS, ZnO, Co, and CoO database structures. The crystallographic planes (111), (220) and (311) for the hexagonal system were given to the Bragg's peak at $2\theta = 28.89°, 47.56°, 56.79°$

respectively. The ZnS matrix was successfully filled with Co^{2+} ions, which occupied the Zn^{2+} sites. The absence of the typical rGO signal in the XRD pattern for ZnS-rGO and Co-ZnS-rGO NSs could possibly be caused by the formation of ZnS NSs between rGO layers, which would have damaged the rGO's regular layered structure and so the graphene was incorporated into the cobalt doped ZnS lattice. The XRD investigation suggested that the doping elements of cobalt were properly substituted into Zn-S lattice, as there were no secondary or impurity phases identified this was evident since there was absence of peaks due to cobalt, cobalt sulfide, or any other contaminant indicating that cobalt may have been substituted into the ZnS lattice.

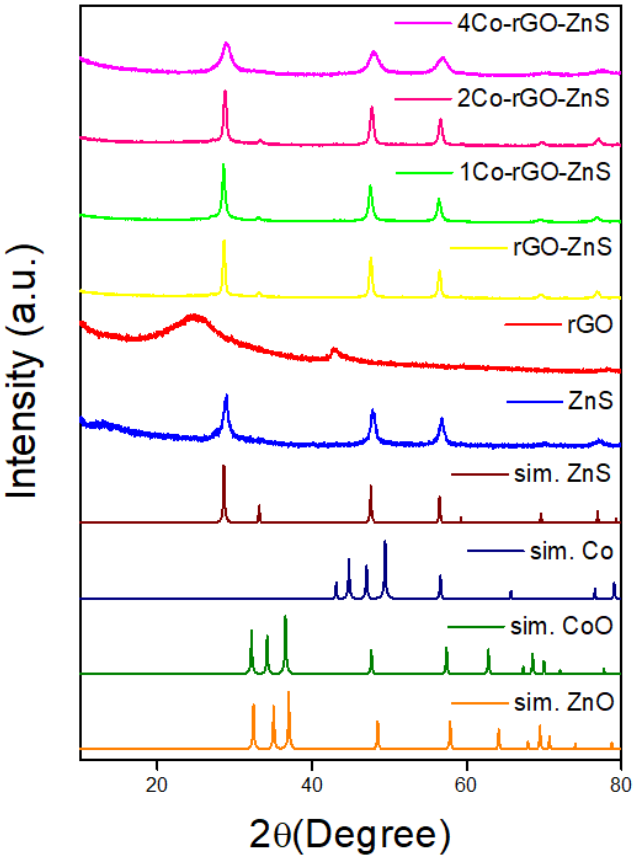

Figure 4.55: Pure ZnS-4Co-ZnS-rGO

(g) *6Co-ZnS-rGO*

The Figure 4.56 describes the powder XRD patterns of the syn-

thesized GO, rGO and 1, 2, 4 and 6% cobalt doped ZnS-rGO NSs. These patterns exhibited a comparable level of symmetry to the modelled ZnS, ZnO, Co, and CoO database structures. The crystallographic planes (111), (220), and (311) for the hexagonal system were given to the Bragg's peak at $2\theta = 28.96°, 47.97°, 56.84°$ respectively. The ZnS matrix was successfully filled with Co^{2+} ions, which occupied the Zn^{2+} sites. The absence of the typical rGO signal in the XRD pattern for ZnS-rGO and $Co_xZn_{1-x}S$ rGO nanostructures could possibly be caused by the formation of ZnS NSs between rGO layers, which would damage the reduced GO regular layered structure and so the graphene was incorporated into the cobalt-doped ZnS lattice.

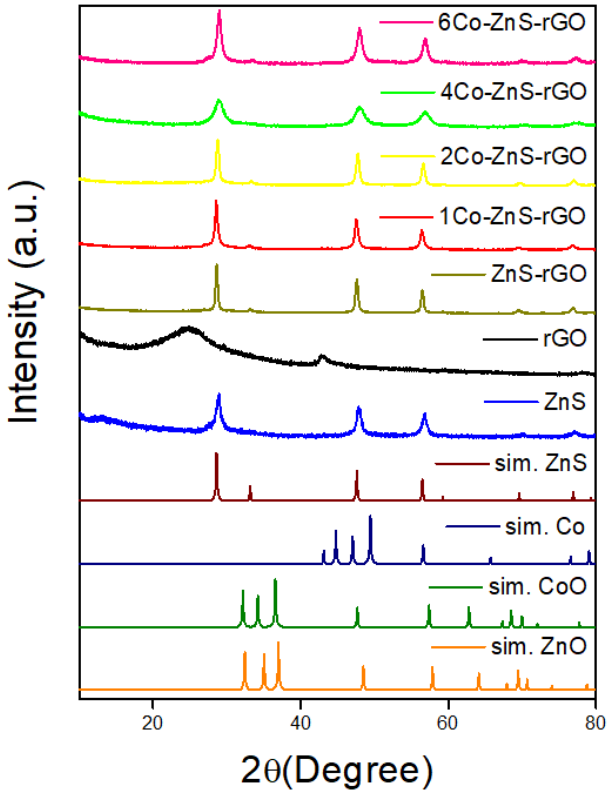

Figure 4.56: Pure ZnS-6Co-ZnS-rGO

The peak positions of the cobalt doped samples significantly shift upward in the 2θ values indicates that Co^{2+} (0.58 Å) has a smaller ionic radius compared to that of Zn^{2+} (0.74Å) in the ZnS Zaware

et al. (2017); L. Wang et al. (2017); Gurugubelli et al. (2022). Due to the ionic radius of cobalt being slightly smaller (0.58) than that of Zn, the peak positions of samples that contain cobalt exhibit a little shift towards lower 2θ values as depicted in Figure 4.57. The results mentioned above show that Co^{2+} ions were successfully incorporated into the ZnS matrix and occupied the Zn^{2+} sites. On the other hand, it is observed that the replacement of Zn^{2+} ions by Co^{2+} ions result in decrease in intensity of the XRD peaks, which implies that the degree of crystallinity of the samples decreases. Dopant addition causes changes in the peak intensity and position. Peak broadening indicates nanocrystal formation in the samples and broadening increases with the substitution of Zn^{2+} ions by Co^{2+} ions. The broad diffraction peaks may have been obtained due to the small particle effect. At a low angle, peak broadening is critical for particle size calculation.

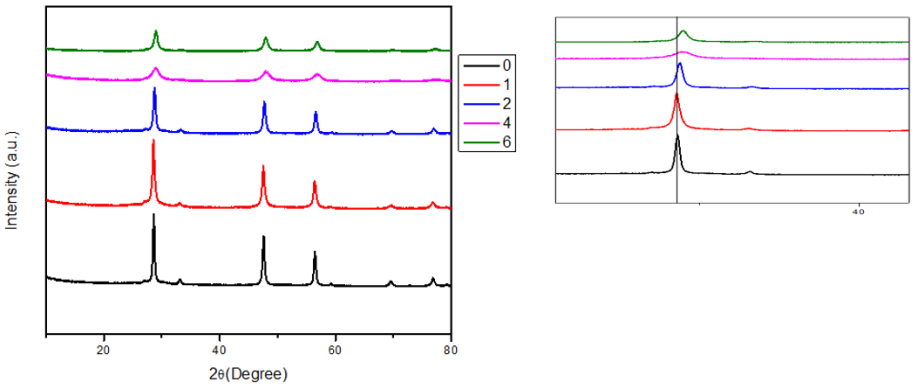

Figure 4.57: XRD patterns of as-prepared pure Co-ZnS-rGO NSs as a function of dopant concentration

The preferred orientation was along (111) plane due to its highest peak intensity throughout the entire samples. The attained three XRD peaks are matched well with simulated data files (CIF) which reflected that all the synthesized samples possessed the cubic structure of ZnS.

(h) *Crystallite Sizes*

The average crystalline size was calculated using Debye-Scherrer formula Viswanath et al. (2014) as shown in Equation 4.7. where D is the crystal size of the catalyst, k the X-ray wavelength, β the Full Width at Half Maximum (FWHM) of the diffraction peak (radian), K is a constant (0.89) and θ is the diffraction angle at the maximum. The incorporation of Co elevates the FWHM which reflects the shrinkage of crystallite size. As a result, the current XRD patterns validates the phase singularity of the manufactured samples without the need for further phases. In Ni added ZnS nanostructures, the same shift along higher diffraction angles was reported by Kaur et al. (2016).

$$D = \frac{K\alpha}{\beta cos\theta} \tag{4.7}$$

The size was confirmed with SEM which also revealed the spherical structure of particles. Substitution of cobalt into the ZnS lattice is evident by the absence of any peaks corresponding to either cobalt, cobalt sulfide or any other impurity. The FWHM of XRD peaks for all the samples have almost the same value revealing that the deposited NSs are comprised of crystallites with almost equal sizes as shown in Table B.1. The following Equations; 4.8 and Equation 4.9 were used to calculate the lattice d spacing and lattice constant respectively.

$$d_{hkl} = \frac{\lambda}{2sine\theta} \tag{4.8}$$

$$d_{hkl}\sqrt{h^2 + k^2 + l^2} \tag{4.9}$$

FWHM of the XRD peaks for each sample was roughly the same, indicating that the crystallites in the formed NSs were of almost comparable size. The Scherrer equation yields a crystallite size of 23.5, 18.5, 16.7, 16.2 and 11.1 nm on average for the $Co_xZn_{1-x}S$ rGO nanostructures at x = 0, 1, 2, 4, 6 respectively as described in Table B.2.

(i) **Lattice Parameters** After doping, it was discovered that the lattice parameter a value was lower at values of 5.394, 5.387, 5.377, 5.75, and 5.354 Å at x = 0, 1, 2, 4, 6 than it was in pure ZnS which was a standard value of 5.406 Å. With the exception of the anticipated change in the structure of ZnS caused by cobalt doping, the observed decrease in lattice constant was sufficiently close to the stated values.

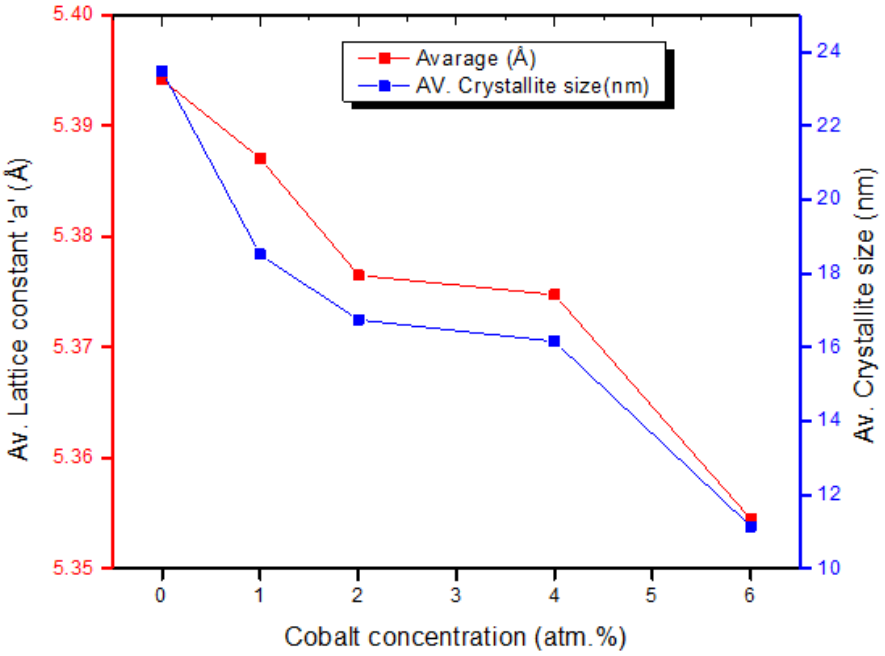

Figure 4.58: Lattice parameter and crystalline size versus Cobalt concentration obtained by Scherrer

All of the samples' FWHM of XRD peak values are nearly identical, demonstrating that the crystallite sizes in the deposited thin films are nearly comparable. The fluctuation in lattice constant as a function of

dopant concentration is as a result of the decrease of size due to the generation of lattice disorder by the Co addition as shown in Figure 4.58. This is a typical alloying behaviour, which arises due to the difference in the lattice constant as well as the atomic radii of Co and Zn. This is also well discussed by Reddy et al. (2014); M. S. Akhtar et al. (2015); W. Wang et al. (2021).

XRD data confirmed single phase nature of polycrystalline samples and revealed that complete solid solution was formed between cobalt and zinc. Origin software was used to determine detail structural analysis of the samples and lattice parameters of polycrystalline $Co_xZn_{1-x}S$ rGO NSs. Lattice parameter and unit cell volume decreased monotonically with increased cobalt atomic content. FWHM of all the synthesized $Co_xZn_{1-x}S$ rGO NSs at x = 0, 1, 2, 4, 6 for the most intense peaks of 111, 220 and 311 were determined. The Scherrer method was used to analyze X-ray patterns in order to calculate the crystallite size and the lattice parameters. The presence of crystalline cubic ZnS NSs with average crystallite sizes in the range of (11-23) nm was confirmed by the XRD pattern.

The calculated lattice parameters were also in the range of (5.35-5.39) Å which were less than that of the standard lattice parameter of 5.406 Å from the JCPD software database. Discussions on the physical qualities, determining the phase composition, structure and particle size was crucial because the structure and XRD pattern of CoS and Co are so dissimilar from those of ZnS, this means that, there isn't any CoS or Co in the precipitates. When the matching concentration ratio was low in $Co_xZn_{1-x}S$ rGO nanostructures, as shown by XRD, there was no discernible Co or CoS signal, otherwise the concentration of Co^{2+} was quite low. This was explained due to the fact that there were fewer lattice planes in these nanocrystals than in the bulk, the peaks in the

diffraction pattern were broader.

The expansion of the peak may also have resulted from the crystal structure's micro-straining caused by defects like dislocation and twinning among other things. Because nanocrystals form spontaneously during chemical reactions, it was thought that these defects were related to materials that were chemically produced and the chemical ligands consequently have very little time to disperse to an energetically advantageous location. It might also happen if an atom doesn't have enough energy to migrate to the right location during the crystallite's formation. After 4 mole percent Co^{2+} ions doped ZnS samples, the XRD peaks becomes larger (wide) with the increase of the Co^{2+} ions dopant which may largely depends on to the alloy fluctuation, amorphous state and increased lattice stress and string in samples.

2. **Chemical vibrations analysis of cobalt doped ZnS decorated with graphene**

FTIR was used to identify certain chemical vibrations present in the material Griffiths (1983); Berthomieu & Hienerwadel (2009); A. Dutta (2017). This characterisation analysis was fairly sensitive, accurate and quick B. C. Smith (2011). The FTIR analysis process involved exposing materials to infrared (IR) radiation. The atomic vibrations of a molecule in the sample were then affected by the IR radiations, leading to a specific energy absorption and/or transmission. As a result, the spectrum resulted to "absorption versus wave number" data. The IR spectrum was divided into three wave number regions: far-IR spectrum $< 400cm^{-1}$, mid-IR spectrum $400 - 4000cm^{-1}$ and near-IR spectrum $4000 - 13000cm^{-1}$. The mid-IR spectrum was the most widely used in the sample analysis, but far and near IR spectrum also contributed in providing information about the samples analyzed.

(a) *ZnS-rGO FTIR data analysis*

Figure 4.59 describes the FTIR analyses of pure ZnS-rGO in various ratio combinations. The reduced graphene oxide IR spectra show large peaks at $3401cm^{-1}$. Alcohols may be an O-H functional group, according to this. At $1735cm^{-1}$, the C=O functional group is observed at its highest. For the C-O stretching vibration, AA strongly decreased GO, resulting in several peaks shifting dramatically between $(1644 - 820)cm^{-1}$. This suggests that AA has a good reduction ability. However, other peaks that corresponded to the oxygen functionalities of graphene oxide, such as carbonyl, hydroxyl, carboxyl and epoxy groups, may have almost disappeared upon reduction Chudziak et al. (2023); CHEN (2016). The GO spectrum's large and high absorption peak at $3401cm^{-1}$ was ascribed to the O-H stretching vibrations. The characteristic stretching vibrations of carboxyl -C=O and -C-O were attributed to the spectral bands at $1735cm^{-1}$ and $1222cm^{-1}$, respectively. $b \approx 1269cm^{-1}$ was the peak that corresponded to the aromatic $-C = C$.

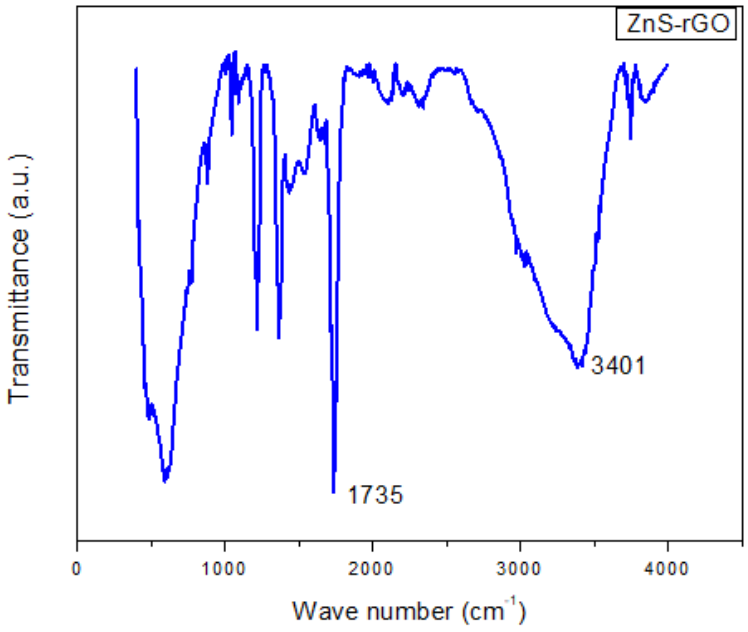

Figure 4.59: FTIR spectra of ZnS decorated with graphene (ZnS-rGO)

(b) *1Co-ZnS-rGO FTIR data analysis*

Figure 4.60 displayed the FTIR analysis of pure $Co_{0.01}Zn_{0.99}S$ rGO NSs in different ratios. Reduced level graphene oxide infrared spectra show prominent peaks at approximately $3422cm^{-1}$. Alcohols are shown as the O–H functional group. However, at $1735cm^{-1}$, the C=O functional group was most noticeable. As the graphene oxide was drastically reduced by AA, some of the peaks reflecting the oxygen functionalities of GO, such as the carbonyl, hydroxyl, carboxyl, and epoxy groups, may have essentially disappeared. Conversely, additional peaks at $1644cm^{-1}$ and $820cm^{-1}$ shifted significantly for the C-O stretching vibration, suggesting that it may be successfully reduced CHEN (2016). The large and elevated absorption peak observed at $3422cm^{-1}$ in the GO spectrum may have been caused by the O-H stretching vibrations. Carboxyl -C=O and -C-O have characteristic stretching vibrations, which may be responsible for the spectral bands at $1735cm^{-1}$ and $1222cm^{-1}$, respectively.

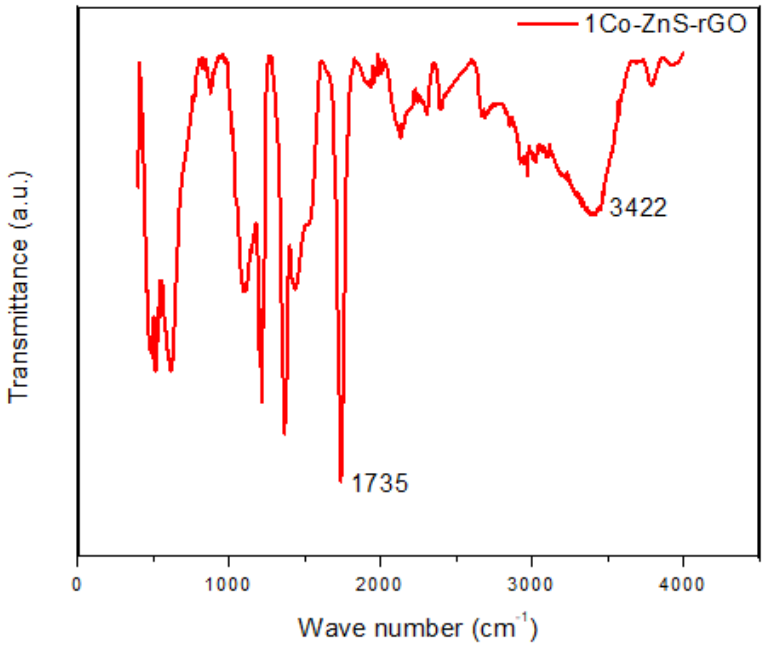

Figure 4.60: FTIR spectra of 1Co doped ZnS decorated with Graphene ($Co_0.01Zn_0.99S$ rGO) NSs

(c) *2Co-ZnS-rGO FTIR data analysis*

The FTIR analysis of pure $Co_{0.02}Zn_{0.98}S$ rGO NSs in various ratios is shown in Figure 4.61. Large peaks can be seen in the reduced graphene oxide IR spectra at $3430cm^{-1}$ indicating that alcohols are an O-H functional group. Even at $1735cm^{-1}$, the maximum value, the C=O functional group was still visible. Some peaks for the C-O stretching vibration saw a considerable shift between $1644 - 820cm^{-1}$, suggesting their good reduction capacity, as a result of the strong reduction of the graphene oxide by AA. On the other hand, it's plausible that the peaks that represent the oxygen functions of GO—such as the epoxy, carboxyl, hydroxyl, and carbonyl groups—nearly disappeared during reduction. The O-H stretching vibrations were identified as the cause of the massive and high absorption peak in the GO spectra at $3430cm^{-1}$. The characteristic carboxyl stretching vibrations of -C=O and -C-O were ascribed to the spectral bands located at $1735cm^{-1}$ and $1222cm^{-1}$ respectively.

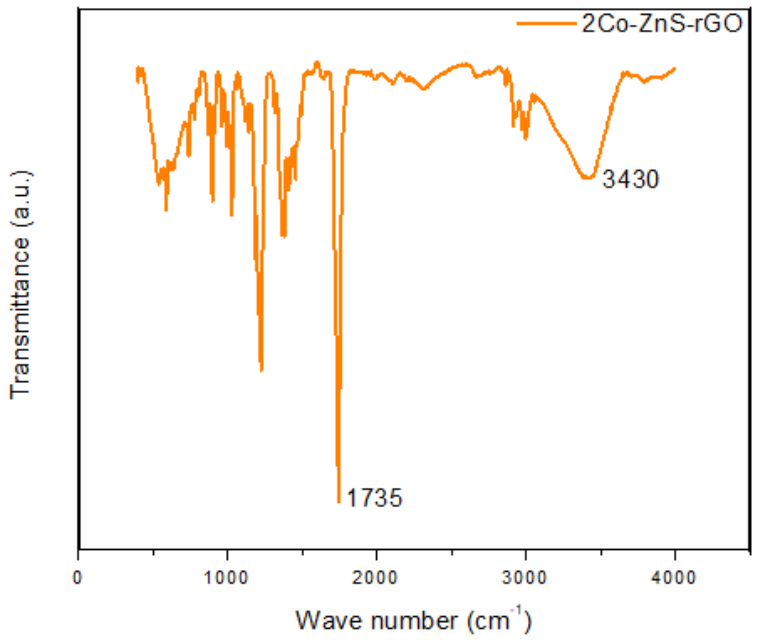

Figure 4.61: FTIR spectra of 2Co doped ZnS decorated with graphene ($Co_0.02Zn_0.98S$ rGO) NSs

(d) *4Co-ZnS-rGO FTIR data analysis*

The FTIR tests in its purest form of $Co_{0.04}Zn_{0.96}S$ rGO NSs in a range of ratios is shown in Figure 4.62. The reduced graphene oxide IR spectra show strong peaks at $3295cm^{-1}$ and the O-H functional group of the alcohols were illustrated. At $1735cm^{-1}$, its maximum, the C=O functional group was still discernible. Some peaks for the C-O stretching vibration showed a large shift between $(1644-820)cm^{-1}$, indicating that the GO had a good ability to reduce, since AA may have strongly reduced graphene oxide. These peaks corresponded to the oxygen functionalities of GO, such as carbonyl, hydroxyl, carboxyl, and epoxy groups, and may have almost vanished upon reduction CHEN (2016); Baye et al. (2020). The origin of the huge and high absorption peak in the GO spectrum at $3295cm^{-1}$ was the O-H stretching vibrations. The stretching vibrations of carboxyl -C=O and -C-O were identified with the spectral bands at $1735cm^{-1}$ and $1222cm^{-1}$, respectively.

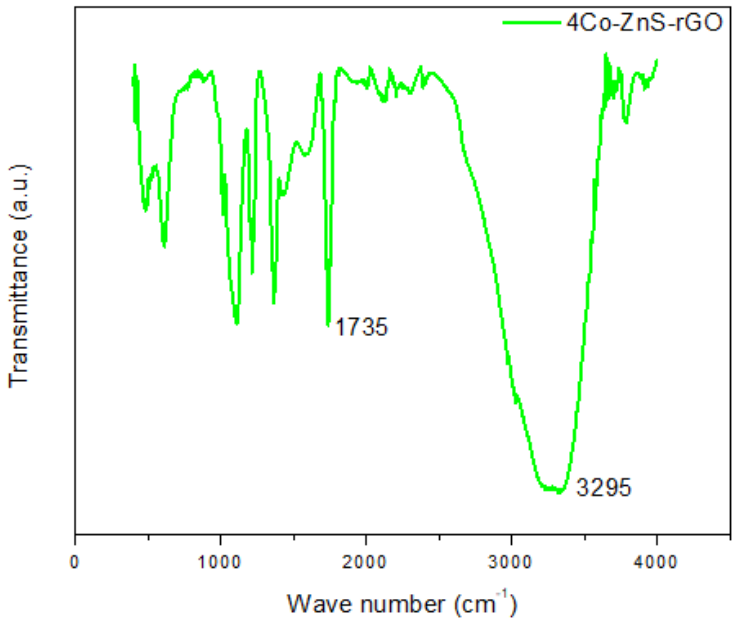

Figure 4.62: FTIR spectra of 4Co doped ZnS decorated with graphene ($Co_0.04Zn_0.96S$ rGO) NSs

(e) *6Co-ZnS-rGO FTIR data analysis*

The FTIR analysis of a combination of $Co_xZn_{1-x}S$ rGO NSs in a variety of ratios and reduced graphene in its purest form is shown in Figure 4.63. Large peaks may be observed in the reduced graphene oxide IR spectra at $3376cm^{-1}$. This suggests that alcohols are an O-H functional group. Nonetheless, the C=O functional group was clearly visible at its maximum value of $1735cm^{-1}$. The strong reduction of graphene oxide by ascorbic acid resulted in a significant shift of some peaks for the C-O stretching vibration between $(1644 - 820)cm^{-1}$, indicating that AA had a good ability to reduce graphene oxide. However, other peaks that corresponded to the oxygen functionalities of GO, such as carbonyl, hydroxyl, carboxyl, and epoxy groups, may have almost completely disappeared upon reduction Baye et al. (2020); CHEN (2016). The O-H stretching vibrations were responsible for the enormous and strong absorption peak observed in the GO spectra at $3376cm^{-1}$. The spectral bands located at $1735cm^{-1}$ and $1222cm^{-1}$, were attributed to the distinctive stretching vibrations of carboxyl -C=O and -C-O respectively. The peak corresponding to the aromatic $-C = C$ was $b \approx 1269cm^{-1}$.

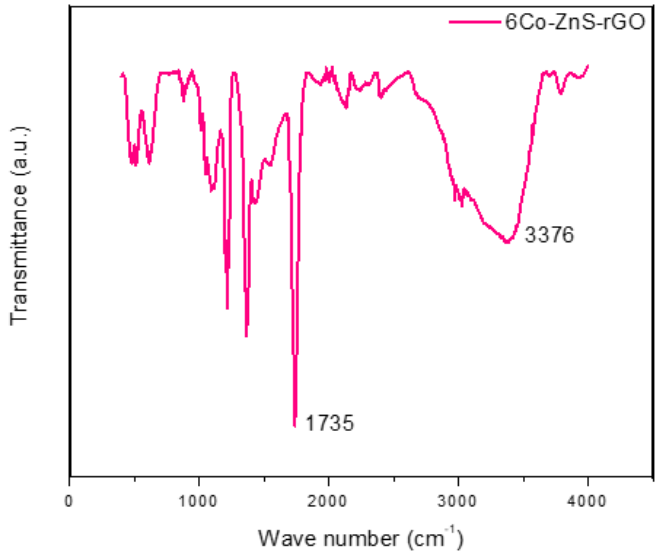

Figure 4.63: FTIR spectra of 6Co doped ZnS decorated with graphene ($Co_0.06Zn_0.94S$ rGO) NSs

(f) *Combined Co-ZnS-rGO FTIR data analysis*

FTIR was the best technique to examine the chemical bonding in the samples and to identify the organic group of the as prepared Cobalt doped ZnS decorated with graphene NSs. The graphene sheets were crucial in helping ZnS NSs to develop and distribute on their surface preventing the sheet's agglomeration Thakre et al. (2021); Qin et al. (2017). FTIR spectra confirmed the presence of $Co_xZn_{1-x}S$ rGO nanostructures as displayed in Figure 4.64. An IR spectrum of reduced graphene oxide revealed large peaks at $3401cm^{-1}$, $3422cm^{-1}$, $3295cm^{-1}$ and $3376cm^{-1}$ confirming C-H bonding. However, the C=O functional group was evident at its highest of $1735cm^{-1}$ in all samples. The peaks corresponding to the oxygen functionalities of GO, such as carbonyl, hydroxyl, carboxyl and epoxy groups may have disappeared upon reduction, whereas some other peaks underwent a substantial shift between $1644cm^{-1}$ to $820cm^{-1}$ for the C-O stretching vibration due to the strong reduction of the graphene oxide by ascorbic acid indicating its good reduction ability Reddy et al. (2014).

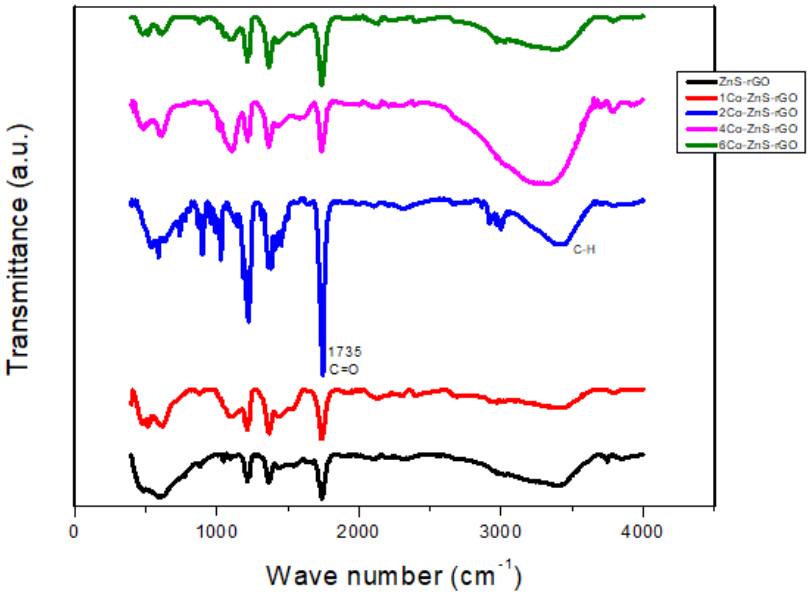

Figure 4.64: FTIR spectra of Co-ZnS-rGO nanostructures

The broad absorption bands for all samples between 1856 to $2790cm^{-1}$ were

attributed to OH stretching vibration, which denoted the persistence of water absorbed on nanostructures surface Kuppayee et al. (2012). The feeble and weak absorption band centered around $875cm^{-1}$ corresponds to the defect states induced by Co substitution in ZnS lattice Coates (1996); Qadri et al. (1999). Zn-S stretching vibrations were caused by the strong bands at 1039 to $1584cm^{-1}$ Rema Devi et al. (2007). The bands that correlated to Zn-S exhibited the best degree of concordance with previous research Y. Tong et al. (2008). O-H stretching vibrations accounted for the broad and strong absorption peak located at $(3401, 3422, 3430, 3295$ and $3376)cm^{-1}$ in the GO spectrum. The characteristic stretching vibrations of carboxyl -C=O and -C-O were attributed to the spectral bands at $1735cm^{-1}$ and $1222cm^{-1}$, respectively. The aromatic $-C = C$ was linked to the peak at $b \approx 1269cm^{-1}$. Functional groups containing oxygen were present on the GO nanosheets, as indicated by the peaks at $1039cm^{-1}$ (alkoxy -C-O) and $1222cm^{-1}$ (epoxy -C-O). This results were also consistent with that of Sujiono et al. (2020).

3. **Chemical and physical characteristics analysis of cobalt doped ZnS decorated with graphene**

RS was an effective non-destructive method for characterizing $Co_xZn_{1-x}S$ rGO NSs, identifying their phases and transitions thus provided some insights about the interactions at the nanoscale Roy et al. (2021). Raman scattering phenomenon has been widely used to study the doping, morphology, size, shape, and orientation of nanomaterials as well as their amorphous or crystalline areas Popović et al. (2011); Drescher & Kneipp (2012). The research of conductivity, structural characteristics and composition of nanostructured materials based on carbon was facilitated by the application of Raman bands Bokobza et al. (2014); Y. Wang et al. (1990). Experimentally, the method was easily accessible and done both at room temperature and ambient pressure. RS depends on a wide range of experimental factors, including light polarization, photon energy, temperature, pressure and en-

vironmental changes Jones et al. (2019). One important metric that could be acquired from RS that explains about the defects and structural disorder was the $\frac{Id}{Ig}$ ratio, which is sometimes referred to as the D band to G band intensity ratio. The disorder induced peak is represented by the D band, while the first-order scattering from sp^2 carbon atoms is represented by the G band. Depending on the fitting approach, the intensities of the bands was found by utilizing peak height. Important details regarding the structural disorder and defects in the cobalt doped ZnS decorated with graphene were provided by the Equation 2.4 ratio. Whereas a lower ratio denoted fewer faults and a more ordered structure, a greater ratio implied a higher amount of structural disorder and defects.

(a) *ZnS-rGO RS data analysis*

The ZnS-rGO Raman shift is shown in the spectra Figure 4.65. The two primary, noticeable bands of GO, are situated at $\approx$ 1331 and $1586cm^{-1}$, respectively, reflecting the D and G bands of graphene. While high frequency carbon-hydrogen (C-H) vibrations were observed at roughly $1233 - 1500cm^{-1}$, low frequency carbon-carbon (C-C) vibrations were found at roughly $650 - 1233cm^{-1}$. There was an additional C=C, C=O double bond at $1500 - 2000cm^{-1}$. Primary bands were centered at stretching vibrations since hydrogen was lighter than carbon and its vibrations occurs more frequently. At a frequency of roughly $1705cm^{-1}$, the spectra also displayed vibrations of two carbon atoms joined by a strong double bond (C=C). The strength of the bond also affects bond vibration rates. The bands at $200 - 650cm^{-1}$ region appeared to be created by the same chemicals, with the exception of the band at $429cm^{-1}$, which was caused by ZnS spectra light. The D peak formed as a result of intrinsic structural faults, dangling bonds and disruptions to the symmetric hexagonal graphitic lattice. The G band of phonon vibrations in sp^2 bonded carbon materials was linked to the E_{2g} mode.

The D band at $1331cm^{-1}$ became prominent, suggesting that the sheets may have undergone extensive oxidation and that the sp^2 character may have been obliterated. Equation 2.4, gave a value of 0.839 intensity ratio which was used to assess the average size and degree of disorder of the sp^2 domains of graphite materials.

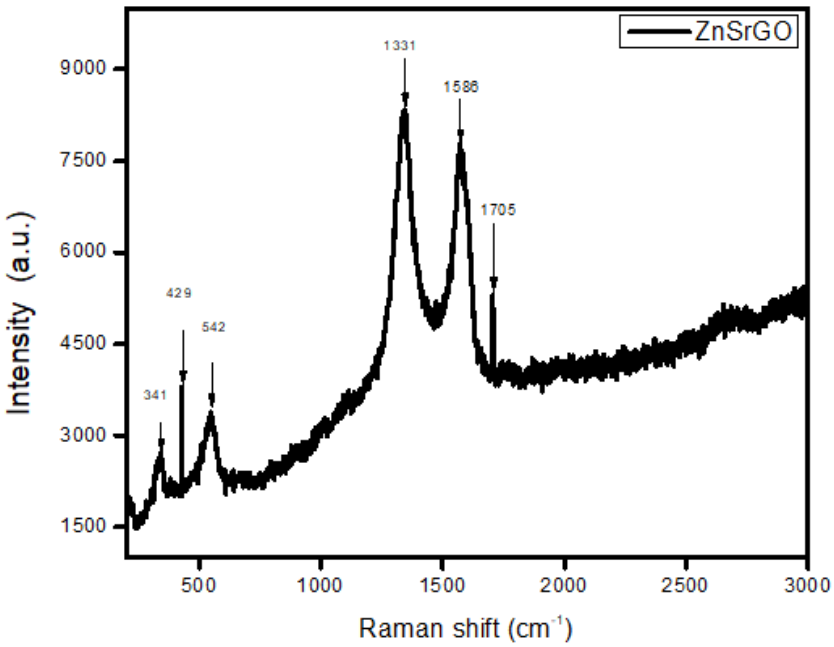

Figure 4.65: Raman spectra of ZnS-rGO nanostructures

(b) *1Co-ZnS-rGO RS data analysis*

The Raman shift of $Co_0.01Zn_0.99S$ rGO NSs was identified in the spectra shown in Figure 4.66. The two primary, noticeable bands of GO, were situated at approximately $1334cm^{-1}$ and $1582cm^{-1}$, respectively, reflecting the D and G bands of graphene. Low frequency carbon-carbon (C-C) vibrations were discovered at $\approx 650 - 1233cm^{-1}$, while high frequency carbon-hydrogen (C-H) vibrations were recorded at roughly $1233 - 1500cm^{-1}$. A second C=C, C=O double bond was present at $1500 - 2000cm^{-1}$ main bands concentrated at stretching vibrations and the vibrations of hydrogen were more frequent than those of carbon because of its smaller weight. The spectra showed the vibra-

tions of two carbon atoms connected by a strong double bond (C=C) at a frequency of about $1705cm^{-1}$. This occurred at a higher frequency of C-C at $650-1233cm^{-1}$, in contrast to a weaker single bond between two carbon atoms. Bond vibration rates were also influenced by the bond strength. With the exception of the band at $430cm^{-1}$, which was induced by ZnS spectra light, the bands in the $200-650cm^{-1}$ area seem to have been produced by the same chemicals. Intrinsic structural defects, dangling bonds, and disruptions to the symmetric hexagonal graphitic lattice are responsible for the formation of the D peak. The G band in sp^2 bonded carbon materials was linked to the E_2g mode of phonon vibrations. The D band at $1334cm^{-1}$ became prominent, suggesting that the sheets may have undergone extensive oxidation and that the sp^2 character may have been exterminated. The intensity ratio of the D and G bands, yielded an estimate of the average size and degree of disorder of 0.843 for the sp^2 domains of graphite materials.

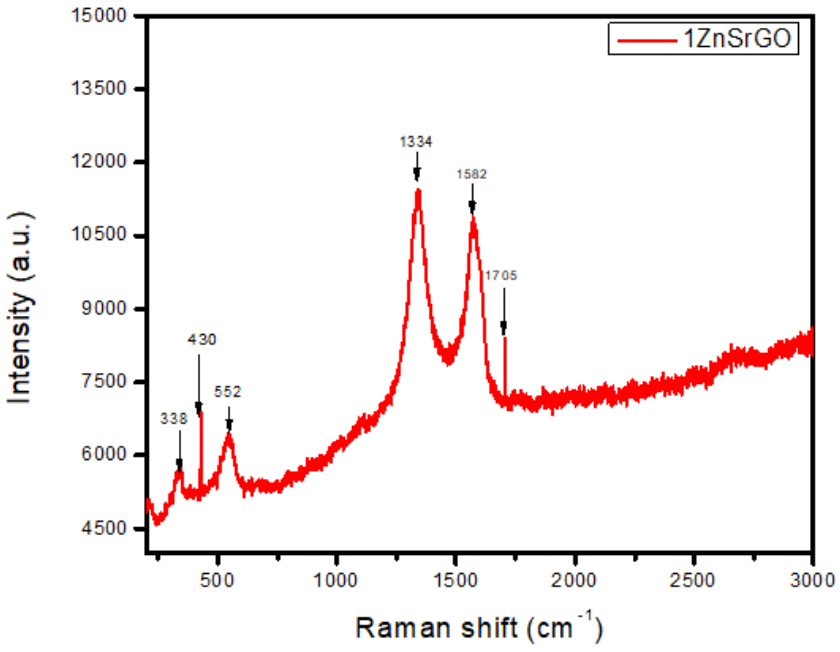

Figure 4.66: Raman spectra of 1Co-ZnS-rGO nanostructures

(c) *2Co-ZnS-rGO RS data analysis*

The Raman shift of $Co_{0.02}Zn_{0.98}S$ rGO NSs was identified in the spec-

tra shown in Figure 4.67. The two prominent, primary bands of GO, are situated at approximately 1338 and $1576cm^{-1}$, respectively, representing the D and G bands of graphene. While high frequency carbon-hydrogen (C-H) vibrations were observed at roughly $1233 - 1500cm^{-1}$, low frequency carbon-carbon (C-C) vibrations were found at roughly $650 - 1233cm^{-1}$. There was also an additional C=C, C=O double bond at $1500 - 2000cm^{-1}$. Hydrogen vibrates at a higher frequency than carbon because it is lighter than carbon. The vibrations of two carbon atoms connected by a strong double bond (C=C) were visible in the spectra with a frequency of about $1706cm^{-1}$. Compared to two carbon atoms connected by a weaker single bond, this occured at a larger frequency of C-C of $650 - 1233cm^{-1}$. Bond vibration rates were impacted by bond strength as well. The emergence of the D peak was caused by internal structural defects, dangling bonds and edge defects that disturb the symmetric hexagonal graphitic lattice. The E_{2g} mode of phonon vibrations was linked to the G band in sp^2 bonded carbon materials. There was a pronounced D band at $1338cm^{-1}$, which suggested that there were defects in the sheets due to substantial oxidation and the destruction of the sp^2 character. The intensity ratio of the D and G bands Equation 2.4, yielded a value of 0.849 when used to assess the average size and degree of disorder of the sp^2 domains of graphite materials at large.

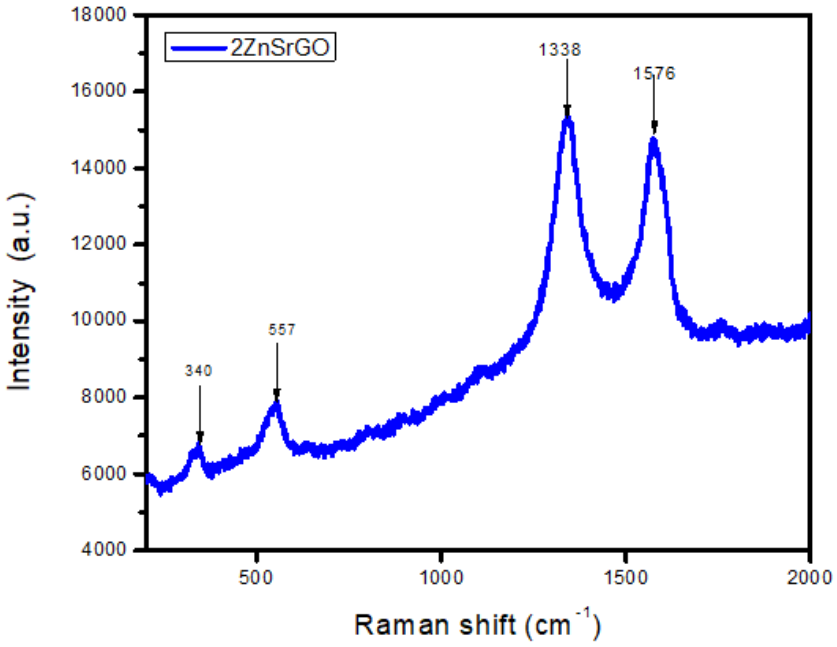

Figure 4.67: Raman spectra of 2Co-ZnS-rGO nanostructures

(d) *4Co-ZnS-rGO RS data analysis*

The Raman shift at $Co_{0.04}Zn_{0.96}S$ rGO NSs was observed in the spectra shown in Figure 4.68. The two visible, primary bands of GO, are located in between $1343cm^{-1}$ and $1578cm^{-1}$, respectively, representing the D and G bands of graphene. Low frequency carbon-carbon (C-C) vibrations were seen at $\approx 650 - 1233cm^{-1}$, while high frequency carbon-hydrogen (C-H) vibrations were observed at roughly $1233 - 1500cm^{-1}$. An additional C=C, C=O double bond was observed at $1500 - 2000cm^{-1}$. The spectra additionally displayed the vibrations of two carbon atoms joined by a strong double bond, (C=C), at a frequency of $\approx 1706cm^{-1}$. This occurred at a higher frequency of $650 - 1233cm^{-1}$ as opposed to two carbon atoms connected by a weaker single bond. The D peak developed as a result of suspending bonds, symmetric hexagonal graphitic lattice changes and intrinsic structural imperfections. The G band in sp^2 bonded carbon materials was linked to the E_{2g} mode of phonon vibrations. When the D band at $1343cm^{-1}$ developed, it was apparent that the sp^2 character had been eliminated

and that the sheets may have undergone severe oxidation-induced imperfections development. Equation 2.4, yielded an estimate of the average size and degree of disorder of the sp^2 domains of graphite materials at approximately 0.851.

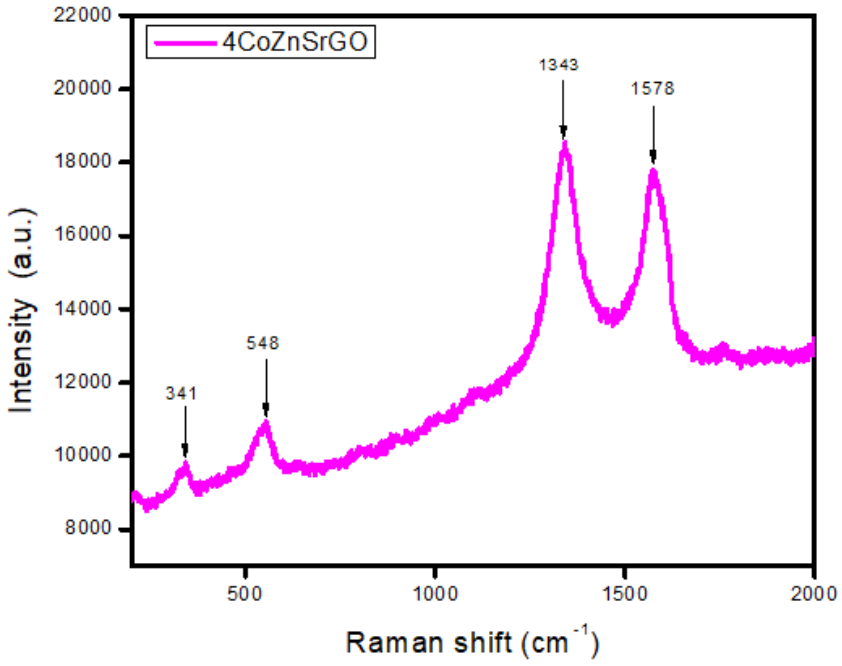

Figure 4.68: Raman spectra of 4Co-ZnS-rGO nanostructures

(e) *6Co-ZnS-rGO RS data analysis*

$Co_{0.06}Zn_{0.94}S$ rGO NSs Raman shift was identified in the spectra as shown in Figure 4.69. The two prominent major bands of GO are positioned at 1354 and $1579cm^{-1}$, respectively representing the D and G bands of graphene. At approximately $650 - 1233cm^{-1}$, Low frequency carbon-carbon (C-C) vibrations were recorded at about $650-1233cm^{-1}$, while high frequency carbon-hydrogen (C-H) vibrations were observed at about $1233 - 1500cm^{-1}$. Extra C=C, C=O double bonds were present at $1500 - 2000cm^{-1}$. In addition, the spectra showed vibrations at a frequency of roughly $1706cm^{-1}$ corresponding to two carbon atoms joined by a strong double bond (C=C). This was more frequent at $650-1233cm^{-1}$ than it was for two carbon atoms joined by a weaker single bond. The ZnS spectra light appeared to form a band at $600cm^{-1}$

and this band was created by the same chemicals as the bands in the $200-650cm^{-1}$ area. The D peak formed as a result of dangling bonds, symmetric hexagonal graphitic lattice disturbances and intrinsic structural faults. The D band at $1354cm^{-1}$ became prominent, suggesting that the sheets may have undergone extensive oxidation and that the sp^2 character may have been eliminated. Generally speaking, the Equation 2.4, which yielded a value of 0.857, can be used to assess the average size and degree of disorder of the sp^2 domains of graphite materials.

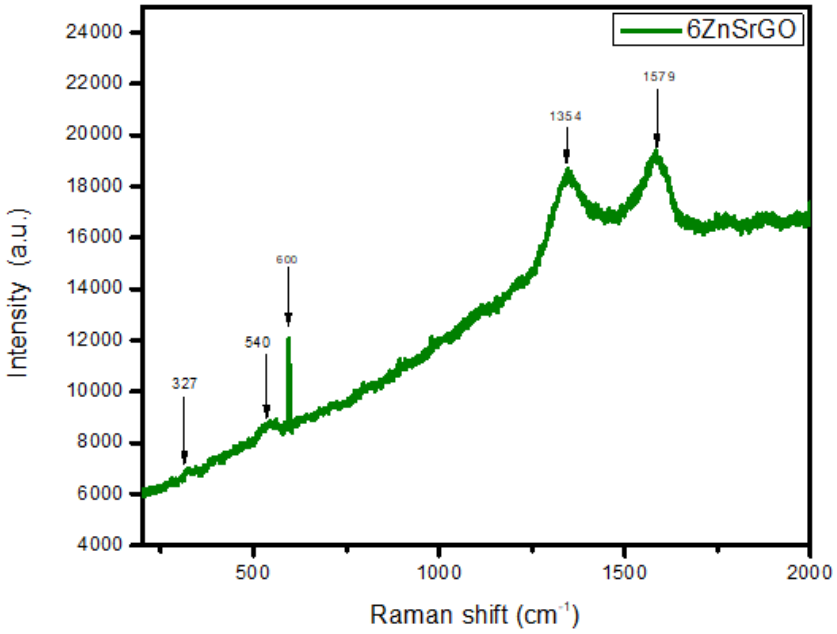

Figure 4.69: Raman spectra of 6Co-ZnS-rGO nanostructures

(f) *Combined Co-ZnS-rGO RS data analysis*

The spectra Figure 4.70 demonstrated that strong bonds and light atoms exhibit substantial Raman shifts. The four curves show the variation in the spectra as well as the similarities in the cobalt doped ZnS decorated with graphene matrix from samples with concentrations of 1, 2, 4 and 6% amt. of cobalt content. The D and G bands of graphene are represented by the two main, conspicuous bands of GO, which are located at $\approx$ 1341 and $1573cm-1$ respectively. Low frequency carbon-carbon (C-C) vibrations were at approximately $650-1233cm^{-1}$,

while high frequency carbon-hydrogen (C-H) vibrations were found at about $1233-1500cm^{-1}$ in the 1, 2, 4 and 6% $Co_xZn_{1-x}S$ rGO spectra. At $1500-2000cm^{-1}$, there was additionally a C=C, C=O double bond given that hydrogen is lighter than carbon, its vibrations have a greater frequency than carbon's. The spectra also showed the vibrations of two carbon atoms connected by a strong double bond C=C at a frequency of about $1706cm^{-1}$ compared to the two carbon atoms connected by a weaker single bond.

With the exception of the band at $429cm^{-1}$, which may have been caused by ZnS spectra light, the bands in the $200-650cm^{-1}$ region appear to be caused by the same compounds. The D peak formed as a result of intrinsic structural faults, dangling bonds and disruptions to the symmetric hexagonal graphitic lattice. The G band of phonon vibrations in sp^2 bonded carbon materials was linked to the E_{2g} mode. The D band at $1353cm^{-1}$ became prominent, suggesting that the sheets may have undergone extensive oxidation and that the sp^2 character had been wiped out.

Generally, the intensity ratio of the D and G bands Equation 2.4 was used to assess the average size and degree of disorder of the sp^2 domains of graphite materials at (x = 0, 1, 2, 4, 6). It was observed that the Equation 2.4 ratios of Co_xZn_1-xS rGO NSs increased somewhat from 0.84-0.86. This finding suggests that the Co_xZn_1-xS rGO NSs were doped with additional defects as opposed to fewer GO. This result implies that more impurities were doped and GO was reduced in the Co_xZn_1-xS rGO NSs.

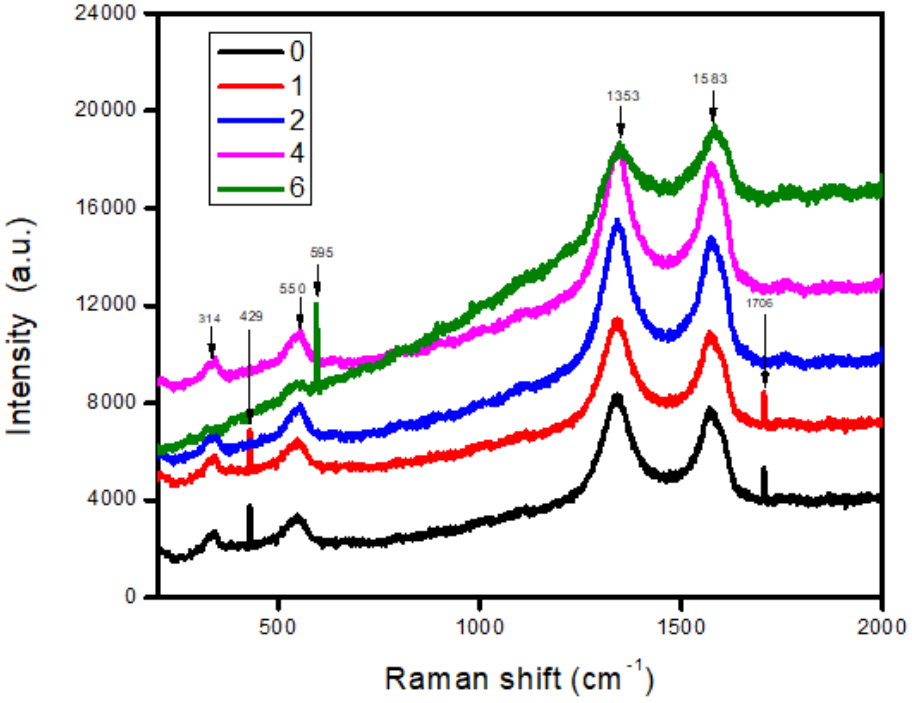

Figure 4.70: Raman spectra of Co-ZnS-rGO nanostructures

RS was able to identify the $Co_xZn_1 - xS$ rGO NSs by the Raman shifts and relative intensities of all the Raman bands of the material respectively E. Smith & Dent (2019); Vandenabeele (2013). The frequencies of vibration depended on the masses of the atoms involved and the strength of the bonds between them. Heavy atoms and weak bonds had low Raman shifts McCreery (2005). Due to this, RS equipment proved to be a crucial characterization tool for researching the interfacial properties at the length scale, which was necessary for designing and creating the multi functional material systems and technologies for the NSs.

4. **Binding energy analysis of cobalt doped ZnS nanostructures decorated with graphene**

The electron spectroscopy for chemical analysis (ESCA) provided crucial information on the elemental and binding energies of $Co_xZn_1 - xS$ rGO NSs surfaces and interfaces Stevie & Donley (2020). The surface composition and chemical state of the $Co_xZn_{1-x}S$ rGO NSs were further confirmed by

XPS measurements. In XPS, an X-ray beam accelerated the surface atoms of the samples, leading to the release of photo-electrons and was able to calculate the amount and kinetic energy of electrons that escaped from the top from 0 to 10 nm of the sample. Each atom in the sample had its core electrons, hence the NSs core electrons absorbed the energy of the X-ray beam as it stroked the surface of the sample. Each element required different amount of energy to liberate the core electron and then identified Krishna & Philip (2022). The investigated materials possessed distinctive properties that made it possible to identify the components of its surface using binding energy.

The elemental signals from the sample's surface were substantially more visible than those from deeper within since XPS only catches electrons that escape from the sample surface and reach the detector Korin et al. (2017). The element's chemical surroundings also resulted in a "chemical shift" in the binding energy. Layer thickness, homogeneity and surface chemistry of the surface coatings and films were all assessed. The core of XPS analysis was knowing where and how big the peaks were on the survey scans and the high-resolution spectra data. Shard (2020).

The peak position (The X-Axis)

The location of a peak on the x-axis provides the chemical and elemental composition in a XPS analysis. The "Binding Energy" axis is commonly displayed in electron volts (eV), which are determined by the energy differential between the x-ray source and the photoelectron being detected. Van der Heide (2011).

The peak intensity axis (The Y-Axis)

On the y-axis of an XPS examination, the intensity of the surface material is recorded. This much of a specific element is visible on the surface. Frequently, this axis displays the total number of photoelectrons counts per

second Venezia (2003). A survey scan is the term used to describe the measurement of photoelectron intensity vs binding energy between 1,200 eV and zero eV.

2% cobalt doped ZnS decorated with graphene

($Co_{0.02}Zn_{0.98}S$ rGO) NSs surface compositions and its elemental studies were carried out using the XPS technique.

(a) *2Co-ZnS-rGO survey data analysis*

The Figure 4.71 shows the overall XPS for $Co_{0.02}Zn_{0.98}S$ rGO spectra. The binding energies for $co2p^{\frac{3}{2}}$ and $co2p^{\frac{1}{2}}$ are centered at around 812 eV and 771 eV, Zn2p at 1052-1023.17eV, O1s at 545-527.32 eV, C1s between 298 eV and 280 eV, S2p at 174.87-157 eV respectively, according to the XPS survey spectra at 2% cobalt doping. Peak width was broad to show the presence of more than one Co species such as Co2p (C=O), Co2p (OH) and Co2p metal which showed the presence of cobalt atoms at Co^{2+} state in the ZnS lattice. Figure 4.71 displayed signal peaks for Zn, S, C, Co and O at their standard binding energies, which were associated with a ZnS environment. Strong evidence for the production of the $Co_{0.02}Zn_{0.98}S$ rGO NSs was provided by the aforementioned data. Moreover, three distinct peaks centered at 288.64, 286.19, and 286.19 eV corresponded to the C-C, C-OH and O=C–OH groups, respectively and were visible in the C1s deconvolution spectrum.

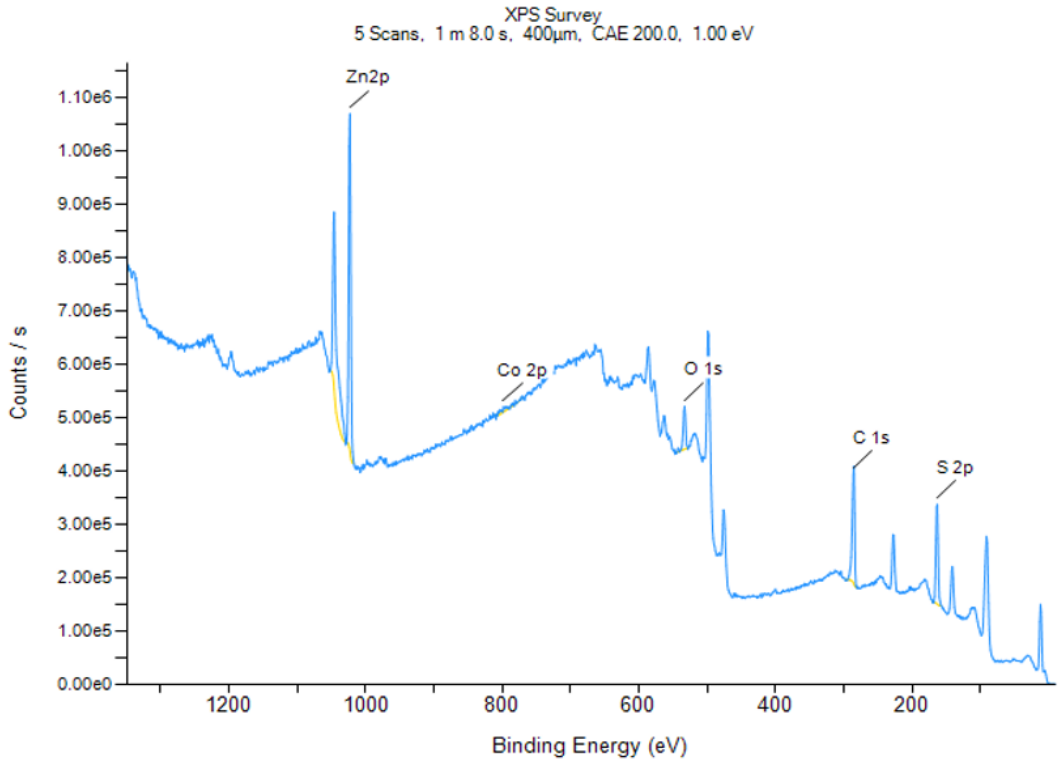

Figure 4.71: General high-resolution XPS spectra of 2% cobalt doped ZnS decorated with graphene.

(b) *2Co-ZnS-rGO 2c1s data analysis*

Three peaks may be seen in the Figure 4.72 representing carbon atoms in various functional groups. Largely delocalized sp^2 hybridized carbon atoms may have been responsible for the major peak at 284.4 eV and the separate peaks at 288.64 eV (C=O) and 286.19 eV (C-O), which have different binding energies at 2% cobalt doped ZnS decorated with graphene. This may be caused by largely delocalized sp^2 hybridized carbon atoms. Figure 4.72 displayed the C1*s* peak of GO's narrow scan XPS spectrum. With their centers at 288.64, 286.19 and 286.19 eV, three Gaussian peaks could be separated from this peak.

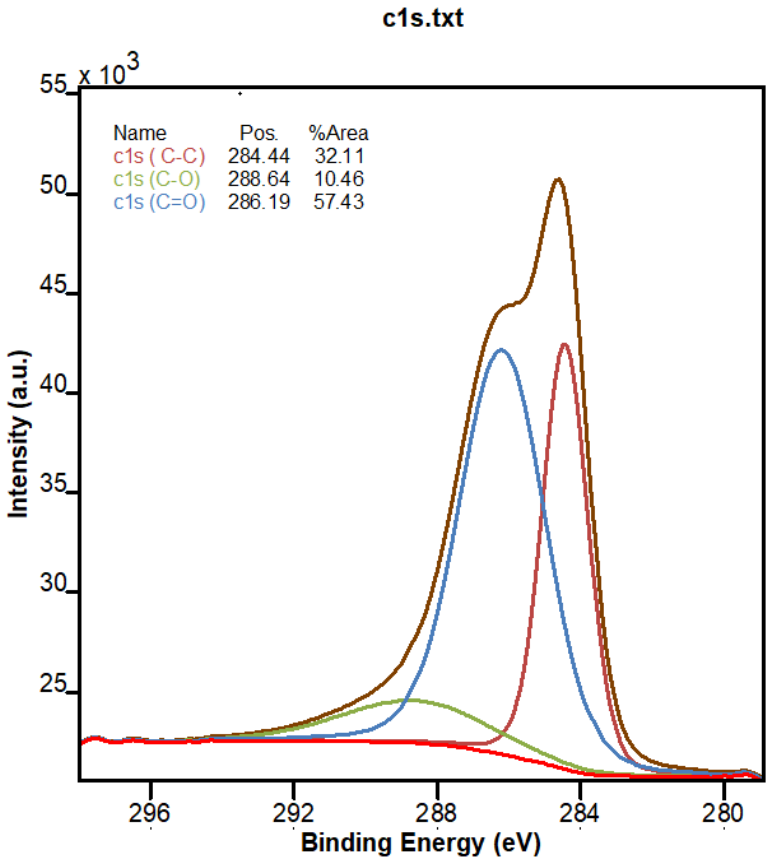

Figure 4.72: High resolution XPS spectra of c1s in 2% cobalt doped ZnS decorated with graphene ($Co_{0.02}Zn_{0.98}S$ rGO) NSs

(c) *2Co-ZnS-rGO Co2p data analysis*

The existence of strong satellite features for Co2p rules out the possibility of the presence of CoO phase as seen in Figure 4.73. The Co2p XPS spectrum at 2% cobalt doping indicates binding energies for $Co2p^{\frac{3}{2}}$ and $Co2p^{\frac{1}{2}}$ that were centered at roughly 781.9 eV and 801.92 eV, respectively indicating cobalt atoms in ZnS lattice.

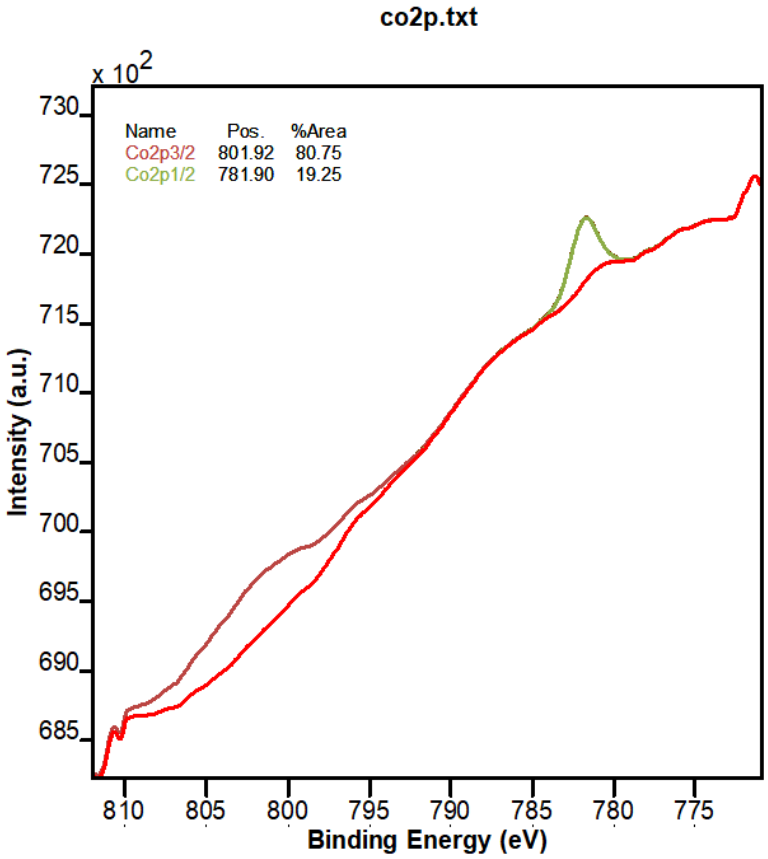

Figure 4.73: High resolution XPS spectra of Co2p in 2% cobalt doped ZnS decorated with graphene ($Co_{0.02}Zn_{0.98}S$ rGO) NSs

(d) *2Co-ZnS-rGO 2o1s data analysis*

The broad and asymmetric XPS spectra of O1s, Figure 4.74 indicates the presence of several oxygen species. Curve fitting has been used to solve this, with one location at 531.7 eV and the other at 533.4 eV. The former was composed of intrinsic O atoms bound to metals (Co and Zn), whereas the later was associated with adsorbed oxygen.

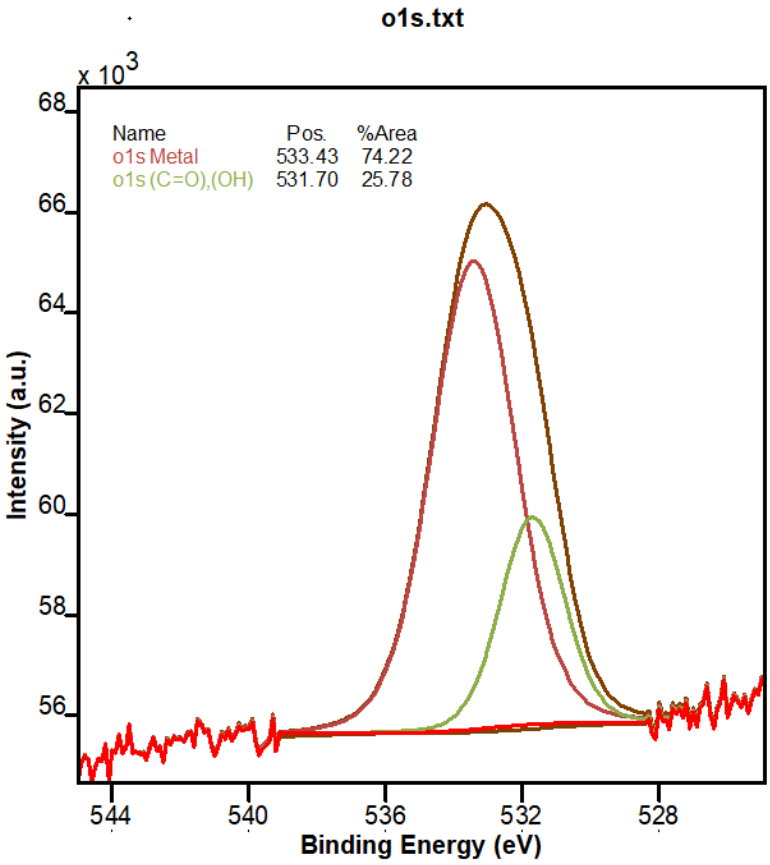

Figure 4.74: High resolution XPS spectra of o1s in 2% cobalt doped ZnS decorated with graphene ($Co_{0.02}Zn_{0.98}S$ rGO) NSs

(e) *2Co-ZnS-rGO s2p data analysis*

The S2p XPS spectrum at 2% cobalt doping indicates binding energies at $S2p^{\frac{3}{2}}$ and $S2^{\frac{1}{2}}$ that are centered at roughly 163.7 eV and 162 eV, respectively as shown in the Figure 4.75. As a result, the surface production of $S2p^{\frac{3}{2}}$ and $S2p^{\frac{3}{2}}$ indicated sulfur atoms in ZnS lattice. The XPS spectra of S2p at 2% cobalt doping shows binding energies attributed to $S2p^{\frac{3}{2}}$ and $S2^{\frac{1}{2}}$ and the bindings, are generally centered at 163.73 eV and 161.97 eV, respectively. This is consistent with a prior result on Co_9S_8 crystals P.-K. Chen et al. (2012). In summary, the aforementioned findings was demonstrated by S.-H. Chang et al. (2013). Consequently, oxides of $S2p^{\frac{3}{2}}$ *and* $S2^{\frac{1}{2}}$ develop near the surface. This suggested that the more the cobalt doping present, the more binding energy is needed for the synthesis of S2p oxides at the surface

of the nanostructures. As a result, the XPS spectra indicated a significant interaction between the two phases and further demonstrated the effective synthesis of $Co_xZn_{1-x}S$ rGO NSs Fang et al. (2011).

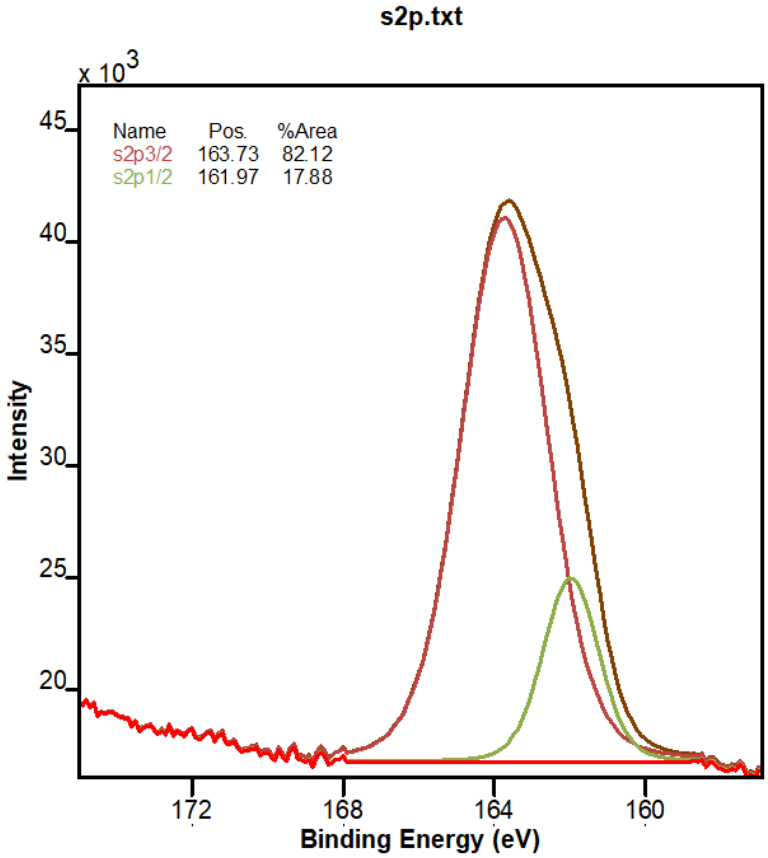

Figure 4.75: High resolution XPS spectra of s2p in 2% cobalt doped ZnS decorated with graphene ($Co_{0.02}Zn_{0.98}S$ rGO) NSs

(f) *2Co-ZnS-rGO zn2p data analysis*

The Zn2p XPS spectrum in Figure 4.76 after the 2% cobalt doping demonstrates that the binding energies of $Zn2p^{\frac{3}{2}}$ and $Zn2p^{\frac{1}{2}}$ are localized at the surface at roughly 1023.3 eV and 1046.6 eV, respectively. On the other hand, Zn2p hydroxide (OH) (1035.7 eV) and oxide (1040.7 eV) may be produced at an a noticeable amount.

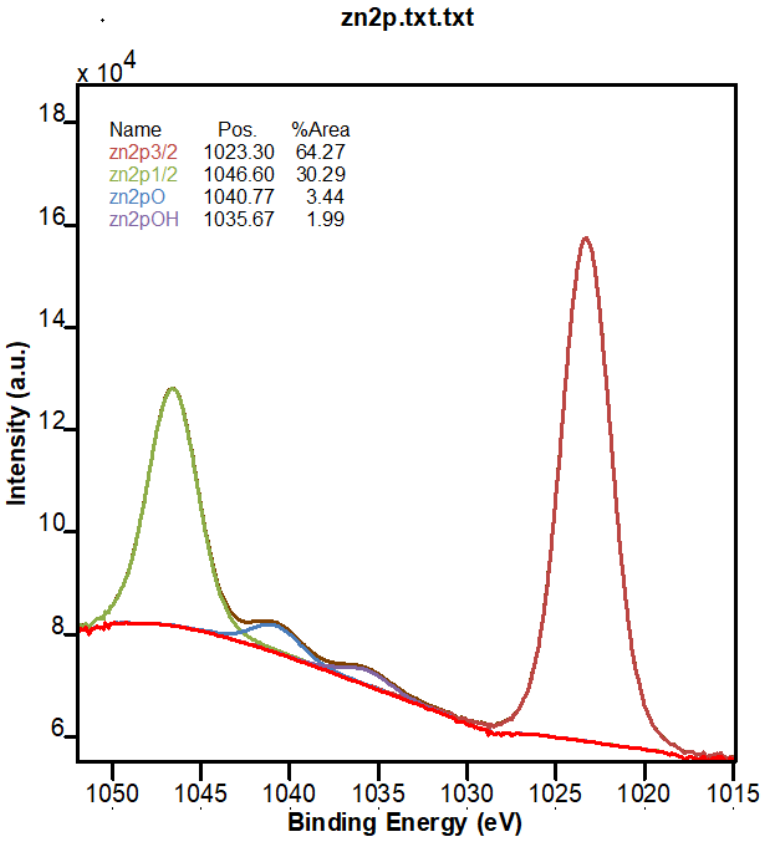

Figure 4.76: High resolution XPS spectra of zn2p in 2% cobalt doped ZnS decorated with graphene ($Co_{0.02}Zn_{0.98}S$ rGO) NSs

4% cobalt doped ZnS decorated with graphene

The oxidation states of the elements were further supported by XPS analysis as shown in Figure 4.77. In the core level of XPS spectra, the binding energy of $Co_xZn_{1-x}S$ rGO nanostructures are described.

(a) *4Co-ZnS-rGO survey data analysis*

The binding energies for $Co2p^{\frac{3}{2}}$ and $Co2p^{\frac{1}{2}}$ are centered at around 812 eV and 771 eV, Zn2p at 1052-1016.48 eV, O1s at 541.45-525.45 eV, C1s between 298 eV and 279eV, S2p at 174.87-157 eV respectively, according to the XPS survey spectra at 4% cobalt doping. Peak width was broad to show the presence of more than one Co species such as Co2p (C=O), Co2p (OH) and Co2p metal which showed the presence of cobalt atoms at Co^{2+} state in ZnS lattice. Zinc sulfide environ-

ments were represented by the Zn, S, C, Co and O signal peaks in sample Figure 4.77 at their corresponding standard binding energies. The creation of the $Co_{0.04}Zn_{0.96}S$ rGO NSs was strongly supported by the aforementioned data. Also, the C1s deconvolution spectrum displayed three distinct peaks that were located at 284.8 eV, 290.19 eV and 287.73 eV, respectively and this corresponded to the C–C, C–OH and O=C–OH groups.

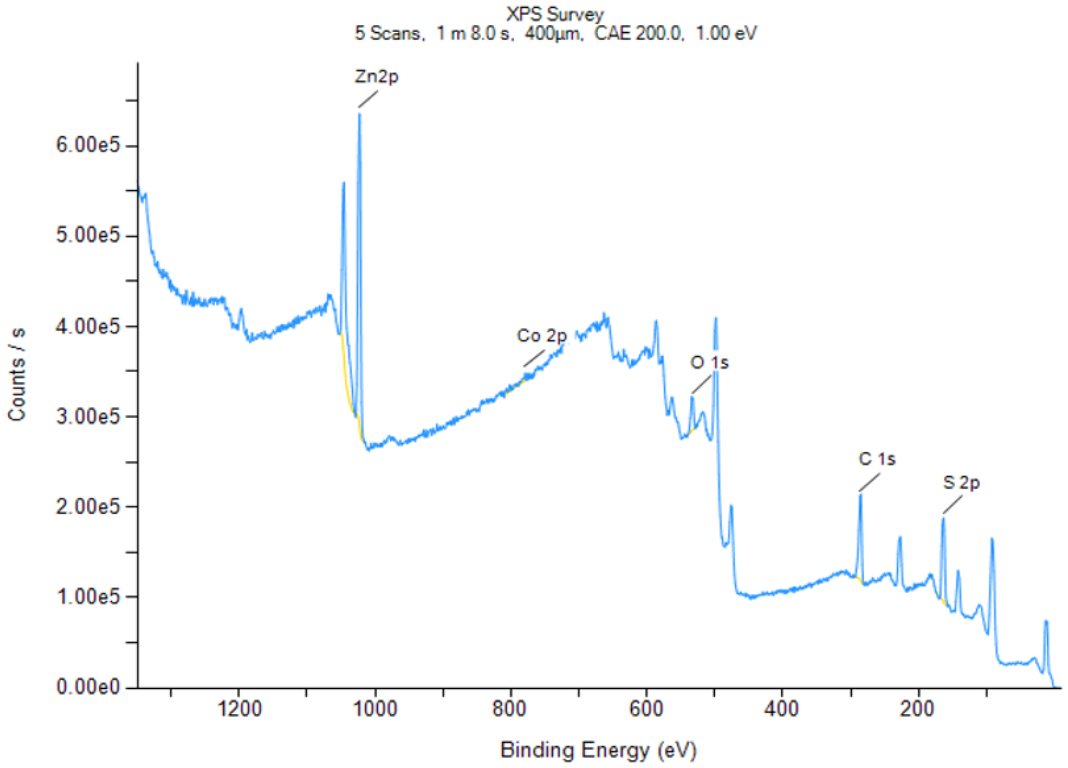

Figure 4.77: General high resolution XPS spectra of 4% cobalt doped ZnS decorated with graphene ($Co_{0.04}Zn_{0.96}S$ rGO) NSs

(b) *4Co-ZnS-rGO zn2p data analysis*

From the Figure 4.78, the XPS spectrum of Zn2p showed only a small binding energy shift in the $Zn2p^{\frac{3}{2}}$ region of 1021-1024 eV, modal value. However, $Zn2p^{\frac{3}{2}}$ centered at 1046 eV shows a binding energy region 1044-1047 eV due to more than one Zn species hence preserving the spin-orbit split. The Figure 4.78 displays the C1s peak of $Co_{0.04}Zn_{0.96}S$ rGO NSs scan XPS spectrum. Three Gaussian peaks with centers at

284.8 eV, 290.19 eV and 287.73 eV could be separated from this peak. The peak located at 290.19.5 eV was attributed to C from the C–OH and C=O groups, whereas the peak at 284.8 eV was due to the sp^2 carbon atom. Closely linked to the $O = C - OH$ carboxylic group was the peak at 287.73 eV.

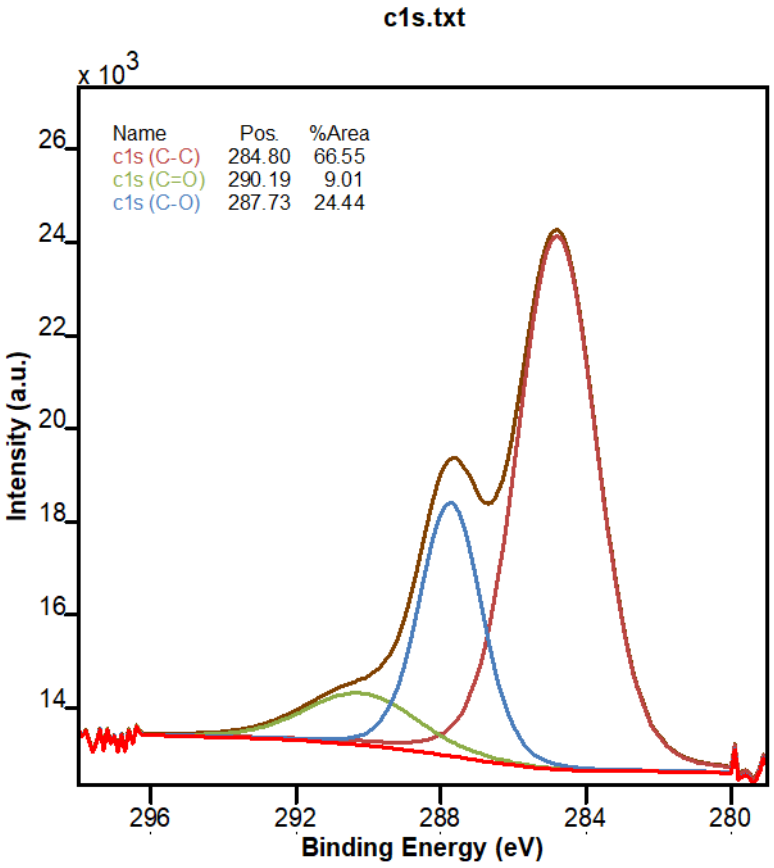

Figure 4.78: High resolution XPS spectra of c1s in 4% cobalt doped ZnS decorated with graphene ($Co_{0.04}Zn_{0.96}S$ rGO) NSs

(c) *4Co-ZnS-rGO 4co2p data analysis*

The Co2p XPS spectra at 4% cobalt doping in Figure 4.79 showed that the binding energies for $Co2p^{\frac{3}{2}}$ and $Co2p^{\frac{1}{2}}$ were centered at around 799.56 eV and 782 eV, respectively. Peak width was broad to indicate the existence of many Co species, including Co2p C=O, Co2p (OH) and Co2p metal, describing the presence of cobalt atoms in the ZnS lattice in the Co^{2+} state. The core level of the Co2p spectrum was deconstructed into two shakeup satellites referred to as "Sats" and two spin–orbit

doublets. $Co2p^{\frac{3}{2}}$ and $Co2p^{\frac{1}{2}}$ were responsible for the first doublet, which occurred at 799.56 eV and 782 eV and the second, which occurred at 787.63 and 794.79 eV S.-H. Chang et al. (2013). The attribution of the doublets to $Co2p^{\frac{3}{2}}$ and $Co2p^{\frac{1}{2}}$ is in consistence with Fang et al. (2011) findings. At 787.63 eV and 794.79 eV, the binding energies of Co2p were observed. There was a significant interaction between the ($Co_{0.04}Zn_{0.96}S$ rGO) NSs and the surrounding ZnS-rGO shell when compared to the XPS spectra of pure Co_9S_8 nanocrystals, which were at 787.63eV and 794.79 eV.

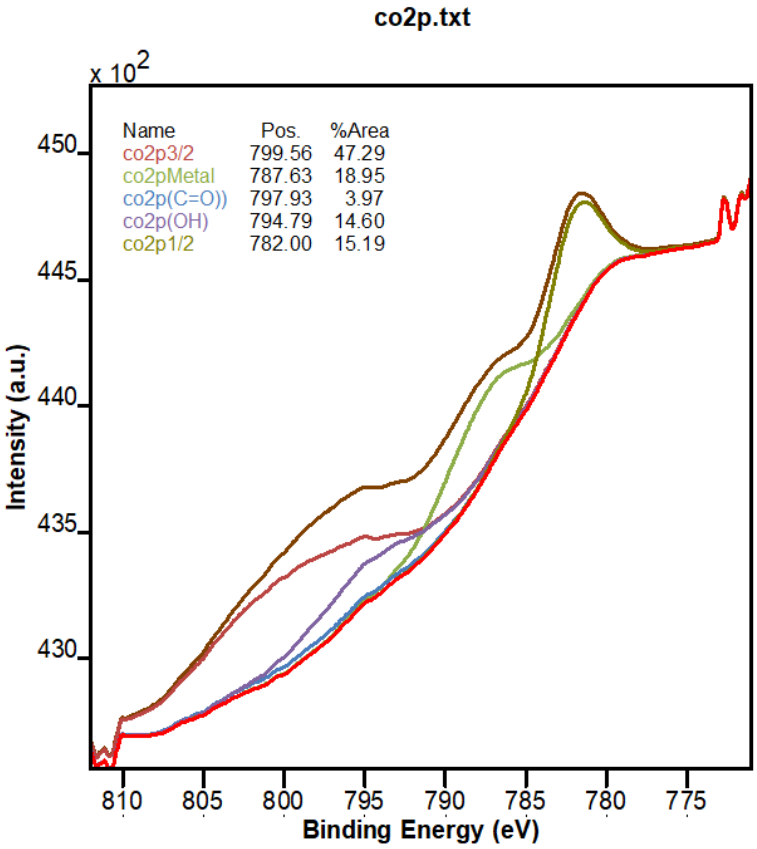

Figure 4.79: High resolution XPS spectra of Co2p in 4% cobalt doped ZnS decorated with graphene ($Co_{0.04}Zn_{0.96}S$ rGO) NSs

(d) *4Co-ZnS-rGO 4o1s data analysis*

Figure 4.80 illustrates the wide and asymmetric XPS spectra of O1s, which indicates the presence of many oxygen species. The initial O1s, which is located at 531.64 eV, might consist of intrinsic oxygen atoms

bound to metals (Zn and Co). In order to generate metal hydroxides at the surface, the second O1s at 533.4 eV may be linked to a carbon double bond, while the third O1s is at 533.8 eV.

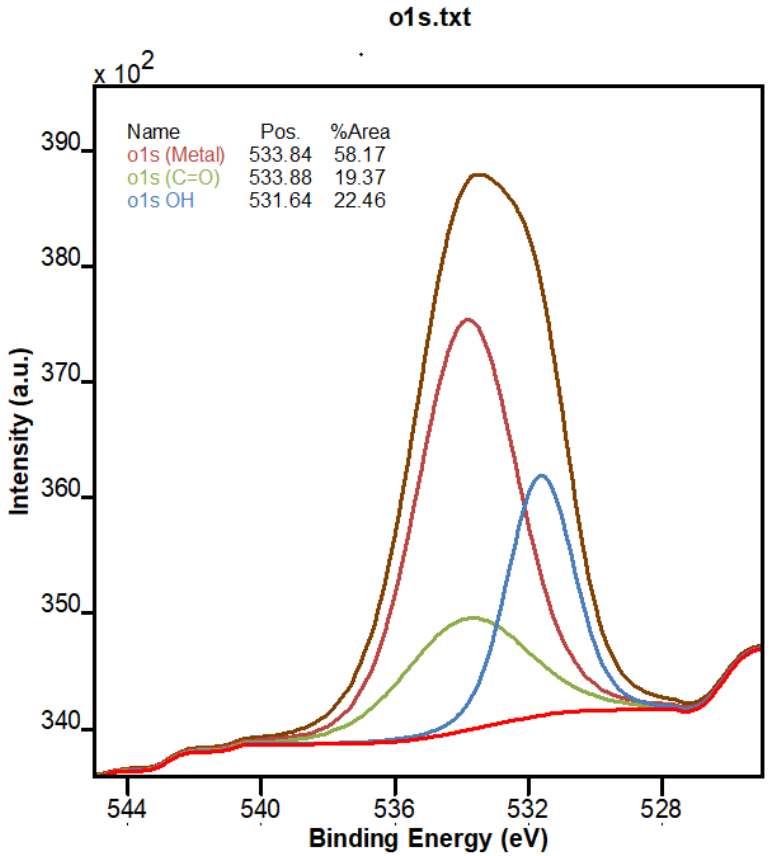

Figure 4.80: High resolution XPS spectra of o1s in 4% cobalt doped ZnS decorated with graphene ($Co_{0.04}Zn_{0.96}S$ rGO) NSs

(e) *4Co-ZnS-rGO 4s2p data analysis*

The binding energies assigned to the $S2p^{\frac{3}{2}}$ and $S2p^{\frac{3}{2}}$ bindings at 4% cobalt doping are shown in Figure 4.81. These are roughly centered at 164.64 eV and 162.27 eV, respectively. This is in good agreement with a previous report on Co_9S_8 crystalsS.-H. Chang et al. (2013). $S2p^{\frac{3}{2}}$ and $S2p^{\frac{3}{2}}$ oxides are consequently generated at the surface. This suggests that the more cobalt doping there is, the more binding energy is needed for the nanostructures' surface to produce S2p oxides. The synthesized $Co_xZn_{1-x}S$ rGO NSs was further demonstrated by the XPS spectra, which also indicated a strong interaction between the two phases.

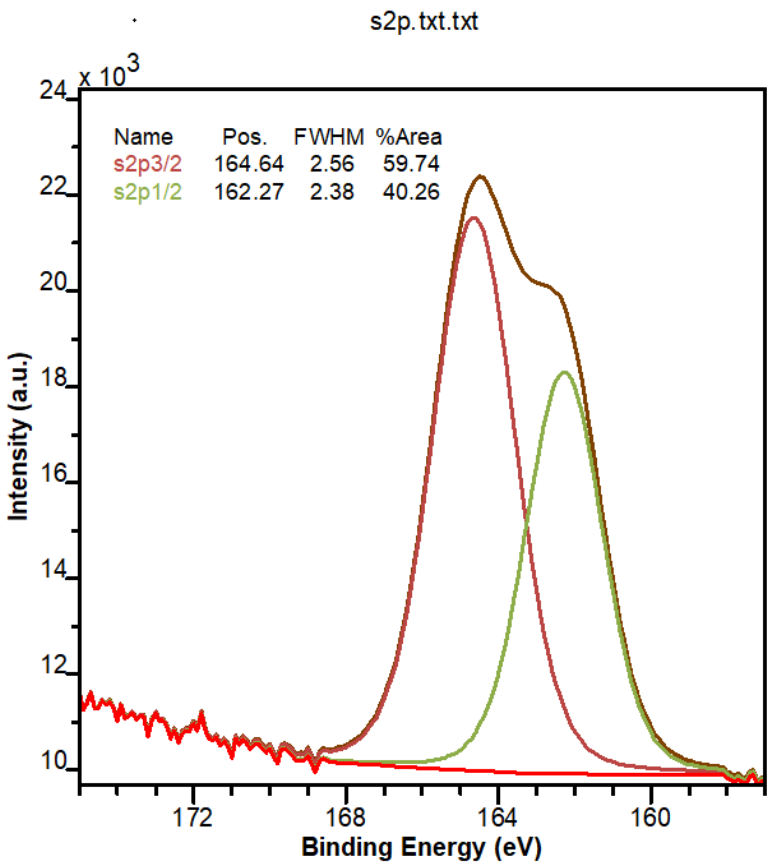

Figure 4.81: High resolution XPS spectra of S2p in 4% cobalt doped ZnS decorated with graphene ($Co_{0.04}Zn_{0.96}S$ rGO) NSs

(f) *4Co-ZnS-rGO 4zn2p data analysis*

From the Figure4.82, the XPS spectrum of Zn2p showed only a small binding energy shift in the $Zn2p^{\frac{3}{2}}$ region. Peak width was broad to show the presence of more than one Zn species. The Zn2p XPS spectrum, as shown in Figure 4.82, only exhibited a little binding energy shift in the $Zn2p^{\frac{3}{2}}$ area of 1021 eV to 1024 eV modal value. The broad peak width indicated the presence of many Zn species. On the other hand, $Zn2p^{\frac{1}{2}}$, which was centered at 1046 eV, exhibited a binding energy region of (1044–1047) eV because it contained several Zn species, maintaining the spin–orbit split. Two shakeup satellites and three spin–orbit doublets comprised the core level of the Zn2p spectrum. $Zn2p^{\frac{3}{2}}$ and $Zn2p^{\frac{1}{2}}$ were responsible for the first doublet at 1021.96 eV, 1042.22 eV, 1024.69 eV and the second at 1044.89 eV, 1047.81 eV, 1046.35 eV, respectively as

also explained by Chan & Ceder (2010).

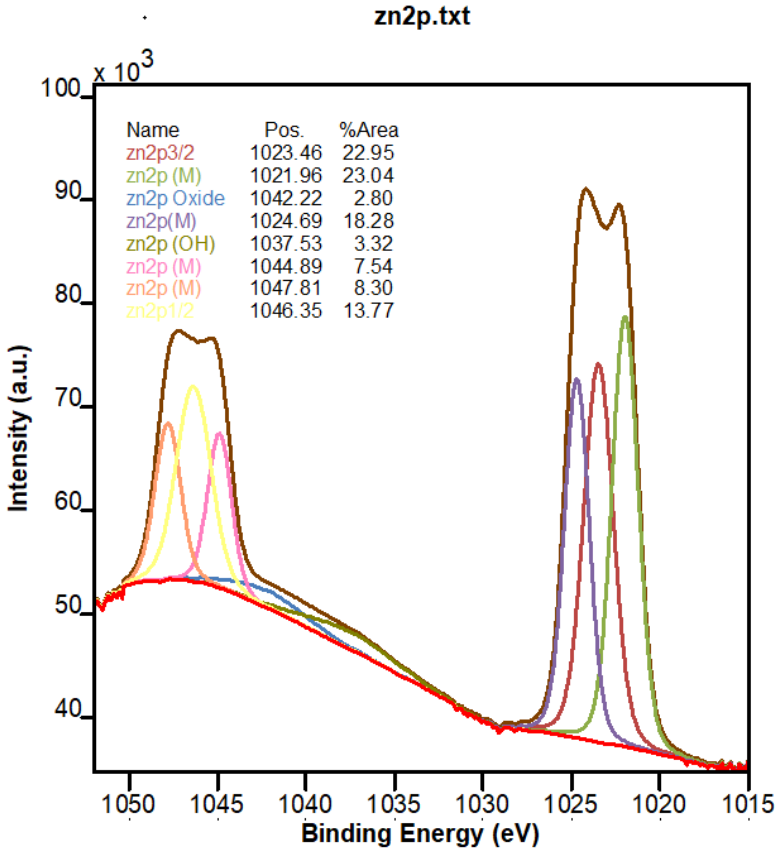

Figure 4.82: High resolution XPS spectra of Zn2p in 4% cobalt doped ZnS decorated with graphene ($Co_{0.04}Zn_{0.96}S$ rGO) NSs

Transition metals can have multiple oxidation states, depending on the surrounding environment (gas atmosphere, pressure and temperature) and the ionic species they are bonded to Zhong et al. (2019). Understanding the relationship between catalytic surfaces and their performance was crucial for the design of new transition metal catalysts and the optimization of those already in use. XPS provided powerful spectroscopic tools J. Hou et al. (2020) to obtain the chemical information of solid surfaces of the cobalt doped ZnS decorated with graphene NSs. The ability of TM to have multiple oxidation states and potentially exchange them during reaction makes them a suitable platform to explore many oxidation and reduction catalytic processes Y. Zhou et al. (2018). It is known that catalysts are not static but dynamic Zafeiratos et al. (2010) and the interaction with the gasses involved in the re-

action (both reactants and products) can dramatically affect their chemical composition and consequently their catalytic properties Puga (2018)

5. **Morphological analysis of cobalt doped ZnS nanostructures decorated with graphene**

   SEM was an effective tool for studying surface morphology of $Co_xZn_{1-x}S$ rGO NSs and electron beams in a raster scan pattern were used to get an image of it. The signals produced by the electrons' interactions with the sample's atoms revealed details about the sample's surface topography, composition and other characteristics like electrical conductivity and the near-surface or surface Lieber & Wang (2007). The sample and the electron beam came into contact and signals were produced as a result of these interactions. The secondary electron emission signal (SE) and the back-dispersed electron emission (BSE) were the most significant. The signals were processed, translated into an analytical spectrum and displayed as X-ray pictures Y. Chen et al. (2004); J. Liu et al. (2005).

   The scanner's microscope was an appropriate tool for comprehending, analyzing and describing the morphology of micro-structures and determining the chemical composition of the cobalt doped ZnS nanostructures decorated with graphene. The graphene sheets weren't completely flat; instead, they showed minute inherent roughening and out of plane deformations (wrinkles). Typical SEM micrographs of reduced graphene cobalt doped ZnS: at (1,2, 4 and 6 at.%) nanostructures are discussed.

   (a) *1Co-ZnS-rGO SEM data analysis*

   Figure 4.83 shows SEM image of $Co_{0.01}Zn_{0.99}S$ rGO NSs revealing that ZnS NSs were completely covered on the surface of graphene as seen in Figure 4.83(**f**, **b** and**c**). The electronic connection between ZnS and graphene sheets was made possible by the close contact between the two materials. This might enhance the photocatalytic activity and charge

separation of the composite photocatalysts as shown in Figure 4.83(**d** and**e**). SEM images revealed graphene sheets emerged and the ZnS nanostructures were dispersed and coated by graphene sheets. Figure 4.83 (**a**) showed the SEM images of rGO with wrinkles which were probably caused by the oxygen functionalization and the resultant defects during its preparation.

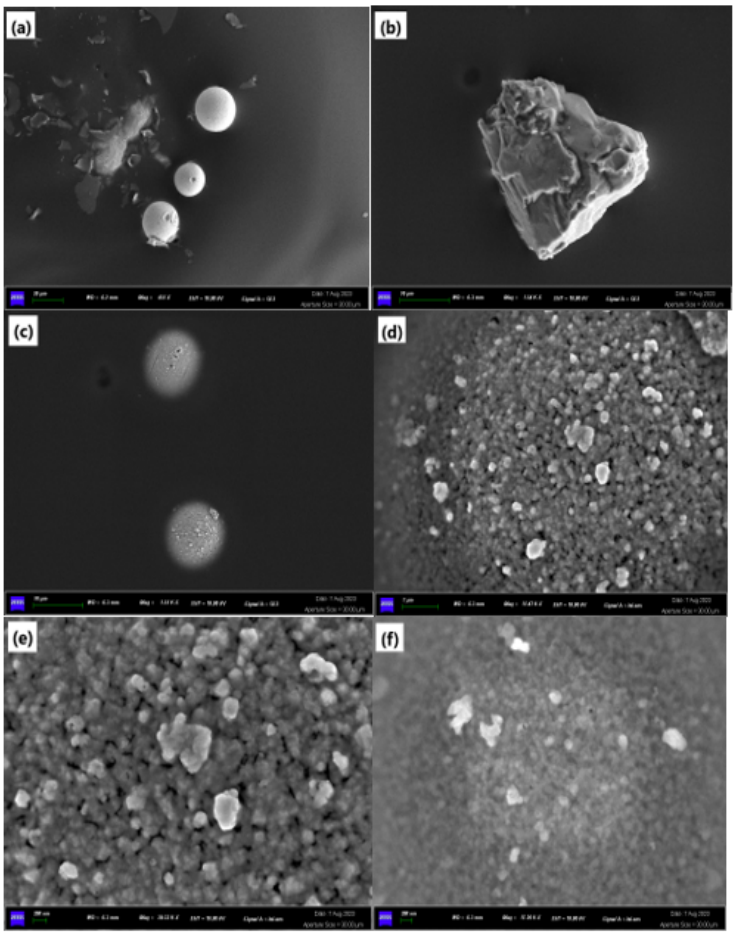

Figure 4.83: SEM micrographs for 1Co-ZnS decorated with graphene.

(b) *2Co-ZnS-rGO SEM data analysis*

ZnS doped with cobalt has been tightly and consistently deposited on the surface of the graphene layers as seen in Figure 4.84. Figure 4.84(**a** and **b**) shows a well spread $Co_{0.02}Zn_{0.98}S$ rGO NSs anchored on the graphene surface. This may enhance the electrons transfer hence reduce recombination of electrons. This means that graphene will be

able to increase the surface area for UV absorption thus continuous photocatalytsis process for hydrogen production. From Figure 4.84 (**c** and **e**) Co doped ZnS is uniformly and firmly fixed on the surface of graphene sheets. The figure further demonstrates that, in the absence of graphene, no normal ZnS aggregates could have been produced as compared as to ZnS/graphene composites created. This finding clearly suggests that the development of homogeneous ZnS aggregates depends on the presence of graphene. Figure 4.84 (**d**) shows how the cobalt doped ZnS is poised on the surface of graphene. Figure 4.84 (**f**) shows a homogeneous distribution of $Co_{0.02}Zn_{0.98}S$ rGO NSs also attached on to the surface of the graphene sheets with a high density of aggregates.

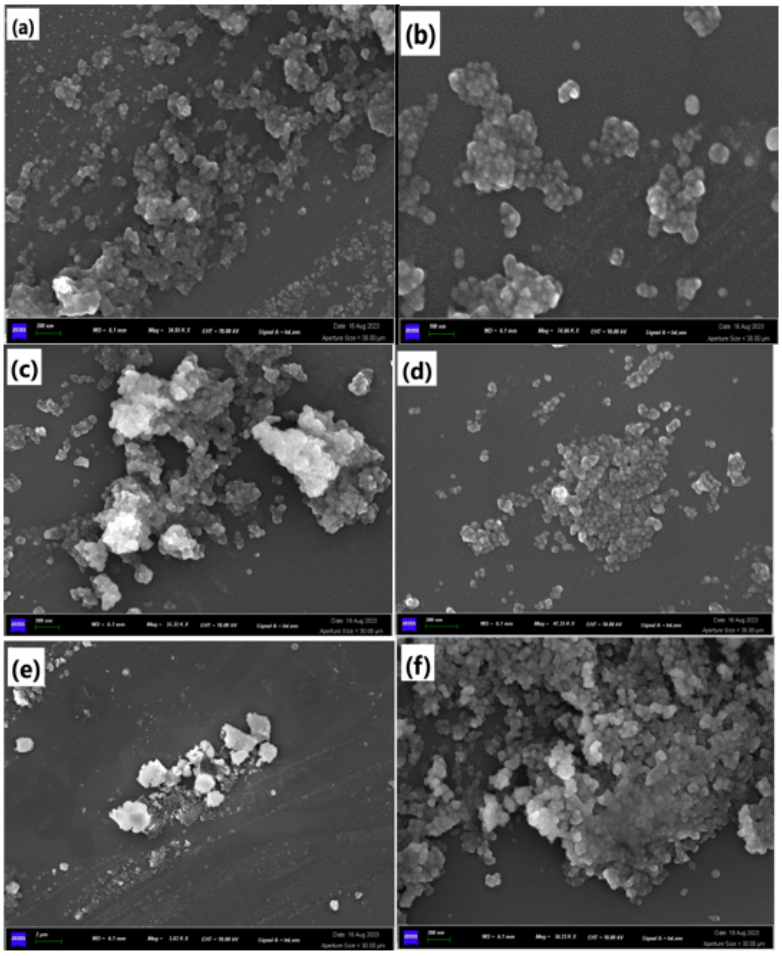

Figure 4.84: SEM micrographs for 2Co-ZnS decorated with graphene.

(c) *4Co-ZnS-rGO SEM data analysis*

ZnS doped with cobalt has been tightly and consistently deposited on the surface of the graphene layers as seen in figure 4.85. This demonstrates that under the same conditions used to prepare ZnS/graphene composites, no regular ZnS aggregates would have grown without the presence of graphene. This finding clearly suggests that graphene was essential for the creation of homogeneous ZnS aggregates and that graphene plays a crucial role in this process. The images in Figure 4.85 demonstrated that when dopant concentration increases, the size of agglomerations gradually decreases. Co doped ZnS NSs completely covered the surface of graphene as shown in Figure 4.85 (**a**). The electronic connection between cobalt doped ZnS and graphene sheets was made possible by the close contact between the two materials as seen in Figure 4.85 (**b** and **f**). This might enhance the photocatalytic activity and charge separation of the photocatalysts. Indicating a strong contact between aggregates and graphene sheets, the aggregates were firmly fixed on the surface of graphene sheets with a high density as shown in Figure 4.85 (**c** and **d**). Such a relationship, in conjunction with the excellent mechanical flexibility of graphene sheets, precludes the aggregation of ZnS aggregates, as demonstrated also in Figure 4.85 (**e**). In order to effectively prevent the closely stacking of graphene sheets, the aggregates on their surface can function as spacers, preventing or at least lessening the loss of their high active surface area.

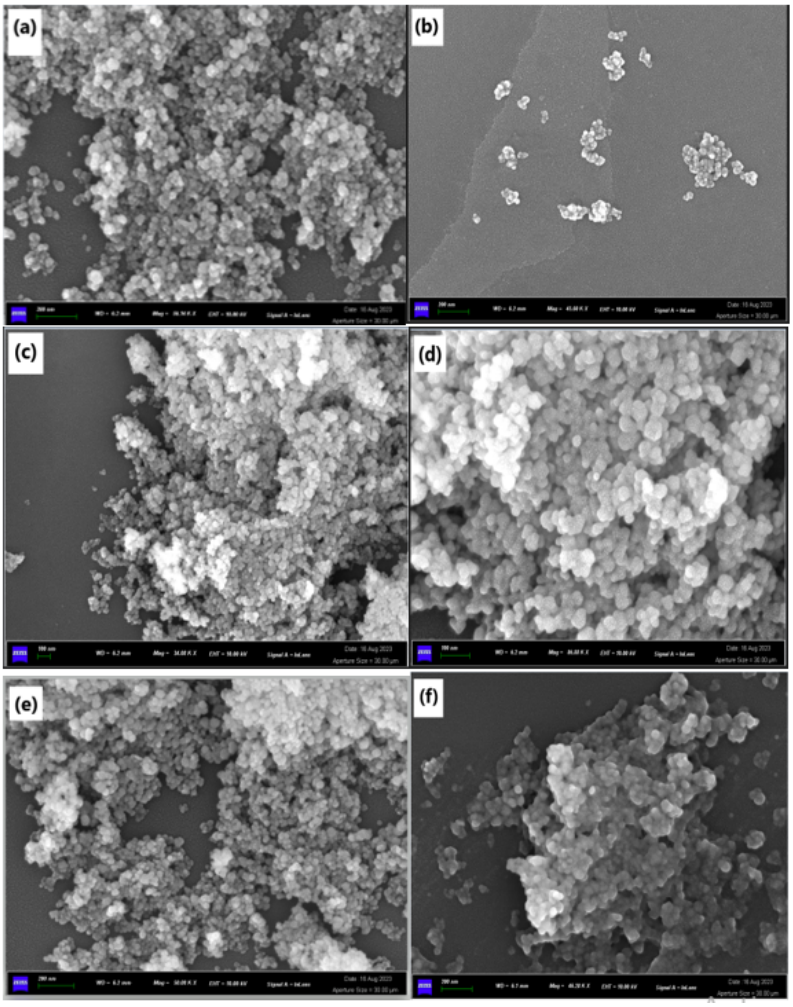

Figure 4.85: SEM micrographs for 4Co-ZnS decorated with graphene.

(d) *6Co-ZnS-rGO SEM data analysis*

Figure 4.86 illustrates that Cobalt doped ZnS has been tightly and consistently deposited on the surface of the graphene layers. $Co_{0.06}Zn_{0.94}S$ NSs shown in Figure 4.86 (**a** and **b**) are firmly adhered to the graphene surface. According to Figure 4.86 (**c** and **d**) the first nuclei of cobalt doped ZnS were supported by rGO sheets, which also inhibited the growth and aggregation of the nanostructures Xie et al. (2013). The $Co_xZn_{1-x}S$ maybe found scattered throughout the surface of rGO as seen in Figure 4.86 (**d**), providing sufficient contacting surface for GO and ZnS NSs as well as likely good carrier transport potential as also shown in Figure 4.86(**e** and **f**). The SEM images 4.86 shows a possible

tiny aggregation of NSs, which may jave been caused by a higher cobalt content of 6%Co. The likelihood of aggregate formation increases with doping level. To mitigate the recombination effect, graphene might have helped to separate the cobalt doped ZnS. Because of the higher cobalt content at 6%, there could be a slight aggregation of the NSs in 6 amt.% compared to 1, 2, and 4 amt.%.

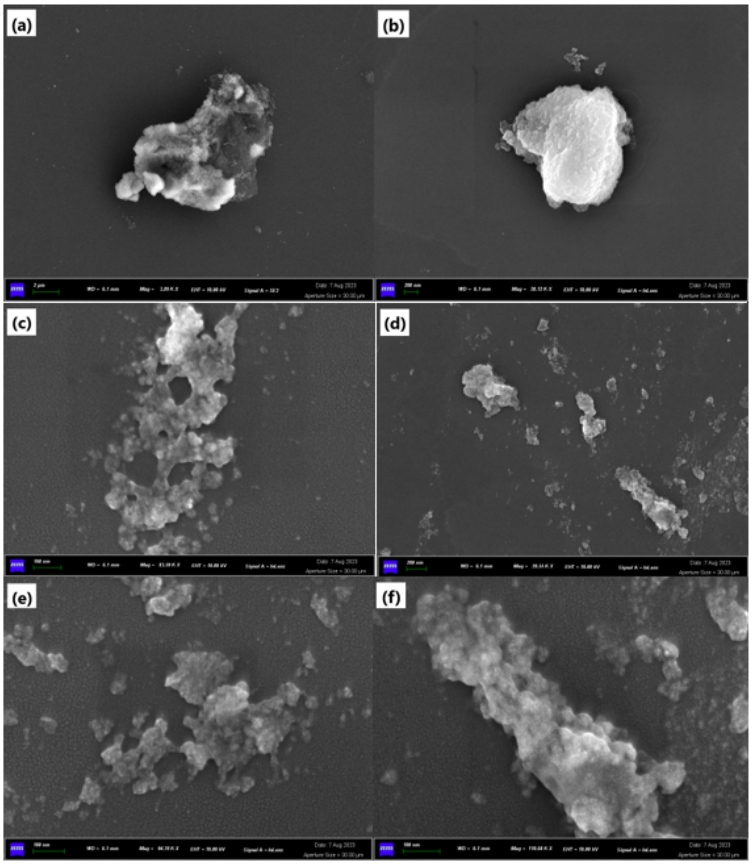

Figure 4.86: SEM micrographs for 6Co-ZnS decorated with graphene.

This research unequivocally established that graphene was essential for the creation of homogeneous cobalt doped ZnS aggregates which led to an effective interaction between NSs and graphene sheets. This interaction in conjunction with the mechanical flexibility of graphene sheets was expected to hinder the aggregation of ZnS nanoparticles. The enhancement was due to the adaptive structure of the 2D graphene sheets and the Co-ZnS/graphene composites' strong contact to successfully avoid volume expansion, contrac-

tion and Co-ZnS agglomeration during the charge/discharge process. The phenomenon known as surface Plasmon allowed reduced graphene oxide to absorb light Zou et al. (2020); Sajeev et al. (2023). In order to slow down photons and create more active sites for photocatalytic reactions on nanostructures, the optical absorption at the resonance frequency could have been effectively boosted by light surface Plasmon resonances. The strength of these peaks reduced as rGO was added to Co-ZnS because recombination of e^- and (h^+) occurs at a slower pace. The properties of reduced graphene include a high electrical conductivity and an adequate capacity for electron storage. The amount of e^- and h^+ recombination was minimized since it could take in and transport excited electrons from Co-ZnS Mahvelati-Shamsabadi & Goharshadi (2018); Y. Hu et al. (2021); L. Zheng et al. (2020); J. Zhang et al. (2012). Therefore, compared to $Co_xZn_{1-x}S$ nanostructures, the $Co_xZn_{1-x}S$ rGO has higher photocatalytic activity as it was proved in photocatalytic activity experiment.

4.3.2 Optical analysis of Cobalt doped ZnS nanostructures surface layers

Absorption and Transmittance analysis

In spectroscopy, transmittance and absorbance are two related but distinct parameters. The primary distinction between absorbance and transmittance is that the former gauges how much incident light is absorbed as it passes through a substance, whereas the latter gauges how much light is transmitted. Absorbance can be identified as the amount of light which is absorbed by a given sample. Transmittance can be recognized as the amount of light passed through that sample. Both of these concepts are very important in fields such as analytical chemistry, spectrometry, quantitative and qualitative analysis, physics and various other fields. The intensity of incident and transmitted light can be used to

measure the transmittance through a sample solution. The sample's absorbance can then be determined using the value for transmittance. When ZnS is in bulk form, the band gap is large (3.5–3.9 eV) Bhargava et al. (1994); Y. Yang et al. (1996) but when ZnS is in nano form, the band gap widens. The UV-vis absorption spectra of the cobalt doped ZnS-rGO NS samples were measured in order to examine their optical characteristicsSud & Sharma (2016) as discussed.

1. *ZnS-rGO UV-vis data analysis*

   Figure 4.87 depicts the UV absorption spectrum of ZnS-rGO. The ZnS characteristic peak corresponding to 3.65 eV band gap was shifted to shorter wavelengths as the size of particle decreased. This blue shift was attributed to the quantum confinement effect at nano scale. The absorption edge of the sample was well below the visible wavelength i.e., below 400 nm approximately (320-400 nm) Ebrahimi et al. (2020). The two band absorption spectra of the ZnS- rGO NSs were discovered to have maxima at 240 and 364 nm, respectively. The bands may match the $\pi - \pi^*$ transition of the aromatic (C–C) and (C=C) bonds as well as the $\eta - \pi^*$ transition of the carbonyl functional group. The observation of the shift of the NSs absorption peak to a longer wavelength (364 nm) in correlation with the aromatic (C–C) bond's $\pi - \pi^*$ transition implies that GO may have been reduced and the (C-C) bonds restored in the graphene sheets Y. Zhang, Ma, et al. (2012).

   The UV emission peak position gradually shifted from 365 nm to 364 nm. The blue shift of the UV emission peak originated from the interaction between the cobalt doped ZnS NSs and the graphene sheets. The physical mechanism might be attributed to the Burstein Moss effect Burstein (1954); Moss (1954). Some graphene sheet electrons may have diffused towards the ZnS during the formation of (ZnS-rGO) combinations and collected at the interface between the two materials to form potential barriers. The diffusion of the electrons into ZnS may have been hampered by the obstacles. These electrons might reside in the states at the base of ZnS conduction band.

After thermal relaxation, the conduction band's low energy levels may have a sizable population.

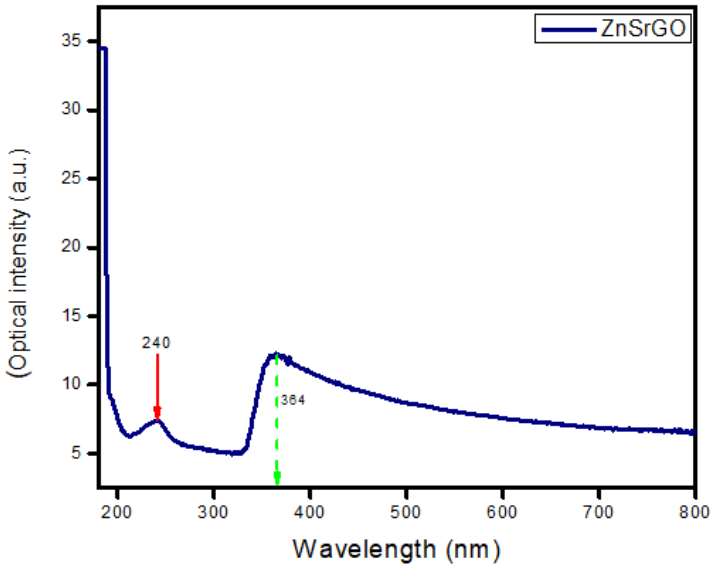

Figure 4.87: UV absorption spectra of ZnS with graphene decoration.

2. *1Co-ZnS-rGO UV-vis data analysis*

The rise in optical transmittance with wavelength was also noted. The transmittance values show that thin films of cobalt doped ZnS decorated with graphene were a good material for collecting solar energy, especially when utilized as a good photocatalyst. Figure 4.88 illustrates the UV absorption spectrum of ($Co_{0.01}Zn_{0.99}S$ rGO) NSs. As the particle size decreases, the ZnS characteristic peak, which corresponds to the 3.66 eV band gap, shifts to shorter wavelengths. This blue shift is due to the phenomena of nanoscale quantum confinement. The two band absorption spectra of the GO solution were discovered to have maxima at 238 and 348 nm, respectively.

The bands match the $\pi - \pi^*$ transition of the aromatic C–C and C=C bonds as well as the $\eta - \pi^*$ transition of the carbonyl functional group. The observation of the shift of the absorption peak to a longer wavelength 364 nm in correlation with the aromatic C–C bond's $\pi - \pi$ transition implies that GO

may have been reduced and the C–C bonds restored in the graphene sheets Y. Zhang, Ma, et al. (2012). The absorbance of pure ZnS was significantly lower than the intensity of the absorbance of the ($Co_0.01Zn_0.99S$ rGO NSs. This greater absorbance could be attributed to the absorption contribution from the graphene sheets and a modification of the fundamental mechanism of excitation output adhering to irradiation. Furthermore, a discernible decrease in the band gap was observed by the slight shift (red shift) of the absorption maxima towards the higher wavelength region. These observations imply a strong coupling between cobalt doped ZnS and graphene sheets. These interactions might be crucial for improving the separation of the photogenerated electron-hole pairs, which would raise the photocatalytic activity.

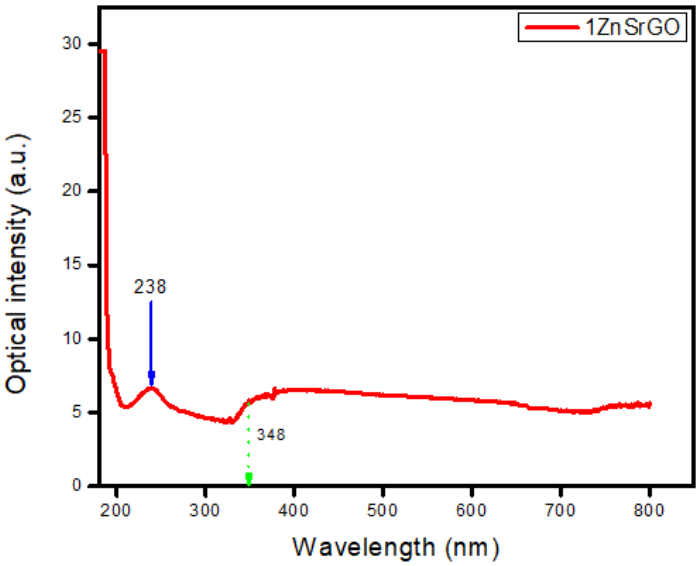

Figure 4.88: UV absorption spectra of 1% cobalt doped ZnS decorated with graphene ($Co_{0.01}Zn_{0.99}S$ rGO NSs

3. *2Co-ZnS-rGO UV-vis data analysis*

The ultraviolet absorption spectra of ($Co_{0.02}Zn_{0.98}S$ rGO NSs is described in Figure 4.89. The ZnS characteristic peak lies at shorter wavelengths and shifts with decreasing particle size, corresponding to the 3.66 eV band gap. Nano-scale quantum confinement might be the cause of this blue shift.

Maximums were found at 238 and 350 nm, respectively, in the two band absorption spectra of the GO solution. The $\eta - \pi^*$ transition of the carbonyl functional group and the $\pi - \pi^*$ transition of the aromatic C-C and C=C bonds were matched by the bands. When the GA absorption peak was observed to shift to a longer wavelength 350 nm, it was suggested that GO may have been reduced and the C-C bonds repaired in the aromatic C-C bond during the $\pi - \pi$ transition.

In comparison to the intensity of the absorbance of the ($Co_{0.02}Zn_{0.98}S$ rGO) NSs, the absorbance of pure ZnS was much lower. This increased absorbance may be explained by the absorption effect of the graphene sheets as well as a change in the basic mechanism of the excitation output that adheres to radiation. Moreover, a minor movement of the absorption maxima towards the higher wavelength region indicated a noticeable decrease in the band gap. These findings suggest a significant connection between graphene sheets and Co-ZnS NSs. Enhancing the separation of the electron-hole pairs produced by photocatalysts may depend on these interactions, hence increasing the photocatalytic activity.

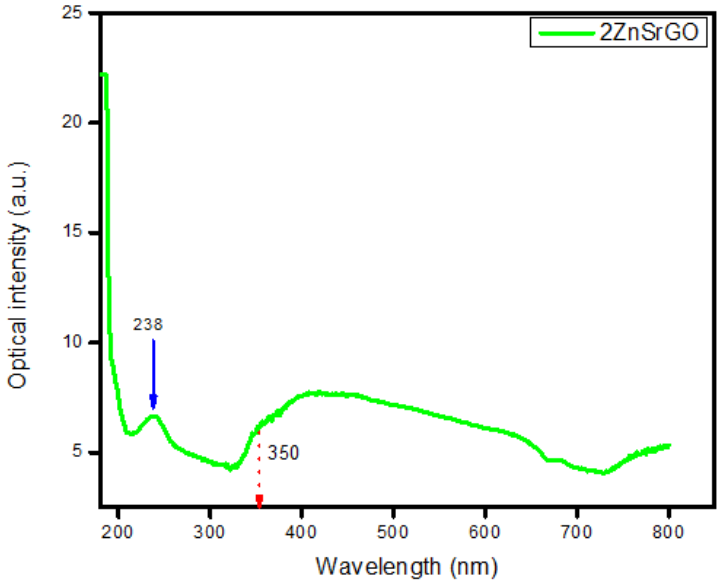

Figure 4.89: UV absorption spectra of 2% cobalt doped ZnS decorated with graphene ($Co_{0.02}Zn_{0.98}S$ rGO) NSs

4. *4Co-ZnS-rGO UV-vis data analysis*

Figure 4.90 demonstrates the UV absorption spectra of ($Co_{0.04}Zn_{0.96}S$ rGO) NSs. As the particle size decreases, the ZnS characteristic peak, which corresponds to the 3.66 eV band gap, shifts to shorter wavelengths. When compared to ZnS-rGO's absorption threshold at about 365 nm, the doping ions significantly shifted absorption shifts into the visible area. This blue shift is due to nanoscale quantum confinement. Maximums in the two band absorption spectra of the GO solution were discovered at 239 and 338 nm, respectively. The bands match the $\pi - \pi^*$ transition of the aromatic C-C and C=C bonds and the $\eta - \pi^*$ transition of the carbonyl functional group.

It is hypothesized that during the $\pi - \pi$ transition, GO may have been lowered and the C-C bonds in the aromatic C-C bond repaired when the ($Co_{0.04}Zn_{0.96}S$ rGO) NSs absorption peak shifts to a longer wavelength 338 nm. The absorption effect of the graphene sheets and a modification in the fundamental mechanism of the excitation output that clings to radiation can both account for this higher absorbance. Additionally, a little shift of the absorption maxima in the direction of the higher wavelength area suggested that the band gap was decreasing somewhat. These results imply a strong relationship between ZnS and graphene sheets. These interactions may be necessary to improve the separation of the electron hole pairs created by photocatalysis, hence raising the photocatalytic activity.

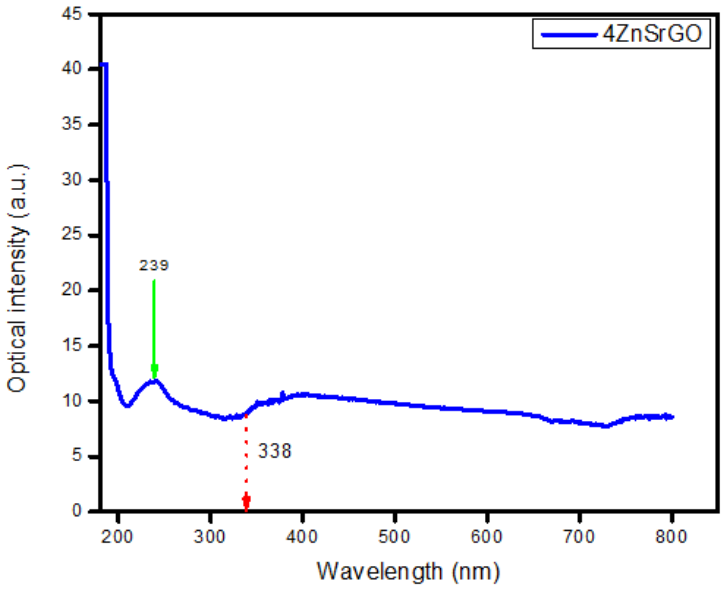

Figure 4.90: UV absorption spectra of 4% cobalt doped ZnS decorated with graphene ($Co_{0.04}Zn_{0.96}S$ rGO) NSs

5. *6Co-ZnS-rGO UV-vis data analysis*

   UV absorption spectrum of ($Co_{0.06}Zn_{0.94}S$ rGO) NSs' UV absorption spectra is illustrated in Figure 4.91. The ZnS characteristic peak lies at shorter wavelengths and shifts with decreasing particle size, corresponding to the 3.66 eV band gap. The doping ions considerably shifted absorption shifts into the visible area in comparison to ZnS-rGO's absorption threshold at roughly 365 nm. An effect known as nanoscale quantum confinement could be the cause of this blue shift. At 236 and 319 nm, respectively, maximums were found in the two band absorption spectra of the GO solution.

   The aromatic C-C and C=C bonds' $\pi - \pi^*$ transition and the carbonyl functional group's $\eta - \pi^*$ transition were matched by the bands. logically, when the ($Co_{0.06}Zn_{0.94}S$ rGO) NSs absorption peak shifted to a longer wavelength 319 nm, GO may have been decreased and the C-C bonds in the aromatic C-C bond may have been repaired during the $\pi - \pi$ transition. This greater absorbance can be explained by the absorption effect of the graphene sheets as well as a change in the basic mechanism of the excitation output that clings to radiation. Furthermore, a little movement of the absorption max-

ima toward the higher wavelength region indicated a possible gradual decrease in the band gap. These findings suggest a close connection between Co-ZnS NSs and graphene sheets. To increase the spacing of the electron-hole pairs produced by photocatalysis and hence the photocatalytic activity, certain interactions might be required.

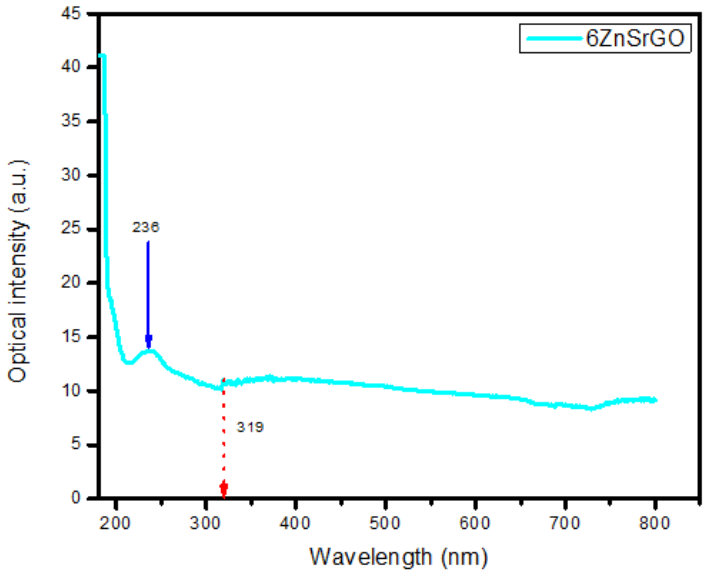

Figure 4.91: UV absorption spectra of 6% cobalt doped ZnS decorated with graphene ($Co_{0.06}Zn_{0.94}S$ rGO) NSs

6. *Combined Co-ZnS-rGO UV-vis data analysis*

The UV absorption spectrum of Co_xZn_1-xS rGO at x = 0, 1, 2, 4, 6 was observed as shown in Figure 4.92. The ZnS characteristic peak corresponding to 3.66 eV band gap was shifted to shorter wavelengths as the size of particles decreased. Figure presents the transmittance spectra of pure of cobalt doped ZnS rGO in a range of 320 to 560nm with an excitation wavelength of 340nm at a step size of 1nm. This blue shift is attributed to the quantum confinement effect at nano scale. The absorption edge of all the samples was well below the visible wavelength i.e., below 400 nm approximately (320 nm to 400 nm) Ebrahimi et al. (2020).

The two band absorption spectra of the GO solution were discovered to have maxima at 240 and 365 nm, respectively. The bands match the $\pi - \pi^*$ tran-

sition of the aromatic C–C and C=C bonds as well as the $\eta - \pi^*$ transition of the carbonyl functional group. The observation of the shift of the NSs absorption peak to a longer wavelength (365 nm) in correlation with the aromatic C–C bond's $\pi - \pi$ transition implies that GO may have been reduced and the C–C bonds restored in the graphene sheets Y. Zhang, Ma, et al. (2012). The UV emission peak position gradually shifted from 366 nm to 341 nm. The blue-shift of the UV emission peak originated from the interaction between the Co-ZnS nanostructures and the graphene sheets. The physical mechanism might be attributed to the Burstein–Moss effect Burstein (1954); Moss (1954). Some graphene sheet electrons may diffuse towards the ZnS during the formation of ZnS/GR combinations and collect at the interface between the two materials to form potential barriers.

The diffusion of the electron into ZnS might be hampered by the obstacles. These electrons might reside in the states at the base of ZnS's conduction band. After thermal relaxation, the conduction band's low energy levels may have a sizable population. Both the increase of absorption intensity as well as shift of absorption edge along long wavelength region may be noticed by the substitution of Co into (Zn-S) lattice. The reduced absorption intensity by cobalt addition may be due to the decrease of size and also the proper incorporation of Co^{2+} ions in the position of Zn^{2+} ions where the ionic radius of Co^{2+} ions is lower than that of Zn^{2+} ions as described by XRD results. The existing shift of absorption edge may have been supported by the size reduction which promote the energy gap to higher value.

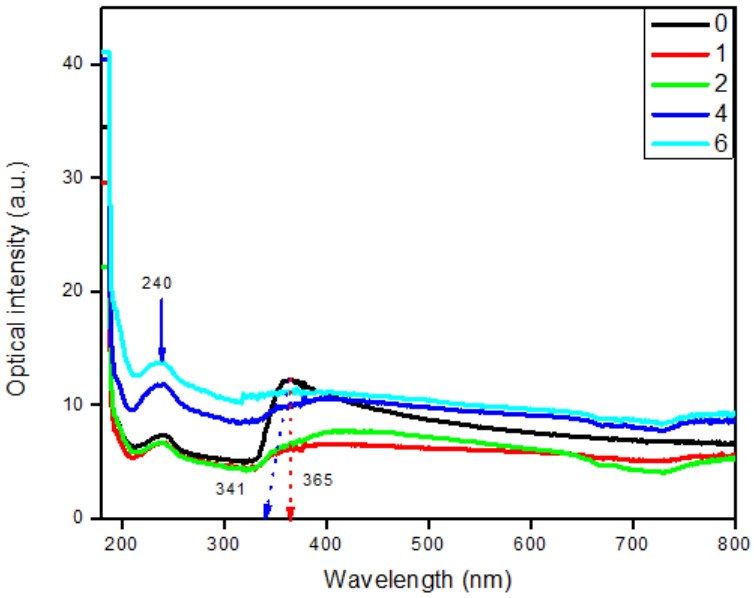

Figure 4.92: UV absorption spectra of combined (0, 1, 2, 4 and 6% cobalt doped ZnS decorated with graphene.

In addition, the cobalt doping may have stimulated more defects hence created the irregularity or imperfections through (Zn-S) lattice owing to the ionic radius variation which may be a probable reason for the reduction in absorption intensity as explained by J. Zhu et al. (2017). The light scattering by grain boundaries and the reflection of incident light by cobalt clusters in lattice (Zn-S) may have also reduced the absorption intensity Reddy et al. (2014). An extra possibilities for the charge carriers to vanish may have been created by the interaction of the excited ZnS particles and the graphene sheets.

These interfacial charge transfer events are represented by emission quenching Kamat et al. (2002); Subramanian et al. (2003) excited ZnS NSs to the GO to form reduced graphene in the current investigations. Such reductive radicals cannot be formed without ZnS. In heterogeneous photocatalysis using semiconductor materials (TiO2, ZnO, ZnS, etc.), charge recombination in semiconductor particulates is frequently a concern Y. Zhang, Zhang, et al. (2012); X. Huang et al. (2012); Qian et al. (2011); Lv et al. (2011); G. Wang et al. (2011); Shen et al. (2010); Y. Liu et al. (2015). The performance of

photocatalysis should be enhanced if semiconductor particles are anchored on a graphene scaffold, which should also enhance photoinduced charge separation.

4.3.3 Electronic analysis of cobalt doped ZnS nanostructures surface layers

Optical band gap energy estimation

The energy required to excite an electron from the valence band to the conduction band is known as the band gap energy of a semiconductor. For the purpose of forecasting semiconductor photophysical and photochemical properties, an accurate estimate of the band gap energy is essential Makuła et al. (2018). Tauc formulae Equation 4.10 Theyvaraju & Muthukumaran (2015) was used to calculate the absorption edges of $Co_xZn_{1-x}S$ rGO NSs from their absorption data, where E_g was energy gap and the exponent n was taken as 0.5 or 2, the correlation between the absorption coefficient and the photon energy was explored.

This allowed to evaluate the influence of cobalt through band structure as well as electronic transition. The samples' direct band gap was indicated by the linear portion of the symbol hv. Tauc plot was used to determine the band gap and UV absorption spectra by graphing hv versus $(\alpha hv)^2$. Calculating the energy band gap of a semiconductor material using UV-Vis absorption data was done with the help of Origin software.

$$(\alpha hv)^n = A(hv - E_g) \tag{4.10}$$

In this equation, α is the absorption coefficient expressed as

$$\alpha = \frac{4\pi k}{\lambda} \tag{4.11}$$

Where h is Planck's constant $(6.6 * 10^{-34} J - s)$, v is the frequency of the incident

photon, A is a proportionality constant (which is determined by the index of refraction, electron, and hole effective masses; however, it is usually taken as 1 for amorphous materials), and E_g is the optical band gap energy expressed as $E_g = \frac{hc}{\lambda}$ where c is the velocity of light ($3 * 10^8 m/s$ and λ is the absorbed wavelength. The important term is the exponent n, which denotes the nature of the electronic transition, that is, when $n = 2$ it is a direct allowed transition and when it is equal to $\frac{1}{2}$, it is an indirect allowed transition. For $n = \frac{2}{3}$ it is a direct forbidden transition and for $n = \frac{1}{3}$ an indirect forbidden transition. Typically, the allowed transitions dominate the basic absorption processes, giving either direct or indirect transitions. Thus, the basic procedure for a Tauc analysis was to acquire optical absorbance data for a sample in question that spans a range of energies from below the band gap transition to above it. Plotting the $(\alpha hv)n$ versus hv was a matter of testing $n = 2$ or $n = \frac{1}{2}$ to compare which provides the better fit and thus identify the correct transition type. Then by extrapolating linear part of the curve, a line was drawn where $\alpha = 0$. The point where it touched the x axis, was the optical band gap energy of the NSs. First the material was checked for direct band gap at $n = 2$. Using Tauc equation for direct band gap Equation 4.12 to calculate the band gap energy.

$$(\alpha hv)^2 = A(hv - E_g) \tag{4.12}$$

The indirect band gap was also checked at $n = 0.5$ and its Tauc equation was written as;

$$(\alpha hv)^{0.5} = A(hv - E_g) \tag{4.13}$$

Absorbance data was used and Tauc equation $n = 2$ was used to check for direct band gap for all the five samples using Equation 4.12 and 4.13

$$hv = \frac{1240}{wavelength} \tag{4.14}$$

on the x axis.

$$(2.303 * Absorbance * Energy)^2 \tag{4.15}$$

on the y axis. The defect states in optical band gap region were represented by an optical parameter called the Urbach energy. These localized defect states in the band gap region was responsible for the formation of absorption tail in the absorption spectra which was termed as Urbach tail and the energy associated with it hence Urbach energy. The Urbach energy can be extracted from absorption spectra and can be calculated using the following Equation 4.16.

$$\alpha = \alpha_o expo\left(\frac{E}{E_u}\right) \tag{4.16}$$

where α is the absorption coefficient, α_o is the incident photon energy which is equal to hv and E_u is the Urbarch energy. The Urbarch energy is estimated from $\ln \alpha$ versus photon energy plot. The reciprocal of the obtained slope by fitting linear part of the curve which gives the value of the Urbach energy E_u which is given by Equation 4.17;

$$E_u = \frac{1}{Slope} \tag{4.17}$$

The fundamental band gap energies of the $Co_xZn_{1-x}S$ rGO NSs samples were measured and examined using optical absorption. These energies were related to both direct and indirect transitions. Energy gap analysis Wasim et al. (2001, 1998) suggests that the Urbach effect seen in the absorption spectra of the $Co_xZn_{1-x}S$ rGO NSs may be caused by the combined influence of impurities, structural disorders and interactions between the exciton and lattice in the system. Defects with intrinsic charge alter the structure of the chemical bond, affecting the charge distribution and therefore the band gap, index of refraction, optical absorption and other properties.

Electronic transition was necessary for inter-band transitions in $Co_xZn_{1-x}S$ rGO NSs crystals. Cobalt ion defects may induce band tail states that lead to band narrowing. In semiconductors and insulators, the basic absorption edge, sometimes called the Urbach tail, rises exponentially below the energy band gap Urbach (1953). In the literature, phonons, impurities, excitons, and structural disorders in the materials have been associated with the observed exponential tails Dow & Redfield (1972); Cody et al. (1981); Wasim et al. (1998).

ZnS photo excitation electrons consequently need $Eg+ \triangle E_b$ energy. $\triangle E_b$ is the additional energy needed to transfer the free electrons to the open electronic sub levels toward the bottom of the conduction band. This adjustment of $\triangle E_b$ is refereed as the Burstein Moss shift. The ZnS lattice would absorb more Π electrons as the ZnS to graphene mass ratio increased. As a result, the barrier between ZnS and graphene would increase. Additionally, this would result in a rise in the $\triangle E_b$ Burstein Moss shift. The result could be an optical band gap that gradually widens. As the optical band gap grows, there would be a gradual drop in optical intensity because there would be less photogenerated electrons in ZnS.

1. Bandgap of ZnS-rGO

   Using a Tauc plot, the band gap for the UV absorption spectra of ZnS-rGO was also determined. The direct band gap of 4.86 eV was recorded as shown in Figure 4.93. It was evident that every ZnS-rGO NSs sample had a strong band of absorption edges at the UV region, which spanned at 180–340 nm and a weak band of absorption at the visible area. It was evident that the blue shift phenomena happened and that all of the ZnS-rGO NSs sample's direct band gap value was higher than bulk ZnS's (3.67 eV). The blue shift phenomenon may have resulted from changes in the electronic transition caused by the quantum size effect. When the size of the NSs decreases, the energy gap widens and the optical absorption band shifts to the short wave direction.

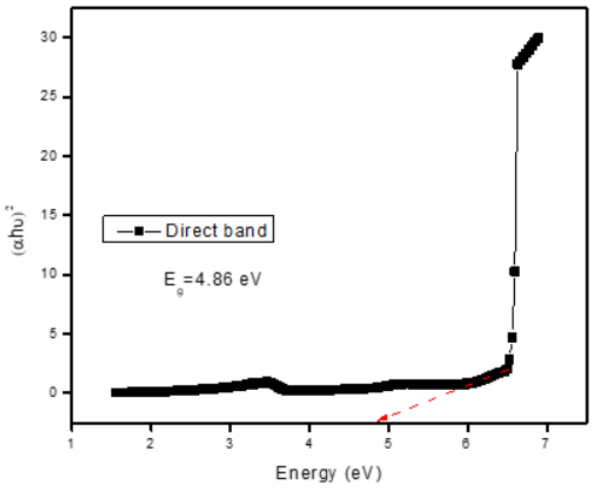

Figure 4.93: Direct band gap of ZnS decorated with graphene.

The band gap of the synthesized ZnS-rGO materials was acquired from the plot between $(\alpha hv)^{0.5}$ and hv was revealed in Figure 4.94. A 0 eV indirect band gap was found for pure ZnS-rGO. The observed lower band gap (red shift) at low doping concentration could be attributed to the s-p-d spin exchange interactions. These interactions may enhance the correction probability of the positive and negative potential to the valence band edge and the conduction band, respectively and cause band gap narrowing K. J. Kim & Park (2004).

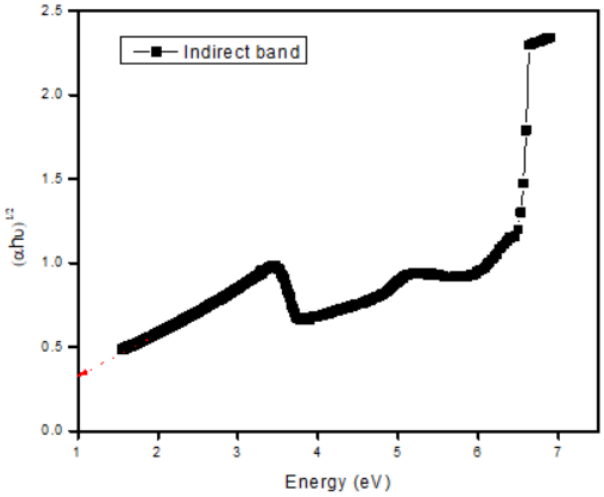

Figure 4.94: Indirect band gap of ZnS decorated with Graphene.

The ZnS-rGO NSs absorption spectra were checked for the Urbach effect

using the UV-vis data calculations, as illustrated in Figure 4.95. In the sub-band gap region of the ZnS-rGO NSs, the fundamental absorption edge (i.e., Urbach tails) developed exponentially, suggesting that impurities, thermal and structural disorders and exciton lattice interactions may have had a significant impact on the optical properties. The steepness parameter, the exciton peak and the measured temperature dependence of the Urbach energy in the ZnS-rGO NSs showed how important these parameters were in the absorption edge. The ZnS-rGO NSs' absorption coefficients, or "Urbach tails," demonstrated an exponential growth immediately below the free exciton peak.

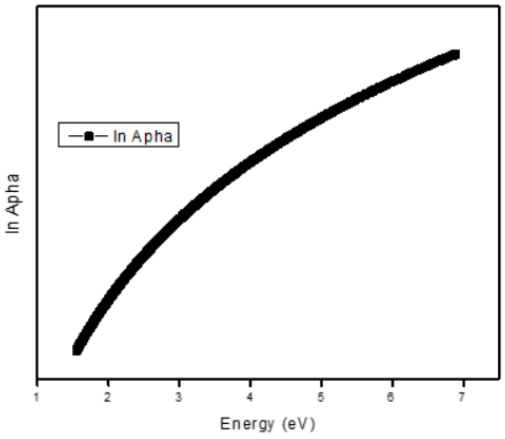

Figure 4.95: Natural logarithm Alpha of ZnS decorated with graphene.

2. Bandgap of 1Co-ZnS-rGO

The band gap of the synthesized $Co_{0.01}Zn0.99S$ rGO NSs was illustrated by the plot between $(\alpha hv)^2$ and hv in Figure 4.96. The direct band gap of pure $Co_{0.01}Zn0.99S$ rGO NSs was found to be 4.62 eV. The E_g value was obtained by extrapolating the linear portion to the photon energy axis in the figure 4.96. The structural bonding of ZnS, which was made by the $3d$ electrons in Co^{2+} atoms, may have become imperfect when Co^{2+} ions were substituted because they may have produced a dislocated or irregular atoms. The stimulated *s, p, d* exchange interaction by cobalt between the *s*

and p electrons from ZnS and $3d$ electrons from Co^{2+} ions may have been responsible for the reduction in energy gap P. Ghosh et al. (2007). The addition of Co^{2+} may have regenerated the newer energy levels closer to the valence band of ZnS which could be another possible reason for current shrinkage in energy gap Mote & Dole (2021).

By Co-doping, where Co^{2+} ions with smaller ionic radius can substitute Zn^{2+} ions at substitutional sites, the energy gap would be increased. The inclusion of Co^{2+} causes the Zn-Co-S lattice to release additional free charge carriers, changing the Fermi level and causing them to travel closer to the conduction band and reduce the energy gap Malek et al. (2015). The Burstein-Moss shift, or blue shift of energy gap, is the current improvement brought on by Co^{2+} doping J. Yang et al. (2013). The presence of poor crystallinity caused by Co^{2+} addition also significantly contributes to the widening of the energy gap Tan et al. (2005). When Co is added to ZnS, the energy gap decreases and at the same time, the size of the NSs increases slightly, obeying the size effect Yoon et al. (2008).

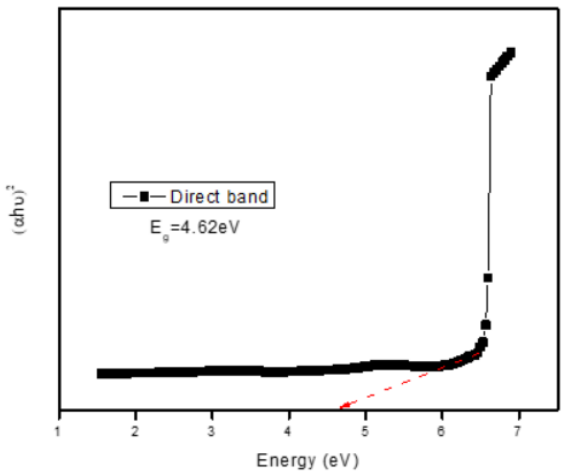

Figure 4.96: Direct band gap of 1% cobalt doped ZnS decorated with graphene.

As shown in Figure4.97, the band gap of the synthesized $Co_{0.01}Zn0.99S$ rGO NSs was obtained from the plot between $(\alpha hv)^{0.5}$ and hv. 1.94 eV is found to be the indirect band gap of pure 1Co-ZnS-rGO. Spin d exchange interactions

may be responsible for the red shift, or reduced band gap, that is seen at low doping concentrations. Band gap narrowing may result from an increase in the correction probabilities of the positive and negative potentials to the valence band edge and the conduction band, respectively, under the s-d and p-d exchange interactions.

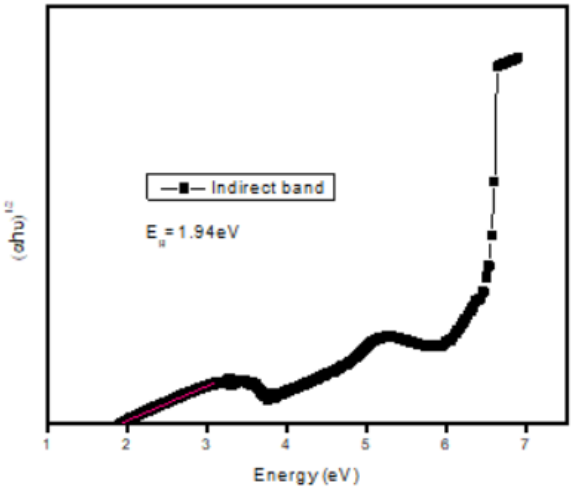

Figure 4.97: Indirect band gap of 1% cobalt doped ZnS decorated with graphene.

The exponential equation 4.16 defines the empirical Urbach rule, which governs the relationship between the optical absorption coefficient and photon energy. Figure 4.98 showed how Urbach energy was estimated by plotting $In\alpha$ against photon energy, where the reciprocal gradient of the straight line fitted to the curve yields the value of Urbach energy Melsheimer & Ziegler (1985). This allowed the examination of the impact of Co^{2+} ions on the transitions between the extended band tails of DOS in the valence and conduction bands. It is clear that an increase in Co^{2+} concentration progressively relies on an exponential rise in Urbach energy. Urbach energy behavior varies with Co^{2+} content and this can be attributed to defects in the structural bonding and expanding disordered atoms as a result of the introduction of $3d$ inter band states of Co^{2+} ions. According to Rai (2013), these findings have also been shown for other comparable doped semiconductors, such as pure ZnO. Urbach energy and optical band gap changes show that an increase in Co^{2+}

content broadens the Urbach energy while decreasing the optical band gap energy, in the opposite direction Chandrasekar et al. (2015).

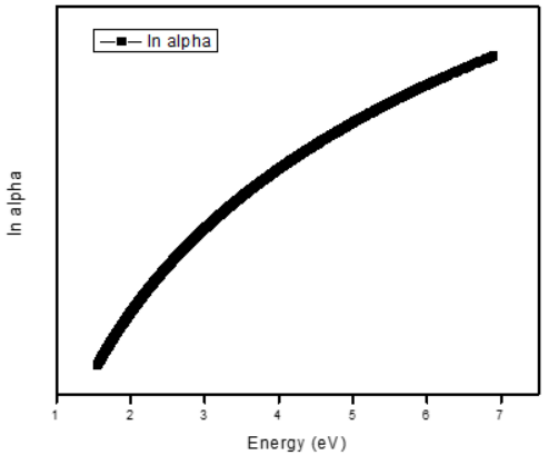

Figure 4.98: Natural logarithm Alpha of 1% cobalt doped ZnS decorated with graphene.

3. Bandgap of 2Co-ZnS-rGO

The band gap of the synthesized $Co_{0.02}Zn_{0.98}S$ rGO NSs were acquired from the plot between $(\alpha hv)^2$ and hv as revealed in Figure 4.99. The direct band gap of pure $Co_{0.02}Zn_{0.98}S$ rGO NSs was found to be 5.46 eV. It was clear that $Co_{0.02}Zn_{0.98}S$ rGO NSs samples exhibited a strong absorption edges band at UV region in the range of 180–340 nm and poor absorption at visible region. It was clearly that the direct band gap values of all $Co_{0.02}Zn_{0.98}S$ rGO NSs samples were greater than that of bulk ZnS (3.67 eV) and blue shift phenomenon occurred. The structural bonding of ZnS made by the $3d$ electrons in $Co2+$ atoms, became imperfect when $Co2+$ ions were substituted because they produced dislocations or irregular atoms. The stimulated s, p, d exchange interaction by cobalt between the s and p electrons from ZnS and $3d$ electrons from Co^{2+} ions may be responsible for the reduction in energy gap P. Ghosh et al. (2007). The addition of Co^{2+} re-generated the newer energy levels closer to the valence band of ZnS Mote & Dole (2021).

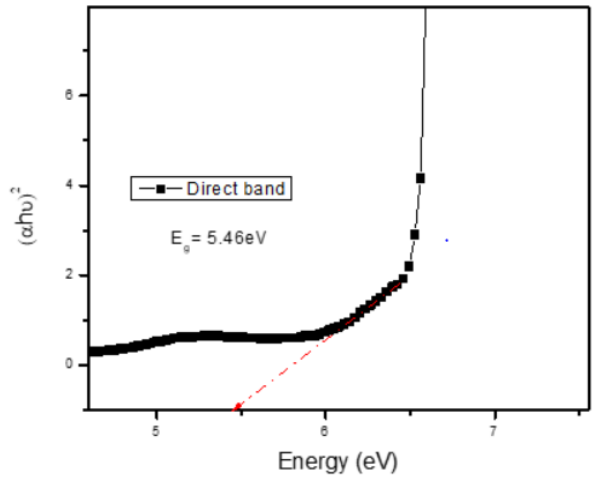

Figure 4.99: Direct Band Gap of 2Cobalt doped ZnS decorated with Graphene.

The plot between $(\alpha hv)^{0.5}$ and hv provided the band gap of the synthesized $Co_{0.02}Zn_{0.98}S$ rGO NSs, as shown in Figure 4.97. For pure $Co_{0.02}Zn_{0.98}S$ rGO NSs, the indirect band gap was measured and found to be 1.60 eV. At low doping concentration, the observed decreased band gap (red shift) might be explained by spin-d exchange interactions between s, p and d. The positive and negative potentials' correction probabilities to the valence band edge and the conduction band, respectively, are increased by exchange interactions between s and p, which might result in a reduction of the band gap.

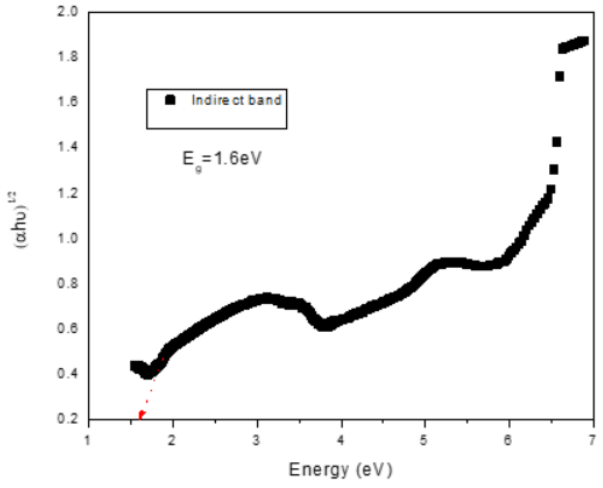

Figure 4.100: Indirect band gap of 2% cobalt doped ZnS decorated with graphene.

Figure 4.101 described how Urbach energy was estimated by plotting $In\alpha$ against photon energy, where the reciprocal gradient of the straight line fitted to the curve yields the value of Urbach energy Melsheimer & Ziegler (1985). This allowed the examination of the impact of Co^{2+} ions on the transitions between the extended band tails of density of states in the valence and conduction bands. It is clear that more increase of Co^{2+} concentration progressively relied on an exponential rise in Urbach energy. Urbach energy behavior varies with Co^{2+} content and this can be attributed to defects in the structural bonding and expanding disordered atoms as a result of the introduction of $3d$ inter band states of Co^{2+} ions.

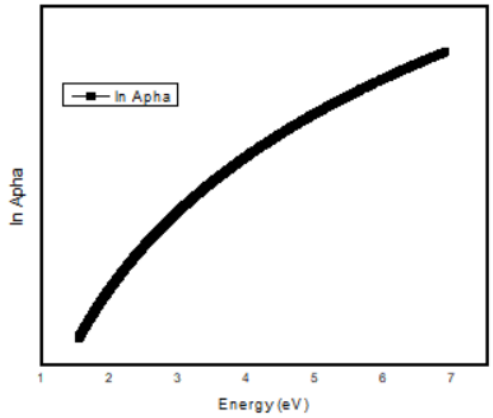

Figure 4.101: Natural logarithm Alpha of 2% cobalt doped ZnS decorated with graphene.

4. Bandgap of 4Co-ZnS-rGO

As shown in Figure4.102, the band gap of the fabricated $Co_{0.04}Zn_{0.96}S$ rGO NSs was obtained from the curve between $(\alpha hv)^2$ and hv. It was discovered that pure 4Co-ZnS-rGO NSs had a direct band gap of 4.99 eV. The results demonstrated that $Co_{0.04}Zn_{0.96}S$ rGO NSs samples may have had a weak absorption in the visible region and a high absorption edges band in UV range of 180-340 nm. The $Co_{0.04}Zn_{0.96}S$ rGO NSs had a direct band gap value that was evidently higher than bulk ZnS's (3.67 eV) with the blue shift phenomenon present. When Co^{2+} ions are substituted, dislocated or

irregular atoms are produced, which compromises the structural bonding of ZnS formed by the $3d$ electrons in Co^{2+} atoms. The lowering of energy gap is caused by the enhanced s, p and d exchange interaction of cobalt between the $3d$ electrons from Co^{2+} ions and the s, p electrons from ZnS P. Ghosh et al. (2007).

The energy gap may have enlarged by cobalt doping, where 4% of Co^{2+} ions with smaller ionic radius substituted Zn^{2+} ions at substitutional sites. The Zn-Co-S lattice may have been altered by the addition of Co, releasing more free charge carriers that move towards the conduction band and widen the energy gap by altering the Fermi level. The present improvement caused by Co doping is known as the Burstein-Moss shift, or blue shift of energy gap J. Yang et al. (2013).

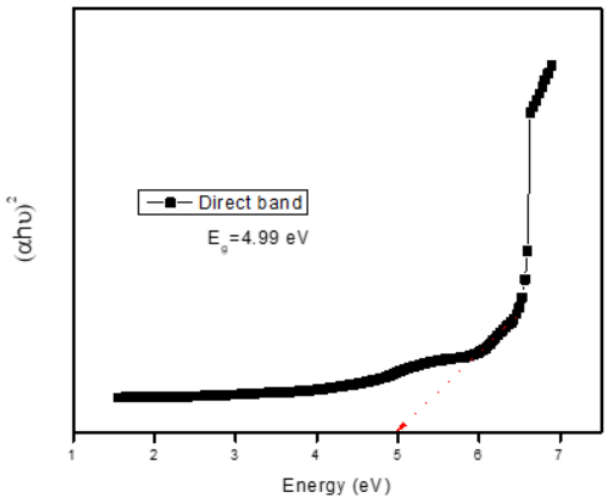

Figure 4.102: Direct band gap of 4% cobalt doped ZnS decorated with graphene.

As seen in Figure 4.103, the band gap of the developed $Co_{0.04}Zn_{0.96}S$ rGO NSs was displayed from the plot between $(\alpha hv)^{0.5}$ and hv. The indirect band gap of 1.48 eV for pure 4Co-ZnS-rGO NSs was found to exist. The s, p and d spin exchange interactions might represent the cause of the observed lowered band gap (red shift) at low doping concentration. The s, d and p d exchange interactions may contribute to band gap narrowing through improving the correction probability of the positive and negative potential

to the valence band edge and the conduction band respectively P. Ghosh et al. (2007); A. Sharma et al. (2021). It was clear that the direct band gap value of $Co_{0.04}Zn_{0.96}S$ rGO NSs were greater than that of bulk ZnS (3.67 eV) and blue shift phenomenon may have occurred. The structural bonding of ZnS, which may have been made by the $3d$ electrons in Co^{2+} atoms, might have been imperfect when Co^{2+} ions were substituted because they produced dislocated or irregular atoms. The addition of Co^{2+} may have regenerated the newer energy levels closer to the valence band of ZnS which could be a possible reason for current decrease in energy gap Mote & Dole (2021). The inclusion of 4% Co causes the Zn-Co-S lattice to release additional free charge carriers, changing the Fermi level and causing them to travel closer to the conduction band and widen the energy gap.

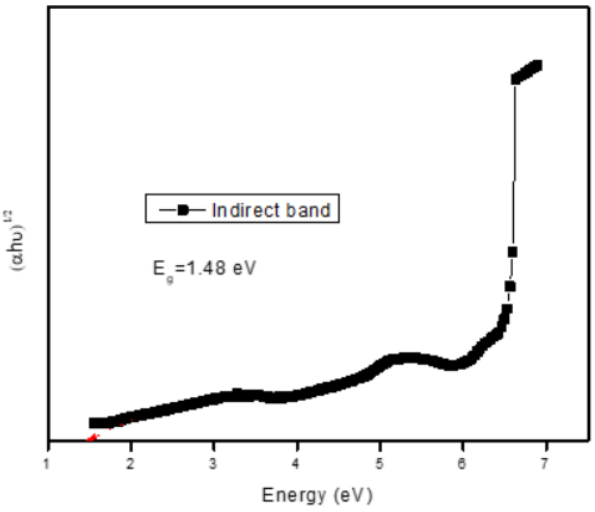

Figure 4.103: Indirect band gap of 4% cobalt doped ZnS decorated with graphene.

Urbach energy was determined by plotting $In\alpha$ against photon energy, as illustrated in Figure 4.104. The value of Urbach energy was determined by taking the reciprocal gradient of the straight line fitted to the curve Melsheimer & Ziegler (1985). This was made possible in order to investigate the effect of Co^{2+} ions on the transitions between the valence and conduction bands' extended band tails of density of states. It was evident that an exponential increase in Urbach energy was necessary for a further increase

in Co^{2+} concentration. As a result of defects in the structural bonding and the expansion of disordered atoms due to the introduction of $3d$ inter band states of Co^{2+} ions, Urbach energy behavior varies with Co^{2+} concentration.

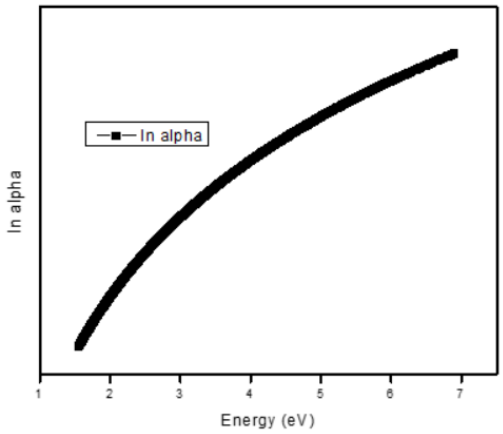

Figure 4.104: Natural logarithm Alpha of 4% cobalt doped ZnS decorated with graphene.

5. Bandgap of 6Co-ZnS-rGO

As demonstrated by Figure 4.105, the band gap of the synthesized $Co_{0.06}Zn_{0.94}S$ rGO NSs was obtained from the plot between $(\alpha hv)^2$ and hv. The direct band gap of pure $Co_{0.06}Zn_{0.94}S$ rGO NSs was found to be 5.23 eV. The findings show that all $Co_xZn_{1-x}S$ rGO NSs samples exhibited a significant absorption edges band in the UV range of 180-340 nm and modest absorption in the visible region. With the blue shift phenomena present, the direct band gap value of $Co_{0.06}Zn_{0.94}S$ rGO NSs was clearly larger than that of bulk ZnS 3.67 eV. Dislocated or irregular atoms are created when Co^{2+} ions are substituted, endangering the structural bonding of ZnS, which was formed by the $3d$ electrons in Co^{2+} atoms.

The improved s, p and d exchange interaction by cobalt between the s and p electrons from ZnS and the $3d$ electrons from Co^{2+} ions may have lowered the energy gap P. Ghosh et al. (2007). The addition of Co^{2+}, which regenerated the newer energy levels closer to ZnS's valence band, may have provided another logical explanation for the current reduction of the energy

gap Mote & Dole (2021). Cobalt doping may have widened the energy gap by allowing Co^{2+} ions with a lower ionic radius to replace Zn^{2+} ions at substitutional sites. The inclusion of cobalt may have modified the Zn-Co-S lattice, releasing more free charge carriers that migrate into the conduction band and change the Fermi level, so widening the energy gap. The blue shift of the energy gap, sometimes referred to as the Burstein-Moss shift J. Yang et al. (2013) may have been the cause of improvement brought about by Co doping.

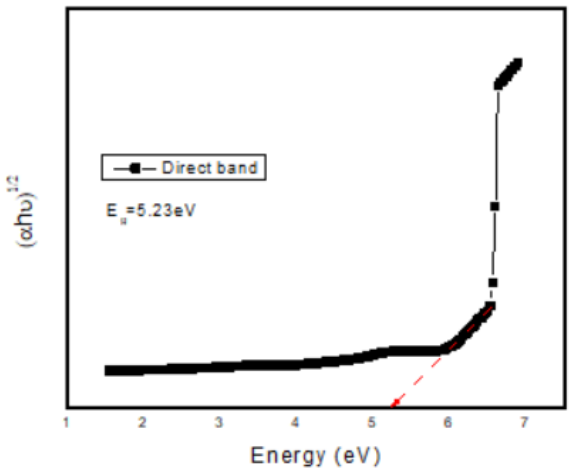

Figure 4.105: Direct band gap of 6% cobalt doped ZnS decorated with graphene.

The plot between $(\alpha hv)^{0.5}$ and hv provided the band gap of the synthesized $Co_{0.06}Zn_{0.94}S$ rGO NSs, as shown in Figure 4.106. It turns out that pure $Co_{0.06}Zn_{0.94}S$ rGO NSs, had an indirect band gap of 1.30 eV. The s-d and p spin exchange interactions could be the cause of the observed reduced band gap at low doping concentration. The s-d and s-p exchange interactions may have led to band gap narrowing by increasing the correction probability of the positive and negative potential to the valence band edge and the conduction band respectively. It was clear that the direct band gap values of $Co_{0.06}Zn_{0.94}S$ rGO NSs were greater than that of bulk ZnS 3.67 eV. The structural bonding of ZnS, which was made by the $3d$ electrons in Co^{2+} atoms, became imperfect when Co^{2+} ions were substituted because they

may have produced dislocated or irregular atoms.

The stimulated s, d and p exchange interaction by cobalt between the s and p electrons from ZnS and $3d$ electrons from Co^{2+} ions may have been responsible for the reduction in energy gap P. Ghosh et al. (2007). The addition of Co^{2+} regenerated the newer energy levels closer to the valence band of ZnS which could be a possible reason for current decrease in energy gap Mote & Dole (2021). By Cobalt doping, where 6% Co^{2+} ions with smaller ionic radius could substitute Zn^{2+} ions at substitutional sites, which may cause the energy gap to increase. The inclusion of Co may have caused the Zn-Co-S lattice to release additional free charge carriers, changing the Fermi level and causing them to travel closer to the conduction band and widen the energy gap. When Co is added to ZnS, the energy gap decreases and at the same time, the size of the NSs increases slightly, obeying the size effect Yoon et al. (2008); Kiptarus et al. (2023).

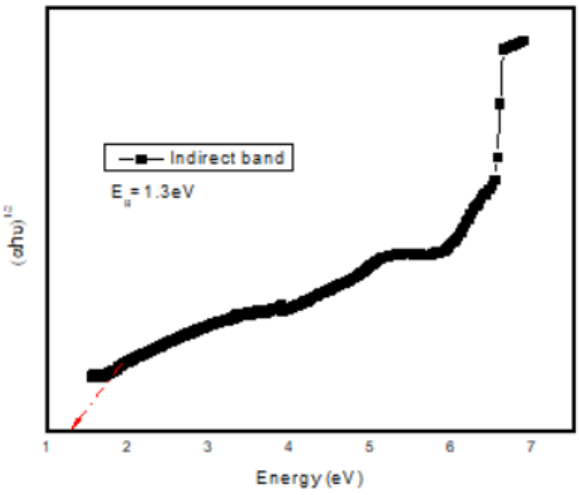

Figure 4.106: Indirect Band Gap of 6% Cobalt doped ZnS decorated with Graphene.

Plotting $In\alpha$ against photon energy allowed for the determination of Urbach energy, as shown in Figure 4.107. The reciprocal gradient of the straight line fitted to the curve was used to calculate the Urbach energy value Melsheimer & Ziegler (1985). This was made possible in order to study the impact

of Co^{2+} ions on the extended band tails of density of states transitioning between the valence and conduction bands. It is clear that a further increase in Co^{2+} concentration required an exponential increase in Urbach energy. Urbach energy behavior fluctuates with Co^{2+} concentration due to defects in the structural bonding and the expansion of disordered atoms caused by the introduction of $3d$ inter band states of Co^{2+} ions.

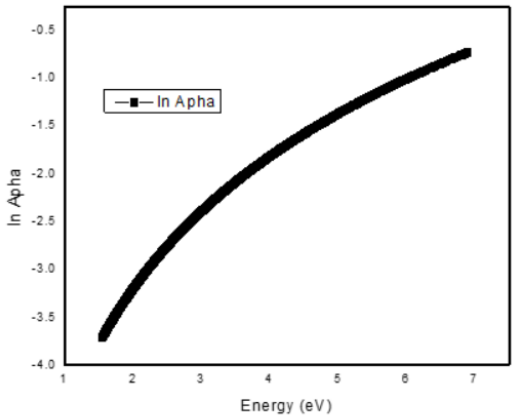

Figure 4.107: Natural logarithm Alpha of 6% cobalt doped ZnS decorated with graphene.

The band gap of ZnS NSs can be changed to modify their electronic characteristics. The massive band gap that doping creates, or the blue shift, can be connected to the confinement effect in nanostructure. The wavelength shift makes the material viable now in the UV spectrum. The optical band gap values were computed using a Tauc plot after experimental observations of $Co_xZn_{1-x}S$ rGO NSs. The band gap of pure $Co_xZn_{1-x}S$ rGO NSs at x = 0, 1, 2, 4 and 6 was found to be 4.86 eV, 4.62 eV, 5.46 eV, 4.99 eV, and 5.23 eV, respectively, when measured experimentally. The values of 0 eV, 1.94 eV, 1.60 eV, 1.48 eV and 1.30 eV were discovered for the indirect band gap at x = 0, 1, 2, 4 and 6 respectively. The band gap of graphene decorated cobalt doped ZnS changed with doping concentration. An energy blue shift was brought about by the expansion of the band gap brought on by increased doping.

The variation in the sample's absorption coefficient and the position of the

absorption peak may have been caused by the progressive doping substitution of the $Co_xZn_{1-x}S$ rGO NSs lattice. It is evident that all of the $Co_xZn_{1-x}S$ rGO NSs samples showed low absorption in the visible area and a high absorption edges band at the UV region, which ranges from 180 to 340 nm. The blue shift phenomenon was brought about by changes in the electronic transition's quantum size effect when NSs decreased, the energy gap widened and the optical absorption band shifted in the direction of short waves.

However, when surface tension is high and particle size is small, the lattice becomes distorted, lattice constants decrease, the bond length shortens due to internal distortion, and the infrared absorption band shifts to a higher wave number. This interface effect is what causes the spectral blue shift of nanomaterials and variations in the Co^{2+} content expand the Urbach energy and decrease the optical band gap energy in the opposite direction, as demonstrated by variations in the Urbach energy and optical band gap Chandrasekar et al. (2015)

4.4 Photo-activity evaluation of cobalt doped ZnS nanostructures surface layers decorated with graphene for photocatalytic hydrogen production

Photocatalytic hydrogen production performances of $Co_xZn_{1-x}S$ photocatalysts prepared with different (Co/Zn) precursor concentration ratios at (x= 0, 0.01, 0.02, 0.04, 0.06) with and without graphene decoration for water splitting recorded in Table B.3 and Table B.4 are demonstrated in Figure 4.108 (**a**) and Figure 4.109 (**a**) respectively. The results showed that hydrogen production rates of $Co_xZn_{1-x}S$ with and without rGO at (x=0.04) cobalt loading recorded the highest photocatalytic hydrogen production mean value after 720 minutes under UV light irradiation. According to the data presented in Figure 4.108 (**a**), the hydrogen

yield attained at the optimal cobalt loading at (x = 0.04) was 3201.562$\mu molh^{-1}$, whereas at (x = 0.06), the lowest hydrogen yield was 987.432$\mu molh^{-1}$. Additionally, as seen in Figure 4.109 (**a**), the hydrogen generation rates of $Co_xZn_{1-x}S$ rGO at (x = 0.04) recorded a maximum yield of 7648.9$\mu molh^{-1}$ and the lowest being 6% at 2398.7$\mu molh^{-1}$. This demonstrated that, under UV light irradiation, the photocatalytic reaction reached equilibrium after 720 minutes. Photo-catalyst with the largest surface area showed the highest hydrogen production efficiency.

All the $Co_xZn_{1-x}S$ rGO samples showed the highest mean value than for $Co_xZn_{1-x}S$ as demonstrated in Figure 4.108(**b**) and Figure 4.109(**b**) which describes the error bars for cobalt doped ZnS without and with graphene. The data mean error bars are presented in the column in Figure 4.108(**b**) and Figure 4.109(**b**) respectively, which also depict the data distribution. It is conclusively shown statistically that the maximum mean value of the hydrogen evolution rate occurs at a concentration of 4%. As can be seen in Figure 4.108(**b**), there are no appreciable differences across the data sets since the mean hydrogen evolution response for each sample group overlaps.

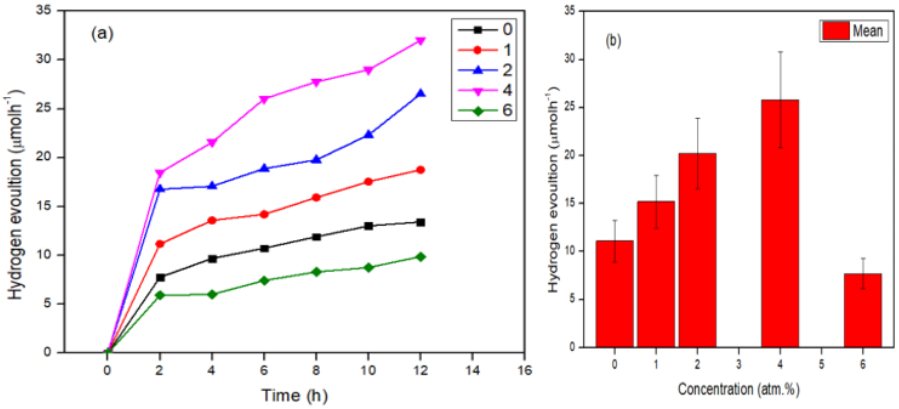

Figure 4.108: Variation of hydrogen production from pure cobalt doped ZnS NSs without graphene (**a**) treatment time, (**b**) concentration of cobalt; The error bars represent plus or minus one standard error of the mean.

The height of each column in the Figure 4.109 (**b**) represents the mean hydrogen generation of cobalt doped ZnS decorated with graphene. According to the graph, the concentration of 4% contributes the largest amount to the evolution

of hydrogen, while the concentration of 6% contributes the least. This could be explained by an overabundance of dopant, which results in lower absorption at the visible spectrum hence less evolution of hydrogen S. Cao & Piao (2020); S. Chen et al. (2017).

The current overlapping of error bars in these two figures indicates that concentration didn't cause any significant difference in hydrogen evolution and variability in the data can be attributed to systemic and random errors.

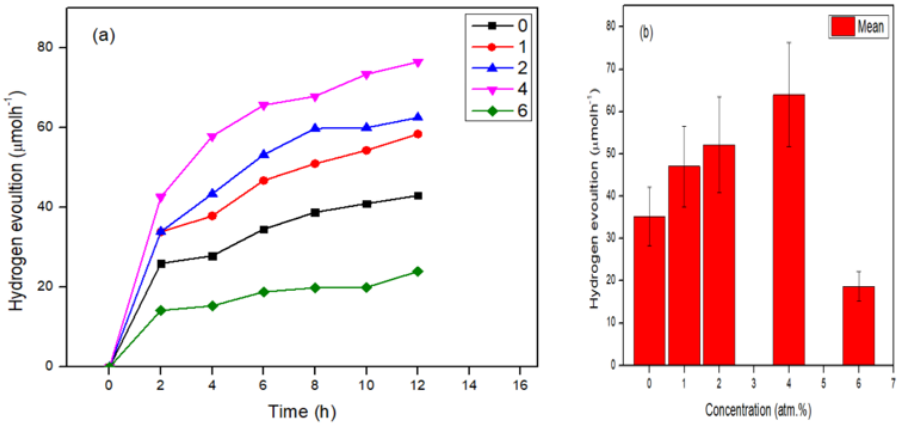

Figure 4.109: Variation of hydrogen production from pure cobalt doped ZnS NSs decorated with graphene (**a**) treatment time, (**b**) concentration of cobalt; The error bars represent plus or minus one standard error of the mean.

4.5 Optimization of cobalt doped ZnS decorated with graphene for hydrogen production

As indicated in Table B.6, the highest order polynomial was chosen, where the extra terms were significant and the model was not aliased. The model that maximized the Adjusted R^2 and the Predicted R^2, as shown in Table B.7, was the main focus. After factor coding, Type III - Partial sum of squares was obtained. According to Table B.8, the model's F-value of 309.01 indicates that it was significant. The probability of an F-value this large occurring owing to noise was merely 0.01%. The model terms were significant if the P-value was less than 0.0500. Sig-

nificant model terms in this instance included A, B, B^2, A^2B, A^3, A^2B^2, and A^4. The model terms were not significant if the values were higher than 0.1000.

The Adjusted R^2 of 0.9933 and the Predicted R^2 of 0.9712 agreed reasonably well; that is, Table B.9 shows that the difference was less than 0.2. The ratio of signal to noise was assessed by Adeq Precision. The model can be utilized to navigate the design space because a ratio of larger than 4 is preferred and 60.915 suggested an appropriate signal. As seen in Table B.10, the coefficient estimate indicated the expected change in response per unit change in factor value while all other factors were held constant. The total average response of all the runs in an orthogonal design was the intercept.

To predict the response for specific amounts of each element, the equation in terms of coded factors, as shown in Table B.11, was employed. To predict the response for specific amounts of each element, Table B.12 provided an equation in terms of the actual factors. In this case, the levels for each element were given in the original units.

4.5.1 Diagnostics

The Figure 4.110(**a**) shows that the data points are approximately linear hence normality in the error term. Residuals vs. Predicted checked for consistent variation across the prediction range and showed a random scatter of predicted residuals centred on zero as seen in Figure 4.110(**b**) hence no transformation was needed. There was really no cause for alarm since all the runs that differed from the predicted value were all within the red control limits as seen in the Figure 4.110(**c and d**).

A closer look into Box-Cox Plot Figure 4.111(**a**) provided further information about whether or not the data needed to be transformed. Plotting the log of the residual variation showed that the optimal transform was attained at the location where the log residual (y axis) was lowest. There was no need for a transform because the best transform (green line) was in relation to the transformation that

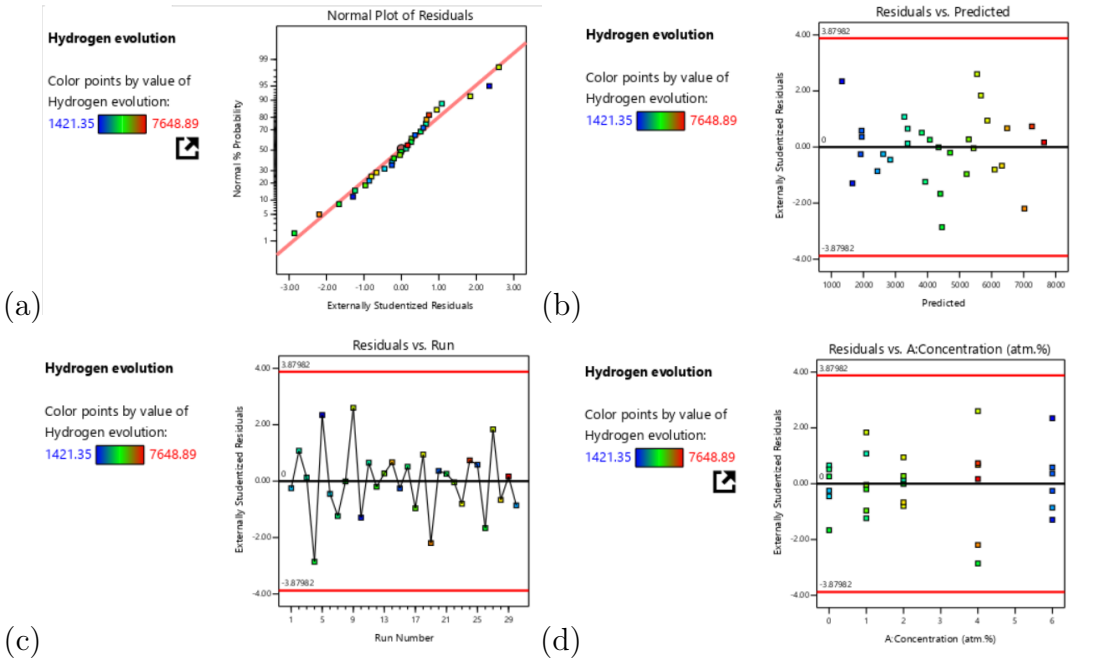

Figure 4.110: A plot of normal, residuals versus predicted, runs and concentration as a function of hydrogen evolution

was being used at the time (blue line) and was near to or within the 95% confidence interval (red lines).

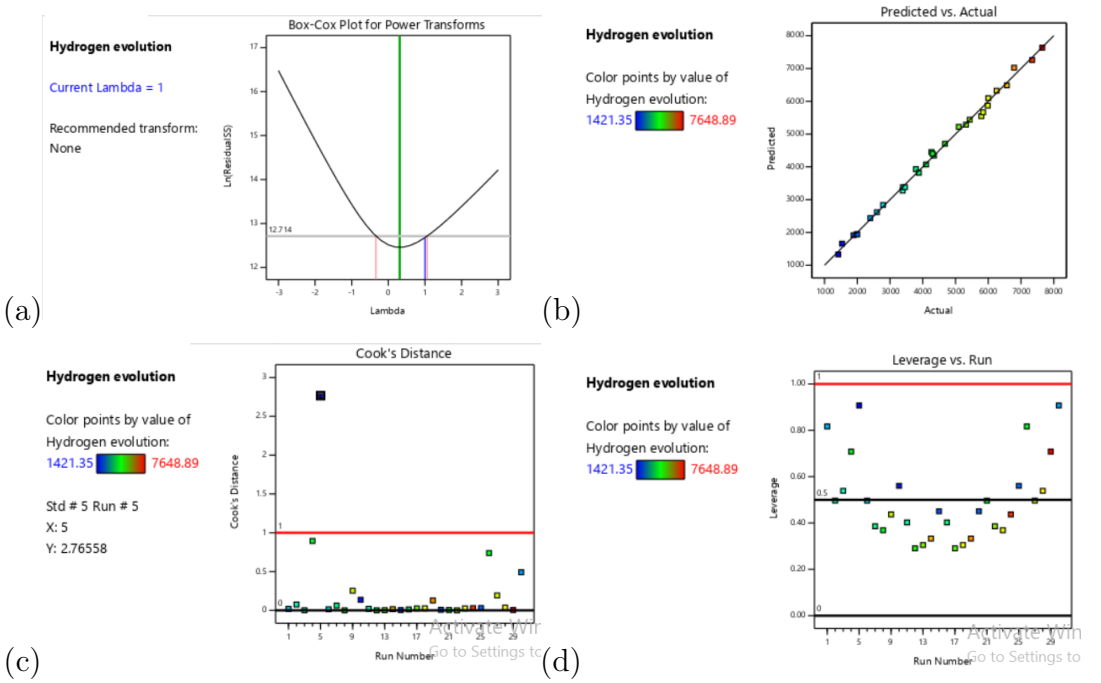

Figure 4.111: A plot of Box-Cox, predicted verse actual, cooks distance and leverage diagnosis

Since there was just one run outside of the range—highlighted run number 5

in Figure 4.112(**a**)—the other values remained under control. The following runs in the DFBETAS plot, as shown in Figure ⌋4.112(**b**), showed an outlier for few runs in which their levels fell below the threshold to start the reaction: 4, 9, 19 for A, 5 and 9 for B, and 4, 5, 9 and 26 for AB. As a result, this diagnostic was highly useful in identifying the areas of the experiment where things went wrong.

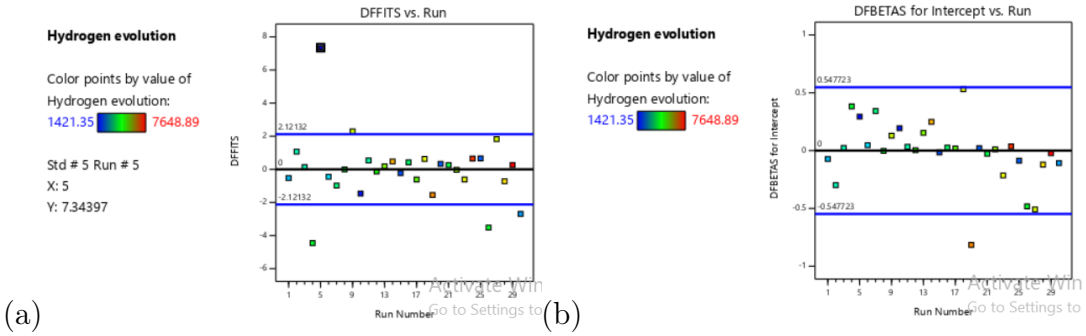

Figure 4.112: A plot of DFITS and DFBETAS diagnosis's

4.5.2 Model graphs

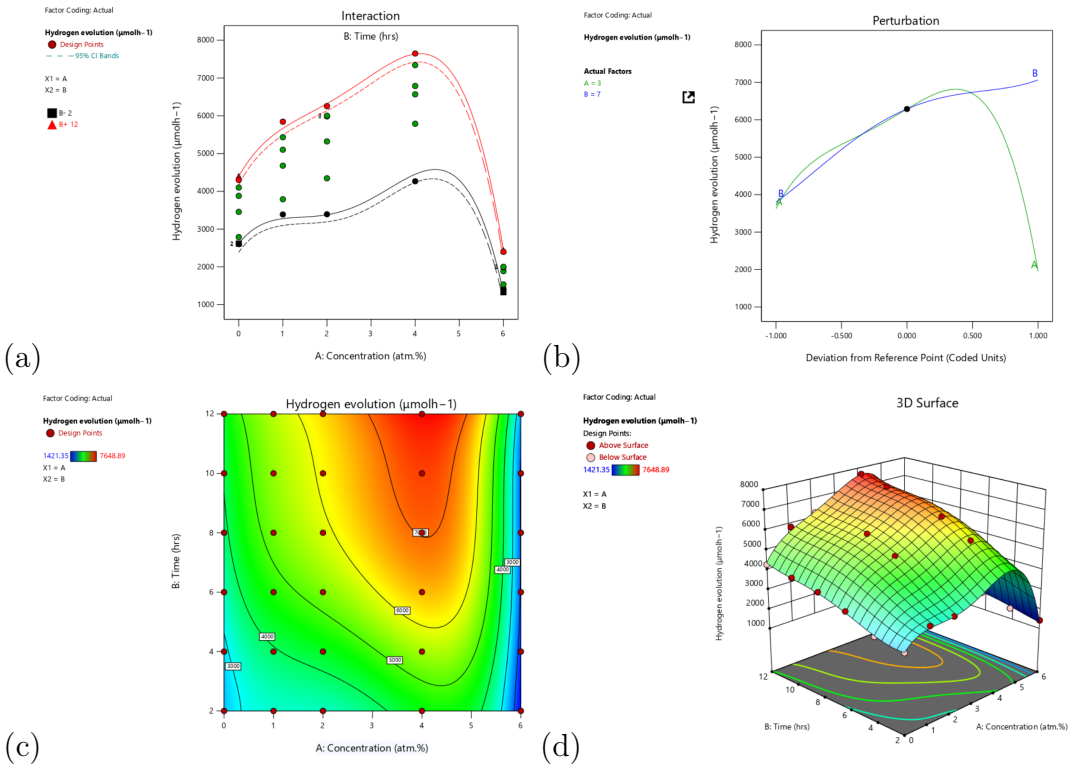

Figure 4.113: A plot of hydrogen evolution as a function of time and concentration

The use of perturbation plots makes it easier to see every factor at a given location in the design space on a single plot. The impacts of one, all or interacting factors were displayed, respectively, in the one factor, all factors and interactions plots. The plot of perturbations with all other factors held constant at the reference value. Figure 4.113(**a and b**) illustrates how the response varies as each factor travels away from the selected reference point. The middle of the design space, or the coded zero level of each factor was the reference point.

For response surface designs, the contour and 3D surface plot, which visualized the reaction over the two parameters, were especially helpful. As can be observed in Figure 4.113(**c**), the surface became 'hot' at higher response levels, turning yellow in the '6000s and red over 7000 for hydrogen evolution.

For an enhanced comprehension of how the response varied in relation to the two components, consider the response surface shown in Figure 4.113(**d**). This offered an incredibly strong impression of how to optimize the response.

4.5.3 Numerical optimization

Numerical optimization determined the maximum, minimum, in range or target for the hydrogen evolution model and also provided the greatest overall desirability as depicted.

Table 4.1: Constraints

Name	Goal	Lower Limit	Upper Limit	Lower Weight	Upper Weight	Importance
A:Concentration	is in range	0	6	1	1	3
B:Time	maximize	2	12	1	1	3
Hydrogen evolution	maximize	1421.35	7648.89	1	1	3

The constraints in Table 4.1 were optimized and 13 solutions were found as demonstrated in Table 4.2 for maximum hydrogen evolution yields. The criteria for the optimized factors (concentration and time) were selected at 4.11 atm.% and 12 hours respectively as shown in Table 4.3. The interaction between time and concentration showed that hydrogen production was maximum at 4.11 atm.% and 12 hours respectively as depicted in Figure 4.114 and Figure 4.115. The

Table 4.2: Solutions

Number	Concentration	Time	Hydrogen evolution	Desirability	
1	4.112	12.000	7644.336	1.000	Selected
2	4.136	12.000	7643.915	1.000	
3	4.075	12.000	7643.275	1.000	
4	4.166	12.000	7642.147	0.999	
5	4.030	12.000	7639.359	0.999	
6	4.213	12.000	7636.322	0.999	
7	4.000	12.000	7635.227	0.999	
8	3.857	12.000	7599.868	0.996	
9	4.351	12.000	7597.183	0.996	
10	4.415	12.000	7567.064	0.993	
11	3.698	12.000	7535.234	0.991	
12	4.537	12.000	7484.474	0.987	
13	3.550	12.000	7455.606	0.984	

interactions plots, showed the effects of one, all, or interacting factors.

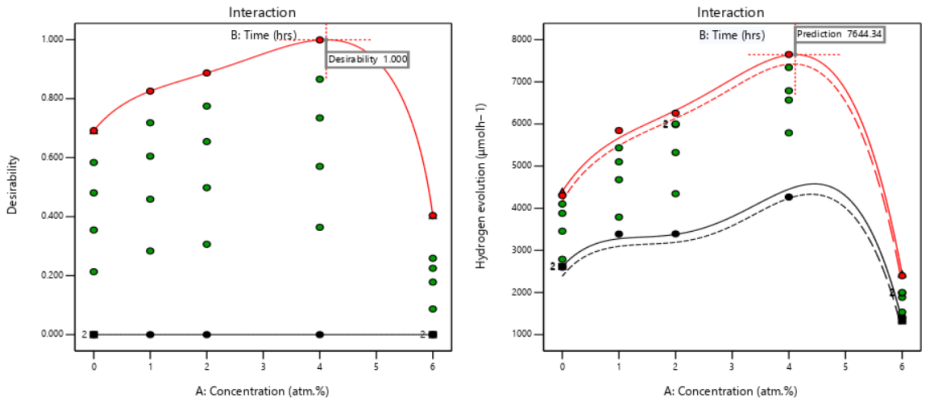

Figure 4.114: Interactions of desirability and hydrogen evolution as a function of time and concentration

Table 4.3: Factors

Factor	Name	Level	Low Level	High Level	Std. Dev.	Coding
A	Concentration	4.11	0.0000	6.00	0.0000	Actual
B	Time	12.00	2.00	12.00	0.0000	Actual

4.5.4 Point Prediction

Table 4.4 illustrates the point of prediction, showing the lower bound , Confidence = 95% and population = 99%.

Table 4.4: Point of prediction

Solution 1 of 9 Response	Predicted Mean	Predicted Median	Observed	Std Dev	SE Mean	95% CI low for Mean	95% CI high for Mean	95% TI low for 99% Pop	95% TI high for 99% Pop
Hydrogen evolution	7644.34	7644.34		146.388	126.666	7422.28		7016.23	

It was simpler to show every factor at a specific point in the design space on a single plot following optimization when perturbation plots were used. Figure 4.115 and Figure 4.116 showed how the response changed while keeping all other factors constant at the reference value.

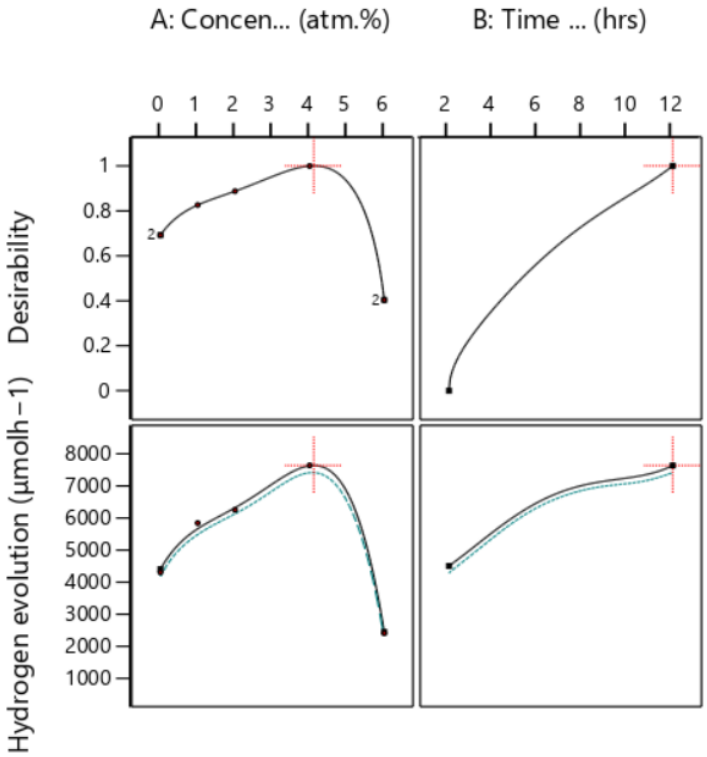

Figure 4.115: A plot of the desirability of time and concentration for hydrogen evolution

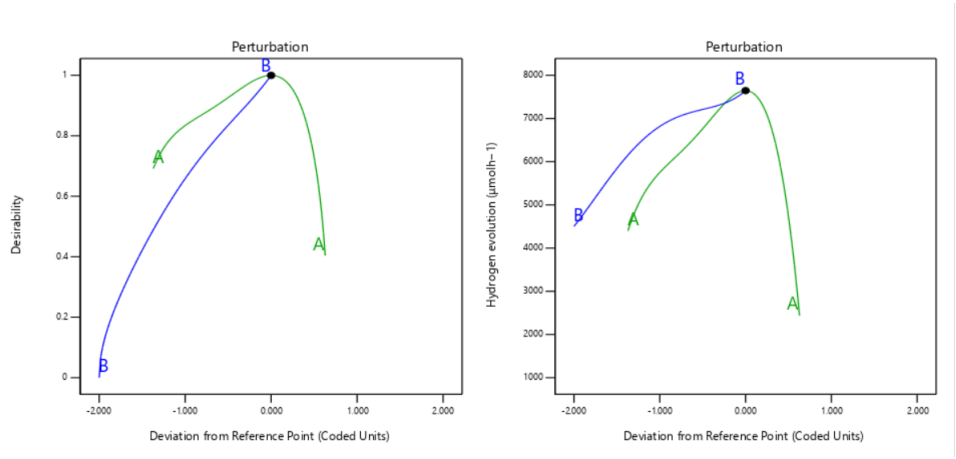

Figure 4.116: A plot of desirable perturbations for hydrogen evolution

Following optimization, as seen in Figures 4.117 and 4.118, respectively, the contour and 3D surface plot response over two factors became "hot" at higher response levels, yellow in the '6000's, and red above 7000 with a desirability of 0.999 with hydrogen evolution at 7644.34 $\mu molh^{-1}$ as the maximum yield which demonstrates a reliable prediction model with stable variances within a broad range of the independent variables. It is clear that to maximise yield it is necessary to have the high settings of concentration (X_1) and time (X_2) as shown in the overlay plot to get maximum hydrogen evolution as demonstrated in Figure 4.119 with a maximum yield at 7644.34 $\mu molh^{-1}$.

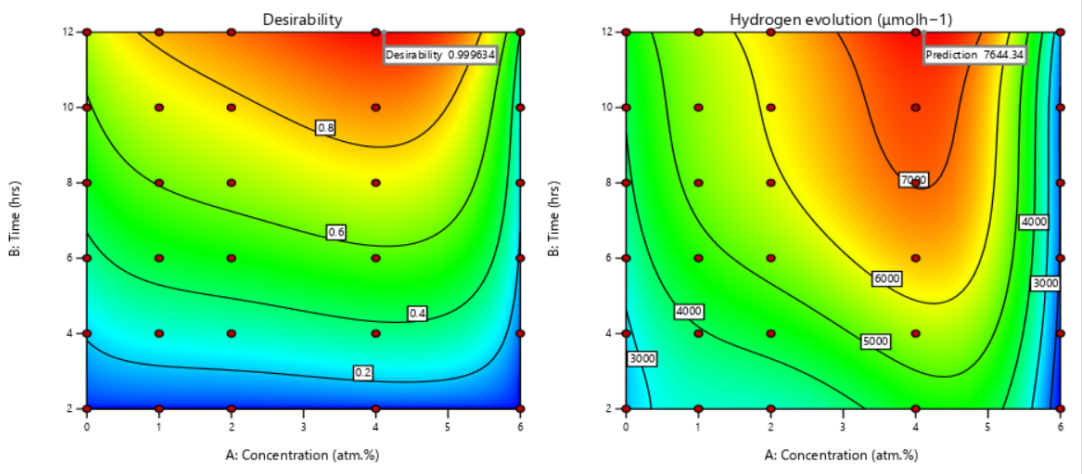

Figure 4.117: Contour desirability of hydrogen evolution as a function of time and concentration

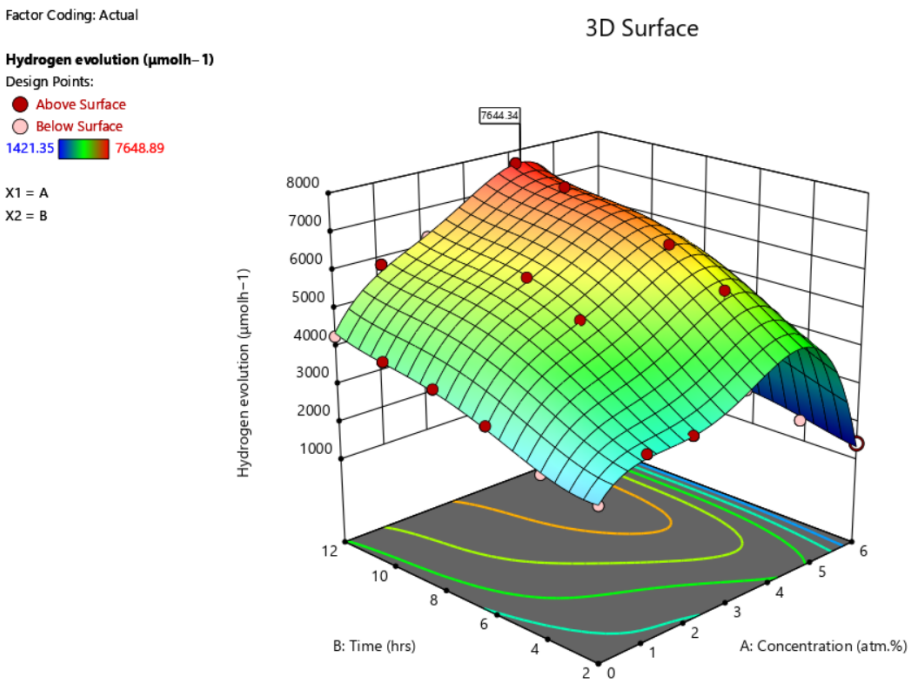

Figure 4.118: 3D surface response of hydrogen evolution

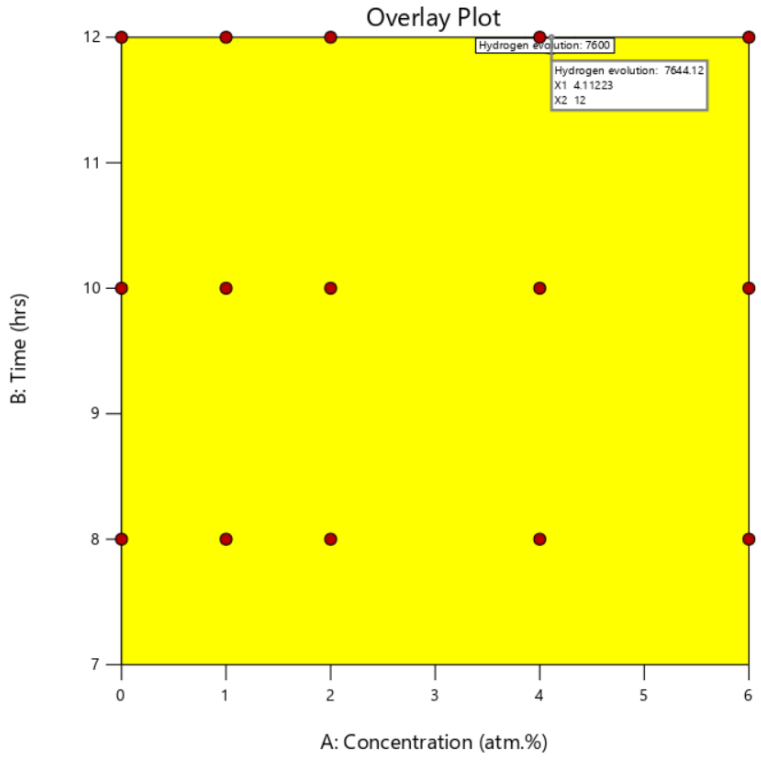

Figure 4.119: Overlay plot of hydrogen evolution as a function of time and concentration

4.6 Proposed mechanism of cobalt doped ZnS decorated with graphene for hydrogen production

To further understanding of how photo-generated charge carriers separate in Co, band structure computational study was performed Y. Zhu et al. (2020, 2024). The improved ZnS's photocatalytic activity was revealed by the use of cobalt doped ZnS band edge alignment computations. Normal hydrogen electrode (NHE), valence band maximal potential (VBM), and conduction band maximum (CBM) have been presented as a result of these analyses Z. Wang et al. (2023); Xi et al. (2021). According to density functional theory (DFT) calculations, the maximum position of cobalt conduction band at various concentrations is more negative than the reduction potential of H^+/H_2 (0.0 V vs. normal hydrogen electrode (NHE) at pH=0), suggesting that Co can be used for photocatalytic water splitting for H_2 evolution.

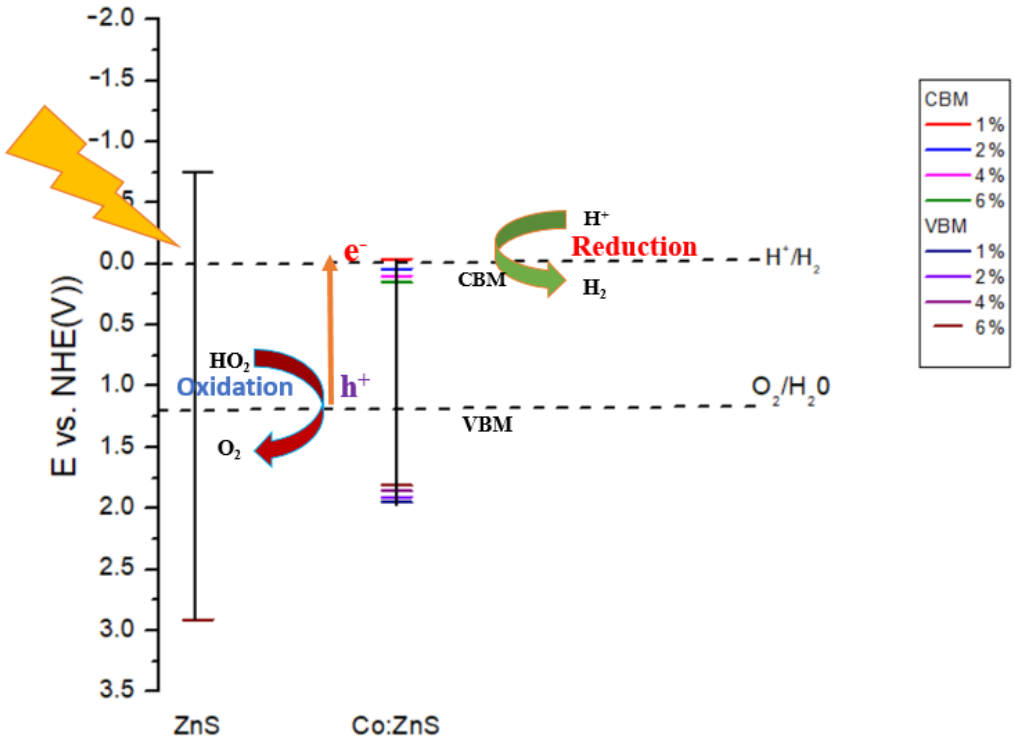

Figure 4.120: A schematic representation of the photo-generated charge carriers transfer channels and photocatalytic H_2 development for cobalt doped ZnS decorated with graphene

A charge transfer channel was predicted at the interface between Co and ZnS under visible light irradiation since, as Figure 4.120 demonstrates that the Co NSs have more negative conduction bands than ZnS, which permits efficient electron migration from cobalt to ZnS.

With the suggested mechanism referring to Figure 4.121, electrons (e^-) may be triggered from the valence band to the conduction band and migrate to the graphene sheets whenever the ZnS graphene photo-catalyst is subjected to light. Graphene electronic conductivity makes it a useful medium for transporting electrons generated by photons from ZnS's surface to graphene. Hydrogen can be created via the combination of the adsorbed (H^+) ions and electrons.

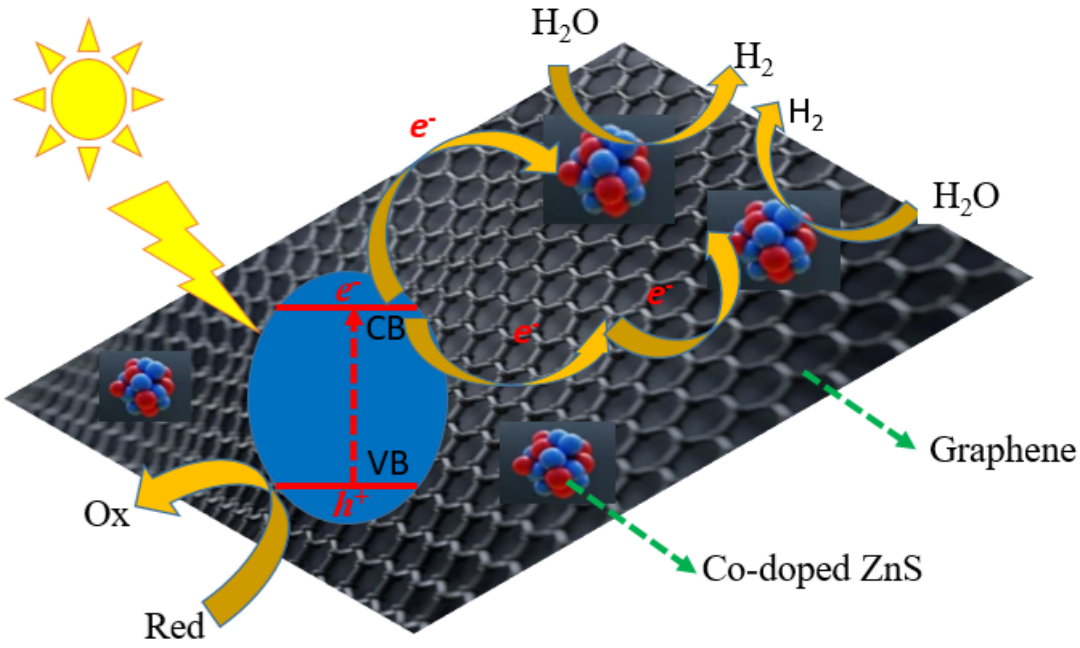

Figure 4.121: The proposed photocatalytic mechanism for cobalt doped ZnS decorated with graphene

Notably photocatalysts can exhibit a high degree of activity because photocatalytic hydrogen generating processes may occur over a larger reaction area, such as the ZnS surfaces and graphene layer S. Kumar et al. (2020). A similar process that enables charge transfer, separation, and photocatalytic hydrogen production in the reduced graphene oxide $Zn_xCd_{1-x}S$ system was proposed by Y. Zhang, Zhang, et al. (2012); Q. Li et al. (2014).

While Paulson et al. (2023) investigated the effects of interfacial contact on the characteristics of $\alpha - Fe2O3$@ rGO nanocomposite and their enhanced solar light photocatalysis, C.-J. Chang et al. (2015) proposed nickel doped ZnS festooned graphene composites. Furthermore, an improved visible light photocatalytic activity of ZnS/S-graphene quantum dots reinforced with Ag_2S nanoparticles for optical degradation was reported by Nekooei et al. (2022). A three-dimensional graphene-based photocatalyst was also proposed by N. R. A. M. Shah et al. (2021); this catalyst's structure may improve charge transfer, increase light adsorption, and broaden the accessible active surface, all of which could raise photocatalytic efficiency.

Chapter 5

Conclusion and Recommendation

5.1 Conclusion

The desire for hydrogen energy is sparked by the search for a clean energy that can replace conventional fossil fuels in an environmentally responsible manner. The creation of cost-effective and efficient catalysts for PEC water splitting is crucial for the production of hydrogen. Water and solar energy are abundant on earth and producing hydrogen using photocatalyst, water and solar simulated light is a sought technique since it is both environmentally and commercially viable. The current research has stepped up huge efforts in establishing and designing a photocatalytic material via a facile hydrothermal technique that can be used to produce hydrogen gas through the use of cheaply, non toxic and abundant cobalt doped ZnS NSs decorated with graphene, utilizing sunlight. From this work the following conclusions can be drawn;

Theoretical simulations showed that, the stability of TM dopants in 2D ZnS was critically dependent on the d character of the dopant, their concentration and dopant site. Incorporation of Mn, Fe, Co and Cu dopants in to 2D ZnS NSs surface layers induces band edge states which is ideal for PEC water splitting and other applications. From the results obtained it is evident that, TM dopants that produce little lattice strain, such as Co, Mn, Cu and Fe, can be readily

incorporated in to ZnS due to their low formation energies and appropriate band energies. The d states of Cu, Mn, Fe and Co and sulphur defects were responsible for the narrowing of the band gap of ZnS 2D layers.

In addition, Zn-rich synthesis conditions were found to be favorable for introduction of TM dopants compared to S-rich conditions with Cu and Co exhibiting the highest stability, whereas, Mn and Fe showing decreasing levels of stability. Mn and Fe (for dopant concentration between 1-6%) were found to induce reduction of band gap energy by 15-60% and 19-51%, respectively, while Cu and Co dopants of similar concentrations induced a more significant reduction of band gap energy by 37-78% and 26-75% respectively. Additionally, band edge alignment analysis showed that 2D ZnS doped with 4% and 2% Cu and Co falls below the redox potential of water (H^+/H_2), thus are projected to induce significant blue shift leading to improved PEC activity. Therefore, these finding can assist in the optimization of 2D ZnS for enhanced PEC water splitting.

Different $Co_xZn_{1-x}S$ rGO photocatalysts and visible light active nano-crystalline ZnS-rGO were fabricated utilizing a simple hydrothermal method. The influence of cobalt doping (0. 1, 2, 4 and 6 atm%) on the structure, morphology, optical characteristics and PEC performance of the hydrothermally synthesized TM doped ZnS NSs decorated with graphene were examined. The production of the Co doped ZnS NSs decorated with graphene revealed a crystalline cubic phase with crystallite sizes in the range of 11.1-23.5 nm and the lattice parameter (a) after doping were at lower levels of (5.394, 5.387, 5.377, 5.75, and 5.354) Åcompared to a standard value of 5.406 Å, this was validated by XRD, FTIR and RS.

GO was successfully converted into graphene sheets. Microscopy analysis revealed that the cobalt doped ZnS NSs decorated with graphene sheets had a spheroidal, cuboidal and paper like structure. XPS revealed the chemical information of solid surfaces of the cobalt doped ZnS decorated with graphene and the ability of cobalt dopant to have multiple oxidation states and potentially exchange them during reaction. In the UV wavelength region, UV-vis revealed a

highly transparent nanostructure in the wavelength range of 180-800 nm, as well as a discernible and quick increment in transmittance and band gaps were greatly reduced, as demonstrated by the blue shift that appeared at the ZnS absorption edge which may have resulted from rGO and Co doping.

The photocatalytic activity findings demonstrated that, after 720 minutes of UV light irradiation, the hydrogen production rates of $Co_xZn_{1-x}S$ with and without rGO at (x=0.04) cobalt loading recorded the greatest photocatalytic hydrogen production mean value. The results of $Co_xZn_{1-x}S$ show that the lowest hydrogen yield was $987.432\mu molh^{-1}$ at (x = 0.06), while the maximum hydrogen yield reached at the optimal cobalt loading at (x = 0.04) was $3201.562\mu molh^{-1}$. Furthermore, for $Co_xZn_{1-x}S$ rGO at (x = 0.04), the hydrogen generation rates showed a maximum yield of $7648.9\mu molh^{-1}$ and a minimum yield of 6% at $2398.7\mu molh^{-1}$. This showed that the photocatalytic reaction reached equilibrium after 720 minutes of UV light irradiation. The photocatalyst with the largest surface area had the highest efficiency of hydrogen production. Following optimization, thirteen solutions for the highest hydrogen evolution yields were obtained after the constraints were optimized. The criteria for the optimized factors, namely concentration and time, were determined to be 4.11 atm.% and 12 hours, respectively.

In this work, enhanced photocatalytic performances of graphene and cobalt doped ZnS may have resulted from good contact between ZnS NSs and graphene. The decoration of graphene sheets with Co-ZnS NSs may have potentially helped to prevent the agglomeration and restacking of the ($Co_xZn_{1-x}S$ rGO) NSs'. A distinctive design, which has a wide surface area, a more active sites, good electron transport characteristics and effective light harvesting and localizing capabilities. Graphene may have improved the transit of electrons photo-generated in ZnS NSs, increasing the photo conversion efficiency of the system because of the quantity of delocalized electrons from the conjugated sp^2 bonded carbon network. It is clear that the combination of graphene and cobalt doped ZnS NSs simultaneously solved almost all key thermodynamic and kinetic scientific problems in every step during

the photocatalysis. Consequently, the photocatalytic activities of the cobalt doped ZnS decorated with graphene were significantly increased, providing an intriguing possibility to create highly effective photocatalysts.

All elements of the theoretical research agreed with the experimental findings. The results showed how important it was to regulate Co doping and how the nanostructures' inclusion of graphene substantially reduced the rate of electron-hole recombination. Improved solar energy utilization came from the narrowing of band gaps brought on by the mutually beneficial interaction of rGO and Co in the nanostructures. Extensive analysis of its development, characterisation and hydrogen assessment methods demonstrated that cobalt doped ZnS decorated with graphene is an excellent photocatalyst for hydrogen synthesis. Furthermore, the results obtained showed that improved transfer of photo-generated electrons, increased surface area and better dispersion-absorption properties all contributed to higher photocatalytic hydrogen generation activity.

Based on the results obtained from the current research, I recommend the adoption of the present designed material system (cobalt doped ZnS decorated with graphene) because it provides the novel points in precise synthesis, mechanism exploration and application. This study adopts a facile hydrothermal and annealing reaction methods in the synthesis of pure cobalt doped ZnS decorated with graphene NSs. Indeed, hydrothermal method produced homogeneous, crystalline nanostructures as confirmed by XRD and SEM characterization techniques consistent with previous studies, thus provide validation. In addition, the mechanism for photo-electrochemical water splitting has been developed based on experimental measurements complemented with density functional analysis which showed the role of dopant in tuning the electronic band edge thus moderating its optical response. The main findings of this study were;

- DFT calculations with regards to the band alignment relative to the redox potential of water revealed that the valence band maximum of the different concentration of cobalt doped ZnS NSs remained strongly positive above the

oxidation potential of O_2/H_2O, favouring oxygen evolution with the reduction potential remaining negative below the reduction potential of H^+/H_2, thus maybe applicable in PEC.

- Extensive analysis of its development (simple hydrothermal technique) where noticeable improved solar energy utilization came from the narrowing of band gaps brought on by the mutually beneficial interaction of rGO and Co in the nanostructures.

- Characterization techniques such as XRD, XPS, RS, FTIR, UV-vis and SEM were conducted to investigate the structural, electronic and optical properties of the cobalt doped ZnS NSs surface layers decorated with graphene.

- Hydrogen assessment demonstrated that cobalt doped ZnS decorated with graphene was an excellent photo-catalyst for hydrogen synthesis.

5.2 Recommendation

The following are the areas of further studies which might improve the quality of the current work;

- It is strongly recommended that in situ and/or operando techniques be used in the future to enable exact control of characteristic parameters and real time monitoring, which may provide exceptional insights into the hydrogen production process. By improving the associated ex situ procedures, this methodology can help expose specifics about the properties, such as structural, chemical, morphological and other changes which can be further improved to fulfill commercial requirements

- Future work on synthesis optimization is necessary to build commercially viable technology

- To investigate the studied photocatalytic materials, a functioning prototype that can be integrated into commercial reactors should be established.

References

Abdul Nasir, J., Munir, A., Ahmad, N., Haq, T. u., Khan, Z., & Rehman, Z. (2021). Photocatalytic z-scheme overall water splitting: Recent advances in theory and experiments. *Advanced Materials*, *33*(52), 2105195.

Abraham, N., & Probert, M. (2008). Improved real-space genetic algorithm for crystal structure and polymorph prediction. *Physical Review B*, *77*(13), 134117.

Abraham, N. L., & Probert, M. I. (2006). A periodic genetic algorithm with real-space representation for crystal structure and polymorph prediction. *Physical Review B*, *73*(22), 224104.

Adams, D. M., Brus, L., Chidsey, C. E., Creager, S., Creutz, C., Kagan, C. R., ... others (2003). Charge transfer on the nanoscale: current status. *The Journal of Physical Chemistry B*, *107*(28), 6668–6697.

Adetayo, A., Runsewe, D., et al. (2019). Synthesis and fabrication of graphene and graphene oxide: A review. *Open journal of composite materials*, *9*(02), 207.

Agorku, E. S., Mamo, M. A., Mamba, B. B., Pandey, A. C., & Mishra, A. K. (2015). Cobalt-doped zns-reduced graphene oxide nanocomposite as an advanced photocatalytic material. *Journal of Porous Materials*, *22*, 47–56.

Ahmad, H., Kamarudin, S., Minggu, L. J., & Kassim, M. (2015). Hydrogen from photo-catalytic water splitting process: A review. *Renewable and Sustainable Energy Reviews*, *43*, 599–610.

Ahmed, M. A., & Mohamed, A. A. (2023). Recent progress in semiconductor/graphene photocatalysts: synthesis, photocatalytic applications, and challenges. *RSC advances*, *13*(1), 421–439.

Akhtar, A., Boochani, A., Elahi, S. M., Amiri, M., & Molamohammadi, M. (2017). Reflectivity and refractivity index enhancement in h doped zns graphene sheet: A first-principles study. *Optik*, *144*, 446–458.

Akhtar, M. S., Alghamdi, Y. G., Malik, M. A., Khalil, R. M. A., Riaz, S., & Naseem, S. (2015). Structural, optical, magnetic and half-metallic studies of cobalt doped zns thin films deposited via chemical bath deposition. *Journal of Materials Chemistry C*, *3*(26), 6755–6763.

Aliofkhazraei, M., Walsh, F. C., Zangari, G., Köçkar, H., Alper, M., Rizal, C., ... others (2021). Development of electrodeposited multilayer coatings: A re-

view of fabrication, microstructure, properties and applications. *Applied Surface Science Advances*, *6*, 100141.

Almuhammady, A. K., Salem, K. F., Alloosh, M. T., Saleh, M. M., Alnaddaf, L. M., & Al-Khayri, J. M. (2021). Nanomaterials fundamentals: Classification, synthesis and characterization. *Nanobiotechnology: Mitigation of Abiotic Stress in Plants*, 77–99.

Amirav, L., & Alivisatos, A. P. (2010). Photocatalytic hydrogen production with tunable nanorod heterostructures. *The Journal of Physical Chemistry Letters*, *1*(7), 1051–1054.

Amutha, R., Lee, G.-J., Wu, J. J., Sathish, M., & Sillanpää, M. E. (2013). Synthesis and electrochemical properties of biporous α-fe2o3 superstructures. *Journal of Nanoscience and Nanotechnology*, *13*(10), 6635–6643.

An, X., & Jimmy, C. Y. (2011). Graphene-based photocatalytic composites. *Rsc Advances*, *1*(8), 1426–1434.

Arai, T., Senda, S.-i., Sato, Y., Takahashi, H., Shinoda, K., Jeyadevan, B., & Tohji, K. (2008). Cu-doped zns hollow particle with high activity for hydrogen generation from alkaline sulfide solution under visible light. *Chemistry of Materials*, *20*(5), 1997–2000.

Arutyunov, V. S., & Lisichkin, G. V. (2017). Energy resources of the 21st century: Problems and forecasts. can renewable energy sources replace fossil fuels. *Russian Chemical Reviews*, *86*(8), 777.

Ashokkumar, R., Geetha, K., & Prabukanthan, P. (2015). Synthesis of ni2+ionsdopped znsnano particles by chemical precipitation method and their characterization. *Journal of Non-Oxide Glasses Vol*, *7*(1), 13–21.

Axelevitch, A., & Apter, B. (2017). Preparation and study of doped zns thin films. *Microelectronic Engineering*, *170*, 39–43.

Azouaoui, A., Haoua, M. E., Salmi, S., Grini, A. E., Benzakour, N., Hourmatallah, A., & Bouslykhane, K. (2020). Structural, electronic, and magnetic properties of m n 4 n perovskite: Density functional theory calculations and monte carlo study. *Journal of Superconductivity and Novel Magnetism*, *33*, 1507–1512.

Bai, S., Zhang, N., Gao, C., & Xiong, Y. (2018). Defect engineering in photocatalytic materials. *Nano Energy*, *53*, 296–336.

Balayeva, N. O., & Mamiyev, Z. (2022). Integrated processes involving adsorption, photolysis, and photocatalysis. In *Hybrid and combined processes for air pollution control* (pp. 117–153). Elsevier.

Balayeva, N. O., & Mamiyev, Z. Q. (2016). Synthesis and characterization of ag2s/pva-fullerene (c60) nanocomposites. *Materials Letters*, *175*, 231–235.

Bang, J. H., Helmich, R. J., & Suslick, K. S. (2008). Nanostructured zns: Ni2+ photocatalysts prepared by ultrasonic spray pyrolysis. *Advanced Materials*,

20(13), 2599–2603.

Baran, T., Wojtyła, S., Dibenedetto, A., Aresta, M., & Macyk, W. (2015). Zinc sulfide functionalized with ruthenium nanoparticles for photocatalytic reduction of co2. *Applied Catalysis B: Environmental*, *178*, 170–176.

Barceloux, D. G., & Barceloux, D. (1999). Cobalt. *Journal of Toxicology: Clinical Toxicology*, *37*(2), 201–216.

Barhoum, A., & García-Betancourt, M. L. (2018). Physicochemical characterization of nanomaterials: Size, morphology, optical, magnetic, and electrical properties. In *Emerging applications of nanoparticles and architecture nanostructures* (pp. 279–304). Elsevier.

Batlle, X., Moya, C., Escoda-Torroella, M., Iglesias, Ò., Rodríguez, A. F., & Labarta, A. (2022). Magnetic nanoparticles: From the nanostructure to the physical properties. *Journal of Magnetism and Magnetic Materials*, *543*, 168594.

Bauer, C., Treyer, K., Antonini, C., Bergerson, J., Gazzani, M., Gencer, E., ... others (2022). On the climate impacts of blue hydrogen production. *Sustainable Energy & Fuels*, *6*(1), 66–75.

Baumgart, E. (2000). Stiffness—an unknown world of mechanical science. *Injury*, *31*(Suppl 2), B14–23.

Baye, A. F., Appiah-Ntiamoah, R., Amalraj, J., Reddy, K. K., & Kim, H. (2020). Graphene oxide interlayered ga-doped fese2 nanorod: a robust nanocomposite with ideal electronic structure for electrochemical dopamine detection. *Electrochimica Acta*, *363*, 137245.

B Djurisic, A., Y Chen, X., & H Leung, Y. (2012). Recent progress in hydrothermal synthesis of zinc oxide nanomaterials. *Recent patents on nanotechnology*, *6*(2), 124–134.

Bell, N. J., Ng, Y. H., Du, A., Coster, H., Smith, S. C., & Amal, R. (2011). Understanding the enhancement in photoelectrochemical properties of photocatalytically prepared tio2-reduced graphene oxide composite. *The Journal of Physical Chemistry C*, *115*(13), 6004–6009.

Bellani, S., Antognazza, M. R., & Bonaccorso, F. (2019). Carbon-based photocathode materials for solar hydrogen production. *Advanced Materials*, *31*(9), 1801446.

Belver, C., Bedia, J., Gómez-Avilés, A., Peñas-Garzón, M., & Rodriguez, J. J. (2019). Semiconductor photocatalysis for water purification. In *Nanoscale materials in water purification* (pp. 581–651). Elsevier.

Berthomieu, C., & Hienerwadel, R. (2009). Fourier transform infrared (ftir) spectroscopy. *Photosynthesis research*, *101*, 157–170.

Bhargava, R., Gallagher, D., Hong, X., & Nurmikko, A. (1994). Optical properties

of manganese-doped nanocrystals of zns. *Physical Review Letters*, *72*(3), 416.

Bokobza, L., Bruneel, J.-L., & Couzi, M. (2014). Raman spectroscopy as a tool for the analysis of carbon-based materials (highly oriented pyrolitic graphite, multilayer graphene and multiwall carbon nanotubes) and of some of their elastomeric composites. *Vibrational Spectroscopy*, *74*, 57–63.

Bokov, D., Turki Jalil, A., Chupradit, S., Suksatan, W., Javed Ansari, M., Shewael, I. H., ... Kianfar, E. (2021). Nanomaterial by sol-gel method: synthesis and application. *Advances in Materials Science and Engineering*, *2021*, 1–21.

Bol, A., & Meijerink, A. (1998). Long-lived mn 2+ emission in nanocrystalline z n s: M n 2+. *Physical Review B*, *58*(24), R15997.

Bonde, J., Moses, P. G., Jaramillo, T. F., Nørskov, J. K., & Chorkendorff, I. (2009). Hydrogen evolution on nano-particulate transition metal sulfides. *Faraday discussions*, *140*, 219–231.

Boretti, A. (2023). *Supply of abundant and low-cost total primary energy to a growing world needs nuclear energy and hydrogen energy storage* (Vol. 48) (No. 5). Elsevier.

Bourgoin, J. (2012). *Point defects in semiconductors ii: Experimental aspects* (Vol. 35). Springer Science & Business Media.

Brovelli, S., Schaller, R. D., Crooker, S., García-Santamaría, F., Chen, Y., Viswanatha, R., ... Klimov, V. I. (2011). Nano-engineered electron–hole exchange interaction controls exciton dynamics in core–shell semiconductor nanocrystals. *Nature communications*, *2*(1), 280.

Bunaciu, A. A., UdriŞTioiu, E. G., & Aboul-Enein, H. Y. (2015). X-ray diffraction: instrumentation and applications. *Critical reviews in analytical chemistry*, *45*(4), 289–299.

Burda, C., Lou, Y., Chen, X., Samia, A. C., Stout, J., & Gole, J. L. (2003). Enhanced nitrogen doping in tio2 nanoparticles. *Nano letters*, *3*(8), 1049–1051.

Burstein, E. (1954). Anomalous optical absorption limit in insb. *Physical review*, *93*(3), 632.

Caizer, C. (2016). Nanoparticle size effect on some magnetic properties. *Handbook of nanoparticles*, *475*.

Cao, S., & Piao, L. (2020). Considerations for a more accurate evaluation method for photocatalytic water splitting. *Angewandte Chemie International Edition*, *59*(42), 18312–18320.

Cao, S., Zhao, C., Han, T., & Peng, L. (2016). Hydrothermal synthesis, characterization and gas sensing properties of the wo3 nanofibers. *Materials Letters*, *169*, 17–20.

Cao, X., He, Q., Shi, W., Li, B., Zeng, Z., Shi, Y., ... Zhang, H. (2011). Graphene

oxide as a carbon source for controlled growth of carbon nanowires. *Small*, *7*(9), 1199–1202.

Cassone, G. (2020). Nuclear quantum effects largely influence molecular dissociation and proton transfer in liquid water under an electric field. *The journal of physical chemistry letters*, *11*(21), 8983–8988.

Cavaliere, P. (2023). Electrocatalysts for water splitting. In *Water electrolysis for hydrogen production* (pp. 383–426). Springer.

Chabou, N., Birouk, B., Aida, M., & Raskin, J.-P. (2019). Deposition time and annealing effects on morphological and optical properties of zns thin films prepared by chemical bath deposition. *Mater. Sci.-Pol*, *37*(3), 404–416.

Chai, B., Xu, M., Yan, J., & Ren, Z. (2018). Remarkably enhanced photocatalytic hydrogen evolution over mos2 nanosheets loaded on uniform cds nanospheres. *Applied Surface Science*, *430*, 523–530.

Chai, L., Du, J., Xiong, S., Li, H., Zhu, Y., & Qian, Y. (2007). Synthesis of wurtzite zns nanowire bundles using a solvothermal technique. *The Journal of Physical Chemistry C*, *111*(34), 12658–12662.

Chan, M. K., & Ceder, G. (2010). Efficient band gap prediction for solids. *Physical review letters*, *105*(19), 196403.

Chandrasekar, L. B., Chandramohan, R., Vijayalakshmi, R., & Chandrasekaran, S. (2015). Preparation and characterization of mn-doped zns nanoparticles. *International Nano Letters*, *5*, 71–75.

Chang, C.-J., Chu, K.-W., Hsu, M.-H., & Chen, C.-Y. (2015). Ni-doped zns decorated graphene composites with enhanced photocatalytic hydrogen-production performance. *International Journal of Hydrogen Energy*, *40*(42), 14498–14506.

Chang, S.-H., Lu, M.-D., Tung, Y.-L., & Tuan, H.-Y. (2013). Gram-scale synthesis of catalytic co9s8 nanocrystal ink as a cathode material for spray-deposited, large-area dye-sensitized solar cells. *ACS nano*, *7*(10), 9443–9451.

Chauhan, A., Sudhaik, A., Raizada, P., Khan, A. A. P., Singh, A., Van Le, Q., ... others (2023). Enhancement strategies for znse based photocatalysts: application to environmental remediation and energy conversion. *Process Safety and Environmental Protection*, *170*, 415–435.

Chaurasiya, R., & Dixit, A. (2019). Transition metal doped zns monolayer: the first principles insights. In *The physics of semiconductor devices: Proceedings of iwpsd 2017* (pp. 49–56).

Chen, A., & Holt-Hindle, P. (2010). Platinum-based nanostructured materials: synthesis, properties, and applications. *Chemical reviews*, *110*(6), 3767–3804.

CHEN, B. (2016). Ascorbic acid go reduction as alternative rgo production.

Chen, H., Wan, K., Zheng, F., Zhang, Z., Zhang, Y., & Long, D. (2021). Mecha-

nism insight into photocatalytic conversion of lignin for valuable chemicals and fuels production: A state-of-the-art review. *Renewable and Sustainable Energy Reviews*, *147*, 111217.

Chen, J., Li, Y., Huang, L., Li, C., & Shi, G. (2015). High-yield preparation of graphene oxide from small graphite flakes via an improved hummers method with a simple purification process. *Carbon*, *81*, 826–834.

Chen, L., Msigwa, G., Yang, M., Osman, A. I., Fawzy, S., Rooney, D. W., & Yap, P.-S. (2022). Strategies to achieve a carbon neutral society: a review. *Environmental Chemistry Letters*, *20*(4), 2277–2310.

Chen, P., Lee, G., Davies, S., Masten, S., Amutha, R., & Wu, J. (2013). Hydrothermal synthesis of coral-like au/zno catalyst and photocatalytic degradation of orange ii dye. *Materials Research Bulletin*, *48*(6), 2375–2382.

Chen, P., Ye, J., Wang, H., Ouyang, L., & Zhu, M. (2021). Recent progress of transition metal carbides/nitrides for electrocatalytic water splitting. *Journal of Alloys and Compounds*, *883*, 160833.

Chen, P.-K., Lee, G.-J., Anandan, S., & Wu, J. J. (2012). Synthesis of zno and au tethered zno pyramid-like microflower for photocatalytic degradation of orange ii. *Materials Science and Engineering: B*, *177*(2), 190–196.

Chen, S., Huang, D., Xu, P., Xue, W., Lei, L., Cheng, M., ... Deng, R. (2020). Semiconductor-based photocatalysts for photocatalytic and photoelectrochemical water splitting: will we stop with photocorrosion? *Journal of Materials Chemistry A*, *8*(5), 2286–2322.

Chen, S., Takata, T., & Domen, K. (2017). Particulate photocatalysts for overall water splitting. *Nature Reviews Materials*, *2*(10), 1–17.

Chen, W., Yan, L., & Bangal, P. R. (2010). Preparation of graphene by the rapid and mild thermal reduction of graphene oxide induced by microwaves. *Carbon*, *48*(4), 1146–1152.

Chen, X., Lou, Y., Dayal, S., Qiu, X., Krolicki, R., Burda, C., ... Becker, J. (2005). Doped semiconductor nanomaterials. *Journal of nanoscience and nanotechnology*, *5*(9), 1408–1420.

Chen, X., Yang, N., Liu, X., & Yu, R. (2013). Structure dependent photoluminescence and magnetic properties of co: Zns nanostructures. *Physica Scripta*, *88*(3), 035703.

Chen, Y., Campbell, L., & Zhou, W. (2004). Self-catalytic branch growth of sno2 nanowire junctions. *Journal of crystal growth*, *270*(3-4), 505–510.

Chen, Y., Zou, C., Mastalerz, M., Hu, S., Gasaway, C., & Tao, X. (2015). Applications of micro-fourier transform infrared spectroscopy (ftir) in the geological sciences—a review. *International journal of molecular sciences*, *16*(12), 30223–30250.

Chen, Z., Dinh, H. N., Miller, E., et al. (2013). *Photoelectrochemical water splitting* (Vol. 344). Springer.

Choi, H.-J., Seong, H.-K., Chang, J., Lee, K.-I., Park, Y.-J., Kim, J.-J., ... Yang, P. (2005). Single-crystalline diluted magnetic semiconductor gan: Mn nanowires. *Advanced Materials*, *17*(11), 1351–1356.

Chu, P. K., & Li, L. (2006). Characterization of amorphous and nanocrystalline carbon films. *Materials chemistry and physics*, *96*(2-3), 253–277.

Chudziak, T., Montes-García, V., Czepa, W., Pakulski, D., Musiał, A., Valentini, C., ... others (2023). A comparative investigation of chemical reduction of graphene oxide for electrical engineering applications. *Nanoscale*.

Clarke, T. M., & Durrant, J. R. (2010). Charge photogeneration in organic solar cells. *Chemical reviews*, *110*(11), 6736–6767.

Cline, C. (1972). The pauli exclusion principle in pre-equilibrium decay. *Nuclear Physics A*, *195*(2), 353–360.

Coates, J. P. (1996). The interpretation of infrared spectra: Published reference sources. *Applied spectroscopy reviews*, *31*(1-2), 179–192.

Cobalt, E. (1990). Cobalt and cobalt alloys. *Metals Handbook: Nonferrous Alloys and Special-purpose Materials. Properties and selection*, *2*, 446.

Cody, G., Tiedje, T., Abeles, B., Brooks, B., & Goldstein, Y. (1981). Disorder and the optical-absorption edge of hydrogenated amorphous silicon. *Physical Review Letters*, *47*(20), 1480.

Coey, J. M. (2010). *Magnetism and magnetic materials*. Cambridge university press.

Cui, P., Lee, J., Hwang, E., & Lee, H. (2011). One-pot reduction of graphene oxide at subzero temperatures. *Chemical Communications*, *47*(45), 12370–12372.

Cullity, B. D. (1956). *Elements of x-ray diffraction*. Addison-Wesley Publishing.

Czerw, R., Foley, B., Tekleab, D., Rubio, A., Ajayan, P. M., & Carroll, D. (2002). Substrate-interface interactions between carbon nanotubes and the supporting substrate. *Physical Review B*, *66*(3), 033408.

da Rocha, C. G., Manning, H. G., O'Callaghan, C., Ritter, C., Bellew, A. T., Boland, J. J., & Ferreira, M. S. (2015). Ultimate conductivity performance in metallic nanowire networks. *Nanoscale*, *7*(30), 13011–13016.

Del Águila, A. G., Groeneveld, E., Maan, J. C., de Mello Donegá, C., & Christianen, P. C. (2016). Effect of electron-hole overlap and exchange interaction on exciton radiative lifetimes of cdte/cdse heteronanocrystals. *ACS nano*, *10*(4), 4102–4110.

De Martino, S., Falanga, M., Godano, C., & Lauro, G. (2003). Logarithmic schrödinger-like equation as a model for magma transport. *Europhysics Letters*,

63(3), 472.

Devaraju, M. K., & Honma, I. (2012). Hydrothermal and solvothermal process towards development of limpo4 (m= fe, mn) nanomaterials for lithium-ion batteries. *Advanced Energy Materials*, *2*(3), 284–297.

Devi, L. G., & Kavitha, R. (2013). A review on non metal ion doped titania for the photocatalytic degradation of organic pollutants under uv/solar light: Role of photogenerated charge carrier dynamics in enhancing the activity. *Applied Catalysis B: Environmental*, *140*, 559–587.

Dholam, R., Patel, N., Adami, M., & Miotello, A. (2009). Hydrogen production by photocatalytic water-splitting using cr-or fe-doped tio2 composite thin films photocatalyst. *International Journal of Hydrogen Energy*, *34*(13), 5337–5346.

Dietl, T., Ohno, o. H., Matsukura, a. F., Cibert, J., & Ferrand, e. D. (2000). Zener model description of ferromagnetism in zinc-blende magnetic semiconductors. *science*, *287*(5455), 1019–1022.

Dincer, I., & Acar, C. (2015). A review on clean energy solutions for better sustainability. *International Journal of Energy Research*, *39*(5), 585–606.

Dolabella, S., Borzì, A., Dommann, A., & Neels, A. (2022). Lattice strain and defects analysis in nanostructured semiconductor materials and devices by high-resolution x-ray diffraction: theoretical and practical aspects. *Small Methods*, *6*(2), 2100932.

Dong, Y., Du, X.-q., Liang, P., & Man, X.-l. (2020). One-pot solvothermal method to fabricate 1d-vs4 nanowires as anode materials for lithium ion batteries. *Inorganic Chemistry Communications*, *115*, 107883.

Dow, J. D., & Redfield, D. (1972). Toward a unified theory of urbach's rule and exponential absorption edges. *Physical Review B*, *5*(2), 594.

Drescher, D., & Kneipp, J. (2012). Nanomaterials in complex biological systems: insights from raman spectroscopy. *Chemical Society Reviews*, *41*(17), 5780–5799.

Dresselhaus, M. S., & Dresselhaus, G. (2002). Intercalation compounds of graphite. *Advances in physics*, *51*(1), 1–186.

Du, P., & Eisenberg, R. (2012). Catalysts made of earth-abundant elements (co, ni, fe) for water splitting: recent progress and future challenges. *Energy & Environmental Science*, *5*(3), 6012–6021.

Du, X., Huang, J., Zhang, J., Yan, Y., Wu, C., Hu, Y., ... others (2019). Modulating electronic structures of inorganic nanomaterials for efficient electrocatalytic water splitting. *Angewandte Chemie International Edition*, *58*(14), 4484–4502.

Dutta, A. (2017). Fourier transform infrared spectroscopy. *Spectroscopic methods for nanomaterials characterization*, 73–93.

Dutta, K., Manna, S., & De, S. (2009). Optical and electrical characterizations of zns nanoparticles embedded in conducting polymer. *Synthetic Metals*, *159*(3-4), 315–319.

Ealia, S. A. M., & Saravanakumar, M. P. (2017). A review on the classification, characterisation, synthesis of nanoparticles and their application. In *Iop conference series: materials science and engineering* (Vol. 263, p. 032019).

Ebrahimi, S., Yarmand, B., & Naderi, N. (2020). High-performance uv-b detectors based on mnxzn1-xs thin films modified by bandgap engineering. *Sensors and Actuators A: Physical*, *303*, 111832.

Egbedina, A. O., Bolade, O. P., Ewuzie, U., & Lima, E. C. (2022). Emerging trends in the application of carbon-based materials: A review. *Journal of Environmental Chemical Engineering*, *10*(2), 107260.

Eßmann, V., Barwe, S., Masa, J., & Schuhmann, W. (2016). Bipolar electrochemistry for concurrently evaluating the stability of anode and cathode electrocatalysts and the overall cell performance during long-term water electrolysis. *Analytical Chemistry*, *88*(17), 8835–8840.

Esswein, A. J., & Nocera, D. G. (2007). Hydrogen production by molecular photocatalysis. *Chemical reviews*, *107*(10), 4022–4047.

Eyasu, A., Yadav, O. P., & Bachheti, R. (2013). Photocatalytic degradation of methyl orange dye using cr-doped zns nanoparticles under visible radiation. *Int. J. Chem. Tech. Res*, *5*(4), 1452–1461.

Fadojutimi, P. O., Gqoba, S. S., Tetana, Z. N., & Moma, J. (2022). Transition metal dichalcogenides [mx2] in photocatalytic water splitting. *Catalysts*, *12*(5), 468.

Fajrina, N., & Tahir, M. (2019). A critical review in strategies to improve photocatalytic water splitting towards hydrogen production. *International Journal of Hydrogen Energy*, *44*(2), 540–577.

Fang, X., Zhai, T., Gautam, U. K., Li, L., Wu, L., Bando, Y., & Golberg, D. (2011). Zns nanostructures: from synthesis to applications. *Progress in Materials Science*, *56*(2), 175–287.

Faunce, T. A., Lubitz, W., Rutherford, A. B., MacFarlane, D., Moore, G. F., Yang, P., ... others (2013). Energy and environment policy case for a global project on artificial photosynthesis. *Energy & Environmental Science*, *6*(3), 695–698.

Fecht, H., Hellstern, E., Fu, Z., & Johnson, W. (1990). Nanocrystalline metals prepared by high-energy ball milling. *Metallurgical Transactions A*, *21*, 2333–2337.

Fernandez-Garcia, M., Martinez-Arias, A., Hanson, J., & Rodriguez, J. (2004). Nanostructured oxides in chemistry: characterization and properties. *Chemical reviews*, *104*(9), 4063–4104.

Ferrari, A. C., Meyer, J. C., Scardaci, V., Casiraghi, C., Lazzeri, M., Mauri, F., ... others (2006). Raman spectrum of graphene and graphene layers. *Physical review letters*, *97*(18), 187401.

Ferrari, A. C., & Robertson, J. (2000). Interpretation of raman spectra of disordered and amorphous carbon. *Physical review B*, *61*(20), 14095.

Frame, F. A., & Osterloh, F. E. (2010). Cdse-mos2: a quantum size-confined photocatalyst for hydrogen evolution from water under visible light. *The Journal of Physical Chemistry C*, *114*(23), 10628–10633.

Freysoldt, C., Grabowski, B., Hickel, T., Neugebauer, J., Kresse, G., Janotti, A., & Van de Walle, C. G. (2014). First-principles calculations for point defects in solids. *Reviews of modern physics*, *86*(1), 253.

Fujishima, A., & Honda, K. (1972). Electrochemical photolysis of water at a semiconductor electrode. *nature*, *238*(5358), 37–38.

Fujishima, A., Zhang, X., & Tryk, D. A. (2007). Heterogeneous photocatalysis: from water photolysis to applications in environmental cleanup. *International journal of hydrogen energy*, *32*(14), 2664–2672.

Gajdoš, M., Hummer, K., Kresse, G., Furthmüller, J., & Bechstedt, F. (2006). Linear optical properties in the projector-augmented wave methodology. *Physical Review B*, *73*(4), 045112.

Gan, Y. X., Jayatissa, A. H., Yu, Z., Chen, X., & Li, M. (2020). Hydrothermal synthesis of nanomaterials. *Journal of Nanomaterials*, *2020*, 1–3.

Gaur, L. K., Kumar, P., Kushavah, D., Khiangte, K. R., Mathpal, M. C., Agrahari, V., ... Agarwal, A. (2019). Laser induced phase transformation influenced by co doping in tio2 nanoparticles. *Journal of Alloys and Compounds*, *780*, 25–34.

Ghorai, S., Patra, N., Bhattacharyya, D., Jha, S. N., Ray, B., Chatterjee, S., & Ghosh, A. K. (2019). Influence of chromium concentration on the structural, electronic structure, optical and temperature dependent magnetic properties of zns nanocrystals. *Journal of Materials Science: Materials in Electronics*, *30*, 11652–11664.

Ghorashi, A. H., & Maranlou, H. (2021). Essential infrastructures and relevant policies for renewable energy developments in oil-rich developing countries: Case of iran. *Renewable and Sustainable Energy Reviews*, *141*, 110839.

Ghosh, P., Ahmed, S. F., Jana, S., & Chattopadhyay, K. (2007). Photoluminescence and field emission properties of zns: Mn nanoparticles synthesized by rf-magnetron sputtering technique. *Optical Materials*, *29*(12), 1584–1590.

Ghosh, S., Verma, P., Cramer, C. J., Gagliardi, L., & Truhlar, D. G. (2018). Combining wave function methods with density functional theory for excited states. *Chemical reviews*, *118*(15), 7249–7292.

Gialanella, S., Malandruccolo, A., Gialanella, S., & Malandruccolo, A. (2020).

Superalloys. *Aerospace Alloys*, 267–386.

Giamarchi, T. (2003). *Quantum physics in one dimension* (Vol. 121). Clarendon press.

Giannozzi, P., Baroni, S., Bonini, N., Calandra, M., Car, R., Cavazzoni, C., ... others (2009). Quantum espresso: a modular and open-source software project for quantum simulations of materials. *Journal of physics: Condensed matter*, *21*(39), 395502.

Giorgalli, M. (2021). Optimization of tumor growth in a syngeneic balb/c murine tumor model using magnetic nanoparticles.

Glass, C. W., Oganov, A. R., & Hansen, N. (2006). Uspex—evolutionary crystal structure prediction. *Computer physics communications*, *175*(11-12), 713–720.

Gonçalves, G., Vila, M., Bdikin, I., de Andrés, A., Emami, N., Ferreira, R. A., ... Marques, P. A. (2014). Breakdown into nanoscale of graphene oxide: confined hot spot atomic reduction and fragmentation. *Scientific reports*, *4*(1), 6735.

Gopinath, C. S., & Nalajala, N. (2021). A scalable and thin film approach for solar hydrogen generation: a review on enhanced photocatalytic water splitting. *Journal of Materials Chemistry A*, *9*(3), 1353–1371.

Gorni, T., Baseggio, O., Delugas, P., Baroni, S., & Timrov, I. (2022). turbomagnon–a code for the simulation of spin-wave spectra using the liouville-lanczos approach to time-dependent density-functional perturbation theory. *Computer Physics Communications*, *280*, 108500.

Goudarzi, A., Aval, G. M., Park, S. S., Choi, M.-C., Sahraei, R., Ullah, M. H., ... Ha, C.-S. (2009). Low-temperature growth of nanocrystalline mn-doped zns thin films prepared by chemical bath deposition and optical properties. *Chemistry of Materials*, *21*(12), 2375–2385.

Griffiths, P. R. (1983). Fourier transform infrared spectrometry. *Science*, *222*(4621), 297–302.

Gunnarsson, O., & Lundqvist, B. I. (1976). Exchange and correlation in atoms, molecules, and solids by the spin-density-functional formalism. *Physical Review B*, *13*(10), 4274.

Gurugubelli, T. R., Ravikumar, R., & Koutavarapu, R. (2022). Structural, optical, and luminescence properties of ni 2+-doped zno–cds nanocomposite: Synthesis and investigations for green light emission. *Chemical Papers*, 1–10.

Gutzwiller, M. C. (1970). Energy spectrum according to classical mechanics. *Journal of Mathematical Physics*, *11*(6), 1791–1806.

Hadjisavvas, N., & Theophilou, A. (1984). Rigorous formulation of the kohn and sham theory. *Physical Review A*, *30*(5), 2183.

Hammond, C. (2000). The elements. *Handbook of chemistry and physics*, *81*.

Han, L., Wang, P., & Dong, S. (2012). Progress in graphene-based photoactive nanocomposites as a promising class of photocatalyst. *Nanoscale*, *4*(19), 5814–5825.

Han, T., Meng, F., Zhang, S., Cheng, X., & Oh, J. (2011). Band gap and electronic properties of wurtzite-structure zno co-doped with iia and iiia. *Journal of Applied Physics*, *110*(6).

Hao, X., Wang, Y., Zhou, J., Cui, Z., Wang, Y., & Zou, Z. (2018). Zinc vacancy-promoted photocatalytic activity and photostability of zns for efficient visible-light-driven hydrogen evolution. *Applied Catalysis B: Environmental*, *221*, 302–311.

Harbola, M. K., & Sahni, V. (1989). Quantum-mechanical interpretation of the exchange-correlation potential of kohn-sham density-functional theory. *Physical review letters*, *62*(5), 489.

Hart, G. L., Blum, V., Walorski, M. J., & Zunger, A. (2005). Evolutionary approach for determining first-principles hamiltonians. *Nature materials*, *4*(5), 391–394.

Hassan, I. U., Naikoo, G. A., Salim, H., Awan, T., Tabook, M. A., Pedram, M. Z., ... Saleh, T. A. (2023). Advances in photochemical splitting of seawater over semiconductor nano-catalysts for hydrogen production: A critical review. *Journal of Industrial and Engineering Chemistry*.

Hassan, Q., Abdulateef, A. M., Hafedh, S. A., Al-samari, A., Abdulateef, J., Sameen, A. Z., ... Jaszczur, M. (2023). Renewable energy-to-green hydrogen: A review of main resources routes, processes and evaluation. *International Journal of Hydrogen Energy*.

Hernando, A., Crespo, P., Garcia, M., et al. (2005). Metallic magnetic nanoparticles. *The Scientific World Journal*, *5*, 972–1001.

Hirakawa, T., & Kamat, P. V. (2005). Charge separation and catalytic activity of ag@ tio2 core- shell composite clusters under uv- irradiation. *Journal of the American Chemical Society*, *127*(11), 3928–3934.

Hong, Y., Zhang, J., Wang, X., Wang, Y., Lin, Z., Yu, J., & Huang, F. (2012). Influence of lattice integrity and phase composition on the photocatalytic hydrogen production efficiency of zns nanomaterials. *Nanoscale*, *4*(9), 2859–2862.

Horikoshi, S., & Serpone, N. (2013). Introduction to nanoparticles. *Microwaves in nanoparticle synthesis: fundamentals and applications*, 1–24.

Hou, H., Yuan, Y., Cao, S., Yang, Y., Ye, X., & Yang, W. (2020). Cuins 2 nanoparticles embedded in mesoporous tio 2 nanofibers for boosted photocatalytic hydrogen production. *Journal of Materials Chemistry C*, *8*(32), 11001–11007.

Hou, J., Yang, M., Ke, C., Wei, G., Priest, C., Qiao, Z., ... Zhang, J. (2020). Platinum-group-metal catalysts for proton exchange membrane fuel cells: From

catalyst design to electrode structure optimization. *EnergyChem*, *2*(1), 100023.

Hoy-Benítez, J., Colina-Ruiz, R., Lezama-Pacheco, J., de León, J. M., & Espinosa-Faller, F. (2020). Local atomic structure and lattice defect analysis in heavily co-doped zns thin films using x-ray absorption fine structure spectroscopy. *Journal of Physics and Chemistry of Solids*, *136*, 109154.

Hsieh, S.-H., Lee, G.-J., Chen, C.-Y., Chen, J.-H., Ma, S.-H., Horng, T.-L., ... Wu, J. J. (2013). Hydrothermal synthesis of mesoporous bi 2 o 3/co 3 o 4 microsphere and photocatalytic degradation of orange ii dyes by visible light. *Topics in Catalysis*, *56*, 623–629.

Hsu, M.-H., & Chang, C.-J. (2014). S-doped zno nanorods on stainless-steel wire mesh as immobilized hierarchical photocatalysts for photocatalytic h2 production. *International journal of hydrogen energy*, *39*(29), 16524–16533.

Hu, C., Chen, X., Dai, Q., Wang, M., Qu, L., & Dai, L. (2017). Earth-abundant carbon catalysts for renewable generation of clean energy from sunlight and water. *Nano Energy*, *41*, 367–376.

Hu, Y., Zhou, C., Wang, H., Chen, M., Zeng, G., Liu, Z., ... others (2021). Recent advance of graphene/semiconductor composite nanocatalysts: Synthesis, mechanism, applications and perspectives. *Chemical Engineering Journal*, *414*, 128795.

Huang, D., Wen, M., Zhou, C., Li, Z., Cheng, M., Chen, S., ... others (2020). Znxcd1-xs based materials for photocatalytic hydrogen evolution, pollutants degradation and carbon dioxide reduction. *Applied Catalysis B: Environmental*, *267*, 118651.

Huang, X., Zhou, X., Qian, K., Zhao, D., Liu, Z., & Yu, C. (2012). A magnetite nanocrystal/graphene composite as high performance anode for lithium-ion batteries. *Journal of alloys and compounds*, *514*, 76–80.

Hughart, J. L., & Bashor, M. M. (1999). *Industrial chemicals and terrorism: human health threat analysis, mitigation and prevention*. Agency for Toxic Substances and Disease Registry.

Hummers Jr, W. S., & Offeman, R. E. (1958). Preparation of graphitic oxide. *Journal of the american chemical society*, *80*(6), 1339–1339.

Iqbal, A. A., Sakib, N., Iqbal, A. P., & Nuruzzaman, D. M. (2020). Graphene-based nanocomposites and their fabrication, mechanical properties and applications. *Materialia*, *12*, 100815.

Iwase, A., Ng, Y. H., Ishiguro, Y., Kudo, A., & Amal, R. (2011). Reduced graphene oxide as a solid-state electron mediator in z-scheme photocatalytic water splitting under visible light. *Journal of the American Chemical Society*, *133*(29), 11054–11057.

Izzo, F., Germinario, C., Grifa, C., Langella, A., & Mercurio, M. (2020). External reflectance ftir dataset (4000–400 cm- 1) for the identification of relevant

mineralogical phases forming cultural heritage materials. *Infrared Physics & Technology*, *106*, 103266.

Jafari, T., Moharreri, E., Amin, A. S., Miao, R., Song, W., & Suib, S. L. (2016). Photocatalytic water splitting—the untamed dream: a review of recent advances. *Molecules*, *21*(7), 900.

Jain, A., Shin, Y., & Persson, K. A. (2016). Computational predictions of energy materials using density functional theory. *Nature Reviews Materials*, *1*(1), 1–13.

Jain, R., Mahto, T. K., & Mahto, V. (2016). Rheological investigations of water based drilling fluid system developed using synthesized nanocomposite. *Korea-Australia Rheology Journal*, *28*, 55–65.

Jay Chithra, M., Sathya, M., & Pushpanathan, K. (2015). Effect of ph on crystal size and photoluminescence property of zno nanoparticles prepared by chemical precipitation method. *Acta Metallurgica Sinica (English Letters)*, *28*, 394–404.

Ji, Z., Shen, X., Song, Y., & Zhu, G. (2011). In situ synthesis of graphene/cobalt nanocomposites and their magnetic properties. *Materials Science and Engineering: B*, *176*(9), 711–715.

Jiang, B., Tian, C., Zhou, W., Wang, J., Xie, Y., Pan, Q., ... others (2011). In situ growth of tio2 in interlayers of expanded graphite for the fabrication of tio2–graphene with enhanced photocatalytic activity. *Chemistry–A European Journal*, *17*(30), 8379–8387.

Jiang, C., Moniz, S. J., Wang, A., Zhang, T., & Tang, J. (2017). Photoelectrochemical devices for solar water splitting–materials and challenges. *Chemical Society Reviews*, *46*(15), 4645–4660.

Jiang, L., Yang, M., Zhu, S., Pang, G., & Feng, S. (2008). Phase evolution and morphology control of zns in a solvothermal system with a single precursor. *The Journal of Physical Chemistry C*, *112*(39), 15281–15284.

Jiang, Y., Peng, Z., Zhang, S., Li, F., Liu, Z., Zhang, J., ... Wang, K. (2018). Facile in-situ solvothermal method to synthesize double shell znin2s4 nanosheets/tio2 hollow nanosphere with enhanced photocatalytic activities. *Ceramics International*, *44*(6), 6115–6126.

Jones, R. R., Hooper, D. C., Zhang, L., Wolverson, D., & Valev, V. K. (2019). Raman techniques: fundamentals and frontiers. *Nanoscale research letters*, *14*, 1–34.

Jothibas, M., Manoharan, C., Jeyakumar, S. J., Praveen, P., Punithavathy, I. K., & Richard, J. P. (2018). Synthesis and enhanced photocatalytic property of ni doped zns nanoparticles. *Solar Energy*, *159*, 434–443.

Joy, J., Mathew, J., & George, S. C. (2018). Nanomaterials for photoelectrochemical water splitting–review. *International Journal of hydrogen energy*, *43*(10), 4804–4817.

Juine, R. N., Sahu, B. K., & Das, A. (2021). Recyclable zns qds as an efficient photocatalyst for dye degradation under the uv and visible light. *New Journal of Chemistry*, *45*(13), 5845–5854.

Kalogirou, S. A. (2023). *Solar energy engineering: processes and systems*. Elsevier.

Kamat, P. V. (2011). Graphene-based nanoassemblies for energy conversion. *The Journal of Physical Chemistry Letters*, *2*(3), 242–251.

Kamat, P. V., Huehn, R., & Nicolaescu, R. (2002). A "sense and shoot" approach for photocatalytic degradation of organic contaminants in water. *The Journal of Physical Chemistry B*, *106*(4), 788–794.

Kang, T., Park, K., Deressa, G., & Kim, J. (2018). Drastic enhancement of blue-to-orange color conversion efficiency in heavily-doped zns: Mn2+ phosphor and its application in white leds. *Journal of Luminescence*, *194*, 551–556.

Kaur, N., Kaur, S., Singh, J., & Rawat, M. (2016). A review on zinc sulphide nanoparticles: from synthesis, properties to applications. *J Bioelectron Nanotechnol*, *1*(1), 1–5.

Kazempour, M., Namazi, H., Akbarzadeh, A., & Kabiri, R. (2019). Synthesis and characterization of peg-functionalized graphene oxide as an effective ph-sensitive drug carrier. *Artificial cells, nanomedicine, and biotechnology*, *47*(1), 90–94.

Keimer, B., & Moore, J. (2017). The physics of quantum materials. *Nature Physics*, *13*(11), 1045–1055.

Kelley, S. O., & Barton, J. K. (1999). Electron transfer between bases in double helical dna. *Science*, *283*(5400), 375–381.

Khaki, M. R. D., Shafeeyan, M. S., Raman, A. A. A., & Daud, W. M. A. W. (2017). Application of doped photocatalysts for organic pollutant degradation-a review. *Journal of environmental management*, *198*, 78–94.

Khan, K., Tareen, A. K., Aslam, M., Wang, R., Zhang, Y., Mahmood, A., ... Guo, Z. (2020). Recent developments in emerging two-dimensional materials and their applications. *Journal of Materials Chemistry C*, *8*(2), 387–440.

Khan, M. R., Chuan, T. W., Yousuf, A., Chowdhury, M., & Cheng, C. K. (2015). Schottky barrier and surface plasmonic resonance phenomena towards the photocatalytic reaction: study of their mechanisms to enhance photocatalytic activity. *Catalysis Science & Technology*, *5*(5), 2522–2531.

Khan, S. A., Khan, S. B., Khan, L. U., Farooq, A., Akhtar, K., & Asiri, A. M. (2018). Fourier transform infrared spectroscopy: fundamentals and application in functional groups and nanomaterials characterization. *Handbook of materials characterization*, 317–344.

Khosravi, A. A., Kundu, M., Kuruvilla, B. A., Shekhawat, G., Gupta, R., Sharma, A., ... Kulkarni, S. (1995). Manganese doped zinc sulphide nanoparticles by

aqueous method. *Applied Physics Letters*, *67*(17), 2506–2508.

Kibble, T., & Berkshire, F. H. (2004). *Classical mechanics*. world scientific publishing company.

Kim, B. H., Hackett, M. J., Park, J., & Hyeon, T. (2014). Synthesis, characterization, and application of ultrasmall nanoparticles. *Chemistry of Materials*, *26*(1), 59–71.

Kim, K. J., & Park, Y. R. (2004). Optical investigation of zn 1- x fe x o films grown on al 2 o 3 (0001) by radio-frequency sputtering. *Journal of Applied Physics*, *96*(8), 4150–4153.

Kiptarus, J. J., Korir, K. K., Githinji, D. N., & Kiriamiti, H. K. (2023). Improved photocatalytic performance of cobalt doped zns decorated with graphene nanostructures under uv-visible light: Towards efficient h2 production.

Kiptarus, J. J., Korir, K. K., Githinji, D. N., & Kiriamiti, H. K. (2024). A review of design and development of selected transitional metal doped zinc sulphide nanostructure surface layers decorated with graphene for hydrogen production. *Internation journal of Materials Engineering*, *14*(1), 12-24.

Kiptarus, J. J., Muumbo, A. M., Makokha, A. B., & Kimutai, S. K. (2015). Characterization of selected mineral ores in the eastern zone of kenya: case study of mwingi north constituency in kitui county. *International Journal of Mining Engineering and Mineral Processing*, *4*(1), 8–17.

Kodama, R. (1999). Magnetic nanoparticles. *Journal of magnetism and magnetic materials*, *200*(1-3), 359–372.

Kohn, W., & Sham, L. J. (1965). Self-consistent equations including exchange and correlation effects. *Physical review*, *140*(4A), A1133.

Kokilavani, S., Syed, A., Thomas, A. M., Elgorban, A. M., Al-Rashed, S., Raju, L. L., & Khan, S. S. (2021). Integrating ag2wo4 on vs4 nanoplates with synergy of plasmonic photocatalysis and boosted visible-light harvesting and its antibacterial applications. *Journal of Alloys and Compounds*, *865*, 158810.

Komarneni, S., Noh, Y. D., Kim, J. Y., Kim, S. H., & Katsuki, H. (2010). Solvothermal/hydrothermal synthesis of metal oxides and metal powders with and without microwaves. *Zeitschrift für Naturforschung B*, *65*(8), 1033–1037.

Kong, M., Li, Y., Chen, X., Tian, T., Fang, P., Zheng, F., & Zhao, X. (2011). Tuning the relative concentration ratio of bulk defects to surface defects in tio2 nanocrystals leads to high photocatalytic efficiency. *Journal of the American Chemical Society*, *133*(41), 16414–16417.

Korin, E., Froumin, N., & Cohen, S. (2017). Surface analysis of nanocomplexes by x-ray photoelectron spectroscopy (xps). *ACS Biomaterials Science & Engineering*, *3*(6), 882–889.

Korir, K., Benecha, E., Nyamwala, F., & Lombardi, E. (2021). Tuning elec-

tronic structure of zno nanowires via 3d transition metal dopants for improved photo-electrochemical water splitting: An ab initio study. *Materials Today Communications*, *26*, 101929.

Kotov, N. A., Dékány, I., & Fendler, J. H. (1996). Ultrathin graphite oxide–polyelectrolyte composites prepared by self-assembly: Transition between conductive and non-conductive states. *Advanced Materials*, *8*(8), 637–641.

Kripal, R., Gupta, A. K., Mishra, S. K., Srivastava, R. K., Pandey, A. C., & Prakash, S. (2010). Photoluminescence and photoconductivity of zns: Mn2+ nanoparticles synthesized via co-precipitation method. *Spectrochimica Acta Part A: Molecular and Biomolecular Spectroscopy*, *76*(5), 523–530.

Krishna, D. N. G., & Philip, J. (2022). Review on surface-characterization applications of x-ray photoelectron spectroscopy (xps): Recent developments and challenges. *Applied Surface Science Advances*, *12*, 100332.

Kudo, A., & Miseki, Y. (2009). Heterogeneous photocatalyst materials for water splitting. *Chemical Society Reviews*, *38*(1), 253–278.

Kudo, A., & Sekizawa, M. (2000). Photocatalytic h2 evolution under visible light irradiation on ni-doped zns photocatalyst. *Chemical Communications*(15), 1371–1372.

Kulkarni, M., Mazare, A., Gongadze, E., Perutkova, Š., Kralj-Iglič, V., Milošev, I., ... Mozetič, M. (2015). Titanium nanostructures for biomedical applications. *Nanotechnology*, *26*(6), 062002.

Kumar, H., Venkatesh, N., Bhowmik, H., Kuila, A., et al. (2018). Metallic nanoparticle: a review. *Biomed. J. Sci. Tech. Res*, *4*(2), 3765–3775.

Kumar, N., Purohit, L., & Goswami, Y. (2015). Synthesis of cu doped zns nanostructures on flexible substrate using low cost chemical method. In *Aip conference proceedings* (Vol. 1675).

Kumar, S., Kumar, A., Kumar, A., & Krishnan, V. (2020). Nanoscale zinc oxide based heterojunctions as visible light active photocatalysts for hydrogen energy and environmental remediation. *Catalysis Reviews*, *62*(3), 346–405.

Kuppayee, M., Nachiyar, G. V., & Ramasamy, V. (2012). Enhanced photoluminescence properties of zns: Cu2+ nanoparticles using pmma and ctab surfactants. *Materials science in semiconductor processing*, *15*(2), 136–144.

Kurnia, F., & Hart, J. N. (2015). Band-gap control of zinc sulfide: Towards an efficient visible-light-sensitive photocatalyst. *ChemPhysChem*, *16*(11), 2397–2402.

Kurnia, F., Ng, Y. H., Amal, R., Valanoor, N., & Hart, J. N. (2016). Defect engineering of zns thin films for photoelectrochemical water-splitting under visible light. *Solar Energy Materials and Solar Cells*, *153*, 179–185.

Kurnia, F., Ng, Y. H., Tang, Y., Amal, R., Valanoor, N., & Hart, J. N. (2016).

Zns thin films for visible-light active photoelectrodes: effect of film morphology and crystal structure. *Crystal Growth & Design*, *16*(5), 2461–2465.

Lai, J., Niu, W., Luque, R., & Xu, G. (2015). Solvothermal synthesis of metal nanocrystals and their applications. *Nano Today*, *10*(2), 240–267.

Lashgari, H., Boochani, A., Shekaari, A., Solaymani, S., Sartipi, E., & Mendi, R. T. (2016). Electronic and optical properties of 2d graphene-like zns: Dft calculations. *Applied Surface Science*, *369*, 76–81.

Lavin-Lopez, M. d. P., Paton-Carrero, A., Sanchez-Silva, L., Valverde, J., & Romero, A. (2017). Influence of the reduction strategy in the synthesis of reduced graphene oxide. *Advanced Powder Technology*, *28*(12), 3195–3203.

Lee, C., Chou, C., Huang, J., Hsu, C.-S., & Nguyen, T.-P. (2008). Investigations of organic light emitting diodes with cdse (zns) quantum dots. *Materials Science and Engineering: B*, *147*(2-3), 307–311.

Lee, G.-J., Anandan, S., Masten, S. J., & Wu, J. J. (2016). Photocatalytic hydrogen evolution from water splitting using cu doped zns microspheres under visible light irradiation. *Renewable Energy*, *89*, 18–26.

Lee, G.-J., Chen, H.-C., & Wu, J. J. (2019). (in, cu) co-doped zns nanoparticles for photoelectrochemical hydrogen production. *International journal of hydrogen energy*, *44*(1), 110–117.

Lee, G.-J., & Wu, J. J. (2017). Recent developments in zns photocatalysts from synthesis to photocatalytic applications—a review. *Powder technology*, *318*, 8–22.

Leghissa, P., Ferrari, M., Piazzolla, S., Caironi, M., Parigi, P., & Lebbolo, E. (1994). Cobalt exposure evaluation in dental prostheses production. *Science of the total environment*, *150*(1-3), 253–257.

Letts, E., Sun, Y., Key, D., Jordan, B., & Hashimoto, T. (2018). X-ray characterization technique for the assessment of surface damage in gan wafers. *Journal of Crystal Growth*, *501*, 13–17.

Lewis, N. S., & Nocera, D. G. (2006). Powering the planet: Chemical challenges in solar energy utilization. *Proceedings of the National Academy of Sciences*, *103*(43), 15729–15735.

Li, C., & Shi, G. (2011). Synthesis and electrochemical applications of the composites of conducting polymers and chemically converted graphene. *Electrochimica Acta*, *56*(28), 10737–10743.

Li, C., Yang, Y., Lv, L., Huang, H., Wang, Z., & Yang, S. (2008). Fabrication and magnetic characteristic of ferrimagnetic bulk mn4n. *Journal of alloys and compounds*, *457*(1-2), 57–60.

Li, J., & Wu, N. (2015). Semiconductor-based photocatalysts and photoelectrochemical cells for solar fuel generation: a review. *Catalysis Science & Technol-*

ogy, *5*(3), 1360–1384.

Li, J., & Zhang, J. Z. (2009). Optical properties and applications of hybrid semiconductor nanomaterials. *Coordination Chemistry Reviews*, *253*(23-24), 3015–3041.

Li, Q., Lin, S., Ma, D., & Wang, B. (2019). Photoluminescence properties and threshold effect of zns: Ag nanoparticles synthesized by a hydrothermal process. *International Journal of Modern Physics B*, *33*(06), 1950027.

Li, Q., Meng, H., Yu, J., Xiao, W., Zheng, Y., & Wang, J. (2014). Enhanced photocatalytic hydrogen-production performance of graphene–znxcd1- xs composites by using an organic s source. *Chemistry–A European Journal*, *20*(4), 1176–1185.

Li, X., Raorane, C. J., Xia, C., Wu, Y., Tran, T. K. N., & Khademi, T. (2023). Latest approaches on green hydrogen as a potential source of renewable energy towards sustainable energy: Spotlighting of recent innovations, challenges, and future insights. *Fuel*, *334*, 126684.

Li, X., Yu, J., Low, J., Fang, Y., Xiao, J., & Chen, X. (2015). Engineering heterogeneous semiconductors for solar water splitting. *Journal of Materials Chemistry A*, *3*(6), 2485–2534.

Li, Y., Sun, Y., Qin, Y., Zhang, W., Wang, L., Luo, M., ... Guo, S. (2020). Recent advances on water-splitting electrocatalysis mediated by noble-metal-based nanostructured materials. *Advanced Energy Materials*, *10*(11), 1903120.

Lieber, C. M., & Wang, Z. L. (2007). Functional nanowires. *MRS bulletin*, *32*(2), 99–108.

Lisjak, D., & Mertelj, A. (2018). Anisotropic magnetic nanoparticles: A review of their properties, syntheses and potential applications. *Progress in Materials Science*, *95*, 286–328.

Liu, J. (2010). Fuzzy modularity and fuzzy community structure in networks. *Eur. Phys. J. B.*, *77*, 547-557.

Liu, J., Yu, M., & Zhou, W. (2005). Well-aligned mn-doped zno nanowires synthesized by a chemical vapor deposition method. *Applied physics letters*, *87*(17).

Liu, W., Wan, Y., Xiong, Y., & Gao, P. (2022). Green hydrogen standard in china: Standard and evaluation of low-carbon hydrogen, clean hydrogen, and renewable hydrogen. *International Journal of Hydrogen Energy*, *47*(58), 24584–24591.

Liu, Y., Xu, X., Lu, T., Sun, Z., Chua, D. H., & Pan, L. (2015). Nitrogen-doped electrospun reduced graphene oxide–carbon nanofiber composite for capacitive deionization. *Rsc Advances*, *5*(43), 34117–34124.

Liu, Z., Liu, Q., Huang, Y., Ma, Y., Yin, S., Zhang, X., ... Chen, Y. (2008).

Organic photovoltaic devices based on a novel acceptor material: graphene. *Advanced materials*, *20*(20), 3924–3930.

Lostaglio, M., Jennings, D., & Rudolph, T. (2015). Description of quantum coherence in thermodynamic processes requires constraints beyond free energy. *Nature communications*, *6*(1), 6383.

Lucarini, V., Saarinen, J. J., Peiponen, K.-E., & Vartiainen, E. M. (2005). *Kramers-kronig relations in optical materials research* (Vol. 110). Springer Science & Business Media.

Lv, T., Pan, L., Liu, X., Lu, T., Zhu, G., & Sun, Z. (2011). Enhanced photocatalytic degradation of methylene blue by zno-reduced graphene oxide composite synthesized via microwave-assisted reaction. *Journal of Alloys and Compounds*, *509*(41), 10086–10091.

Ma, R., Zhou, Y., Bi, H., Yang, M., Wang, J., Liu, Q., & Huang, F. (2020). Multidimensional graphene structures and beyond: Unique properties, syntheses and applications. *Progress in Materials Science*, *113*, 100665.

Ma, X., Dai, Y., Yu, L., & Huang, B. (2016). Interface schottky barrier engineering via strain in metal–semiconductor composites. *Nanoscale*, *8*(3), 1352–1359.

Maeda, K. (2011). Photocatalytic water splitting using semiconductor particles: history and recent developments. *Journal of Photochemistry and Photobiology C: Photochemistry Reviews*, *12*(4), 237–268.

Maeda, K., Teramura, K., Lu, D., Takata, T., Saito, N., Inoue, Y., & Domen, K. (2006). Photocatalyst releasing hydrogen from water. *Nature*, *440*(7082), 295–295.

Mageswari, A., Srinivasan, R., Subramanian, P., Ramesh, N., & Gothandam, K. M. (2016). Nanomaterials: classification, biological synthesis and characterization. *Nanoscience in Food and Agriculture 3*, 31–71.

Mahmoud, M. S., Ahmed, E., Farghali, A., Zaki, A., Abdelghani, E. A., & Barakat, N. A. (2018). Influence of mn, cu, and cd–doping for titanium oxide nanotubes on the photocatalytic activity toward water splitting under visible light irradiation. *Colloids and Surfaces A: Physicochemical and Engineering Aspects*, *554*, 100–109.

Mahvelati-Shamsabadi, T., & Goharshadi, E. K. (2018). Zns nanospheres/reduced graphene oxide photoanode for highly efficient solar water oxidation. *Solar Energy*, *161*, 226–234.

Mai, V., Vanderborght, B., Haidegger, T., Khamis, A., Bhargava, N., Boesl, D. B., ... others (2022). The role of robotics in achieving the united nations sustainable development goals—the experts' meeting at the 2021 ieee/rsj iros workshop [industry activities]. *IEEE Robotics & Automation Magazine*, *29*(1), 92–107.

Makuła, P., Pacia, M., & Macyk, W. (2018). *How to correctly determine the band gap energy of modified semiconductor photocatalysts based on uv–vis spectra*

(Vol. 9) (No. 23). ACS Publications.

Malcıoğlu, O. B., Gebauer, R., Rocca, D., & Baroni, S. (2011). turbotddft–a code for the simulation of molecular spectra using the liouville–lanczos approach to time-dependent density-functional perturbation theory. *Computer Physics Communications*, *182*(8), 1744–1754.

Malek, M. F., Mamat, M. H., Md Sin, N. D., & Rusop, M. (2015). Effects of sn dopant on structural and optical properties of zno thin film prepared by sol-gel route. *Applied Mechanics and Materials*, *773*, 617–621.

Mamiyev, Z., & Balayeva, N. O. (2022). Metal sulfide photocatalysts for hydrogen generation: A review of recent advances. *Catalysts*, *12*(11), 1316.

Mandal, G., & Ganguly, T. (2011). Applications of nanomaterials in the different fields of photosciences. *Indian Journal of physics*, *85*, 1229–1245.

Marcano, D. C., Kosynkin, D. V., Berlin, J. M., Sinitskii, A., Sun, Z., Slesarev, A., ... Tour, J. M. (2010). Improved synthesis of graphene oxide. *ACS nano*, *4*(8), 4806–4814.

McCreery, R. L. (2005). *Raman spectroscopy for chemical analysis*. John Wiley & Sons.

McHugh, P. J., Stergiou, A. D., & Symes, M. D. (2020). Decoupled electrochemical water splitting: from fundamentals to applications. *Advanced Energy Materials*, *10*(44), 2002453.

Melsheimer, J., & Ziegler, D. (1985). Band gap energy and urbach tail studies of amorphous, partially crystalline and polycrystalline tin dioxide. *Thin Solid Films*, *129*(1-2), 35–47.

Mendil, R., Ayadi, Z. B., & Djessas, K. (2016). Effect of solvent medium on the structural, morphological and optical properties of zns nanoparticles synthesized by solvothermal route. *Journal of Alloys and Compounds*, *678*, 87–92.

Meng, L.-Y., Wang, B., Ma, M.-G., & Lin, K.-L. (2016). The progress of microwave-assisted hydrothermal method in the synthesis of functional nanomaterials. *Materials Today Chemistry*, *1*, 63–83.

Michel Sellier, J., & Kapanova, K. G. (2017). On the hydrogen atom beyond the born–oppenheimer approximation. *International Journal of Quantum Chemistry*, *117*(21), e25433.

Mikhaylova, M., Kim, D. K., Bobrysheva, N., Osmolowsky, M., Semenov, V., Tsakalakos, T., & Muhammed, M. (2004). Superparamagnetism of magnetite nanoparticles: dependence on surface modification. *Langmuir*, *20*(6), 2472–2477.

Mohapatra, R., Kaundal, J., & Goswami, Y. (2021). Synthesis of reduced graphene oxide/zinc sulfide nano composites with sonochemical route. *Chalcogenide Lett*, *18*(5), 255–262.

Monkhorst, H. J., & Pack, J. D. (1976). Special points for brillouin-zone integrations. *Physical review B*, *13*(12), 5188.

Montes-Navajas, P., Asenjo, N. G., Santamaría, R., Menéndez, R., Corma, A., & García, H. (2013). Surface area measurement of graphene oxide in aqueous solutions. *Langmuir*, *29*(44), 13443–13448.

Montoya, J. H., Seitz, L. C., Chakthranont, P., Vojvodic, A., Jaramillo, T. F., & Nørskov, J. K. (2017). Materials for solar fuels and chemicals. *Nature materials*, *16*(1), 70–81.

Moon, H., Goh, M. S., Cha, M., Kim, U.-S., Whang, H. S., Son, N., & Kang, M. (2022). Explosive hydrogen evolution from water splitting without sacrificial agent from the c, n co-doped zn defective zns particle. *Applied Surface Science*, *606*, 154787.

Moradi, Z., Jahromi, S. Z., & Ghaedi, M. (2021). Design of active photocatalysts and visible light photocatalysis. In *Interface science and technology* (Vol. 32, pp. 557–623). Elsevier.

Mørup, S. (2003). Spin-canting and transverse relaxation at surfaces and in the interior of ferrimagnetic particles. *Journal of Magnetism and Magnetic Materials*, *266*(1-2), 110–118.

Moss, T. (1954). The interpretation of the properties of indium antimonide. *Proceedings of the Physical Society. Section B*, *67*(10), 775.

Mote, V. D., & Dole, B. (2021). Structural, optical, and magnetic properties of mn-doped zns nanoparticles. *Journal of Materials Science: Materials in Electronics*, *32*(1), 420–429.

Motornyi, O., Vast, N., Timrov, I., Baseggio, O., Baroni, S., & Dal Corso, A. (2020). Electron energy loss spectroscopy of bulk gold with ultrasoft pseudopotentials and the liouville-lanczos method. *Physical Review B*, *102*(3), 035156.

Mu, Q., Jiang, G., Chen, L., Zhou, H., Fourches, D., Tropsha, A., & Yan, B. (2014). Chemical basis of interactions between engineered nanoparticles and biological systems. *Chemical reviews*, *114*(15), 7740–7781.

Murugadoss, G. (2012). Luminescence properties of co-doped zns: Ni, mn and zns: Cu, cd nanoparticles. *Journal of Luminescence*, *132*(8), 2043–2048.

Muruganandham, M., Amutha, R., Lee, G.-J., Hsieh, S.-H., Wu, J. J., & Sillanpaa, M. (2012). Facile fabrication of tunable bi2o3 self-assembly and its visible light photocatalytic activity. *The Journal of Physical Chemistry C*, *116*(23), 12906–12915.

Muruganandham, M., Lee, G.-J., Wu, J. J., Levchuk, I., & Sillanpaa, M. (2013). By-product assisted hydrothermal synthesis of inooh microflower composed of nanosheets. *Materials Letters*, *98*, 86–89.

M'hid, A. A., Li, G., Boughrara, M., Kerouad, M., & Wang, Q. (2024). Tuning the

magnetic properties of doped zns using transition metal doping: A multi-scale computational approach. *Materials Today Communications*, *38*, 107825.

Naeem, H., Tofil, H. M., Soliman, M., Hai, A., Zaidi, S. H. H., Kizilbash, N., ... Siddiq, M. (2023). Reduced graphene oxide-zinc sulfide nanocomposite decorated with silver nanoparticles for wastewater treatment by adsorption, photocatalysis and antimicrobial action. *Molecules*, *28*(3), 926.

Nair, A. K., Mayeen, A., Shaji, L. K., Kala, M. S., Thomas, S., & Kalarikkal, N. (2018). Optical characterization of nanomaterials. In *Characterization of nanomaterials* (pp. 269–299). Elsevier.

Naresh, V., & Lee, N. (2021). A review on biosensors and recent development of nanostructured materials-enabled biosensors. *Sensors*, *21*(4), 1109.

Navarro Yerga, R. M., Álvarez Galván, M. C., Del Valle, F., Villoria de la Mano, J. A., & Fierro, J. L. (2009). Water splitting on semiconductor catalysts under visible-light irradiation. *ChemSusChem: Chemistry & Sustainability Energy & Materials*, *2*(6), 471–485.

Nekooei, A., Miroliaei, M. R., Nejad, M. S., & Sheibani, H. (2022). Enhanced visible-light photocatalytic activity of zns/s-graphene quantum dots reinforced with ag2s nanoparticles. *Materials Science and Engineering: B*, *284*, 115884.

Nellist, M. (2016). Fa l. laskowski, f. lin, tj mills and sw boettcher. *Acc. Chem. Res*, *49*, 733.

Netz, B., Davidson, O., Bosch, P., Dave, R., Meyer, L., et al. (2007). Climate change 2007: Mitigation. contribution of working group iii to the fourth assessment report of the intergovernmental panel on climate change. summary for policymakers. *Climate change 2007: Mitigation. Contribution of Working Group III to the Fourth Assessment Report of the Intergovernmental Panel on Climate Change. Summary for Policymakers.*.

Ng, K. H., Lai, S. Y., Cheng, C. K., Cheng, Y. W., & Chong, C. C. (2021). Photocatalytic water splitting for solving energy crisis: Myth, fact or busted? *Chemical Engineering Journal*, *417*, 128847.

Ng, Y. H., Iwase, A., Kudo, A., & Amal, R. (2010). Reducing graphene oxide on a visible-light bivo4 photocatalyst for an enhanced photoelectrochemical water splitting. *The Journal of Physical Chemistry Letters*, *1*(17), 2607–2612.

Ni, Z., Wang, H., Kasim, J., Fan, H., Yu, T., Wu, Y. H., ... Shen, Z. (2007). Graphene thickness determination using reflection and contrast spectroscopy. *Nano letters*, *7*(9), 2758–2763.

Novoselov, K. S., Geim, A. K., Morozov, S. V., Jiang, D., Katsnelson, M. I., Grigorieva, I. V., ... AA (2005). Two-dimensional gas of massless dirac fermions in graphene. *nature*, *438*(7065), 197–200.

Nozik, A. J. (2008). Multiple exciton generation in semiconductor quantum dots. *Chemical Physics Letters*, *457*(1-3), 3–11.

Nüchter, M., Ondruschka, B., Bonrath, W., & Gum, A. (2004). Microwave assisted synthesis–a critical technology overview. *Green chemistry*, *6*(3), 128–141.

Obaidat, I. M., Issa, B., & Haik, Y. (2015). Magnetic properties of magnetic nanoparticles for efficient hyperthermia. *Nanomaterials*, *5*(1), 63–89.

Omurzak, E., Mashimo, T., Sulaimankulova, S., Takebe, S., Chen, L., Abdullaeva, Z., ... others (2011). Wurtzite-type zns nanoparticles by pulsed electric discharge. *Nanotechnology*, *22*(36), 365602.

Ortega-Guerrero, A., Fumanal, M., Capano, G., & Smit, B. (2020). From isolated porphyrin ligands to periodic al-pmof: A comparative study of the optical properties using dft/tddft. *The Journal of Physical Chemistry C*, *124*(39), 21751–21760.

Palani, G., Apsari, R., Hanafiah, M. M., Venkateswarlu, K., Lakkaboyana, S. K., Kannan, K., ... Yadav, C. H. (2022). Metal-doped graphitic carbon nitride nanomaterials for photocatalytic environmental applications—a review. *Nanomaterials*, *12*(10), 1754.

Parola, S., Julián-López, B., Carlos, L. D., & Sanchez, C. (2016). Optical properties of hybrid organic-inorganic materials and their applications. *Advanced Functional Materials*, *26*(36), 6506–6544.

Patel, P. C., Ghosh, S., & Srivastava, P. (2015). Antiferromagnetic coupling in co-doped zns. *Journal of materials science*, *50*, 7919–7929.

Patel, R., Park, J. T., Patel, M., Dash, J. K., Gowd, E. B., Karpoormath, R., ... Kim, J. H. (2018). Transition-metal-based layered double hydroxides tailored for energy conversion and storage. *Journal of Materials Chemistry A*, *6*(1), 12–29.

Paulson, E., Jothibas, M., & Srinivasan, S. (2023). The effects of interfacial contact on the properties of α-fe2o3@ rgo nanocomposite and their enhanced solar light photocatalysis. *Vacuum*, *211*, 111970.

Peddis, D., Jönsson, P. E., Laureti, S., & Varvaro, G. (2014). Magnetic interactions: a tool to modify the magnetic properties of materials based on nanoparticles. In *Frontiers of nanoscience* (Vol. 6, pp. 129–188). Elsevier.

Perdew, J. P., Burke, K., & Ernzerhof, M. (1996). Generalized gradient approximation made simple. *Physical review letters*, *77*(18), 3865.

Perdew, J. P., Chevary, J. A., Vosko, S. H., Jackson, K. A., Pederson, M. R., Singh, D. J., & Fiolhais, C. (1992). Atoms, molecules, solids, and surfaces: Applications of the generalized gradient approximation for exchange and correlation. *Physical review B*, *46*(11), 6671.

Perdew, J. P., & Wang, Y. (1992). Accurate and simple analytic representation of the electron-gas correlation energy. *Physical review B*, *45*(23), 13244.

Pereira, L. (2017). Experimentally evaluating the origin of dilute magnetism in

nanomaterials. *Journal of Physics D: Applied Physics*, *50*(39), 393002.

Peter, S. C. (2018). Reduction of co2 to chemicals and fuels: a solution to global warming and energy crisis. *ACS Energy Letters*, *3*(7), 1557–1561.

Petroleum, B. (2009). Energy-consumption'! a1" consumption by fuel, 1965-2008. *Statistical Review of World Energy 2009*.

Pickard, C. J., & Needs, R. (2006). High-pressure phases of silane. *Physical review letters*, *97*(4), 045504.

Pickard, C. J., & Needs, R. (2011). Ab initio random structure searching. *Journal of Physics: Condensed Matter*, *23*(5), 053201.

Poornaprakash, B., Chalapathi, U., Kumar, M., Rajitha, B., Reddy, B. P., Vattikuti, S. P., & Park, S.-H. (2020). Tailoring the optical, magnetic, and photocatalytic properties of zns quantum dots by rare-earth ion doping. *Chemical Physics Letters*, *753*, 137609.

Popović, Z. V., Dohčević-Mitrović, Z., Šćepanović, M., Grujić-Brojčin, M., & Aškrabić, S. (2011). Raman scattering on nanomaterials and nanostructures. *Annalen der Physik*, *523*(1-2), 62–74.

Prasad, C., Liu, Q., Tang, H., Yuvaraja, G., Long, J., Rammohan, A., & Zyryanov, G. V. (2020). An overview of graphene oxide supported semiconductors based photocatalysts: Properties, synthesis and photocatalytic applications. *Journal of Molecular Liquids*, *297*, 111826.

Puga, A. V. (2018). On the nature of active phases and sites in co and co 2 hydrogenation catalysts. *Catalysis Science & Technology*, *8*(22), 5681–5707.

Qadri, S., Skelton, E., Hsu, D., Dinsmore, A., Yang, J., Gray, H., & Ratna, B. (1999). Size-induced transition-temperature reduction in nanoparticles of zns. *Physical Review B*, *60*(13), 9191.

Qi, L., Yu, J., & Jaroniec, M. (2011). Preparation and enhanced visible-light photocatalytic h 2-production activity of cds-sensitized pt/tio 2 nanosheets with exposed (001) facets. *Physical Chemistry Chemical Physics*, *13*(19), 8915–8923.

Qian, D., Li, Y., Zhang, Q., Shi, G., & Wang, H. (2011). Anatase tio2 sols derived from peroxotitanium acid and to form transparent tio2 compact film for dye-sensitized solar cells. *Journal of Alloys and Compounds*, *509*(41), 10121–10126.

Qin, Y., Sun, Z., Zhao, W., Liu, Z., Ni, D., & Ma, Z. (2017). Improved photocatalytic properties of zns/rgo nanocomposites prepared with go solution in degrading methyl orange. *Nano-Structures & Nano-Objects*, *10*, 176–181.

Quan, Z., Wang, Z., Yang, P., Lin, J., & Fang, J. (2007). Synthesis and characterization of high-quality zns, zns: Mn2+, and zns: Mn2+/zns (core/shell) luminescent nanocrystals. *Inorganic chemistry*, *46*(4), 1354–1360.

Raabe, D. (2023). The materials science behind sustainable metals and alloys.

Chemical Reviews, *123*(5), 2436–2608.

Radovanovic, P. V., Barrelet, C. J., Gradecak, S., Qian, F., & Lieber, C. M. (2005). General synthesis of manganese-doped ii- vi and iii- v semiconductor nanowires. *Nano Letters*, *5*(7), 1407–1411.

Rahimi-Iman, A. (2020). Advances in functional nanomaterials science. *Annalen der Physik*, *532*(9), 2000015.

Rai, R. (2013). Analysis of the urbach tails in absorption spectra of undoped zno thin films. *Journal of Applied Physics*, *113*(15).

Raizada, P., Soni, V., Kumar, A., Singh, P., Khan, A. A. P., Asiri, A. M., ... Nguyen, V.-H. (2021). Surface defect engineering of metal oxides photocatalyst for energy application and water treatment. *Journal of Materiomics*, *7*(2), 388–418.

Rajabi, H. R., & Farsi, M. (2015). Effect of transition metal ion doping on the photocatalytic activity of zns quantum dots: synthesis, characterization, and application for dye decolorization. *Journal of Molecular Catalysis A: Chemical*, *399*, 53–61.

Ramaniah, L. M., & Boero, M. (2006). Structural, electronic, and optical properties of the diindenoperylene molecule from first-principles density-functional theory. *Physical Review A*, *74*(4), 042505.

Ran, J., Zhang, J., Yu, J., Jaroniec, M., & Qiao, S. Z. (2014). Earth-abundant cocatalysts for semiconductor-based photocatalytic water splitting. *Chemical Society Reviews*, *43*(22), 7787–7812.

Rangan, S., Schulze, H. G., Vardaki, M. Z., Blades, M. W., Piret, J. M., & Turner, R. F. (2020). Applications of raman spectroscopy in the development of cell therapies: State of the art and future perspectives. *Analyst*, *145*(6), 2070–2105.

Ranganatha, S. (2023). Aqueous redox-active electrolytes. *Sustainable Materials for Electrochemical Capacitors*, 247–260.

Rao, C., & Biswas, K. (2009). Characterization of nanomaterials by physical methods. *Annual Review of Analytical Chemistry*, *2*, 435–462.

Ray, S. C. (2015). Application and uses of graphene oxide and reduced graphene oxide. *Applications of graphene and graphene-oxide based nanomaterials*, *6*(8), 39–55.

Razali, M. H., & Ismail, N. A. (2021). Basic concepts and processing of nanostructures materials. In *Nanoscale processing* (pp. 1–32). Elsevier.

Razaq, A., Bibi, F., Zheng, X., Papadakis, R., Jafri, S. H. M., & Li, H. (2022). Review on graphene-, graphene oxide-, reduced graphene oxide-based flexible composites: From fabrication to applications. *Materials*, *15*(3), 1012.

Reber, J. F., & Meier, K. (1984). Photochemical production of hydrogen with zinc

sulfide suspensions. *The Journal of Physical Chemistry*, *88*(24), 5903–5913.

Reddy, D. A., Liu, C., Vijayalakshmi, R., & Reddy, B. (2014). Structural, optical and magnetic properties of zn0. 97- xalxcr0. 03s nanoparticles. *Ceramics International*, *40*(1), 1279–1288.

Reich, S., & Thomsen, C. (2004). Raman spectroscopy of graphite. *Philosophical Transactions of the Royal Society of London. Series A: Mathematical, Physical and Engineering Sciences*, *362*(1824), 2271–2288.

Rema Devi, B., Raveendran, R., & Vaidyan, A. (2007). Synthesis and characterization of mn2+-doped zns nanoparticles. *Pramana*, *68*(4), 679–687.

Rizwan, M., Shoukat, A., Ayub, A., Razzaq, B., & Tahir, M. B. (2021). Types and classification of nanomaterials. In *Nanomaterials: synthesis, characterization, hazards and safety* (pp. 31–54). Elsevier.

Roger, I., Shipman, M. A., & Symes, M. D. (2017). Earth-abundant catalysts for electrochemical and photoelectrochemical water splitting. *Nature Reviews Chemistry*, *1*(1), 0003.

Rowley-Neale, S. J., Randviir, E. P., Dena, A. S. A., & Banks, C. E. (2018). An overview of recent applications of reduced graphene oxide as a basis of electroanalytical sensing platforms. *Applied Materials Today*, *10*, 218–226.

Roy, D., Kanojia, S., Mukhopadhyay, K., & Eswara Prasad, N. (2021). Analysis of carbon-based nanomaterials using raman spectroscopy: principles and case studies. *Bulletin of Materials Science*, *44*, 1–9.

Ruetschi, P., & Amlie, R. (1966). Solubility of hydrogen in potassium hydroxide and sulfuric acid. salting-out and hydration. *The Journal of Physical Chemistry*, *70*(3), 718–723.

Sajeev, V., Rane, S., Ghosh, D., Acharyya, N., Roy Choudhury, P., Mukherjee, A., & Roy Chowdhury, D. (2023). Terahertz sensing of reduced graphene oxide nanosheets using sub-wavelength dipole cavities. *Scientific Reports*, *13*(1), 12374.

Saleh, T. A. (2020). Nanomaterials: Classification, properties, and environmental toxicities. *Environmental Technology & Innovation*, *20*, 101067.

Sankadiya, S., Oswal, N., Jain, P., & Gupta, N. (2016). Synthesis and characterization of fe2o3 nanoparticles by simple precipitation method. In *Aip conference proceedings* (Vol. 1724).

Sarangi, K., Reddy, B., & Das, R. (1999). Extraction studies of cobalt (ii) and nickel (ii) from chloride solutions using na-cyanex 272.: Separation of co (ii)/ni (ii) by the sodium salts of d2ehpa, pc88a and cyanex 272 and their mixtures. *Hydrometallurgy*, *52*(3), 253–265.

Sathre, R., Greenblatt, J. B., Walczak, K., Sharp, I. D., Stevens, J. C., Ager, J. W., & Houle, F. A. (2016). Opportunities to improve the net energy performance

of photoelectrochemical water-splitting technology. *Energy & Environmental Science*, *9*(3), 803–819.

Sayed, M., Yu, J., Liu, G., & Jaroniec, M. (2022). Non-noble plasmonic metal-based photocatalysts. *Chemical Reviews*, *122*(11), 10484–10537.

Schlegel, J. (2023). Alloying elements and steel properties. In *The world of steel: On the history, production and use of a basic material* (pp. 63–103). Springer.

Schön, J., & Jansen, M. (2001). Determination, prediction, and understanding of structures, using the energy landscapes of chemical systems-part i. *Zeitschrift für Kristallographie-Crystalline Materials*, *216*(6), 307–325.

Schroeder, H. A., Nason, A. P., Tipton, I. H., et al. (1967). Essential trace metals in man: cobalt. *Journal of Chronic Diseases*, *20*, 869–890.

Shah, N. R. A. M., Yunus, R. M., Rosman, N. N., Wong, W. Y., Arifin, K., & Minggu, L. J. (2021). Current progress on 3d graphene-based photocatalysts: From synthesis to photocatalytic hydrogen production. *International Journal of Hydrogen Energy*, *46*(14), 9324–9340.

Shah, S. N., Ali, S. I., Ali, S. R., Naeem, M., Bibi, Y., Ali, S. R., ... Sherwani, S. K. (2016). Synthesis and characterization of zinc oxide nanoparticles for antibacterial applications. *Journal of Basic & Applied Sciences*, *12*.

Shakil, M. A., Das, S., Rahman, M. A., Akther, U. S., Majumdar, M. K. H., & Rahman, M. K. (2018). A review on zinc sulphide thin film fabrication for various applications based on doping elements. *Materials Sciences and Applications*, *9*(9), 751–778.

Shang, M., Ma, Z., Su, Y., Shaheen, F., Khan, R., Mohd Tahir, L., ... others (2023). Understanding the importance of sustainable ecological innovation in reducing carbon emissions: investigating the green energy demand, financial development, natural resource management, industrialisation and urbanisation channels. *Economic research-Ekonomska istraživanja*, *36*(2).

Shard, A. G. (2020). Practical guides for x-ray photoelectron spectroscopy: Quantitative xps. *Journal of Vacuum Science & Technology A*, *38*(4).

Sharma, A., Khangarot, R. K., Misra, K. P., Misra, R., Chattopadhyay, S., Babu, P., & Halder, N. (2021). Band gap reduction and quenching of pd exchange interaction in sol-gel derived zn (al, cu) o nanostructures. *Physica Scripta*, *96*(7), 075803.

Sharma, R. K., Kumar, A., Gautam, S., & Goyal, N. (2016). Synthesis and characterization of cobalt doped zns nanoparticles. *Integrated Research Advances*, *3*(1), 26–29.

Sharmin, S. (2023). Spin canting in ferrite nanostructures. In *Ferrite nanostructured magnetic materials* (pp. 71–82). Elsevier.

Shedd, K. B. (2017). Cobalt. *US Geological Survey, US Department of the Interior,*

available at: https://minerals. usgs. gov/minerals/pubs/commodity/cobalt/mcs-2017-cobal. pdf (accessed 21 June 2017).

Shen, X., Wu, J., Bai, S., & Zhou, H. (2010). One-pot solvothermal syntheses and magnetic properties of graphene-based magnetic nanocomposites. *Journal of alloys and compounds*, *506*(1), 136–140.

Shifler, D. A. (2022). Structural alloys in marine service. *LaQue's Handbook of Marine Corrosion*, 453–526.

Shiga, Y., Umezawa, N., Srinivasan, N., Koyasu, S., Sakai, E., & Miyauchi, M. (2016). A metal sulfide photocatalyst composed of ubiquitous elements for solar hydrogen production. *Chemical Communications*, *52*(47), 7470–7473.

Shin, J., Ko, J., Jeong, S., Won, P., Lee, Y., Kim, J., ... Ko, S. H. (2021). Monolithic digital patterning of polydimethylsiloxane with successive laser pyrolysis. *Nature Materials*, *20*(1), 100–107.

Shu, C., Ding, L., & Zhong, W. (2014). Fluorescence resonance energy transfer between znse zns quantum dots and bovine serum albumin in bioaffinity assays of anticancer drugs. *Spectrochimica Acta Part A: Molecular and Biomolecular Spectroscopy*, *131*, 195–202.

Simon, C. A. (2024). *Alternative energy: political, economic, and social feasibility.* Rowman & Littlefield.

Simon, T., Bouchonville, N., Berr, M. J., Vaneski, A., Adrović, A., Volbers, D., ... others (2014). Redox shuttle mechanism enhances photocatalytic h 2 generation on ni-decorated cds nanorods. *Nature materials*, *13*(11), 1013–1018.

Singh, R. K., Kumar, R., & Singh, D. P. (2016). Graphene oxide: strategies for synthesis, reduction and frontier applications. *Rsc Advances*, *6*(69), 64993–65011.

Sivula, K., & Van De Krol, R. (2016). Semiconducting materials for photoelectrochemical energy conversion. *Nature Reviews Materials*, *1*(2), 1–16.

Smith, B. C. (2011). *Fundamentals of fourier transform infrared spectroscopy.* CRC press.

Smith, E., & Dent, G. (2019). *Modern raman spectroscopy: a practical approach.* John Wiley & Sons.

Stevie, F. A., & Donley, C. L. (2020). Introduction to x-ray photoelectron spectroscopy. *Journal of Vacuum Science & Technology A*, *38*(6).

Subramani, T., Lilova, K., Householder, M., Yang, S., Lyons, J., & Navrotsky, A. (2023). Surface energetics of wurtzite and sphalerite polymorphs of zinc sulfide and implications for their formation in nature. *Geochimica et Cosmochimica Acta*, *340*, 99–107.

Subramanian, V., Wolf, E. E., & Kamat, P. V. (2003). Green emission to probe

photoinduced charging events in zno- au nanoparticles. charge distribution and fermi-level equilibration. *The Journal of Physical Chemistry B*, *107*(30), 7479–7485.

Sud, A., & Sharma, R. K. (2016). Study of optical properties of zns thin film using simulation software. *Int. J. App Nat. Sci*, *5*, 13–18.

Sujiono, E. H., Zabrian, D., Dahlan, M., Amin, B., Agus, J., et al. (2020). Graphene oxide based coconut shell waste: synthesis by modified hummers method and characterization. *Heliyon*, *6*(8).

Sumadevi, K., Krishnamurthy, G., Walmik, P., Rani, R. P., Naik, S., Naik, H. B., & Naik, N. (2021). Photocatalytic degradation of eriochrome black-t and evan's blue dyes under the visible light using pva capped and uncapped ag doped zns nanoparticles. *Emergent Materials*, *4*, 447–456.

Sun, Y.-P., Zhou, B., Lin, Y., Wang, W., Fernando, K. S., Pathak, P., ... others (2006). Quantum-sized carbon dots for bright and colorful photoluminescence. *Journal of the American Chemical Society*, *128*(24), 7756–7757.

Sundaram, K., & Khan, A. (1996). Work function determination of zinc oxide films. In *Proceedings of southeastcon'96* (pp. 674–676).

Suryanarayana, C., & Prabhu, B. (2007). Synthesis of nanostructured materials by inert-gas condensation methods. In *Nanostructured materials* (pp. 47–90). Elsevier.

Szabó, T., Tombácz, E., Illés, E., & Dékány, I. (2006). Enhanced acidity and ph-dependent surface charge characterization of successively oxidized graphite oxides. *Carbon*, *44*(3), 537–545.

Tan, S. T., Chen, B., Sun, X., Fan, W., Kwok, H. S., Zhang, X., & Chua, S. (2005). Blueshift of optical band gap in zno thin films grown by metal-organic chemical-vapor deposition. *Journal of Applied Physics*, *98*(1).

Tang, L. A. L., Wang, J., & Loh, K. P. (2010). Graphene-based seldi probe with ultrahigh extraction and sensitivity for dna oligomer. *Journal of the American Chemical Society*, *132*(32), 10976–10977.

Tao, J., Perdew, J. P., Staroverov, V. N., & Scuseria, G. E. (2003). Climbing the density functional ladder: Nonempirical meta–generalized gradient approximation designed for molecules and solids. *Physical review letters*, *91*(14), 146401.

Tatsuma, T., Saitoh, S., Ngaotrakanwiwat, P., Ohko, Y., & Fujishima, A. (2002). Energy storage of tio2- wo3 photocatalysis systems in the gas phase. *Langmuir*, *18*(21), 7777–7779.

Tee, S. Y., Win, K. Y., Teo, W. S., Koh, L.-D., Liu, S., Teng, C. P., & Han, M.-Y. (2017). Recent progress in energy-driven water splitting. *Advanced science*, *4*(5), 1600337.

Tewatia, K., Sharma, A., Sharma, M., & Kumar, A. (2021). Synthesis of graphene

oxide and its reduction by green reducing agent. *Materials Today: Proceedings*, *44*, 3933–3938.

Thakre, K. G., Barai, D. P., & Bhanvase, B. A. (2021). A review of graphene-tio2 and graphene-zno nanocomposite photocatalysts for wastewater treatment. *Water Environment Research*, *93*(11), 2414–2460.

Theyvaraju, D., & Muthukumaran, S. (2015). Preparation, structural, photoluminescence and magnetic studies of cu doped zno nanoparticles co-doped with ni by sol–gel method. *Physica E: Low-dimensional Systems and Nanostructures*, *74*, 93–100.

Thorne, J. E., Zhao, Y., He, D., Fan, S., Vanka, S., Mi, Z., & Wang, D. (2017). Understanding the role of co-catalysts on silicon photocathodes using intensity modulated photocurrent spectroscopy. *Physical Chemistry Chemical Physics*, *19*(43), 29653–29659.

Tian, L., Li, Z., Xu, X., & Zhang, C. (2021). Advances in noble metal (ru, rh, and ir) doping for boosting water splitting electrocatalysis. *Journal of Materials Chemistry A*, *9*(23), 13459–13470.

Tiwari, A., & Dhoble, S. (2017). Critical analysis of phase evolution, morphological control, growth mechanism and photophysical applications of zns nanostructures (zero-dimensional to three-dimensional): a review. *Crystal Growth & Design*, *17*(1), 381–407.

Tong, L., Qiu, F., Zeng, T., Long, J., Yang, J., Wang, R., ... Yang, Y. (2017). Recent progress in the preparation and application of quantum dots/graphene composite materials. *RSC advances*, *7*(76), 47999–48018.

Tong, Y., Jiang, Z., Wang, C., Xin, Y., Huang, Z., Liu, S., & Li, C. (2008). Effect of annealing on the morphology and properties of zns: Mn nanoparticles/pvp nanofibers. *Materials Letters*, *62*(19), 3385–3387.

Tronc, E., Ezzir, A., Cherkaoui, R., Chanéac, C., Noguès, M., Kachkachi, H., ... Jolivet, J. (2000). Surface-related properties of γ-fe2o3 nanoparticles. *Journal of Magnetism and Magnetic Materials*, *221*(1-2), 63–79.

Tseng, A. A., Chen, K., Chen, C. D., & Ma, K. J. (2003). Electron beam lithography in nanoscale fabrication: recent development. *IEEE Transactions on electronics packaging manufacturing*, *26*(2), 141–149.

Tshabalala, Z. P., Oosthuizen, D. N., Swart, H. C., & Motaung, D. E. (2020). Tools and techniques for characterization and evaluation of nanosensors. In *Nanosensors for smart cities* (pp. 85–110). Elsevier.

Tsuji, I., & Kudo, A. (2003). H2 evolution from aqueous sulfite solutions under visible-light irradiation over pb and halogen-codoped zns photocatalysts. *Journal of Photochemistry and Photobiology A: Chemistry*, *156*(1-3), 249–252.

Tuinstra, F., & Koenig, J. L. (1970). Raman spectrum of graphite. *The Journal of chemical physics*, *53*(3), 1126–1130.

Turner, J. A. (2004). Sustainable hydrogen production. *Science*, *305*(5686), 972–974.

Urbach, F. (1953). The long-wavelength edge of photographic sensitivity and of the electronic absorption of solids. *Physical review*, *92*(5), 1324.

Vandenabeele, P. (2013). *Practical raman spectroscopy: an introduction*. John Wiley & Sons.

Vanderbilt, D. (1990). Soft self-consistent pseudopotentials in a generalized eigenvalue formalism. *Physical review B*, *41*(11), 7892.

Van der Heide, P. (2011). *X-ray photoelectron spectroscopy: an introduction to principles and practices*. John Wiley & Sons.

Van Sark, W. G., Frederix, P. L., Van den Heuvel, D. J., Gerritsen, H. C., Bol, A. A., Van Lingen, J. N., ... Meijerink, A. (2001). Photooxidation and photobleaching of single cdse/zns quantum dots probed by room-temperature time-resolved spectroscopy. *The Journal of Physical Chemistry B*, *105*(35), 8281–8284.

Venezia, A. M. (2003). X-ray photoelectron spectroscopy (xps) for catalysts characterization. *Catalysis Today*, *77*(4), 359–370.

Villa, K., Galán-Mascarós, J. R., López, N., & Palomares, E. (2021). Photocatalytic water splitting: advantages and challenges. *Sustainable Energy & Fuels*, *5*(18), 4560–4569.

Viswanath, R., Naik, H. B., Kumar, G. Y., Kumar, P. P., Harish, K., Prabhakara, M., & Praveen, R. (2014). Synthesis and photoluminescence enhancement of pva capped mn2+ doped zns nanoparticles and observation of tunable dual emission: a new approach. *Applied surface science*, *301*, 126–133.

Vivekchand, S., Rout, C. S., Subrahmanyam, K., Govindaraj, A., & Rao, C. N. R. (2008). Graphene-based electrochemical supercapacitors. *Journal of Chemical Sciences*, *120*, 9–13.

Voiry, D., Salehi, M., Silva, R., Fujita, T., Chen, M., Asefa, T., ... Chhowalla, M. (2013). Conducting mos2 nanosheets as catalysts for hydrogen evolution reaction. *Nano letters*, *13*(12), 6222–6227.

Vollath, D. (2008). Nanomaterials an introduction to synthesis, properties and application. *Environmental Engineering and Management Journal*, *7*(6), 865–870.

Wang, C., Chen, Z., Jin, H., Cao, C., Li, J., & Mi, Z. (2014). Enhancing visible-light photoelectrochemical water splitting through transition-metal doped tio 2 nanorod arrays. *Journal of Materials Chemistry A*, *2*(42), 17820–17827.

Wang, F., Jiang, Y., Gautam, A., Li, Y., & Amal, R. (2014). Exploring the origin of enhanced activity and reaction pathway for photocatalytic h2 production on au/b-tio2 catalysts. *Acs Catalysis*, *4*(5), 1451–1457.

Wang, G., Liu, T., Luo, Y., Zhao, Y., Ren, Z., Bai, J., & Wang, H. (2011). Preparation of fe2o3/graphene composite and its electrochemical performance as an anode material for lithium ion batteries. *Journal of Alloys and Compounds*, *509*(24), L216–L220.

Wang, L., Hu, Y., Qi, F., Ding, L., Wang, J., Zhang, X., ... Qu, P. (2020). Anchoring black phosphorus nanoparticles onto zns porous nanosheets: efficient photocatalyst design and charge carrier dynamics. *ACS applied materials & interfaces*, *12*(7), 8157–8167.

Wang, L., Wang, P., Huang, B., Ma, X., Wang, G., Dai, Y., ... Qin, X. (2017). Synthesis of mn-doped zns microspheres with enhanced visible light photocatalytic activity. *Applied Surface Science*, *391*, 557–564.

Wang, P., Huang, B., Zhang, X., Qin, X., Dai, Y., Wang, Z., & Lou, Z. (2011). Highly efficient visible light plasmonic photocatalysts ag@ ag (cl, br) and ag@ agcl-agi. *ChemCatChem*, *3*(2), 360–364.

Wang, Q., Lai, J., & Sun, D. (2016). Review of photo response in semiconductor transition metal dichalcogenides based photosensitive devices. *Optical Materials Express*, *6*(7), 2313–2327.

Wang, W., Li, B., Yang, H.-J., Liu, Y., Gurusamy, L., Karuppasamy, L., & Wu, J. J. (2021). Photocatalytic hydrogen evolution from water splitting using core-shell structured cu/zns/cof composites. *Nanomaterials*, *11*(12), 3380.

Wang, X.-T., Ouyang, T., Wang, L., Zhong, J.-H., & Liu, Z.-Q. (2020). Surface reorganization on electrochemically-induced zn–ni–co spinel oxides for enhanced oxygen electrocatalysis. *Angewandte Chemie*, *132*(16), 6554–6561.

Wang, Y., Alsmeyer, D. C., & McCreery, R. L. (1990). Raman spectroscopy of carbon materials: structural basis of observed spectra. *Chemistry of Materials*, *2*(5), 557–563.

Wang, Y., Kong, B., Zhao, D., Wang, H., & Selomulya, C. (2017). Strategies for developing transition metal phosphides as heterogeneous electrocatalysts for water splitting. *Nano Today*, *15*, 26–55.

Wang, Y., Lv, J., Zhu, L., & Ma, Y. (2010). Crystal structure prediction via particle-swarm optimization. *Physical Review B*, *82*(9), 094116.

Wang, Z., Wei, X., Huang, Y., Zhang, J., & Yang, J. (2023). High solar-to-hydrogen efficiency in asp/gase heterojunction for photocatalytic water splitting: A dft study. *Materials Science in Semiconductor Processing*, *159*, 107393.

Ward, D. A., & Ko, E. I. (1995). Preparing catalytic materials by the sol-gel method. *Industrial & engineering chemistry research*, *34*(2), 421–433.

Wasim, S., Marın, G., Rincón, C., & Sánchez Pérez, G. (1998). Urbach–martienssen's tail in the absorption spectra of the ordered vacancy compound cuin 3 se 5. *Journal of applied physics*, *84*(10), 5823–5825.

Wasim, S., Rincón, C., Marín, G., Bocaranda, P., Hernández, E., Bonalde, I., & Medina, E. (2001). Effect of structural disorder on the urbach energy in cu ternaries. *Physical Review B*, *64*(19), 195101.

Wasly, H. (2018). X-ray analysis for determination the crystallite size and lattice strain in zno nanoparticles. *Journal of Al-Azhar University Engineering Sector*, *13*(49), 1312–1320.

Weinbub, J., & Kosik, R. (2022). Computational perspective on recent advances in quantum electronics: from electron quantum optics to nanoelectronic devices and systems. *Journal of Physics: Condensed Matter*, *34*(16), 163001.

Wiederhorn, S. M., Fields, R. J., Low, S., Bahng, G.-W., Wehrstedt, A., Hahn, J., ... others (2011). Mechanical properties. *Springer Handbook of Metrology and Testing*, 339–452.

Winkler, B., Milman, V., Hennion, B., Payne, M., Lee, M. H., & Lin, J. (1995). Ab initio total energy study of brucite, diaspore and hypothetical hydrous wadsleyite. *Physics and Chemistry of Minerals*, *22*, 461–467.

Woit, P. (2011). *Not even wrong: The failure of string theory and the continuing challenge to unify the laws of physics*. Random House.

Wright, K., & Gale, J. D. (2004). Interatomic potentials for the simulation of the zinc-blende and wurtzite forms of zns and cds: Bulk structure, properties, and phase stability. *Physical Review B*, *70*(3), 035211.

Wu, Q., Miao, W.-s., Zhang, Y.-d., Gao, H.-j., & Hui, D. (2020). Mechanical properties of nanomaterials: A review. *Nanotechnology Reviews*, *9*(1), 259–273.

Wu, X., Lu, G. Q. M., & Wang, L. (2011). Shell-in-shell tio 2 hollow spheres synthesized by one-pot hydrothermal method for dye-sensitized solar cell application. *Energy & Environmental Science*, *4*(9), 3565–3572.

Xi, Y., Chen, W., Dong, W., Fan, Z., Wang, K., Shen, Y., ... Bai, S. (2021). Engineering an interfacial facet of s-scheme heterojunction for improved photocatalytic hydrogen evolution by modulating the internal electric field. *ACS Applied Materials & Interfaces*, *13*(33), 39491–39500.

Xiang, Q., & Yu, J. (2013). Graphene-based photocatalysts for hydrogen generation. *The Journal of Physical Chemistry Letters*, *4*(5), 753–759.

Xiang, Q., Yu, J., & Jaroniec, M. (2012). Graphene-based semiconductor photocatalysts. *Chemical Society Reviews*, *41*(2), 782–796.

Xie, G., Zhang, K., Guo, B., Liu, Q., Fang, L., & Gong, J. R. (2013). Graphene-based materials for hydrogen generation from light-driven water splitting. *Advanced materials*, *25*(28), 3820–3839.

Xu, L., Liang, H.-W., Yang, Y., & Yu, S.-H. (2018). Stability and reactivity: positive and negative aspects for nanoparticle processing. *Chemical reviews*,

118(7), 3209–3250.

Xu, M., Liang, T., Shi, M., & Chen, H. (2013). Graphene-like two-dimensional materials. *Chemical reviews*, *113*(5), 3766–3798.

Xu, X., Pan, L., Han, Q., Wang, C., Ding, P., Pan, J., ... Zhou, Y. (2019). Metallic molybdenum sulfide nanodots as platinum-alternative co-catalysts for photocatalytic hydrogen evolution. *Journal of Catalysis*, *374*, 237–245.

Xue, H., Gong, H., Yamauchi, Y., Sasaki, T., & Ma, R. (2022). Photo-enhanced rechargeable high-energy-density metal batteries for solar energy conversion and storage. *Nano Research Energy*, *1*(1), e9120007.

Xue, L., Shen, C., Zheng, M., Lu, H., Li, N., Ji, G., ... Cao, J. (2011). Hydrothermal synthesis of graphene–zns quantum dot nanocomposites. *Materials Letters*, *65*(2), 198–200.

Yan, J.-l., Chen, G.-j., Cao, J., Yang, W., Xie, B.-h., & Yang, M.-b. (2013). Functionalized graphene oxide with ethylenediamine and 1, 6-hexanediamine. *Carbon*, *52*, 624.

Yang, J., Zhao, X., Shan, X., Fan, H., Yang, L., Zhang, Y., & Li, X. (2013). Blue-shift of uv emission in zno/graphene composites. *Journal of alloys and compounds*, *556*, 1–5.

Yang, X., Pu, C., Qin, H., Liu, S., Xu, Z., & Peng, X. (2019). Temperature- and mn2+ concentration-dependent emission properties of mn2+-doped znse nanocrystals. *Journal of the American Chemical Society*, *141*(6), 2288–2298.

Yang, Y., Xue, S., Liu, S., Huang, J., & Shen, J. (1996). Fabrication and characteristics of zns nanocrystals/polymer composite doped with tetraphenylbenzidine single layer structure light-emitting diode. *Applied physics letters*, *69*(3), 377–379.

Yao, J., Shen, X., Wang, B., Liu, H., & Wang, G. (2009). In situ chemical synthesis of sno2–graphene nanocomposite as anode materials for lithium-ion batteries. *Electrochemistry communications*, *11*(10), 1849–1852.

Yatsunenko, S., Świątek, K., Godlewski, M., Fröba, M., Klar, P., & Heimbrodt, W. (2008). Electron spin resonance investigations of znmns nanoparticles. *Optical Materials*, *30*(5), 753–755.

Yoon, H., Lee, K., Lee, T., Cheong, B., Choi, D., Kim, D., & Kim, W. (2008). Properties of fluorine doped zno thin films deposited by magnetron sputtering. *Solar Energy Materials and Solar Cells*, *92*(11), 1366–1372.

Yu, H., Yu, J., Liu, S., & Mann, S. (2007). Template-free hydrothermal synthesis of cuo/cu2o composite hollow microspheres. *Chemistry of materials*, *19*(17), 4327–4334.

Yu, J., Zhang, J., & Jaroniec, M. (2010). Preparation and enhanced visible-light photocatalytic h 2-production activity of cds quantum dots-sensitized zn 1- x

cd x s solid solution. *Green Chemistry*, *12*(9), 1611–1614.

Yu, L., Ruan, H., Zheng, Y., & Li, D. (2013). A facile solvothermal method to produce zns quantum dots-decorated graphene nanosheets with superior photoactivity. *Nanotechnology*, *24*(37), 375601.

Yu, M., Wang, K., & Vredenburg, H. (2021). Insights into low-carbon hydrogen production methods: Green, blue and aqua hydrogen. *International Journal of Hydrogen Energy*, *46*(41), 21261–21273.

Yuan, X., Su, C.-W., Umar, M., Shao, X., & LobonŢ, O.-R. (2022). The race to zero emissions: Can renewable energy be the path to carbon neutrality? *Journal of Environmental Management*, *308*, 114648.

Zafar, A., Ahmad, K. S., Jaffri, S. B., & Sohail, M. (2020). Physical vapor deposition of sns: Pbs-dithiocarbamate chalcogenide semiconductor thin films: elucidation of optoelectronic and electrochemical features. *Phosphorus, Sulfur, and Silicon and the Related Elements*, *196*(1), 36–46.

Zafeiratos, S., Paloukis, F., Papakonstantinou, G., Teschner, D., Hävecker, M., Vass, E., ... others (2010). A comparative in situ xps study of ptruco catalyst in methanol steam reforming and water gas shift reactions. *Catalysis Today*, *157*(1-4), 250–256.

Zaware, R. V., Borse, R. Y., & Wagh, B. G. (2017). Properties of thin zns: Mn films sprayed by improved method: the role of mn2+ ion concentration. *Materials Science Poland*, *35*(2), 291–302.

Zemlyanov, D. Y. (2023). Practical aspects of xps: From sample preparation to spectra interpretation. In *Applications of x-ray photoelectron spectroscopy to catalytic studies: From routine analysis to cutting-edge surface characterization* (pp. 13–50). World Scientific.

Zhang, H., Chen, Z.-H., Liu, X., & Zhang, F. (2020). A mini-review on recent progress of new sensitizers for luminescence of lanthanide doped nanomaterials. *Nano Research*, *13*, 1795–1809.

Zhang, J., Liu, S., Yu, J., & Jaroniec, M. (2011). A simple cation exchange approach to bi-doped zns hollow spheres with enhanced uv and visible-light photocatalytic h 2-production activity. *Journal of Materials Chemistry*, *21*(38), 14655–14662.

Zhang, J., Yu, J., Jaroniec, M., & Gong, J. R. (2012). Noble metal-free reduced graphene oxide-zn x cd1–x s nanocomposite with enhanced solar photocatalytic h2-production performance. *Nano letters*, *12*(9), 4584–4589.

Zhang, J., Yu, J., Zhang, Y., Li, Q., & Gong, J. R. (2011). Visible light photocatalytic h2-production activity of cus/zns porous nanosheets based on photoinduced interfacial charge transfer. *Nano letters*, *11*(11), 4774–4779.

Zhang, J. Z. (2009). *Optical properties and spectroscopy of nanomaterials*. World Scientific.

Zhang, L.-W., Fu, H.-B., & Zhu, Y.-F. (2008). Efficient tio2 photocatalysts from surface hybridization of tio2 particles with graphite-like carbon. *Advanced Functional Materials*, *18*(15), 2180–2189.

Zhang, X., Chen, Y. L., Liu, R.-S., & Tsai, D. P. (2013). Plasmonic photocatalysis. *Reports on Progress in Physics*, *76*(4), 046401.

Zhang, Y., Ma, H.-L., Zhang, Q., Peng, J., Li, J., Zhai, M., & Yu, Z.-Z. (2012). Facile synthesis of well-dispersed graphene by γ-ray induced reduction of graphene oxide. *Journal of Materials Chemistry*, *22*(26), 13064–13069.

Zhang, Y., Zhang, N., Tang, Z.-R., & Xu, Y.-J. (2012). Graphene transforms wide band gap zns to a visible light photocatalyst. the new role of graphene as a macromolecular photosensitizer. *ACS nano*, *6*(11), 9777–9789.

Zhao, X., Xue, Z., Chen, W., Wang, Y., & Mu, T. (2020). Eutectic synthesis of high-entropy metal phosphides for electrocatalytic water splitting. *ChemSusChem*, *13*(8), 2038–2042.

Zheng, B., Fan, J., Chen, B., Qin, X., Wang, J., Wang, F., ... Liu, X. (2022). Rare-earth doping in nanostructured inorganic materials. *Chemical Reviews*, *122*(6), 5519–5603.

Zheng, K., & Branicio, P. S. (2020). Synthesis of metallic glass nanoparticles by inert gas condensation. *Physical Review Materials*, *4*(7), 076001.

Zheng, L., Teng, F., Ye, X., Zheng, H., & Fang, X. (2020). Photo/electrochemical applications of metal sulfide/tio2 heterostructures. *Advanced Energy Materials*, *10*(1), 1902355.

Zheng, M., Liu, S., Li, J., Qu, D., Zhao, H., Guan, X., ... Sun, Z. (2014). Integrating oxaliplatin with highly luminescent carbon dots: an unprecedented theranostic agent for personalized medicine. *Advanced Materials*, *26*(21), 3554–3560.

Zhong, L., Chen, D., & Zafeiratos, S. (2019). A mini review of in situ near-ambient pressure xps studies on non-noble, late transition metal catalysts. *Catalysis Science & Technology*, *9*(15), 3851–3867.

Zhou, H., Liu, Y., Zhang, L., Li, H., Liu, H., & Li, W. (2019). Transition metal-doped amorphous molybdenum sulfide/graphene ternary cocatalysts for excellent photocatalytic hydrogen evolution: Synergistic effect of transition metal and graphene. *Journal of colloid and interface science*, *533*, 287–296.

Zhou, J., Zhao, J., & Liu, R. (2020). Defect engineering of zeolite imidazole framework derived zns nanosheets towards enhanced visible light driven photocatalytic hydrogen production. *Applied Catalysis B: Environmental*, *278*, 119265.

Zhou, M., Zhai, Y., & Dong, S. (2009). Electrochemical sensing and biosensing platform based on chemically reduced graphene oxide. *Analytical chemistry*, *81*(14), 5603–5613.

Zhou, Y., Jin, C., Li, Y., & Shen, W. (2018). Dynamic behavior of metal nanoparticles for catalysis. *Nano Today*, *20*, 101–120.

Zhou, Z., Han, F., Guo, L., & Prezhdo, O. V. (2016). Understanding divergent behaviors in the photocatalytic hydrogen evolution reaction on cds and zns: a dft based study. *Physical Chemistry Chemical Physics*, *18*(25), 16862–16869.

Zhu, J., Hu, L., Zhao, P., Lee, L. Y. S., & Wong, K.-Y. (2019). Recent advances in electrocatalytic hydrogen evolution using nanoparticles. *Chemical reviews*, *120*(2), 851–918.

Zhu, J., Mei, S., Yang, W., Zhang, G., Chen, Q., Zhang, W., & Guo, R. (2017). Tunable emission of cu (mn)-doped znins quantum dots via dopant interaction. *Journal of colloid and interface science*, *506*, 27–35.

Zhu, J., Yang, D., Yin, Z., Yan, Q., & Zhang, H. (2014). Graphene and graphene-based materials for energy storage applications. *Small*, *10*(17), 3480–3498.

Zhu, Y., Lv, C., Yin, Z., Ren, J., Yang, X., Dong, C.-L., ... others (2020). A [001]-oriented hittorf's phosphorus nanorods/polymeric carbon nitride heterostructure for boosting wide-spectrum-responsive photocatalytic hydrogen evolution from pure water. *Angewandte Chemie International Edition*, *59*(2), 868–873.

Zhu, Y., Ren, J., Huang, G., Dong, C.-L., Huang, Y.-C., Lu, P., ... Yang, D. (2024). Red phosphorus grafted high-index (116) faceted anatase tio2 for z-scheme photocatalytic pure water splitting. *Advanced Functional Materials*, *34*(9), 2311623.

Zhu, Y.-C., Bando, Y., Xue, D.-F., & Golberg, D. (2004). Oriented assemblies of zns one-dimensional nanostructures. *Advanced Materials*, *16*(9-10), 831–834.

Zou, T., Zhao, B., Xin, W., Wang, Y., Wang, B., Zheng, X., ... Guo, C. (2020). High-speed femtosecond laser plasmonic lithography and reduction of graphene oxide for anisotropic photoresponse. *Light: Science & Applications*, *9*(1), 69.

Zunger, A., & Malyi, O. I. (2021). Understanding doping of quantum materials. *Chemical reviews*, *121*(5), 3031–3060.

Appendix A

Methodology

A.1 Theoeretical simulations

Example of input file; https://drive.google.com/file/d/1m0RF8ng_GDDABQdRcUJ2awERTmPjw
view?usp=drive_link

Table A.1: Lattice data for Ecutwfc

Ecutwfc	***Energy***
15	-321.7022
20	-334.2331
25	-337.4269
30	-338.1801
35	-338.3216
40	-338.3373
45	-338.3394
50	-338.3433

Table A.2: Lattice data for Cell dm (1)

Cell dm (1)	***Energy***
6.1	-337.8551
6.2	-337.9803
6.3	-338.086
6.4	-338.1745
6.5	-338.2473
6.6	-338.3076
6.7	-338.3563
6.8	-338.394
6.9	-338.4217
7.0	-338.4436
7.2	-338.4644
7.4	-338.4672
7.6	-338.4523
7.8	-338.4275
8.0	-338.3945
8.2	-338.3555
8.4	-338.312

Table A.3: Lattice data for Cell dm (3)

Cell dm (3)	***Energy***
1.11	-336.4619
1.31	-337.4105
1.51	-337.8396
1.71	-338.1353
1.91	-338.2915
2.11	-338.333
2.31	-338.3009
2.51	-338.2545
2.81	-338.2142
3.01	-338.2009
3.21	-338.1936
3.41	-338.1887
3.61	-338.1857
3.81	-338.1833

A.1.1 Calculation methods and models for ZnS doped with manganese, copper, cobalt and iron

Table A.4: Total energies for Mn, Cu, Co and Fe

Conc.(atm%)	*Mn*	*Cu*	*Co*	*Fe*
BulkZnS	-7063.82141949 (Ry),-8129.00386964 (Ry)			
1	-7145.69883085	-8103.62002919	-7229.55646273	-7185.75450229
2	-7228.11565941	-8077.81556984	-7396.41060585	-7308.18915583
4	-7393.00186136	-8026.88542906	-7729.60014316	-7553.05404194
6	-7557.96639395	-7974.79097169	-8062.62348994	-7798.02461958

Table A.5: Chemical potential

TM dopant	*Energy*
Zn	-126.50073336
Mn	-208.57850009
S	-20.17827188, -20.63957360
Cu	-122.47343117
Co	-292.69135648
Fe	-248.65195442

Table A.6: Formation energies for Mn, Cu, Co and Fe

Conc.(atm%)	*Mn*	*Cu*	*Co*	*Fe*
1%	10.29	9.92	10.54	10.31
2%	9.95	9.95	9.88	10.03
4%	9.22	9.32	9.07	9.46
6%	8.41	9.86	8.09	8.79

Table A.7: Formation Energies for Mn, Cu, Co and Fe

Conc.(atm%)	***Mn***	***Cu***	***Co***	***Fe***
1%	2.4	-5.2	4.2	3
2%	-1.8	-5.6	-2.8	-0.8
4%	-2.4	-5.8	-4.2	-2.4
6%	-4.6	-6.2	-6.4	-4.4

Table A.8: Fermi energy for Mn, Cu, Co and Fe

Conc.(atm%)	***Mn***	***Cu***	***Co***	***Fe***
BulkZnS	1.7066eV			
1%	4.6021	4.3278	0.2271	4.5440
2%	1.19	2.7024	2.4403	1.1709
4%	1.1423	1.6373	2.2295	1.7509
6%		1.2761	2.7063	0.8012

Table A.9: Manganese

Conc.atm%	***Zn-rich***	***S-rich***
1	2.4	10.3
2	-1.8	10
4	-2.4	9.2
6	-4.6	8.4

Table A.10: Copper

Conc.atm%	*Zn-rich*	*S-rich*
1	-5.2	9.9
2	-5.6	10
4	-5.8	9.3
6	-6.2	9.9

Table A.11: Cobalt

Conc.atm%	*Zn-rich*	*S-rich*
1	4.2	10.5
2	-2.8	9.9
4	-4.2	9.1
6	-6.4	8.1

Table A.12: Iron

Conc.atm%	*Zn-rich*	*S-rich*
1	3.0	10.3
2	-0.8	10.0
4	-2.4	9.5
6	-4.4	8.8

Table A.13: 1 amt.% Zn-S-Rich

TM dopant	*Zn-rich*	*S-rich*
Mn	2.4	10.3
Cu	-5.2	9.9
Co	4.2	10.6
Fe	3	10.3

Table A.14: 2 amt.% Zn-S-Rich

TM dopant	***Zn-rich***	***S-rich***
Mn	-1.8	9.95
Cu	-5.6	9.95
Co	-2.8	9.88
Fe	-0.8	10.03

Table A.15: 4 amt.% Zn-S-rich

TM dopant	***Zn-rich***	***S-rich***
Mn	-2.4	9.22
Cu	-5.8	9.32
Co	-4.2	9.07
Fe	-2.4	9.46

Table A.16: 6 amt.% Zn-S-rich

TM dopant	***Zn-rich***	***S-rich***
Mn	-4.6	8.41
Cu	-6.2	9.86
Co	-6.4	8.09
Fe	-4.4	8.79

Table A.17: Formation energies under the Zn-rich for all the $3d$ TM dopants as a function of dopant concentration

TM Dopants	***n=1%***	***n=2%***	***n=4%***	***n=6%***
Mn	2.4	-1.8	-2.4	-4.6
Cu	-5.2	-5.6	-5.8	-6.2
Co	4.2	-2.8	-4.2	-6.4
Fe	3	-0.8	-2.4	-4.4

Table A.18: Formation energies under the S-rich for all the $3d$ TM dopants as a function of dopant concentration

TM Dopants	***n=1%***	***n=2%***	***n=4%***	***n=6%***
Mn	10.3	10	9.2	8.4
Cu	9.9	10	9.3	9.9
Co	10.5	9.9	9.1	8.1
Fe	10.3	10	9.5	8.8

Table A.19: Formation energy profile of $3d$ transition metal defects in ZnS 2D surface layers under the Z-rich and S-rich condition

TM dopant	***Zn-rich***	***S-rich***
Mn	2.4	10.3
	-1.8	10.0
	-2.4	9.2
	-4.6	8.4
Cu	-5.2	9.9
	-5.6	10.0
	-5.8	9.3
	-6.2	9.9
Co	4.2	10.5
	-2.8	9.9
	-4.2	9.1
	-6.4	8.1
Fe	3.0	10.3
	-0.8	10.0
	-2.4	9.5
	-4.4	8.8

Table A.20: Bandgap1 energy of $3d$ transition metal doped ZnS 2D surface layers at the Zn substitutional as a function of dopant concentrations

Conc.(atm%)	***Mn***	***Cu***	***Co***	***Fe***
1%	1.8	0.6	0.9	1.5
2%	1.4	0.5	0.6	1.0
4%	1.0	0.3	0.3	0.6
6%	0.8	0.2	0.1	0.3

Table A.21: Band edge alignment of the $3d$ transition metal doped ZnS 2D surface layers relative to the redox potential of water for different dopant concentrations (1%, 2%, 4%, 6%)

Sample	***0***	***1***	***2***	***4***	***6***
ZnS	-0.75				2.91
Mn:ZnS		-0.55	-0.51	-0.45	-0.39
Cu:ZnS		-0.09	0.009	0.09	0.14
Co:ZnS		-0.04	0.04	0.1	0.15
Fe:ZnS		-0.48	-0.45	-0.4	-0.37
O_2/HO_2	1.23	1.23	1.23	1.23	1.23
Mn:ZnS		2.55	2.51	2.49	2.44
Cu:ZnS		2.15	2.09	2.03	1.98
Co:ZnS		1.95	1.91	1.86	1.81
Fe:ZnS		2.44	2.39	2.33	2.27

A.2 Development and characterization

`https://photos.app.goo.gl/4GcCFRLTeDqY6e9KA`Photocatalysis reaction process
`https://photos.app.goo.gl/e1D7sDf1GdtkAzhp8`Raman Characterization
`https://photos.app.goo.gl/MJHJsbUAtNXw5b8Y6`XRD Characterization
`https://photos.app.goo.gl/AeqFg2A2JkvYsgJp8`rGO Synthesis
`https://photos.app.goo.gl/SagYTKYjUTrv4yVa9`Furnace/oven heat treatment process

Table A.22: DOE of cobalt doped ZnS decorated with graphene for hydrogen production

Run	Std	Conc. (atm.%)	Time (hrs)	H_2 evolution ($\mu molh^{-1}$)
1	16	0	2	
2	10	1	2	
3	18	2	2	
4	26	4	2	
5	1	6	2	
6	5	0	4	
7	9	1	4	
8	13	2	4	
9	25	4	4	
10	30	6	4	
11	19	0	6	
12	22	1	6	
13	28	2	6	
14	7	4	6	
15	4	6	6	
16	27	0	8	
17	11	1	8	
18	15	2	8	
19	23	4	8	
20	17	6	8	
21	21	0	10	
22	29	1	10	
23	2	2	10	
24	3	4	10	
25	6	6	10	
26	14	0	12	
27	12	1	12	
28	24	2	12	
29	8	4	12	
30	20	6	12	

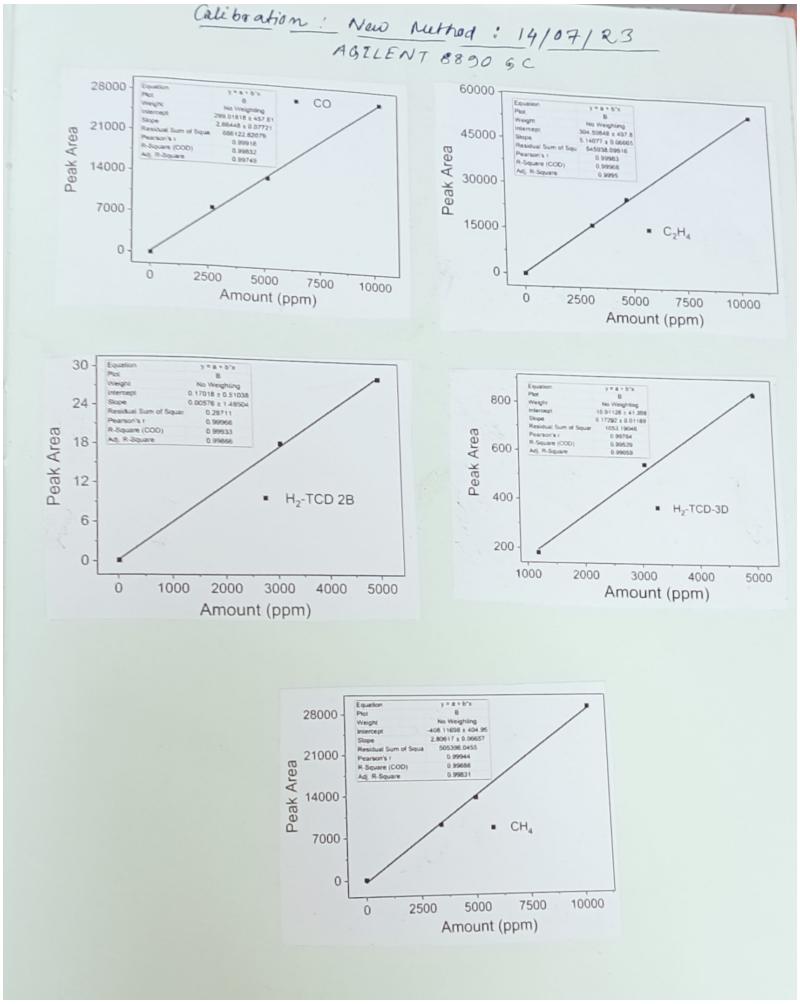

Figure A.1: Agilent 8890 GC Calibration

Table A.23: Hydrogen evolution for cobalt doped ZnS without graphene

Sample	*Peak Area*	*x=R factor*	*y=(H space=50ml)*	*Z= Vol. of media =20ml*	*STP*	*Hydrogen evolution* ($\mu molh^{-1}$)
ZnS	2976.863082	0.004174093	0.417409306	20.87046528	0.9317172	776.431
	3711.157331	0.005203705	0.520370458	26.01852288	1.1615412	967.951
	4116.836499	0.005772539	0.577253914	28.86269568	1.2885132	1073.761
	4562.128911	0.006396919	0.639691853	31.98459264	1.4278836	1189.903
	4990.156665	0.00699709	0.699708979	34.98544896	1.5618504	1301.542
	5147.244719	0.007217355	0.721735526	36.08677632	1.6110168	1342.514
1Co-ZnS	4285.534392	0.006009084	0.600908367	30.04541837	1.34131332	1117.761
	5208.301715	0.007302968	0.730296806	36.51484032	1.6301268	1358.439
	5444.255853	0.007633818	0.763381786	38.16908928	1.7039772	1419.981
	6105.435068	0.008560909	0.856090906	42.80454528	1.9109172	1592.431
	6726.475777	0.009431719	0.943171891	47.15859456	2.1052944	1754.412
	7186.563726	0.010076844	1.007684429	50.38422144	2.2492956	1874.413
2Co-ZnS	6429.548991	0.009015375	0.901537459	45.07687296	2.0123604	1676.967
	6546.352846	0.009179154	0.917915443	45.89577216	2.0489184	1707.432
	7238.392202	0.010149517	1.014951706	50.74758528	2.2655172	1887.931
	7579.506233	0.01062782	1.062781978	53.13909888	2.3722812	1976.901
	8557.08146	0.011998555	1.199855462	59.99277312	2.6782488	2231.874
	10169.85648	0.014259953	1.42599529	71.29976448	3.1830252	2652.521
4Co-ZnS	7081.20063	0.009929106	0.992910643	49.64553216	2.2163184	1846.932
	8273.773164	0.011601306	1.160130586	58.00652928	2.5895772	2157.981
	9973.553928	0.013984702	1.39847017	69.92350848	3.1215852	2601.321
	10647.0634	0.014929082	1.492908211	74.64541056	3.3323844	2776.987
	11109.27157	0.01557718	1.557718042	77.88590208	3.4770492	2897.541
	12274.89851	0.017211597	1.721159731	86.05798656	3.8418744	3201.562
6Co-ZnS	2261.179236	0.003170577	0.317057664	15.8528832	0.707718	589.765
	2307.268163	0.003235202	0.323520154	16.17600768	0.7221432	601.786
	2844.803605	0.003988922	0.398892211	19.94461056	0.8903844	741.987
	3185.587909	0.004466762	0.44667625	22.33381248	0.9970452	830.871
	3356.854221	0.004706908	0.470690842	23.53454208	1.0506492	875.541
	3785.848153	0.005308434	0.530843443	26.54217216	1.1849184	987.432

Table A.24: Hydrogen evolution for cobalt doped ZnS with graphene

Sample	*Peak Area*	*x=R factor*	*y=(H space=50ml)*	*Z= Vol. of media =20ml*	*STP*	*Hydrogen evolution* ($\mu molh^{-1}$)
Co-ZnS-rGo	9971.847783	0.013982309	1.398230938	69.91154688	3.1210512	2600.876
	10695.13068	0.014996481	1.499648102	74.98240512	3.3474288	2789.524
	13253.34023	0.018583547	1.858354714	92.91773568	4.1481132	3456.761
	14875.67733	0.020858353	2.085835315	104.2917658	4.6558824	3879.902
	15721.71451	0.022044648	2.204464819	110.223241	4.9206804	4100.567
	16491.41223	0.023123902	2.31239017	115.6195085	5.1615852	4301.321
1Co-ZnS-rGO	12988.39312	0.018212044	1.821204403	91.06022016	4.0651884	3387.657
	14529.64807	0.020373158	2.03731584	101.865792	4.54758	3789.65
	17938.53397	0.025153025	2.515302451	125.7651226	5.6145144	4678.762
	19555.18904	0.027419863	2.74198633	137.0993165	6.1205052	5100.421
	20829.93259	0.029207281	2.920728115	146.0364058	6.5194824	5432.902
	22405.13792	0.031416	3.1416	157.08	7.0125	5843.75
2Co-ZnS-rGO	13007.61697	0.018238999	1.82389993	91.19499648	4.0712052	3392.671
	16657.64446	0.023356989	2.335698893	116.7849446	5.2136136	4344.678
	20403.92154	0.028609938	2.860993766	143.0496883	6.3861468	5321.789
	22939.84384	0.032165753	3.216575309	160.8287654	7.1798556	5983.213
	23006.71323	0.032259516	3.22595159	161.2975795	7.2007848	6000.654
	23981.58547	0.033626461	3.362646067	168.1323034	7.5059064	6254.922
4Co-ZnS-rGO	16354.23815	0.022931559	2.293155917	114.6577958	5.1186516	4265.543
	22196.41692	0.031123336	3.112333594	155.6166797	6.9471732	5789.311
	25179.75952	0.035306514	3.530651443	176.5325722	7.8809184	6567.432
	26030.9113	0.036499981	3.649998106	182.4999053	8.1473172	6789.431
	28146.07134	0.039465813	3.946581274	197.3290637	8.8093332	7341.111
	29326.11809	0.041120449	4.112044877	205.6022438	9.1786716	7648.893
6Co-ZnS-rGO	5449.500812	0.007641172	0.764117222	38.20586112	1.7056188	1421.349
	5884.886079	0.00825166	0.825166003	41.25830016	1.8418884	1534.907
	7232.644985	0.010141458	1.014145843	50.70729216	2.2637184	1886.432
	7620.814119	0.010685741	1.06857408	53.428704	2.38521	1987.675
	7671.001628	0.010756113	1.075611264	53.7805632	2.400918	2000.765
	9196.533202	0.01289518	1.289518003	64.47590016	2.8783884	2398.657

Appendix B

Results

Table B.1: Crystallite sizes (nm) of cobalt doped ZnS decorated with graphene

SAMPLE	*Peak pos.*	*Peak (Radians)*	*FWHM*	*FWHM in Radians*	*C.size D (nm)*	*AV.C.size(nm)*
ZnS-rGO	28.61191	0.499372035	0.34065	0.005945464	24.06729729	23.47150219
	47.58822	0.830571124	0.3883	0.006777113	22.35970174	
	56.46289	0.985463336	0.3759	0.006560693	23.98750754	
1Co-ZnS-rGO	28.7476	0.501740272	0.45812	0.007995702	17.90143835	18.50384169
	47.72907	0.83302942	0.48678	0.008495914	17.84581703	
	56.60183	0.987888296	0.45652	0.007967777	19.76426968	
2Co-ZnS-rGO	28.5715	0.498666747	0.49993	0.008725425	16.39787196	16.72537994
	47.55354	0.829965844	0.53476	0.009333323	16.23366398	
	56.42062	0.984725585	0.51384	0.0089682	17.54460387	
4Co-ZnS-rGO	28.57171	0.498670412	0.47771	0.008337612	17.16060362	16.1521611
	47.55449	0.829982425	0.55863	0.009749933	15.54006383	
	56.42165	0.984743562	0.57218	0.009986425	15.75581586	
6Co-ZnS-rGO	28.95978	0.505443512	0.71855	0.012541063	11.41871037	11.14340536
	47.97139	0.837258702	0.81731	0.014264751	10.63873032	
	56.83531	0.991963291	0.79424	0.013862103	11.37277538	

Table B.2: Lattice constants for cobalt doped ZnS decorated with graphene

Sample	λ(Å)	M Indices			Bragg(Θ)		Radians	d spacing(Å)	Latt. Const.(Å)	Av. (Å)	S.JCPD(Å)	Error
		h	k	l	2θ	θ						
ZnS-rGO	1.5406	1	1	1	28.71	14.36	0.2505	3.1069	5.3814	5.394	5.406	0.012
		2	2	0	47.59	23.80	0.4153	1.9092	5.4001			
		3	1	1	56.46	28.23	0.4927	1.6285	5.4011			
1Co-ZnS-rGO	1.5406	1	1	1	28.65	14.33	0.2500	3.1133	5.3924	5.387	5.406	0.019
		2	2	0	47.73	23.87	0.4165	1.9039	5.3851			
		3	1	1	56.66	28.33	0.4945	1.6232	5.3836			
2Co-ZnS-rGO	1.5406	1	1	1	28.79	14.40	0.2512	3.0985	5.3667	5.377	5.406	0.029
		2	2	0	47.77	23.89	0.4169	1.9024	5.3809			
		3	1	1	56.68	28.34	0.4946	1.6227	5.3819			
4Co-ZnS-rGO	1.5406	1	1	1	28.89	14.45	0.2521	3.0880	5.3486	5.375	5.406	0.031
		2	2	0	47.56	23.78	0.4150	1.9103	5.4033			
		3	1	1	56.79	28.40	0.4956	1.6198	5.3723			
6Co-ZnS-rGO	1.5406	1	1	1	28.96	14.48	0.2527	3.0807	5.3359	5.354	5.406	0.052
		2	2	0	47.97	23.99	0.4186	1.8949	5.3596			
		3	1	1	56.84	28.42	0.4960	1.6185	5.3680			

Table B.3: Hydrogen evolution for cobalt doped ZnS decorated with graphene

Run	***T(hrs)***	***Hydrogen evolution*** ($\mu molh^{-1}g^{-1}$)				
		ZnS-rGO	***1Co-ZnS-rGO***	***2Co-ZnS-rGO***	***4Co-ZnS-rGO***	***6Co-ZnS-rGO***
1	2	2600.876	3387.657	3392.671	4265.543	1421.349
2	4	2789.524	3789.65	4344.678	5789.311	1534.907
3	6	3456.761	4678.762	5321.789	6567.432	1886.432
4	8	3879.902	5100.421	5983.213	6789.431	1987.675
5	10	4100.567	5432.902	6000.654	7341.111	2000.765
6	12	4301.321	5843.75	6254.922	7648.893	2398.657

Table B.4: Hydrogen evolution for cobalt doped ZnS without graphene

Run	***T(hrs)***	***Hydrogen evolution*** ($\mu molh^{-1}$)				
		ZnS	***1Co-ZnS***	***2Co-ZnS***	***4Co-ZnS***	***6Co-ZnS***
1	2	776.431	1117.7611	1676.967	1846.932	589.765
2	4	967.951	1358.439	1707.432	2157.981	601.786
3	6	1073.761	1419.981	1887.931	2601.321	741.987
4	8	1189.903	1592.431	1976.901	2776.987	830.871
5	10	1301.542	1754.412	2231.874	2897.541	875.541
6	12	1342.514	1874.413	2652.521	3201.562	987.432

Table B.5: Fit summary

Source	Sequential p-value	Lack of Fit p-value	Adjusted R^2	Predicted R^2	
Linear	0.0222		0.1900	0.0562	
2FI	0.7487		0.1622	-0.0647	
Quadratic	< 0.0001		0.8523	0.8041	
Cubic	< 0.0001		0.9678	0.9403	
Quartic	< 0.0001		0.9933	0.9712	Suggested
Fifth	0.3983		0.9936	0.9473	Aliased

Table B.6: Sequential Model Sum of Squares [Type I]

Source	Sum of Squares	df	Mean Square	F-value	p-value	
Mean vs Total	5.659E+08	1	5.659E+08			
Linear vs Mean	2.287E+07	2	1.144E+07	4.40	0.0222	
2FI vs Linear	2.816E+05	1	2.816E+05	0.1048	0.7487	
Quadratic vs 2FI	5.851E+07	2	2.925E+07	61.76	< 0.0001	
Cubic vs Quadratic	9.305E+06	4	2.326E+06	22.55	< 0.0001	
Quartic vs Cubic	1.741E+06	5	3.483E+05	16.25	< 0.0001	Suggested
Fifth vs Quartic	1.170E+05	5	23409.09	1.15	0.3983	Aliased
Residual	2.044E+05	10	20439.84			
Total	6.589E+08	30	2.196E+07			

Table B.7: Model summary statistics

Source	Std. Dev.	R^2	Adjusted R^2	Predicted R^2	PRESS	
Linear	1611.95	0.2459	0.1900	0.0562	8.780E+07	
2FI	1639.36	0.2489	0.1622	-0.0647	9.905E+07	
Quadratic	688.23	0.8778	0.8523	0.8041	1.822E+07	
Cubic	321.16	0.9778	0.9678	0.9403	5.551E+06	
Quartic	146.39	0.9965	0.9933	0.9712	2.677E+06	Suggested
Fifth	142.97	0.9978	0.9936	0.9473	4.906E+06	Aliased

Table B.8: ANOVA for Quartic model

Source	Sum of Squares	df	Mean Square	F-value	p-value	
Model	9.271E+07	14	6.622E+06	309.01	< 0.0001	significant
A-Concentration	4.205E+06	1	4.205E+06	196.21	< 0.0001	
B-Time	3.101E+06	1	3.101E+06	144.69	< 0.0001	
AB	7539.60	1	7539.60	0.3518	0.5619	
A^2	5438.21	1	5438.21	0.2538	0.6217	
B^2	4.043E+05	1	4.043E+05	18.87	0.0006	
A^2B	1.846E+06	1	1.846E+06	86.16	< 0.0001	
AB^2	1335.43	1	1335.43	0.0623	0.8063	
A^3	8.117E+06	1	8.117E+06	378.80	< 0.0001	
B^3	24925.94	1	24925.94	1.16	0.2979	
A^2B^2	4.415E+05	1	4.415E+05	20.60	0.0004	
A^3B	97115.91	1	97115.91	4.53	0.0502	
AB^3	85977.91	1	85977.91	4.01	0.0636	
A^4	1.032E+06	1	1.032E+06	48.16	< 0.0001	
B^4	84873.41	1	84873.41	3.96	0.0651	
Residual	3.214E+05	15	21429.59			
Cor Total	9.303E+07	29				

Table B.9: Fit statistics

Std. Dev.	146.39		R^2	0.9965
Mean	4343.05		Adjusted R^2	0.9933
C.V. %	3.37		Predicted R^2	0.9712
			Adeq Precision	60.9155

Table B.10: Coefficients in Terms of Coded Factors

Factor	Coefficient Estimate	df	Standard Error	95% CI Low	95% CI High	VIF
Intercept	6288.19	1	102.33	6070.08	6506.29	
A-Concentration	2090.18	1	149.22	1772.13	2408.24	16.07
B-Time	1493.31	1	124.15	1228.70	1757.93	10.07
AB	-129.89	1	218.98	-596.63	336.85	16.71
A^2	-268.39	1	532.79	-1404.00	867.21	63.58
B^2	-1416.83	1	326.19	-2112.10	-721.57	23.73
A^2B	-910.09	1	98.05	-1119.07	-701.10	2.79
AB^2	23.30	1	93.34	-175.66	222.26	2.41
A^3	-2925.99	1	150.34	-3246.43	-2605.55	13.12
B^3	139.39	1	129.25	-136.09	414.87	8.16
A^2B^2	760.50	1	167.56	403.36	1117.64	4.15
A^3B	-393.44	1	184.82	-787.37	0.4866	9.33
AB^3	354.49	1	176.98	-22.73	731.71	8.16
A^4	-3228.49	1	465.22	-4220.09	-2236.89	63.73
B^4	561.05	1	281.92	-39.84	1161.94	21.89

Table B.11: Final Equation in Terms of Coded Factors

R1	=
+6288.19	
+2090.18	A
+1493.31	B
-129.89	AB
-268.39	A^2
-1416.83	B^2
-910.09	A^2B
+23.30	AB^2
-2925.99	A^2
+139.39	B^3
+760.50	A^2B^2
-393.44	A^3B
+354.49	AB^3
-3228.49	A^4
+561.05	B^4

Table B.12: Final Equation in Terms of actual Factors

R1	=
+3491.38015	
+713.61237	Concentration
-882.65647	Time
+452.52667	Concentration * Time
-1083.23808	$Concentration^2$
+272.86722	$Time^2$
-41.31460	$\text{Concentration}^{\mathbf{2}}$ * Time
-39.82066	Concentration * $Time^2$
+390.32594	$Concentration^2$
-26.85566	$Time^3$
+3.37999	$\text{Concentration}^{\mathbf{2}}$ * $Time^2$
-2.91438	$\text{Concentration}^{\mathbf{3}}$ * Time
+0.945305	Concentration * $Time^3$
-39.85794	$Concentration^4$
+0.897674	$Time^4$

B.1 Data sets and images using Origin and CASAXPS software

https://drive.google.com/file/d/1EUOKg1FAyfI5wuEWE4DZcm9aPNOlPuk0/view?usp=drive_link FTIR Analysis

https://drive.google.com/file/d/1wppG53aflgfwBg5WmZVqZ_Bx-bFHmp6E/view?usp=drive_link UV-vis Characterization

https://drive.google.com/file/d/13xf5Gz_oJJHnASf8p7cXyR_mY6q-TTNn/view?usp=drive_link Raman Shift Analysis

https://drive.google.com/file/d/1dJGrIfT11wdUrtG9m6jQzJZ2uEwDWqV5/view?usp=drive_link XRD-Without rGO

https://docs.google.com/spreadsheets/d/1hPNb3tUCZ1FHrqkYZjHWacHREOCp-EaJ/edit?usp=drive_link&ouid=101795013904677565451&rtpof=true&sd=true XPS-2 Analysis

https://drive.google.com/file/d/1usDD5saUDf7OmKDOqB24_i2oYEcGfTeW/view?usp=drive_link XRD-With rGO

https://docs.google.com/spreadsheets/d/1k25FVTKAZjn3gVvpOauvEDD7IMy5dbL9/edit?usp=drive_link&ouid=101795013904677565451&rtpof=true&sd=true XPS-4 Analysis

https://docs.google.com/spreadsheets/d/1LRB5rV0y6q_rA02qulf34RP8m9m57eJE/edit?usp=drive_link&ouid=101795013904677565451&rtpof=true&sd=trueLattice Parameters. https://photos.app.goo.gl/Lzhgyhh1f2qwpoSX6GC Data

B.2 Plagiarism Certificate

Appendix

SR486

ISO 9001:2019 Certified Institution

THESIS WRITING COURSE

PLAGIARISM AWARENESS CERTIFICATE

This certificate is awarded to

JOAN JEPTUM KIPTARUS

ENG/DPHIL/IE/02/18

In recognition for passing the University's plagiarism

Awareness test for Thesis entitled **DEVELOPMENT, CHARACTERIZATION AND EVALUATION OF SELECTED TRANSITION METAL DOPED ZINC SULPHIDE NANOSTRUCTURE SURFACE LAYERS DECORATED WITH GRAPHENE FOR WATER SPLITTING** with similarity index of 22% and striving to maintain academic integrity.

Word count: 60044

Awarded by

Prof. Anne Syomwene Kisilu
CERM-ESA Project Leader Date: 09/04/2024